Doctoral Dissertation
Doctoral Program in Chemical Engineering (33th Cycle)

Development and biostability evaluation of hybrid nanoconstructs for cancer therapy based on zinc oxide nanocrystals

Bianca Dumontel
* * * * * *

Supervisor
Prof. Valentina Cauda

Politecnico di Torino
November 2020

I hereby declare that, the contents and organisation of this dissertation constitute my own original work and does not compromise in any way the rights of third parties, including those relating to the security of personal data.

…….....

Bianca Dumontel

Turin, November 27, 2020

Summary

Cancer is a leading cause of death, second only to cardiovascular diseases, and its large diffusion and incidence, together with the numerous drawbacks associated with antitumor traditional therapies, made the research of new diagnostic and therapeutic strategies of paramount importance. In recent years, promising options were offered by nanomedicine which envisages the application of nanomaterials to the medical field to formulate more selective and stable therapeutic tools.

In this context, this PhD thesis focuses on the development of a biocompatible and colloidally stable hybrid nanoconstruct for the targeted treatment of cancer cells. The nanoconstruct, evocatively named TrojaNanoHorse (TNH), would be composed by a therapeutically active core made by chemically synthesized zinc oxide nanocrystals (ZnO NCs) encapsulated in a biomimetic shell of extracellular vesicles (EVs), opportunely functionalized with specific targeting moieties in order to further enhance their selectivity. The proposed hybrid nanoconstruct would combine the intrinsic delivery features of EVs, like their great stability in biological environment and low immunogenicity, with the toxicity of ZnO nanostructures toward cancer cells and the targeting capability of opportune engineered ligands.

More in details, the first part of the experimental work concerned the optimization of ZnO NCs synthesis and their physico-chemical characterization. Indeed, a reliable and reproducible synthetic procedure together with a precise evaluation of the features of the obtained ZnO NCs are essential for the accurate study of their biological effects. In this phase, two synthesis methods (i.e. a conventional solvothermal method and a microwave-assisted synthesis) were evaluated, analyzing the internalization rate and cytotoxicity of the obtained ZnO NCs on KB cancerous cells and decreeing the major reliability of microwave-assisted synthetic method.

The colloidal and chemical stability of synthesized ZnO NCs in the biological environment were then evaluated, analyzing the aggregation and dissolution extent through long-term biostability tests. The stability and the interaction with media components, in fact, would determine the biological identity of nanoparticles, directly affecting the biological response. The assays were performed in different

biological media, evaluating the behavior of eithers pristine and functionalized nanocrystals. In particular, ZnO NCs coated with a shell constituted by synthetic phospholipids were analyzed as a preliminary model of the proposed hybrid nanoconstruct, confirming the stabilizing effect ensured by the lipid envelope.

The actual TNH hybrid nanoconstruct was then developed, combining the synthesized ZnO NCs with EVs extracted from the conditioned cell culture supernatants of KB cancerous cells. The encapsulation was performed through a co-incubation method, optimizing several operating parameters to maximize the interactions between the two components and, thus, the loading efficiency. The effect of the EVs lipid-shielding on the colloidal stability, cellular toxicity and internalization was evaluated, comparing the behaviour of the obtained TNHs with uncoated ZnO NCs. The results evidenced a great improvement of colloidal stability in biological media accompanied by a more efficient internalization in KB cancer cells of TNH nanoconstructs with respect to pristine ZnO NCs. The samples presented a comparable cytotoxicity, highlighting that EVs shielding fully preserve the intrinsic toxicity of ZnO NCs.

The construction of TNH was further optimized in order to obtain a safer and more effective product. Primarily, to overcome safety concerns related to the application of EVs derived from cancer cells, the EVs cell source was changed, extracting the biovesicles from B lymphocytes. Moreover, the loading efficiency was optimized by the application of an active loading method, based on the application of freeze-thaw cycles as active stimulus to destabilize EVs membrane and favor the encapsulation of ZnO NCs. Two different procedures were implemented and analyzed in terms of loading efficiency, colloidal stability and morphology, evidencing the suitability of freeze-thaw method to efficiently encapsulate ZnO NCs within biologically-derived EVs, while preserving their morphology and surface protein expression. Finally, to further improve the TNHs selectivity, a functionalization method to decorate the EVs surface with specific targeting antibodies was designed and preliminary validated.

The results presented in this PhD thesis follow the development of an innovative hybrid nanoconstruct for cancer treatment based on therapeutically active ZnO NCs. The main goal of this study was the biostabilization of synthesized nanocrystals obtained through their encapsulation in EVs. The biological origin of EVs would improve the biomimetic and biocompatible features while guaranteeing the efficient intracellular release and the prominent cytotoxic activity of ZnO, making the whole nanoconstruct a promising candidate for therapeutic applications against cancer cells.

Acknowledgment

The work presented in this thesis is the result of the dedication and support of many people who contributed in different ways to my PhD studies and related research. First and foremost, I would really like to thank my supervisor Prof. Valentina Cauda for giving me this opportunity and for her patience, motivation and willingness. I would also like to thank all the members of TNH lab, Nadia Garino, Tania Limongi, Giancarlo Canavese, Marco Laurenti, Sugata Barui and Silvia Appendino and especially all my PhD colleagues of these three years, Marta, Luisa, Veronica, Marco, Francesca and Andrea who helped me with experiments and shared with me many moments in lab and breaks. I gratefully acknowledge Mauro Raimondo for FESEM analyses, Alberto Casu and Andrea Falqui (King Abdullah University of Science and Technology), Angelica Chiodoni (Italian Institute of Technology of Torino), Doriana Debellis and Roberto Marotta (Italian Institute of Technology of Genova) for TEM analyses and Andrea Giugni (King Abdullah University of Science and Technology) for the development of the theoretical model presented in Chapter 5.

Personally, I would like to thank all the current and former members of my extended office who made the workplace friendly and fun. A big thank goes to my friends, especially Federica for her thoughtfulness, Ivana for the long-distance support, Ilenia for all the brunches and chats and Francesca and Alice for our longtime friendship and constant sustain. A special thank goes to Marta for her positivity, understanding and sincere support. And of course, I deeply thank my parents for their unlimited encouragement and sustain.

To Lina, Nadia
and Massimo

Contents

List of Tables

List of Figures

Chapter 1

Introduction to nanoparticles for cancer treatment and Thesis structure

1.1 Introduction

1.1.1 Cancer

According to the World Health Organization (WHO) cancer is the second most common cause of death worldwide, second only to cardiovascular diseases. Globally, cancer is responsible of 1 in 6 deaths for an estimated amount of 9.6 million deaths in 2018. About 70% of deaths caused by cancer disease occur in low or middle-income countries and the most lethal types of cancers are in order lung, colorectal, stomach, liver and breast cancer. Estimates of cancer incidence and mortality are provided by International Agency for Research on Cancer (IARC), considering 36 types of cancer and 185 countries and territories. These predictions, based on 2018 data and considering demographic changes, calculate that cancer will have an incidence of 29.5 million cases and a mortality equal to 16.4 million in 2040.

From these data and estimates result clear that cancer is a major public health problem globally and the research of new diagnostic and therapeutic options is of prominent importance. In this perspective, the comprehension of the cancer pathophysiology and biological mechanisms is fundamental.

The term ‘cancer’ comprehends more than 100 diseases that can be developed in almost any tissue in the body and present individual features. However, cancer is generally characterized by the uncontrolled division of abnormal cells that can invade surrounding tissues or spread over the body through blood and lymphatic systems (NIH, 2007). A review published by Hanahan and Weinberg in 2000 systematically analyzes the differences between cancerous and normal cells, attributing the complexity of cancer biology to six major hallmarks (Hanahan & Weinberg, 2000). The proposed essential alterations of cells physiology that collectively determine the tumor development are a self-sufficiency in growth signals accompanied by an insensitivity to anti-growth signals, the capability to evading programmed cell death (i.e. apoptosis) and an unlimited replicative potential. Furthermore, cancerous cells can promote angiogenesis to ensure the required provision of oxygen and nutrients and can present a marked tendency to tissue invasion (i.e. metastasize). In an updated edition published in 2010, the authors add two supplementary characteristics. To support the unlimited cell growth and proliferation, cancerous cells present a major reprogram of cellular energy metabolism. Furthermore, malignant cells are commonly able to elude the immunological response of natural killer cells, macrophages and T and B lymphocytes (Hanahan & Weinberg, 2011).

Regarding its origin, cancer disease arises from complex DNA mutation, acting mainly on two categories of genes, i.e. proto-oncogenes and tumor suppressor genes. In normal conditions these genes regulate the cell cycle, respectively promoting or inhibiting the division of cells, and thus guaranteeing the correct tissue and organ development. However, alteration of proto-oncogenes produces oncogenes, which stimulate an excessive cellular division, while tumor suppressor genes are inactivated by the mutation, eliminating the inhibition for cellular

excessive growth (Lodish et al., 2000). The clonal expansion of mutated cell together with the accumulation of other molecular changes will produce the development of cancer malignant state in a multi-step process (Yamamoto et al., 2015). In their evolution, cancerous cells will acquire all the hallmarks previously described generating a tumor mass with abnormal vasculature and ability to produce metastasis, as represented in **Figure 1.1**.

The causes of the mutation can be hereditary or induced by external chemical, physical or biological agents and can affect different cells populations in the lineage hierarchy, producing several tumor subtypes (Visvader, 2011).

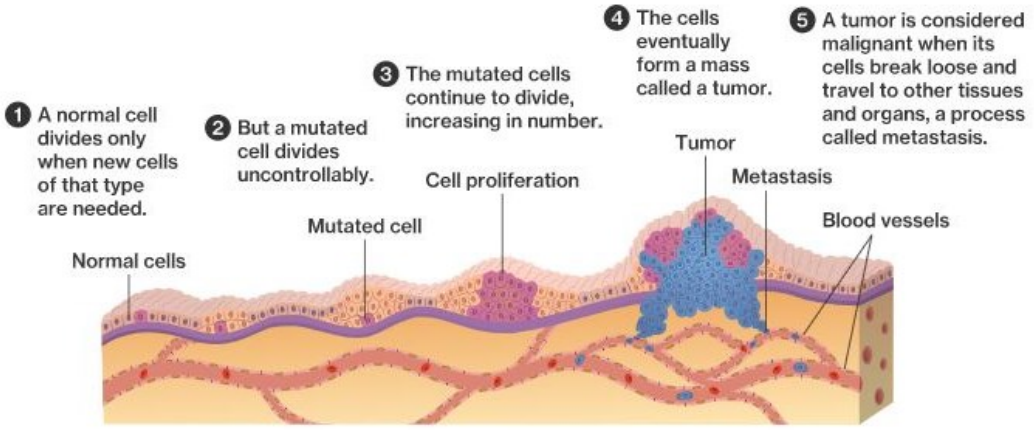

Figure 1.1: Stages of tumor development represented as a multi-steps process from cells mutation to the formation of tumor mass and abnormal vasculature; figure from (NIH, 2007).

1.1.2 Traditional therapies

The large diffusion and incidence of cancer disease have led to the development of different therapeutic options over the years. The most common traditional therapies applied alone or in combination are surgery, chemotherapy and radiotherapy and the selection of the treatment depends on several aspects, like type of cancer, location of the tumoral mass and stage of progression (Arruebo et al., 2011).

For solids tumors, minimally invasive or open surgery are often applied to physically remove the tumor mass from the body. Even though surgical treatment remains one of the basic method for oncology, it is important to mention that it is associated with several side effects characteristic of all the surgical operations and present several problems of recurrence and metastases. To overcome these limitations, the surgical strategy is often combined with adjuvant treatments like radiotherapy and chemotherapy. Radiotherapy and chemotherapy are widely applied also as stand-alone treatments, to treat both solid and circulating tumors. In case of radiotherapy, high energy radiations are employed to directly damage DNA of cancerous cells, impairing the cellular division and growth. The application of radiation therapies can also cause the generation of free radicals which will cause genetic damages, helping cells death (Abbas & Rehman, 2018).

Conversely, chemotherapy consist in the injection of chemical substances (such as alkylating agents, antimetabolites, mitotic inhibitors…) that selectively interact with cells in particular phase of their division, interfering with the process.

However, both therapeutic options present lack of specificity which cause the insurgence of substantial side effects that impair their application. Collateral effects of radiation therapy are connected to the damage of healthy cells and tissues near the treatment area. On the other hand, chemotherapeutic agents could affect not only cancerous cells but also other type of cells, causing collateral effects of variable severity including myelosuppression, hair loss, gastrointestinal damages and compromised wound-healing (Regan, 2007). In addition, chemotherapeutic drugs are characterized by a poor bioavailability, requiring the use of higher doses which increase the probability of side effects and the incidence of drug resistance phenomena (Senapati et al., 2018).

A possible response to this lack of specificity is constituted by immunotherapy or immune-oncology. This gained great attention during the last decade of 1900 and today it is widely applied, with several immunotherapy-based drugs approved by the Food and Drug Administration (FDA). Cancer immunotherapy rely on the artificial stimulation of innate immune system against malignant cells and include a variety of treatments like cancer vaccines, oncolytic virus therapy, immunomodulators, adoptive cells therapy and targeted antibodies (Yiping Yang, 2015). The last category and in particular monoclonal antibodies are largely diffuse at the moment with more than 60 monoclonal antibodies approved by FDA (Tsumoto et al., 2019).

Monoclonal antibodies are classified as passive immunotherapeutics, since they directly bind to target malignant cells recognizing specific or overexpressed tumor receptors. The antigen-antibody bond could then cause the disruption of cellular pathways or activate the recognition of cancer cells by immune system, leading to cell death. The recognition of cancer receptors ensures a more selective treatment of malignant cells, reducing the occurrence of side effects. However, monoclonal antibodies require a precise serological characterization of cancer and normal cells and are, thus, characterized by high production costs. Moreover, they still possess a poor bioavailability and slow biodistribution as well as some side effects (W. Wang et al., 2008) which remain the major issues of conventional cancer treatments.

1.1.3 Nanomedicine

Considering the described drawbacks of traditional therapies, the investigation of innovative treatments with improved selectivity and pharmacokinetic is particularly valuable.

A targeted treatment would guarantee the restriction of the therapeutic effect on a specific category of cells, reducing the non-specific toxicity and, thus, any side effect. More in general, the improvement of treatment selectivity, stability and distribution inside the organism would enhance its efficiency, ensuring an appropriate drug concentration only in the targeted organ or tissue resulting in a

decrease of dose and administration frequency. This would increase the therapeutic index (i.e. the ratio between the maximum tolerated and the minimum effective dose) and the overall drug safety. Indeed, the reduction of fluctuations in drug concentration and the avoidance of toxic over-dosages would consent to limit the insurgence of undesired side effects, improving the life quality of patients (S. I. Shen et al., 2003).

A great opportunity to pursue these goals is offered by nanomedicine. The term "nanomedicine" refers to the application of nanotechnologies to the medical fields. Indeed, materials with size range between 1 and 100 nm, i.e. nanomaterials, possess several interesting physico-chemical features and their dimension guarantees very close interactions with biological components. In this context, nanoparticles with various compositions and morphologies are studied for their application in cancer treatment, exploiting either the intrinsic cytotoxic properties of the nanomaterial or their ability to act as a carrier for traditional chemotherapeutic agents (Lim et al., 2015).

The targeting mechanism of nanomaterials as well as their variety and principal challenges are summarized in the subsequent sections.

1.1.3.1 Nanoparticles: targeting methods

The category of nanomaterials comprehends nanoparticles with very different compositions and properties, which are all linked by the common feature of reduced dimensions. This characteristic is particularly interesting for cancer therapy, since it allows to exploit the typical pathophysiology of tumor areas to enable the specific accumulation of nanomaterials.

As already mentioned, tumor cells promote the angiogenesis, i.e. the formation of new blood vessels, to guarantee the delivery of oxygen and nutrients during their uncontrolled growth. However, compared to healthy tissues, the tumor areas present an altered and non-uniform vasculature. In fact, the new vessels are characterized by a leaky endothelium with larger pores that allow the passage of nanoparticles and are also accompanied by a lack of lymphatic drainage that causes the accumulation of the particles penetrated inside the tissue. Together these pathophysiological features cause the so called enhanced permeability and retention (EPR) effect which is responsible for the higher uptake of nanomaterials or molecules from cancer tissues. The preferential accumulation inside tumor tissues with respect to healthy ones was observed for the first time in 1986 and goes under the name of "passive targeting" (Matsumura & Maeda, 1986).

However, this mechanism present evident limitations, especially related to the redistribution and cellular internalization of nanomaterials extravasated in the interstitial space (X. Wang et al., 2009). These problems gave rise to new approaches that envisage the attachment of specific ligands to the nanomaterials surface, conferring an "active targeting" capability. The active targeting exploits the enhanced or specific expression of particular receptors by cancer cells that can be recognized by different types of molecules, conveniently attached on the nanoparticles surfaces. The class of possible functionalizing agents comprehend

antibodies, aptamers, peptides or other synthetic and biological molecules (X. Wang et al., 2009).

Combined to EPR effect, this second strategy significantly improves the specificity toward malignant cancer cells as schematically represented in **Figure 1.2**. In addition, it also opens the possibility to target circulating cells of hematological tumors (Vinhas et al., 2017).

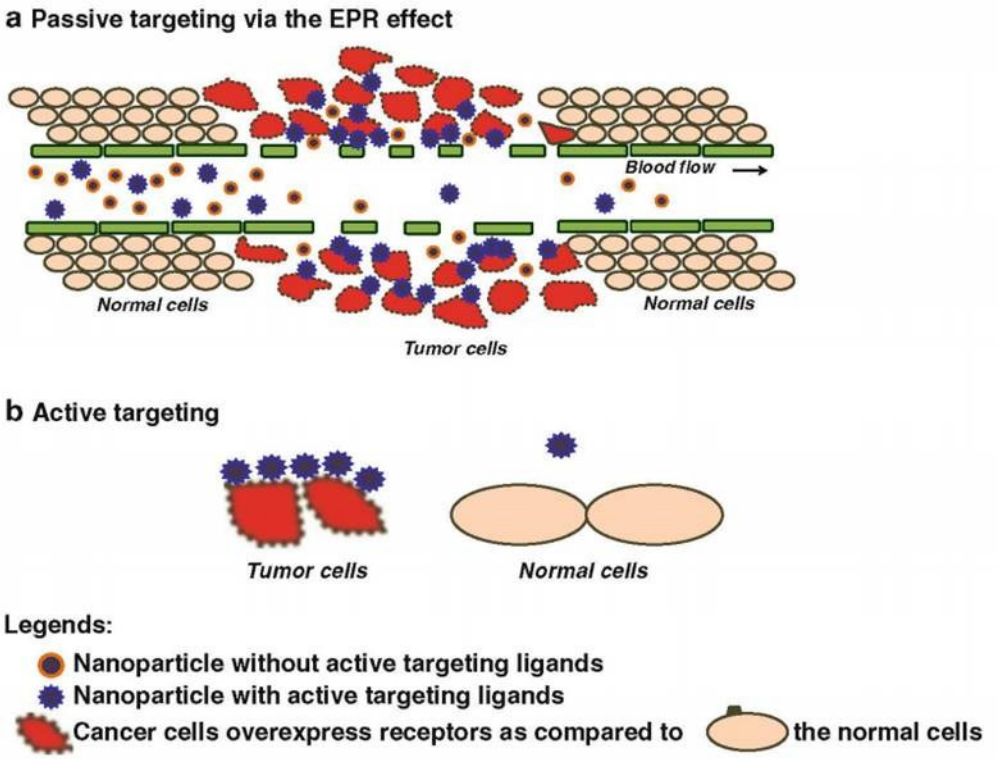

Figure 1.2: Schematic representation of **(a)** active and **(b)** passive targeting mechanisms of nanoparticles; figure from (Upponi & Torchilin, 2014).

1.1.3.2 Nanoparticles: categories and challenges

As already mentioned, the category of nanomaterials investigated for oncological applications comprehend particles with different compositions ranging from lipidic and polymeric nanoparticles to carbon-based and metallic nanoparticles. In addition, they can possess diverse functions and act as therapeutic agents themselves or serve as nanocarriers to transport traditional drugs.

Several types of nanoparticles are applied in combination with traditional chemotherapeutic agents, to stabilize the drugs during blood circulation, improving their biodistribution and avoiding an immediate clearance by the immune system. For this application as nanocarriers, polymeric-based, hydrogels, albumin- and lipid-based nanoparticles are the most widely used, thanks to the ability to incorporate the active principle in their structure through physical and chemical interactions (Estanqueiro et al., 2015). In particular, Doxorubicin-loaded liposomes for the treatment of Kaposi's sarcoma were the first particles approved by FDA in 1995, followed by several other formulation in most recent years (Petre & Dittmer, 2007). For instance, lipids and polymeric carriers functionalized with appropriate

targeting moieties are studied to improve the selectivity of nanocarriers (Estanqueiro et al., 2015). Most recently, the construction of stimuli-responsive systems, constituted by organic nanoparticles able to release their payload following internal or external stimuli (such as pH, ionic strength, temperature, light, ultrasound, …) are widely investigated in order to guarantee a more efficient and selective delivery of the drug (Mura et al., 2013). Between the inorganic nanoparticles, micro and mesoporous silica nanoparticles are promising candidates for drug delivery purposes thanks to their high drug adsorption capability and possibility to achieve stimuli-controlled release (J. Zhu et al., 2017).

Recently, the intrinsic antitumoral properties of several types of nanoparticles were also analysed, considering their possible application as therapeutic or diagnostic tools without the combination with traditional drugs. This category comprehends mainly inorganic nanoparticles, such as metallic, metal oxides and magnetic nanoparticles. For instance, magnetic nanoparticles, primarily constituted by iron or manganese oxides, are applied in combination with alternated magnetic field causing hyperthermia and subsequent tumour thermal ablation (Latorre & Rinaldi, 2009). The same hyperthermia effect was obtained using gold nanoparticles activated by infra-red light (Cherukuri et al., 2010). Moreover, conducting or semiconducting metal oxide nanoparticles, like TiO_2 or CeO_2, are able to cause cells death probably due to their catalytic activity. In fact, these nanoparticles, opportunely stimulated with UV radiation or ultrasound, are able to participate to redox reactions in the cellular environment, increasing the level of reactive oxygen species (ROS) and triggering oxidative stress (Canavese et al., 2018). Finally, semiconducting nanoparticles with very small dimensions (2-10 nm), named quantum dots, are investigated for bioimaging purposes thanks to their peculiar optical properties acquired with the size reduction (Xiong, 2013).

The heterogeneity of the tested materials together with the possibility to tune their properties and properly functionalize their surface are well represented in **Figure 1.3**.

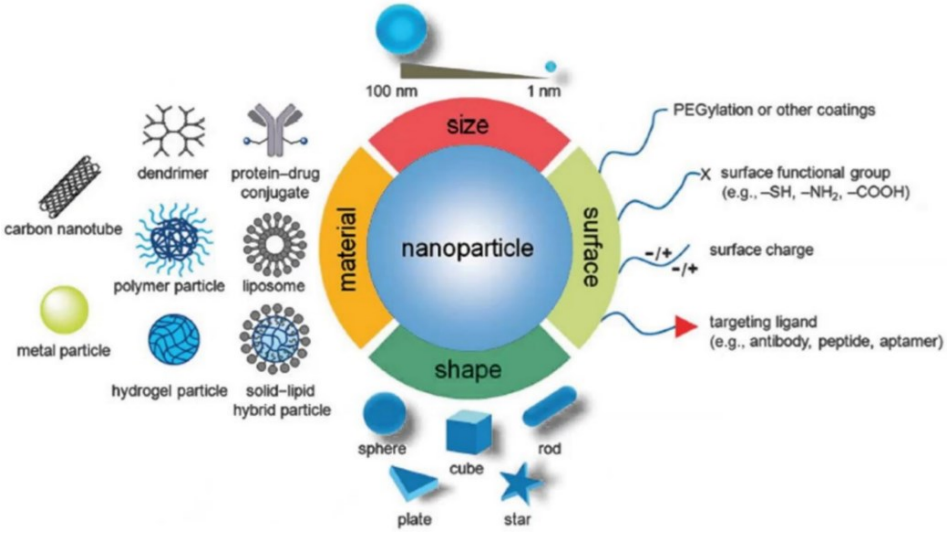

Figure 1.3: Schematic representation of the great variety of nanoparticles investigated for nanomedical applications which present different composition and tunable physico-chemical properties; figure from (Qin et al., 2017).

The reduction to the nanoscale confers to nanomaterials not only the possibility to uniquely interact with cells and tissues but it also guarantees an interesting surface reactivity (Villanueva-Flores et al., 2020). In fact, with respect to bulkier materials, they present an increase of specific area which ensures a high loading capacity and the possibility to properly functionalize their surfaces, for example for targeting purposes. The wide variety of composition and fabrication processes allows also to obtain nanoparticles with multiple and various sizes and shapes. The possibility to actively control and modify the physico-chemical properties of the nanoparticles is a great advantage and allows to obtain tools with optimized therapeutic effects. However, it is really important to implement simple synthetic procedures and avoid multistep processes in order to guarantee the scalability to industrial production while maintaining a precise control of nanomaterials characteristics (Liu et al., 2016).

Moreover, several challenges concerning their *in vivo* distribution, biocompatibility and degradability hinder the effective application of nanoparticles in clinical field (Almeida et al., 2011). Frequently, the toxicity of the nanocarriers is not adequately considered and a lack of biodegradability could cause an ineffective bio-elimination or the formation of toxic byproducts during the degradation process (Nicolas et al., 2013).

Furthermore, once injected in the blood circulation, nanoparticles undergo to protein adsorption which determine their biodistribution. In fact, the absorption and conformational changes of particular proteins (opsonins) are responsible for the recognition of nanoparticles by the immune system and subsequent elimination by mononuclear phagocyte system (MPS) and reticuloendothelial system (RES). This phenomenon regulates the bioavailability and the mean circulation time of nanomaterials inside the organism and could be controlled acting on the physico-chemical properties of the particles. In general, literature studies indicate 150 nm as maximum size limit to avoid MPS clearance and spleen filtration (Moghimi et al., 2012). Concerning the surface properties, nanoparticles with hydrophobic surface and positive charge present higher protein adsorption and elevated clearance rates. Thus, surface functionalization with hydrophilic polymers (like PEG, zwitterionic polymers,..) or biological molecules (like proteins or lipids) are well established, guaranteeing a lower surface fouling and an improvement of circulation time (Limongi et al., 2019). However, more recent studies highlighted also a possible beneficial effect of the proteins adsorption that could facilitate cellular uptake and determine intracellular distribution (Salvioni et al., 2019).

This dual effect of proteins absorption well underlines the complexity of the interactions between nanoparticles and biological media and systems, which clearly entangle the process of optimization of innovative therapeutic nanoparticles.

1.2 Aim of the work and Thesis structure

1.2.1 TrojaNanoHorse (TNH) project

As detailed in the introduction section, the application of nanotechnologies to the clinical and medical fields offers a great opportunity for the development of innovative therapeutic options for the treatment of cancer disease. In fact, nanomedicine allows the production of nanomaterials with tuneable properties able to overcome some drawbacks of traditional therapies, like poor biodistribution, lack of selectivity and insurgence of side effects.

In this context stands the creation of the hybrid nanoconstruct described in this thesis. The work described in this PhD thesis is part of a wider project called "TrojaNanoHorse" founded by a European Research Council (ERC) Starting Grant and led by Prof. Valentina Cauda at Politecnico di Torino. The aim of the project is the construction of a fully biocompatible, non-immunogenic and degradable hybrid nanoconstruct for both cancer treatment and diagnosis in a nanotheranostic innovative approach.

The devised innovative nanoconstruct is composed by a therapeutically active core made by chemically synthesized ZnO crystalline nanoparticles (ZnO NCs) encapsulated in a biomimetic shell of extracellular vesicles (EVs) isolated from conditioned cell culture supernatants. The biologically derived lipid shell would be further functionalized with appropriate targeting ligands to improve their selectivity toward malignant cancer cells. The ZnO was selected as therapeutic material thanks to its intrinsic cytotoxic properties accompanied by interesting optical properties and general safety and biodegradability. The EVs lipid coating had the dual task to improve the biostability and biocompatibility of the nanoconstruct. In fact, the biological origin of EVs guarantees their low immunogenicity and could help to prevent the recognition of ZnO NCs by the immune system. In addition, EVs are normally involved in intercellular communication and so they possess an intrinsic stability in blood circulation as well as a great capability to cross biological barriers. These features are particularly interesting for drug delivery applications and were exploited to stabilize the ZnO NCs in biological environment and ensure a better interaction with cells. Finally, targeting moieties were added to further improve the selectivity of the proposed nanoconstruct. The targets of the project are Daudi cells, a cancerous cell line derived from Burkitt lymphoma, an aggressive type of B cells non-Hodgkin lymphoma. Thus, the chosen targeting moiety was an anti-CD20 monoclonal antibody, directed against CD20 protein, a general marker for B cells on all developmental stages which is over-expressed by lymphomas B-cells. In principle, choosing different targeting ligands, the nanoconstruct could be adapted for the treatment of other types of cancer.

The corresponding mechanism of action envisages the injection of the produced hybrid nanoconstructs inside the body and their selective accumulation inside target cancerous cells, avoiding the clearance by the immune system. At this point, the core of ZnO NCs would exert the cytotoxic activity. Due to its selective cytotoxicity and biomimetic feature, the nanoconstruct was named TrojaNanoHorse (i.e. TNH).

My role in this project mainly concerned the construction and the optimization of TNH hybrid nanoconstruct and the evaluation of its colloidal and chemical stability in the biological environment.

1.2.2 Thesis structure

The results obtained during this work of thesis are divided in four chapters, as described below.

In **Chapter 2** the main properties, the existing synthetic methods and the antitumoral potential of ZnO NCs are described, starting from a brief revision of literature studies. The investigated synthetic procedures and the physico-chemical characterization of the obtained ZnO NCs are then presented. In particular, a novel microwave-assisted solvothermal synthesis was performed and compared with a traditional wet synthetic approach. The obtained ZnO NCs were fully characterized in terms of size, morphology, surface composition and optical properties with particular attention at their colloidal behavior, analyzed in ethanol and water. Moreover, the biological effects of both types of ZnO NCs on cancerous cells were studied, evaluating their internalization rate and cytotoxicity as a function of different synthetic routes and physico-chemical characteristics.

The **Chapter 3** reports the evaluation of colloidal and chemical stability of ZnO NCs in biological fluids and analyze the influence of surface functionalization. An overview of the main challenges and functionalization techniques to improve nanoparticles stability in biological environment are reported in the Introduction section. Experimentally, the synthesized ZnO NCs were coated with a synthetic lipid shell made by 1,2-dioleoyl-sn-glycero-3-phosphocholine (DOPC) as preliminary simulation of the hybrid nanoconstruct. The behavior of pristine and functionalized NCs was then evaluated through biostability assays, performed in phosphate-buffered saline (PBS), simulated body fluid (SBF) and in Eagle's minimal essential medium (EMEM). In particular, the extent of aggregation and dissolution were evaluated, since both parameters could deeply affect the biological application of ZnO NCs.

In **Chapter 4** the optimization of TNH nanoconstruct, obtained combining the synthesized ZnO NCs with extracellular vesicles (EVs), is described. A description of EVs general properties together with the collection protocols and loading methods reported in literature is presented in the Introduction section. The EVs used for the experiments described in this chapter were extracted from conditioned cell culture supernatants of KB cancerous cells through a well-established differential ultracentrifugation protocol and coupled with ZnO NCs following a co-incubation method. The coupling efficiency was optimized adjusting several operating parameters and exploiting a combination of thermodynamic, kinetic and electrostatic mechanisms directly related to the EVs and NCs properties. The effect of the EVs lipid-shielding on the colloidal stability, cellular toxicity and internalization was evaluated, comparing the behaviour of the obtained TNHs with uncoated ZnO NCs.

In **Chapter 5** the principal challenges for the effective biomedical application of EVs are described together with the major methods for vesicles surface functionalization. The reported results concerned a second method for the TNHs construction. Firstly, in order to address safety issues related to the cell of origin, the EVs utilized here were extracted from B lymphocytes, the normal counterpart of Daudi cancerous cells. Moreover, a new coupling procedure based on the application of freeze-thaw cycles as active stimulus to destabilize EVs membranes was defined and investigated in term of coupling efficiency and colloidal stability. Finally, the possibility to decorate EVs surface with anti-CD20 antibodies to improve the TNHs selectivity was investigated.

Chapter 2

Physico-chemical properties and biological effects of synthesized zinc oxide nanocrystals

2.1 Introduction

2.1.1 ZnO NPs: properties and synthesis methods

ZnO is an extensively studied material whose physical characterization in terms of lattice parameters and optical properties dates back to the middle decades of 1900 (Özgür et al., 2005). ZnO is classified as II-IV semiconductor compound with a direct wide band-gap equal to ~3.3 eV at room temperature and it can present three crystalline structures: rocksalt, zinc blende and wurtzite (represented in **Figure 2.1**).

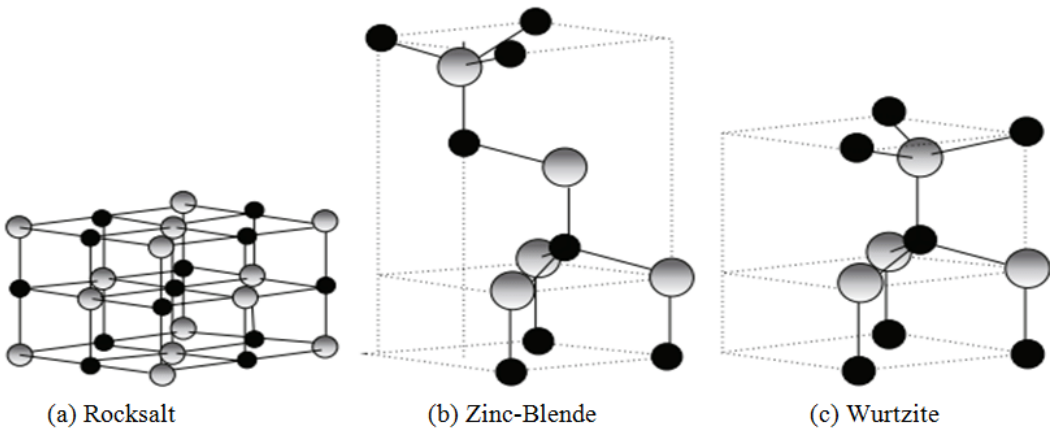

Figure 2.1: ZnO crystalline structures: **(a)** Rocksalt; **(b)** Zinc-Blende and **(c)** Wurtzite. Grey spheres represent Zn atoms while black spheres represent O atoms; figure from (Morkoç & Özgür, 2009).

Under ambient temperature and pressure, the hexagonal wurtzite structure is the most thermodynamically stable. This is composed by two interpenetrating hexagonal closed packed (hcp) sublattices in which each Zn atom is at the centre of a tetrahedron with four O atoms at the corners and vice versa. All the tetrahedrons are oriented in a single direction and the resulting structure is thus composed by an alternation of planes of Zn and O atoms along the *c*-axis. Typically, the tetrahedral coordination is characteristic of sp^3 covalent bonds, but ZnO material shows also a strong ionic behaviour that contribute to increase its band gap value (Morkoç & Özgür, 2009). In addition, the tetrahedral coordination of ZnO results in a non-centrosymmetric structure that provides piezoelectric and pyroelectric properties (Vaseem et al., 2010).

ZnO exhibits interesting optical and luminescent properties. Wurtzitic ZnO normally presents a strong UV adsorption and two photoluminescent emission bands in both UV and visible regions. The emission centred in the UV region, near the adsorption edge of the crystal, is directly connected to the semiconductor nature of ZnO and its band gap and has a relatively high yield thanks to the large exciton binding energy (60 meV) of the material (Chernenko et al., 2018). The origin of the broader band in the green visible region, conversely, is not completely understood and tentatively attributed to the presence of point defects in the crystalline structure and, in particular, to oxygen vacancies (L. Zhang et al., 2010). As well documented in the literature, the interesting optical and luminescent properties of ZnO nanostructures can be efficiently enhanced and modulated acting on their

dimensions and morphologies (Mousavi et al., 2011) or introducing suitable doping elements, such as group III elements or transition metals (Carofiglio et al., 2020).

These peculiar physical properties, along with high thermal and mechanical stability, rigidity and large electron mobility, promoted the application of ZnO structures in several fields of nanotechnology, ranging from energy generation, optoelectronic and sensors to cosmetic and biomedical applications. In addition, ZnO nanostructures can be easily synthesized using accessible raw materials and with low production costs, obtaining nanomaterials with desired size and morphology, requested for the particular application (Cauda et al., 2014).

The synthesis of ZnO can be performed by chemical, physical and biological methods, as schematically represented in **Figure 2.2**. Briefly, physical methods are essentially top-down preparation processes in which an existing material is reduced to nanometric dimension by physical or mechanical means. In contrast, chemical synthesis methods use precursors that react in liquid or gas phase, providing the atomic or molecular units between which the chemical bonds will be formed in a bottom-up approach (Kumar et al., 2018). Finally, the most recently developed biological methods involve enzymes and other biomolecules produced by plants or microorganisms to reduce metal ions to metal oxide ZnO NPs (Mohd Yusof et al., 2019).

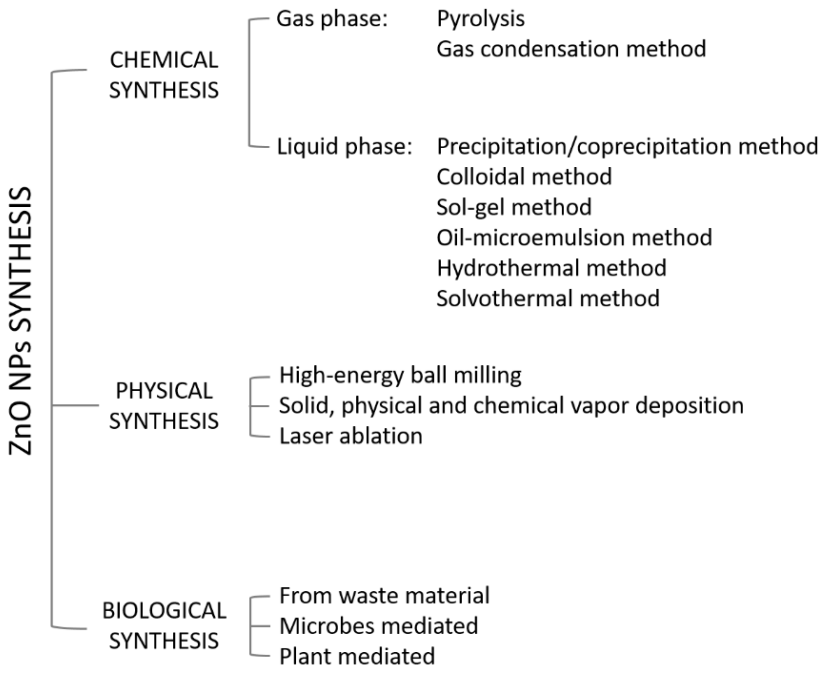

Figure 2.2: Principal synthetic methods for the production of ZnO NPs; figure adapted from (Naveed Ul Haq et al., 2017).

In general, the liquid phase chemical methods are the most widely used to produce ZnO NPs because they present multiple advantages in term of costs, low reaction temperatures and availability of reagents. Most importantly the modulation of synthetic parameters of wet chemical processes allows to obtain a valuable control on the morphology and size of the final products.

The precursors used for the synthesis of ZnO nanomaterials include inorganic salts and organic zinc compounds that are able to hydrolyze in alkaline solutions forming tetrahedral coordination compounds ($(Zn(OH)_4)^{2-}$). The subsequent hydrolysis of these intermediates leads to the formation of crystalline zinc oxide. Based on this general mechanism and opportunely tuning the precursors and solvents or the synthetic conditions, it is possible to obtain different structures including nano- and microparticles, multipods, nanowires and nanorods (Cauda et al., 2014). The possibility to obtain ZnO nanostructures with controlled size and geometries is particularly interesting for biomedical applications. Several studies, in fact, show that both NPs size and morphologies deeply affect their transport inside the body, biodistribution and interaction with cells, tissue and the immune system (Champion et al., 2007).

Moreover, the chemical surface properties of synthesized ZnO NPs, which are essentially regulated by the presence of hydroxyl groups (–OH), impart to ZnO interesting electrostatic characteristics for biomedical applications, as will be further elucidated in the next section. The presence of reactive –OH groups on the ZnO nanoparticles surface also enables their functionalization with several chemical groups or biomolecules in order to enhance their applicative potential in the biomedical field. For instance, PEG (Luo et al., 2014) and other polymers (Zheng et al., 2019) can be used to prevent the nanoparticles aggregation and improve their biocompatibility, *in vivo* circulation and stability. Moreover, surface functionalization with targeting moieties like folic acid, hyaluronan and different kinds of proteins, peptides and nucleic acids are widely reported in literature, allowing the enhancement of ZnO NPs selectivity toward cancer cells (Jiang et al., 2018).

2.1.2 ZnO NPs in biomedical applications

According to the Food and Drug Administration (FDA), ZnO is a "generally recognized as safe" (GRAS) substance and it is considered a biocompatible material, since it can be biodegraded in Zn^{2+} ions and these can become part of organism nutritive elements (Zhou et al., 2006). Zinc cations, in fact, are essential trace elements in the human body and they are involved in multiple physiological and biological processes. In particular, zinc element is the co-factor of more than 300 enzymatic reactions, possess a structural role for several proteins and a regulatory role for both enzymes and proteins, influencing for instance immune, aging and neurological processes (Stefanidou et al., 2006).

This biocompatible feature, along with the previously mentioned physico-chemical characteristics and the possibility of easy synthesis and functionalization, promoted the application of ZnO nanostructures in various biomedical fields. Thanks to their UV adsorption capability, the ZnO NPs were efficiently employed as UV-blocker in sunscreens and self-care products from many years. More recently, ZnO nanostructures have been applied in the fabrication of hydrogen peroxide and glucose biosensors, thanks to the great electronic properties of the material and its stability and biocompatibility (P. Zhu et al., 2016). Similarly, ZnO

NPs are promising candidates between the semiconductor nanocrystals studied for bioimaging purposes because they show excellent and tuneable pholuminescent properties, accompanied by low price and general safety (Xiong, 2013).

However, it is worth to mention that GRAS designation normally refers to materials in their bulk or micrometric forms, while new toxic properties can be acquired when reduced to the nanoscale. As already detailed, ZnO nanostructures are characterized by peculiar mechanical, electronic and optical properties connected to their crystalline structure and to crystals defects, introduced also by the dimensional reduction. In addition, small NPs are characterized by a higher specific surface area that increase the percentage of atoms able to interact with external components, enhancing the material reactivity. Finally, the reduced dimensions are comparable to those of biological occurring molecules and ensure to the NPs an easier and direct interaction with cells and tissues (Rasmussen et al., 2010).

These considerations, together with the widespread use of ZnO nanostructures in various fields of nanotechnology, have promoted a more detailed evaluation of their toxicological potential toward the environment and to both prokaryotic and eukaryotic cells. However, the toxicity observed towards different types of pathogenic fungi (He et al., 2011) and bacteria (Sirelkhatim et al., 2015) opens up the possibility to use ZnO NPs as antimicrobial and antibacterial agents. Moreover, *in vitro* studies evidenced the preferential toxicity of ZnO NPs toward cancerous cells, suggesting their applications as antitumor agents (Hanley et al., 2008; Sasidharan et al., 2011; DeLong et al., 2017).

Some examples of application of ZnO NPs in the treatments of different cancer cell lines are summarized in **Table 2.1**, showing a cytotoxic effect which is dose-dependent and more effective with respect to other metal nanoparticles (Bai Aswathanarayan et al., 2018, Priyadharshini et al., 2014). As will be detailed in the next sections, the toxicity of ZnO NPs is mainly attributed to two mechanisms, i.e. intracellular release of Zn^{2+} ions and production of reactive oxygen species (ROS), and can be deeply affected by nanoparticles physico-chemical parameters. For example, the modification of ZnO NPs optical properties by Al-doping increase the oxidative-stress mediated cytotoxicity (Akhtar et al., 2015), while the nanoparticles size inversely affect the cytotoxic response. i.e. the smallest ZnO NPs showed the highest toxicity levels (Kang et al., 2013). As already mentioned, several studies describe the selective toxicity of ZnO NPs toward cancer cells, which is particularly interesting in the perspective of their therapeutic application, limiting adverse side effects toward normal cells (Hanley et al., 2008). Finally, ZnO NPs can be also used in combination with chemotherapeutic agents or other therapeutic molecules. In these applications the ZnO NPs exploit the function of nanocarrier, improving the delivery of active drugs or molecules inside the cancerous cells. In addition, they present a good release capability thanks to their solubility at low pH values and a synergistic effect which enhances the cytotoxic effect of the payload (Deng & Zhang, 2013, Perera et al., 2020).

Table 2.1: Exemplificative applications of ZnO NPs for *in vitro* treatment of different cancerous cell lines.

Type of NPs	Cell line	Therapeutic effect	Ref
ZnO NPs	HT29 cells (colorectal cancer)	ZnO NPs have significant anticancer activity compared to Au and Fe_2O_3 NPs	(Bai Aswathanarayan et al., 2018)
ZnO NPs	PC3 cells (prostate cancer)	More effective anticancer activity of ZnO NPs with respect to Ag NPs	(Priyadharshini et al., 2014)
ZnO NPs	LoVo cells (colon carcinoma)	Uptake dependent on NPs agglomeration. Contact with acid pH of lysosomes causes Zn^{2+} release, ROS production and DNA damage	(Condello et al., 2016)
ZnO NPs	HeLa cells (cervical carcinoma)	ROS production increased in a dose-dependent manner Cytotoxic effect through apoptotic pathway	(Pandurangan et al., 2016)
ZnO NPs	Caco-2 cells (colorectal adenocarcinoma) HepG2 cells (liver cancer)	ZnO NPs significantly induce cytotoxicity associated with increased intracellular Zn^{2+} ions	(Fang et al., 2017)
Pristine and Al-doped ZnO NPs	MCF-7 cells (breast cancer)	Al doping increase the band gap and enhance cytotoxic effect of ZnO NPs	(Akhtar et al., 2015)
ZnO NPs	Caco-2 cells (colorectal adenocarcinoma)	Time and dose-dependent cytotoxic effect Influence of particles size	(Kang et al., 2013)
ZnO NPs	Jurkat cells (acute T cell leukemia) Hut-78 cells (T cell lymphoma) vs normal T cells	ZnO NPa show preferential cytotoxicity toward cancer cells compared to normal cells (~28-35x)	(Hanley et al., 2008)
ZnO NPs	A375 cells (melanoma) vs normal NIH3T3	ZnO NPs show great selectivity against melanoma cancer cells	(DeLong et al., 2017)
Curcumin-loaded ZnO NPs	RD cells (rhabdomyosarcoma)	Additive anticancer effect of curcumin-loaded ZnO NPs	(Perera et al., 2020)
ZnO NPs with Doxorubicin	SMMC-7721 (hepatocarcinoma)	Increased intracellular concentration of Doxorubicin and synergic effect	(Y. Deng & Zhang, 2013)

2.1.3 ZnO NPs cytotoxicity and selectivity toward cancer cells

Due to the complexity of the parameters affecting the ZnO NPs biological behavior both *in vitro* and *in vivo*, the cytotoxicity mechanisms of ZnO NPs are not yet completely elucidated. Several studies attribute their toxicity to two main mechanisms: *(i)* the release of zinc cations (Zn^{2+}) and *(ii)* the production of reactive oxygen species (ROS).

As already said, zinc does not possess an absolute toxic effect and it is present as trace element in the human body, essential for several physiological and biological processes. In particular, zinc deficiency can cause relevant damages to immune, central nervous, epidermal, gastrointestinal, skeletal and reproductive systems, especially during the growing period, and the recommended daily dose in the diet is of ~10 mg. Even if the concentration of zinc bound to proteins or other ligands is high, the level of free Zn^{2+} present in the cells cytoplasm is really low (in

the order of picomoles) under normal conditions and precisely regulated through homeostatic mechanisms. In particular, the zinc concentration is regulated by metallothioneins, proteins able to bind and sequester Zn^{2+} ions from the cytoplasm, and by transporter proteins, located on the cell membrane and in various cellular organelles, that can regulate intracellular and extracellular zinc levels (Maret, 2017).

These regulation mechanisms are perturbed by the presence of ZnO NPs, which can dissolve, releasing Zn^{2+} ions. *In vitro*, the dissolution can occur either extracellularly due to the contact with culture media (Reed et al., 2012), or intracellularly due to the acidic pH of late endosomes and lysosomes (H. Müller et al., 2010) and it is still unclear if the cytotoxic effect is caused by one specific type of dissolution or a combination of both. Anyway, the release of Zn^{2+} ions from the NPs produces a disequilibrium in zinc homeostasis resulting in different cytotoxic effects. Firstly, mitochondria react to the rising level of zinc with the sequestration of Zn^{2+} cations which cause changes in the membrane potential and the collapse of the organelles with subsequent release of apoptotic signals (J. H. Li et al., 2012). In addition, elevated level of Zn^{2+} can cause the overexpression of methallothioneines, proteins responsible of zinc sequestration. Their massive production is detrimental for the synthesis of other proteins leading to protein activity disequilibrium (Bisht & Rayamajhi, 2016). Finally, the uncontrolled rise of zinc concentration produces dysregulation of signaling processes, generally affecting the cells viability.

The second mechanism of cytotoxicity is related to the direct interaction of ZnO NPs with the cells, leading to the production of reactive oxygen species (ROS) over the limit tolerated by cells.

ROS are radical and non-radical oxygen species generated by the partial reduction of oxygen (such as hydroxyl radical, hydrogen peroxide, superoxide anion, etc.) and they are not exclusively toxic for cells. Actually, ROS species are normally formed as byproducts of cellular metabolism during several physiological processes and they are directly involved in cell signaling and homeostasis (Forrester et al., 2018). As already observed for Zn^{2+} ions, the ROS concentration is precisely controlled by cells under normal conditions but exogenous sources, like ZnO NPs, can cause an overproduction of ROS species, which exceed the cellular antioxidant capacity, originating oxidative stress. During the oxidative stress phase, the overproduced radical species cause direct damages to proteins, lipids and DNA and trigger several signaling pathways that lead to programmed cell death (Bisht & Rayamajhi, 2016).

Concerning the ability of ZnO NPs to produce ROS, several mechanisms have been proposed. The first hypothesized mechanism is related to the semiconductor properties of ZnO (Bogdan et al., 2017). The existence of a gap between the valence band and the conduction band allows electrons, excited with appropriate energy, to create highly reactive electron-hole pairs able to react with oxygen and water present in the cellular environment, generating ROS. As already mentioned ZnO has a band gap of ~3.3 eV and, therefore, the electron promotion can be obtained by irradiation with UV light or with properly tuned ultrasounds (Canavese et al., 2018). However, further literature studies indicate that the formation of electron-

hole pairs is possible even without the application of external stimuli in case of nanostructures. The dimensional reduction, in fact, causes a decrease in the crystalline quality and presence of defects which can migrate to the nanoparticles surface, enhancing the reactivity of the material (Rasmussen et al., 2010).

Moreover, ZnO NPs are able to directly interact with enzymes involved in ROS homeostasis (Molnár et al., 2020) or with the mitochondria, inducing a remodeling of their structure and impairing their functions (Bisht & Rayamajhi, 2016). Finally, other studies hypothesize that the production of ROS is a cytotoxic response related to the activation of pathways in response to the presence of Zn^{2+} ions, generated by the dissolution of NPs in contact with the intracellular environment (Song et al., 2010).

A schematic representation of some of the described cytotoxic effects produced by ZnO NPs is reported in **Figure 2.3**, highlighting the complexity of the phenomenon and the deep interconnection between the proposed mechanisms.

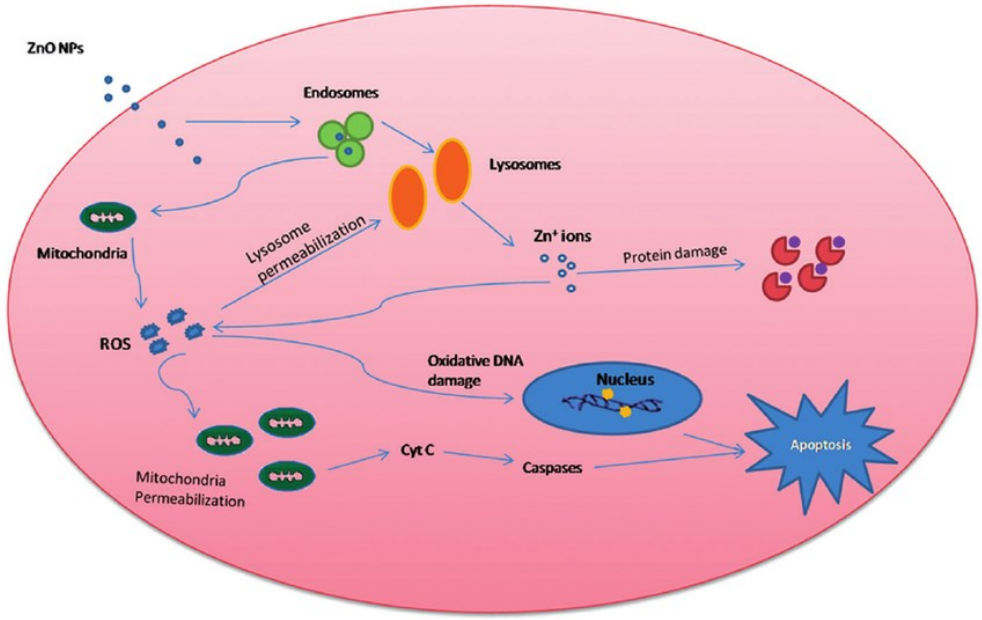

Figure 2.3: Schematic representation of possible cytotoxic mechanisms of ZnO NPs caused by *(i)* the release of Zn^{2+} ions and *(ii)* the production of reactive oxygen species (ROS); figure from (Syama et al., 2014).

Even if not completely elucidated, the discovery of the cytotoxic potential of ZnO NPs promoted their use in nanomedicine applications. Interestingly, ZnO NPs have shown a selective toxicity toward cancerous cells with respect to the healthy counterparts, making them a valuable tool for innovative anti-tumoral treatments.

A possible explanation for this selectivity resides in the small dimensions of the synthesized ZnO NPs, which are able to exploit the EPR effect. In fact, tumor tissues show an altered vascularization, with a discontinuous endothelium characterized by large pores between cells that allow the passage of macromolecules and particles of large size, between 100 and 300 nm depending on the cell line (Tee et al., 2019). In addition, the lack of effective drainage by the lymphatic system leads to an accumulation of the particles penetrated into the tissue. These physiological features, characteristic of tumor masses, are normally

absent in healthy tissues and can thus generate a more effective and preferential accumulation of NPs, denominated “passive targeting”.

Also the interactions between the NPs and the tumor microenvironment (TME) could be important for *in vivo* ZnO NPs selective toxicity. One of the main characteristics of TME, in fact, is its acidity which can conveniently promotes the ZnO NPs dissolution and the subsequent release of cytotoxic Zn^{2+} ions in proximity of cancerous cells (Sasidharan et al., 2011).

The EPR effect and the TME acidity could only explain the interaction of ZnO NPs with *in vivo* cancerous models, whereas the selectivity displayed in the *in vitro* tests involve other parameters of both ZnO NPs and tumor cells.

The ZnO NPs present favorable chemical surface properties, mainly determined by the presence of –OH groups that impart a positive surface charge under physiological pH conditions (Degen & Kosec, 2000). This feature can promote their preferential interactions and subsequent uptake by cancer cells, which have a higher concentration of anionic phospholipids in their membrane compared to healthy cells (Abercrombie & Ambrose, 1962).

In addition, the preferential toxicity toward cancer cells can be attributed to their proliferation status and to ZnO NPs ability to produce ROS. Compared to normal cells, in fact, cancerous cells show a faster metabolism and a subsequent higher intracellular concentration of biological molecules which can act as substrate for ROS production by ZnO NPs. In this perspective, the treatment of cancer cells with ZnO NPs cause a larger generation of ROS, making cancer cells more susceptible to oxidative stress mediated death (Hanley et al., 2008).

2.1.4 Physico-chemical properties affecting ZnO NPs cytotoxicity

Based on the described cytotoxicity and selectivity mechanisms, the influence of physico-chemical properties of ZnO NPs on their biological effect result clear.

Several studies analyze the relationship between the cellular response to ZnO NPs and their size, morphology and surface charge and chemistry, which can be controlled during the synthetic process. For instance, equally-sized ZnO NPs synthesized by wet chemical method using different reaction solvents showed different cytotoxic effects towards Hut-78 lymphoma T cells (Punnoose et al., 2014). In particular, this behavior was attributed to the different chemical groups exposed on the nanoparticles surface and subsequent diverse surface charge value and density. In addition, wet chemical synthesis produces ZnO NPs with higher defectivity and surface reactivity compared to other synthetic procedures (Anders et al., 2018). These synthesis-derived features resulted in faster dissolution kinetics and decreased agglomeration along with enhanced ROS production and, thus, imparted to wet chemical synthesized ZnO NPs a greater toxicity.

Furthermore, the size of ZnO NPs, which can be regulated defining appropriate synthetic parameters, deeply affect the cytotoxic response and interaction with cells. As already mentioned, small ZnO nanostructures were found to be more toxic compared to their larger (Kang et al., 2013) or micrometric counterparts (Nair et al., 2009). Furthermore, the nanoparticles size also affects their cellular

internalization. A recent study showed that smaller ZnO NPs are more easily internalized by human hepatoma HepG2 cells and indicated the endocytosis as major uptake mechanism. In fact, nanoparticles with smaller dimensions would require less energy during the internalization process, while their higher surface area could guarantee a good diffusion into cells membrane (P. Chen et al., 2019). Smaller dimensions and higher surface area could also affect the dissolution rate of ZnO NPs and the subsequent release of potentially cytotoxic Zn^{2+} ions. In fact, a study on the correlation between free intracellular zinc levels and induced cytotoxicity showed that NPs with small dimensions produced higher level of intracellular dissolved zinc, which was accompanied by higher levels of ROS species and more elevated cytotoxic effect (C. Shen et al., 2013).

Considering these results, a reliable and reproducible synthetic procedure followed by a precise physico-chemical characterization of the obtained nanostructures are essential for the effective study of ZnO NPs biological effects. In this perspective, the first part of this PhD thesis consisted in the investigation of an effective synthetic method. More in details, ZnO NCs were produced through a traditional solvothermal synthetic route and an innovative and more reliable microwaves-assisted method. The obtained ZnO NCs were, thus, characterized in term of structure, morphology and surface properties with a particular attention to their colloidal stability and optical properties. Finally, the biological effect of the two synthesized ZnO NCs was assessed, evaluating the cellular internalization and cytotoxicity toward human cervical carcinoma KB cells.

2.2 Materials and Methods

2.2.1 ZnO NCs synthesis and functionalization

2.2.1.1 Conventional and microwave-assisted solvothermal synthesis

ZnO NCs were produced through two different synthetic methods: a conventional solvothermal synthesis (ZnO NCs-st) and a microwave-assisted synthesis (ZnO NCs-mw).

The conventional synthesis was performed as reported by Pacholski et al. (Pacholski et al., 2002) with some modification. In details, zinc acetate dihydrate ($Zn(CH_3COO)_2 \cdot 2H_2O$, 99.99% Sigma Aldrich) was dissolved in methanol (0.09 M, 42 ml) and heated up to 60°C in a 100 ml round-bottom flask under vigorous stirring. When the temperature was reached, 318 µl of bi-distilled (bd) water were added as nucleation promoter and right after a solution of sodium hydroxide (NaOH, BioXtra, ≥98% acidimetric, pellets anhydrous, Sigma-Aldrich) in methanol (0.31 M, 23 ml) was added dropwise in about 20 minutes. The synthesis mixture was maintained at 60°C, under continuous stirring and reflux condition, for 2.5 hours and then washed twice by centrifuging at 3,500g for 10 minutes and resuspending the obtained pellet with fresh ethanol (99%, Sigma-Aldrich).

For the microwave-assisted synthesis, an analogous reaction with the same concentration of zinc precursor was performed in a Teflon reactor vessel equipped with temperature and pressure probes and connected with a microwaves furnace (Milestone START-Synth, Milestone Inc, Shelton, Connecticut). The methanol solution of zinc acetate dihydrate (0.09 M, 60 ml) was prepared directly in a 270 ml Teflon vessel. 480 µl of bi-distilled water and a solution of potassium hydroxide (KOH ≥ 85% pellets, Sigma-Aldrich) in methanol (0.2 M, 35 ml) were then added and the resulting mixture was put in the microwave oven at 60°C for 30 minutes with maximum microwave power 150 W. The reaction suspension was then cooled down and washed twice with ethanol, as already described for conventional synthesis.

2.2.1.2 Functionalization of ZnO NCs with amino-propyl groups

The ZnO NCs obtained by both synthesis methods were further functionalized with amino-propyl groups using 3-amminopropyltrimethoxysilane (APTMS 97%, Sigma Aldrich) as functionalizing agent. Briefly, ethanolic suspensions of ZnO-st or ZnO-mw NCs were heated up to 70°C in a round glass flask under nitrogen gas flow and continuous stirring. After approximately 15 minutes, APTMS was added in a molar ratio of 10 mol% with respect to the total ZnO amount. The reaction was carried out in reflux condition under nitrogen atmosphere for 6 hours and then washed twice by centrifuging (10,000g for 5 minutes) in to order to remove unbound APTMS molecules.

2.2.2 ZnO NCs Characterization

2.2.2.1 X-ray Diffraction

The ZnO NCs obtained by both synthesis methods were characterized by X-ray diffraction (XRD) measurements, in order to investigate their crystalline structure. The samples were deposited drop by drop on a silicon wafer, obtaining an appropriately thick layer of dried ZnO NCs, and then analyzed with a Panalytical X'Pert diffractometer in θ-2θ Bragg-Brentano configuration with a Cu-Kα source of radiation (λ=1.54 Å) operating at 30 mA and 40 kV. The XRD spectra were collected at room temperature (RT), in the 2θ range 20° - 65° with step size 0.02 and acquisition time 100s per step.

2.2.2.2 Electron Microscopy

Detailed information on the size, morphology and structure of pristine and functionalized ZnO NCs were obtained by electron microscopy. All the samples were prepared by depositing a drop of properly diluted ethanolic ZnO NCs suspension on a silicon wafer for field emission scanning electron microscopy (FESEM) or on a holey carbon-coated copper grid for conventional and high resolution transmission electron microscopy (CTEM and HR-TEM respectively).

FESEM analyses were performed by a Carl Zeiss Merlin field emission scanning electron microscope.

CTEM was performed using a FEI Tecnai Spirit microscope working at an acceleration voltage of 120 kV quipped with a Twin objective lens, a LaB6 thermionic electron source and a Gatan Orius CCD camera. HRTEM was performed by using a FEI Titan ST microscope working at an acceleration voltage of 300 kV, equipped with a S-Twin objective lens, an ultra-bright field emission electron source (X-FEG) and a Gatan 2k × 2k CCD camera.

2.2.2.3 X-ray Photoelectron Spectroscopy (XPS)

The chemical composition of the ZnO NCs surface was analyzed through X-ray photoelectron spectroscopy (XPS). The measurements were performed with a PHI 5000 Versaprobe Scanning X-ray photoelectron spectrometer equipped with a monochromatic Al-Kα source of radiation (energy 1486.6 eV) considering a spot with size of 100 μm to collect the photoelectron signal for both high resolution (HR) and survey spectra.

2.2.2.4 Graphite Furnace Atomic Absoprtion Spectroscopy (GF-AAS)

To evaluate the reproducibility of the amino-propyl functionalization, different batches of $ZnO.NH_2$ NCs with known concentration were analyzed through Graphite Furnace Atomic Absorption Spectroscopy (GF-AAS). The samples were mineralized under acidic conditions and the Zn content was determined following

EPA method 289.1. From these results the amount of APTMS conjugated with the ZnO NCs was back-calculated.

2.2.2.5 Dynamic Light Scattering (DLS) and Zeta-Potential measurements

The behavior of ZnO NCs in solution was investigated by the Dynamic Light Scattering (DLS) technique. The different types of ZnO NCs were resuspended in ethanol or bd-water at the concentration of 100 μg/ml, sonicated for 10 minutes and then analyzed with the Zetasizer Nano ZS90 (Malvern Instruments) at room temperature. Zeta-Potential potential measurements were recorded with the same instrument.

2.2.2.6 UV-Vis and Fluorescence Spectroscopy

The optical and luminescent properties of the synthesized ZnO NCs were evaluated through fluorescence and UV-Vis spectroscopy. The UV-Vis spectra were collected with a Multiskan GO microplate UV-Vis Spectrophotometer (Thermo Fisher Scientific), recording the absorbance of NCs suspension in ethanol (concentration 500 μg/ml) in the wavelength range 300-800 nm. All the spectra were background subtracted and elaborated with Tauc's method (Viezbicke et al., 2015) to calculate the optical band gap.

The fluorescence excitation and emission spectra were recorded with a Perkin Elmer LS55 fluorescence spectrometer (PerkinElmer Inc.). The samples (500 μg/ml in ethanol) were placed in a quartz cuvette with 1cm optical path and the wavelength was set at λ_{ex}=380 nm to collect the emission spectra and at λ_{em}=500 nm to collect the excitation spectra. All the measurements were performed with scan/rate 300 nm/min and with 2.5 slits opening.

2.2.3 Biological Tests

In vitro cytotoxicity and internalization assays were performed with both amino-propyl functionalized ZnO-st-NH_2 and ZnO-mw-NH_2 NCs.

KB cell line (ATCC® CCL17), derived from a human cervical carcinoma purchased from the American Type Culture Collection. Cells were cultured in Eagle's minimal essential medium (EMEM, Sigma), supplemented with 10% fetal bovine serum (FBS, Sigma) heat inactivated, penicillin (100 units/ml) and streptomycin (100 μg/ml) and maintained at 37°C under a 5% CO_2 atmosphere.

All the biological tests were performed at least in triplicate and the results were expressed as mean ± SEM (standard error of mean). The experimental data were analyzed using Sigmaplot 14 (demo version, Systat Software Inc.) performing t test and One Way Analysis of Variance (ANOVA). When equal variances are not assumed, the results of Welch's test have been presented and when normality test failed, Mann-Whitney Rank Sum Test has been run. Differences were considered significant at p value < 0.05.

2.2.3.1 Cytotoxicity assay

For cell viability tests, 1.5×10^3 cells/well were seeded in 96-well culture plate (Corning® 96 Well TC-Treated Microplates) and grown for 24 hours at 37°C under 5% CO_2 atmosphere. Then the cell culture medium was replaced with fresh medium containing the nanocrystals. In details, the treating solution were freshly prepared by adding to 1 ml of culture medium the appropriate quantity (0, 10, 25, 20, and 25 μg) of ZnO-st-NH_2 or ZnO-mw-NH_2 NCs taken from a 1 mg/ml ethanolic suspension sonicated for 10 minutes. After 24 hours of incubation with NCs, WST-1 cell proliferation assay was performed. Briefly, 10 μl of WST-1 reagent (Roche) were added to each well and, after 2 hours in dark at 37°C and 5% CO_2, the formazan absorbance was measured at 450 nm with the Multiskan GO microplate spectrophotometer (Thermo Fisher Scientific) using 620 nm as reference wavelength. Since the amount of produced formazan is proportional to the number of metabolically active cells, the absorbance of cells treated with medium alone (control) was set as 100% of viability and all the other values were expressed as percentages with respect to the control.

The calculator tool in the AAT Bioquest webpage (https://www.Aatbio.Com/tools/ic50-calculator) was used to calculate the IC50 value, i.e. the concentration of NCs that inhibit the cells growth by 50% with respect to the control.

2.2.3.2 Cell internalization assay

The internalization of ZnO-st-NH_2 and ZnO-mw-NH_2 NCs in KB cells was investigated by flow cytometry, using a Guava Easycyte 6-2L (Merck Millipore) equipped with two lasers at 488 nm and 642 nm.

The nanocrystals were labeled with the fluorescent probe Atto 633-NHS Ester (Atto-Tec) by adding 2 μg of dye for each mg of NCs suspended in ethanol. The obtained solution was stirred overnight in dark and then washed twice (10,000g for 10 minutes) to remove unbound dye.

1.5×10^5 cells/well were seeded in a 6-well culture plate (Corning® TC-Treated) and grown for 24 hours at 37°C under 5% CO_2 atmosphere. The cell culture medium was then replaced with fresh medium containing 10 μg/ml of NCs or with fresh medium alone as control sample. After 24 hours of incubation the cells were washed twice with PBS, trypsinized, pelleted (130g for 5 minutes) and resuspended in 1 ml of PBS for the analysis. For each sample were recorded 10^4 events positioned in a gate designed to exclude cells debris. The red laser was used for the excitation of the labelled NCs and the fluorescence was detected and analyzed with Guava Incyte software (Merck Millipore); the results were expressed in percentages of positive events calculated with respect to a threshold set upon cells control histogram.

2.3 Results and discussion

2.3.1 Solvothermal synthesis of ZnO NCs: reaction mechanism

ZnO particles with crystalline structure (ZnO NCs) were obtained through solvothermal synthesis using conventional heating method (i.e. silicon oil bath) or microwave-assisted heating. Both methods use zinc acetate ($Zn(Ac)_2$) as zinc precursor and a strong alkali (NaOH or KOH, respectively) as mineralizing agent and follow the same reaction path, represented in the following equations:

$$KOH/NaOH \rightarrow K^+/Na^+_{(aq)} + OH^-_{(aq)} \quad (1)$$

$$Zn(Ac)_2 \rightarrow Zn^{2+}_{(aq)} + 2Ac^-_{(aq)} \quad (2)$$

$$Zn^{2+}_{(aq)} + 2OH^-_{(aq)} \rightarrow Zn(OH)_{2\ (aq)} \quad (3)$$

$$Zn(OH)_{2(aq)} + 2H_2O \rightarrow Zn(OH)_4^{2-} + 2H^+_{(aq)} \quad (4)$$

$$Zn(OH)_4^{2-} + 2H^+_{(aq)} \rightarrow ZnO_{(s)} + 3H_2O \quad (5)$$

Briefly, zinc precursor is hydrolysed by hydroxide ions and reacts with them to form a tetrahedral coordination compound. The formation of crystalline ZnO occurs due to the subsequent dehydration of this intermediate. This sequence of reactions leads to the formation of tiny crystalline nuclei which will grow according to the Ostwald ripening mechanism, forming an ensemble of ZnO crystalline particles (Cauda et al., 2014).

The synthesis was performed in methanol, a markedly polar solvent which helps to obtain particles with desired size and morphology. The molecules of methanol, in fact, strongly interact with the polar faces of ZnO inhibiting the absorption of precursor and crystals growth and, thus, leading to the formation of nanoparticles with hexagonal-oval shape and nanometric size (Ali et al., 2017). The ratio between the reagents was fixed to obtain crystals with nanometric dimension, using a substoichiometric amount of base.

The switch from conventional heating method to microwave-assisted heating had as main goal to obtain a more precise control of nanocrystals properties and a higher reproducibility and repeatability. The interaction of microwave radiation with the molecules of polar solvents causes the rotation of dipoles and the conversion of microwave radiation energy in kinetic energy. The collision and rubbing of the rotating molecules result in the heating of the solution, with a rapid increase of the temperature and low thermal gradient. Thus, the microwave-assisted method ensures a more rapid and homogeneous heating of synthetic precursors with respect to conventional heating methods in which the heat is transferred to reaction vessel by convection, resulting in a greater quality of the obtained nanomaterials (Wojnarowicz et al., 2020).

Due to the higher heating efficiency, microwave-assisted synthesis guarantees also shorter reaction time and energy saving along with higher reaction yields. In the present work microwave-assisted and traditional solvothermal synthesis were performed using the same temperature conditions (T=60 °C) and precursors. Five

times higher yield was obtained applying the microwave with respect to the standard heating and the reaction time was reduced from 2.5 hours to 30 minutes.

2.3.2 Morphological and structural characterization

The crystalline structure of ZnO NCs obtained by the two synthetic methods was analysed through X-Ray diffraction (XRD) measurements. The recorded diffractograms, reported in **Figure 2.4**, were compared with the standard XRD pattern of ZnO (JCPDS card n° 36-1451), confirming the crystalline structure of the synthesized particles. In particular, both ZnO-st NCs and ZnO-mw NCs XRD spectra present peaks at 31.9°, 34.4°, 36.4°, 47.6°, 56.7°, 62.9° indexed as (100), (002), (101), (102), (110) and (103) planes respectively, corresponding to the hexagonal wurtzite phase of crystalline ZnO.

An estimation of the average crystallites size was obtained applying the Debye-Sherrer equation to (101) peak, which present the strongest relative reflection. The calculated mean diameter was equal to 10.5 nm for nanocrystals obtained by conventional solvothermal synthesis (ZnO-st NCs) and 15.5 nm for microwave-assisted synthesis (ZnO-mw NCs).

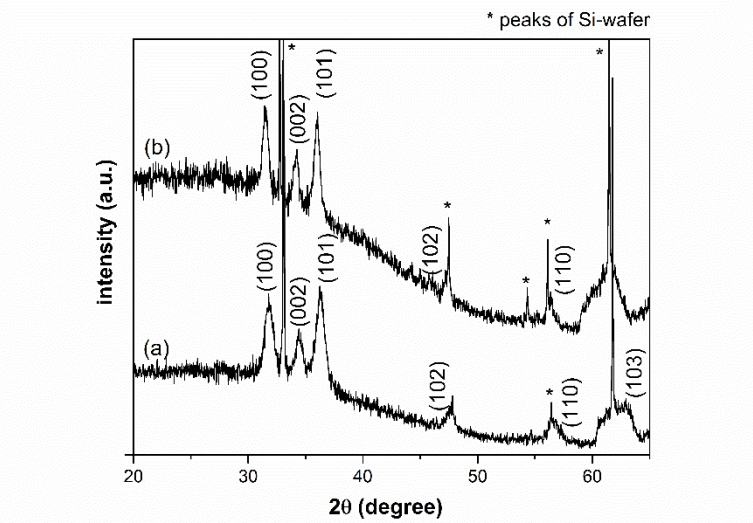

Figure 2.4: XRD spectra of pristine ZnO NCs obtained by **(a)** conventional synthesis (ZnO-st NCs) and **(b)** microwave-assisted synthesis (ZnO-mw NCs).

Details on size and morphology and on synthesis repeatability were obtained by FESEM analyses, performed on different batches of ZnO NCs produced with the two synthetic procedures. Representative FESEM images are shown in **Figure 2.5**, The ZnO NCs synthesized by conventional solvothermal route (**Figure 2.5a**) presented different shapes, both round or more elongated, while NCs obtained by microwave-assisted synthesis showed an homogeneous spherical morphology (**Figure 2.5b**). The higher homogeneity of microwave-assisted synthesis was also confirmed by the dimensional analysis. ZnO-mw NCs, in fact, were characterized by a narrow and highly reproducible particle size distribution, with an average size of 20 nm ± 5 nm. In contrast, conventionally synthesized nanocrystals (ZnO-st NCs) had a wider size distribution, ranging between 6 nm and 20 nm.

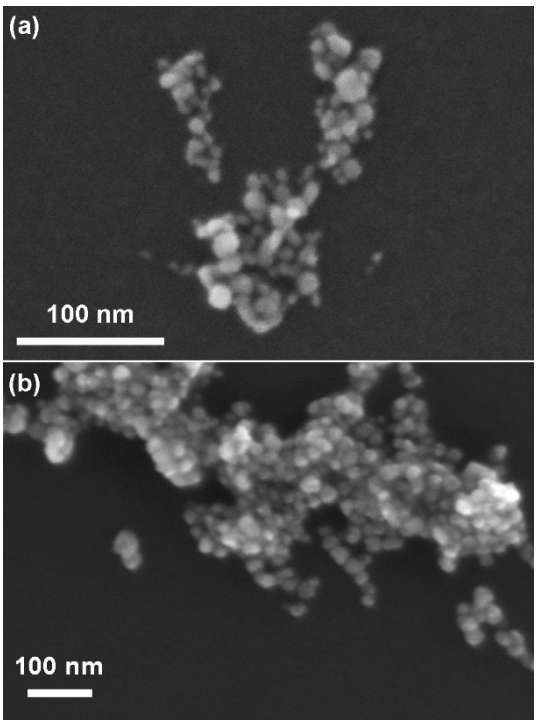

Figure 2.5: FESEM images of pristine ZnO NCs obtained by **(a)** conventional synthesis (ZnO-st NCs) and **(b)** microwave-assisted synthesis (ZnO-mw NCs).

The morphological and structural characterization of pristine and amino-propyl functionalized nanocrystals obtained by the two synthetic methods was completed by TEM analyses.

Results related to nanocrystals produced with standard synthetic method are shown in **Figure 2.6**. As already highlighted by FESEM analyses, conventional TEM image (CTEM, **Figure 2.6a**) confirmed the presence of particles with different morphologies,. The higher magnification and resolution of transmission electron microscopy, allowed to clearly recognize that only a small portion of ZnO-st sample presented a round shape, while the majority of NCs had a short rod-like shape with a constant width of around 7-8 nm and a variable length, up to 40 nm. After the functionalization with amino-propyl groups, the NCs preserved their individual shape and morphology but appeared more aggregated than their not-functionalized counterpart. CTEM image of ZnO-st-NH_2 sample (**Figure 2.6b**) showed NCs clustered in small aggregates and surrounded by an amorphous external shell. Finally, HRTEM measurements on both ZnO-st and ZnO-st-NH_2 NCs (**Figure 2.6c** and **d**) were performed, confirming that particles possessed a monocrystalline structure, without evident defects and with lattice d-spacing and angular distances typical of the ZnO hexagonal structure.

The same measurements were performed on nanocrystals obtained *via* microwave-assisted synthesis, as reported in **Figure 2.7.** Like ZnO-st, both pristine and amino-functionalized ZnO-mw samples presented the wurtzite hexagonal monocrystalline structure (**Figure 2.7c** and **d**), confirming no structural differences between the NCs obtained by the two synthetic procedure. In contrast, in terms of morphology, CTEM images of ZnO-mw NCs (**Figure 2.7a**) displayed a homogeneous particles population with spherical and faceted shape and uniform

size distribution between 15 and 25 nm. The aggregation propensity and the presence of an amorphous external shell surrounding NCs cluster after amino-propyl functionalization was confirmed also for ZnO-mw-NH_2 samples (**Figure 2.7b**).

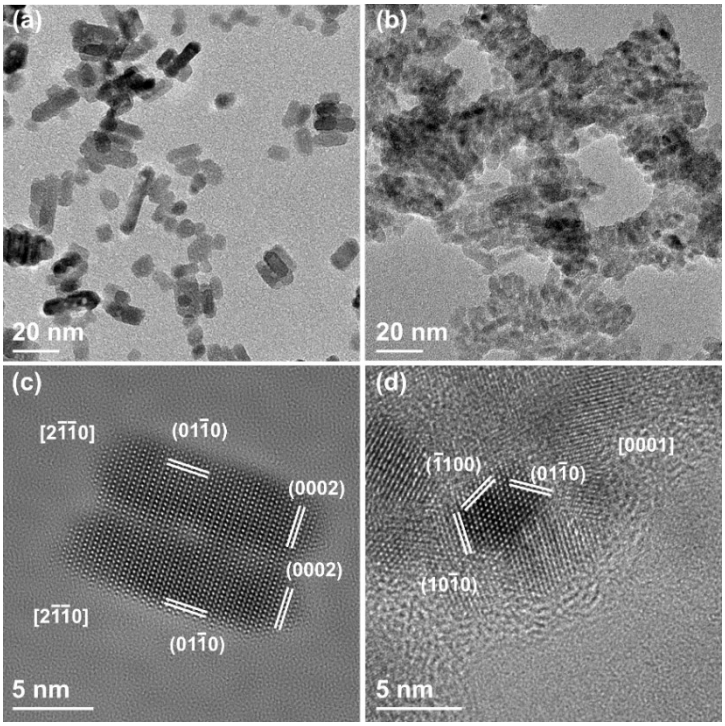

Figure 2.6: Transmission Electron Microscopy images of pristine ZnO-st NCs (**(a)** CTEM and **(c)** HRTEM) and amino-propyl functionalized ZnO-st-NH_2 (**(b)** CTEM and **(d)** HRTEM).

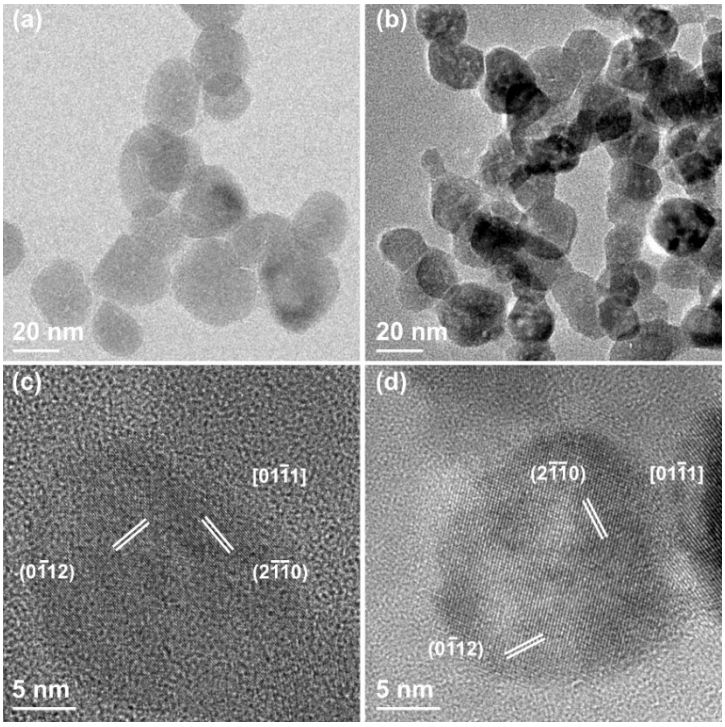

Figure 2.7: Transmission Electron Microscopy images of pristine ZnO-mw NCs (**(a)** CTEM and **(c)** HRTEM) and amino-propyl functionalized ZnO-mw-NH_2 (**(b)** CTEM and **(d)** HRTEM).

2.3.3 Compositional characterization

Considering the prominent role of surface properties in determining the colloidal and biological behavior of nanoparticles, the chemical surface composition of the synthesized NCs was analyzed in detail through X-ray photoelectron spectroscopy (XPS).

Results of XPS analyses on ZnO-st, ZnO-mw and ZnO-mw-NH_2 NCs are shown in **Figure 2.8**; considering the similarities with the other functionalized sample, results on ZnO-st-NH_2 NCs are not reported, All the collected survey spectra (**Figure 2.8** from **a** to **c**) presented Zn and O peaks, as expected, together with a C peak, due to contamination of adsorbates. Peak corresponding to N was detected only in the ZnO-mw-NH_2 functionalized sample.

The relative atomic concentration (%at) of each element was evaluated from the XPS survey scans and reported in **Table 2.2**. From these data, the Zn/O ratio was calculated, considering only the oxygen not bound with C (values reported in the fourth column of **Table 2.2** and marked with **). Briefly, deconvolution on C1s high-resolution (HR) peak was performed (data not shown), in order to determine the amount of O involved in bound with C. This amount was then subtracted from the total oxygen. The resulting ratios were equal to Zn/O=0.99 for NCs obtained by microwave-assisted synthesis, Zn/O=0.90 for standardly synthesized NCs and Zn/O=0.83 for amino-functionalized ZnO-mw-NH_2 NCs. These values revealed an increase in the O amount at the rear surface for the last two samples, easily ascribable to synthesis or functionalization procedures.

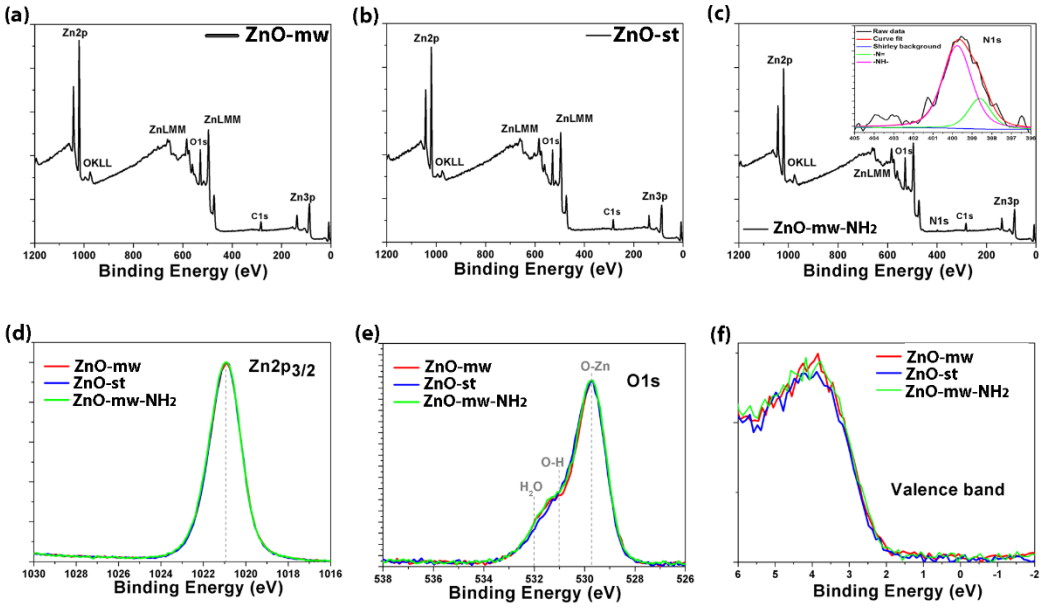

Figure 2.8: XPS analyses: survey scans of **(a)** ZnO-mw NCs, **(b)** ZnO-st NCs and **(c)** ZnO-mw-NH_2 NCs. Inset in panel **(c)** reports the high-resolution (HR) spectra of N1s region of the amino-propyl functionalized ZnO-mw-NH_2 NCs. HR spectra of **(d)** $Zn2p_{3/2}$ and **(e)** O1s regions of the three samples (ZnO-mw NCs in red, ZnO-st NCs in blue and ZnO-mw-NH_2 NCs in green). **(f)** Valence band (VB) signals of the three samples.

Table 2.2: Relative atomic concentration (at%) evaluated from XPS survey spectra and calculated Zn/O ratio. *Amount of oxygen (at%) associated with carbon. **Total amount of oxygen minus the amount of oxygen associated with carbon (%at).

Sample	Atomic concentration (at%)					Ratio
	C	O		N	Zn	Zn/O
ZnO-mw NCs	26.3	5.3*	34.3**	-	34.1	0.99
ZnO-st NCs	27.5	4.7*	35.6**	-	32.2	0.90
ZnO-mw-NH_2 NCs	25.4	1.7*	38.5**	2.4	32.0	0.83

HR curves of the three different samples were also compared to evaluate oxidation state of Zn and O signals (**Figure 2.8d** and **e**, respectively). For the $Zn2p_{3/2}$ curves, the three signals were perfectly overlapped and centered the same binding energy (1020.9 eV), corresponding to the ZnO chemical shift as already reported in literature (Al-Gaashani et al., 2013). Also the O1s region displayed an almost perfect overlap between the three samples. Deconvolution procedures were applied (data not shown) and three contributions were identified: O-Zn bond (592.7 eV), O-H bond (531.0 eV) and residual H_2O (532.0 eV), in good agreement with either experimental and theoretical data reported in literature (Ogata et al., 2004). For the amino-propyl functionalized sample, also N1s region was analyzed (inset of **Figure 2.8c**), and recorded signals were ascribed to imine group –N= (338.6 eV; 22.3%) and amine group –NH– (399.7 eV; 77.7%).

Finally, valence band (VB) signals of the three samples were acquired (**Figure 2.8f**) to evaluate the electronic band adjustment. Briefly, the valence band maximum (VBM) position related to the Fermi energy level (EF) was extracted from XPS measurements and set as the 0 eV of the binding energy scale. Linear fit of the descending part of each spectrum towards EF was performed (data not shown), obtaining the following values: 2.20 eV for ZnO-mw NCs, 2.24 eV for ZnO-st NCs and 2.14 eV for ZnO-mw-NH_2 NCs. These results are in good accordance with values reported in literature for ZnO nanostructured particles (Kamarulzaman et al., 2015).

Taken together, the XPS analyses showed that the switch from conventional heating method to microwave-assisted heating produced ZnO NCs with highly comparable surface chemical properties.

In addition, the presence of N signal in the ZnO-mw-NH_2 sample allowed to confirm the success of functionalization of NCs surface with amino-propyl groups. The presence of amino-propyl groups on nanocrystals surfaces was also indirectly verified by Zeta-Potential measurements, performed on ZnO-mw and ZnO-mw-NH_2 NCs dispersed in bd water. The Zeta-Potential value was equal to 15.8 mV for the ZnO-mw NCs and to 21.7 mV for the amino-propyl functionalized ZnO-mw-NH_2 NCs. The detected positive increment could be ascribed to the protonation of superficial amino groups, forming $–NH^{3+}$ species, further confirming the success of functionalization procedure.

Moreover, in order to evaluate the amount of functionalizing agent (APTMS) effectively conjugated to the NCs and the reproducibility of the functionalization process, three samples of ZnO-mw-NH_2 NCs were analyzed through atomic absorption spectroscopy, assessing their zinc content as reported in **Table 2.3**.

These concentrations were then compared with the overall concentration of the samples, which comprehend the contributions of Zn, O and functionalizing agent, obtained weighing the dried NCs from a known volume of colloidal solution. The comparison allowed to extrapolate the %mol of bound APTMS (**Table 2.3**).

The observed zinc contents were comparable, indicating an adequate reproducibility of the functionalization procedure. The average mol% of bound APTMS was equal to 8.4 mol%, in good accordance with the amount of APTMS introduced at the beginning of the functionalization procedure (i.e. 10 mol%).

Table 2.3: Zinc content of ZnO-mw-NH_2 NCs measured by graphite furnace atomic absorption spectroscopy (GF-AAS) and extrapolated value of bounded APTMS molecules, expressed in mol%.

Sample ZnO-mw-NH_2	Zn [ppm]	Extrapolated %mol APTMS
(i)	27	8.55
(ii)	28.5	7.78
(iii)	28	8.73

2.3.4 Evaluation of colloidal stability

The nanoparticles behaviour in solution is a key parameter for their effective application and it is deeply influenced by their morphological and physico-chemical properties. In this perspective, the colloidal stability of the ZnO NCs obtained by the two synthetic procedure was compared, also evaluating the effect of the functionalization with amino-propyl molecules.

The hydrodynamic size in ethanol and bd water of ZnO NCs synthesized by the two different methods was analysed through Dynamic Light Scattering (DLS) technique. To better assess the repeatability of the proposed synthetic procedures, three different batches of each synthetic approach were analysed and compared. In addition, the stability in ethanol of ZnO-st-NH_2 and ZnO-mw-NH_2 right after the functionalization process and after 9 months of storage was also evaluated. The obtained size distributions are reported in **Figure 2.9** and the related average diameters and polydispersity indexes (PDI) are summarized in **Table 2.4**.

The ZnO-mw NCs obtained by microwave-assisted synthesis appeared well dispersed in both ethanol and water (bottom panel of **Figure 2.9a** and **b**, respectively), showing narrow size distributions, all centered between 50 and 60 nm. This highly repeatable inter-batch behaviour was accompanied by a good intra-batch homogeneity, proven by the PDI values ≤0.2, characteristic of monodisperse samples.

In contrast, conventionally synthesized ZnO-st NCs displayed less constant properties, as already shown by dimensional and morphological characterization. The three tested batches showed broader size distributions in ethanol (top panel of **Figure 2.9a**), with multiple peaks and higher PDI values. The heterogeneity was even more evident in water (top panel of **Figure 2.9b**), where shift toward bigger hydrodynamic diameters (>100 nm) and higher PDI values (>0.5) were detected, indicating lower colloidal stability and samples aggregation.

Regarding the amino-propyl functionalized nanocrystals, both ZnO-st-NH_2 and ZnO-mw-NH_2 measured right after the functionalization process showed a good colloidal stability in ethanol (blue lines in **Figure 2.9c**), with an increase in diameters with respect to their pristine counterparts, possibly due to the presence of functionalizing groups at the surface. With the perspective of biological application, the long-term colloidal stability and the shelf-life of functionalized NCs was evaluated, performing further DLS measurements after nine months of storage in ethanol (**Figure 2.9c**, red lines). This second analysis highlighted that ZnO-mw-NH_2 NCs possessed a reasonably good stability over time, since their size distributions displayed just a minor shift from 120 nm to 96 nm. In contrast, ZnO-st-NH_2 NCs presented a consistent dimensional increase from 140 nm to 360 nm, indicating instability and tendency to aggregation during the storage.

Overall, these results displayed that the more homogenous morphology and size of the nanocrystals obtained by the microwaves-assisted synthesis were reflected in a better colloidal stability and inter-batches reproducibility with respect to the conventionally synthesized counterpart. The good colloidal behaviour was confirmed also after the functionalization procedure, with a little increase of the hydrodynamic size, ascribable to the additional steric hindrance of the amino-propyl groups. The stability in ethanol stock solution was preserved after storage period, suggesting that the synthesized ZnO-mw-NH_2 NCs might be more suitable for biological application.

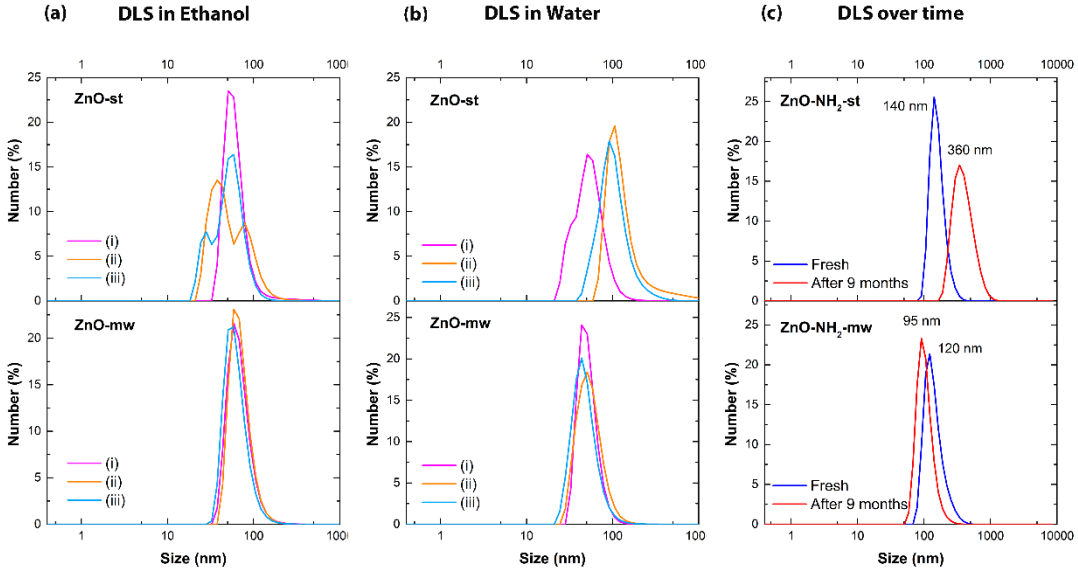

Figure 2.9: Dynamic Light Scattering (DLS) measurements of: pristine ZnO NCs obtained by conventional synthesis (ZnO-st NCs, top panel) and microwave-assisted synthesis (ZnO-mw NCs, bottom panel) in **(a)** ethanol and **(b)** bd water; **(c)** functionalized ZnO-st-NH_2 (top) and ZnO-mw-NH_2 (bottom) NCs in ethanol immediately after the functionalization procedure and after 9 months of storage. All the size distributions are in %number.

Table 2.4: Average diameter (Av. diameter) and polydispersity index (PDI) of the number-weighted size distributions reported in **Figure 2.9**.

		Ethanol		Water				Ethanol	
Sample		**Av. diameter (nm)**	**PDI**	**Av. diameter (nm)**	**PDI**	**Sample**		**Av. diameter (nm)**	**PDI**
ZnO-st NCs	(i)	65	0.28	56	0.52	ZnO-st- NH_2 NCs	Fresh	162	0.26
	(ii)	60*	0.38	155	0.36		After 9 months	410	0.25
	(iii)	53**	0.38	108	0.18				
ZnO-mw NCs	(i)	70	0.19	52	0.12	ZnO-mw-NH_2 NCs	Fresh	144	0.11
	(ii)	71	0.14	56	0.20		After 9 months	105	0.11
	(iii)	64	0.18	49	0.26				

*Peak 1: 40 nm; Peak 2: 92 nm
**Peak 1: 28 nm; Peak 2: 58 nm

2.3.5 Optical and luminescent properties

The physico-chemical characterization of the synthesized nanocrystal was completed with the evaluation of their optical and luminescent properties.

The assessment of the optical and luminescent properties is particularly interesting in the perspective of a biological application of the ZnO NCs, which could be also exploited for bioimaging purposes. As already mentioned, the semiconductor properties of ZnO impart to the NCs a strong adsorption and photoluminescent emission in the UV range. In addition, the presence of structural defects, connected with the reduction of the material to the nanoscale and the synthetic procedure, is probably responsible for the second emission band located in the visible region. Furthermore, several literature studies indicate the profound influence of surface modifications on the photoluminescent behaviour of ZnO NCs (Norberg & Gamelin, 2005). Based on these considerations, the optical and luminescent properties of the ZnO samples obtained by the two synthetic procedures were evaluated both in the pristine and amino-propyl functionalized forms.

The optical properties and the relative band gap were evaluated through UV-Vis adsorption spectroscopy (**Figure 2.10**). Adsorption spectra (**Figure 2.10a**) of pristine and functionalized ZnO NCs obtained by both synthetic methods were collected in the range 300-800 nm, showing highly comparable results. All the samples displayed an intense UV adsorption in the region between 300 and 380 nm while appeared fully transparent in the visible region, above 380 nm, in good accordance with the typical behaviour of crystalline ZnO.

The optical band gap (E_g) was calculated applying the Tauc's method to the registered adsorption spectra. According to this method, a plot of $[F(R)]^n$ in function of the photon energy hν was drawn, assuming n=2 (value indicated for semiconductor with direct band gap, like crystalline ZnO) (Hernández et al., 2014). The resulting plot showed a distinct growth linear region just above the optical adsorption edge. By making a linear fit of this area, it was possible to extrapolate the band gap value, which corresponds to the intercept of the line with the x-axis. The obtained plots are shown in **Figure 2.10b** and the resulting E_g values at room temperature were between 3.32-3.34 eV for all the four analysed samples.

From UV-Vis analysis no significant differences between the NCs obtained by the two synthetic methods were detected, suggesting that the differences in particle size and shape were not enough important to affect the optical properties. Actually, the heterogeneity of size distribution of ZnO-st and ZnO-st-NH_2 samples lied in a range of few nm (6-20 nm, as estimated from FESEM analyses), which is not broader enough to produce differences in the optical response, as confirmed by literature (Morales-Flores et al., 2013).

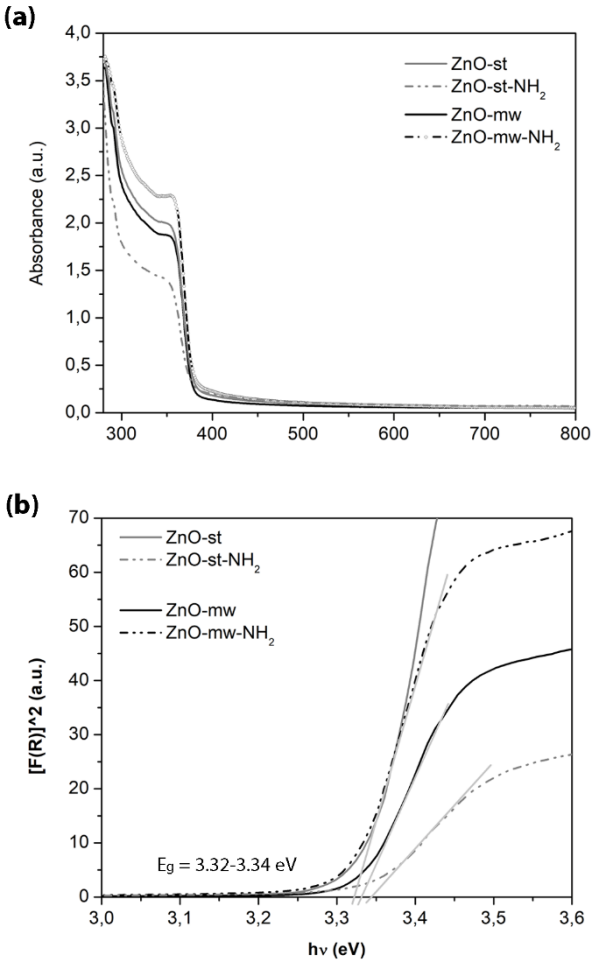

Figure 2.10: (a) UV-Vis absorption spectra and **(b)** optical band gap (E_g) of pristine ZnO NCs obtained by conventional synthesis and microwave-assisted synthesis (solid lines) and their functionalized counterparts (dashed lines).

The luminescent properties of ZnO NCs were analyzed through fluorescence spectroscopy, recording the emission and excitation spectra of pristine ZnO NCs obtained by conventional synthesis and microwave-assisted synthesis and their functionalized counterparts (**Figure 2.11**).

In fluorescence excitation spectra (**Figure 2.11a**), the highest excitation was detected at around 380 nm and both pristine ZnO-st and ZnO-mw NCs showed comparable spectra (solid lines). Conversely, higher excitation intensities were detected for samples with amino-propyl groups (dashed lines), and in particular for ZnO-mw-NH_2 NCs obtained by microwave-assisted synthesis and subsequently functionalized.

A similar behavior was observed also in fluorescence emission spectra (**Figure 2.11b**), recorded with λ_{Ex}=380 nm. All the NCs displayed a broad emission peak in the visible region between 500 and 700 nm, ascribable to a defectivity in the ZnO crystalline structure. Functionalized NCs showed an increase in fluorescent intensity with respect to pristine ZnO.

As already observed for optical properties, these results showed no significant differences between the NCs obtained by the two synthetic procedures. However, fluorescence spectroscopy analyses highlighted that the presence of amino-propyl groups produced an enhancement of ZnO luminescent properties both in the excitonic emission and in the green fluorescence emission. This behaviour is in good accordance with literature data referring to amino-functionalized ZnO QDs and can be ascribed to the electron-donor effects of amine groups, able to enhance the intrinsic fluorescent properties of ZnO (S. Li et al., 2014). Thus, the functionalization with amino groups was proved to be helpful in the perspective of the application of ZnO NCs for bioimaging purposes. Moreover, their presence offers an additional advantage since they can be used for the attachment of further functionalizing moieties.

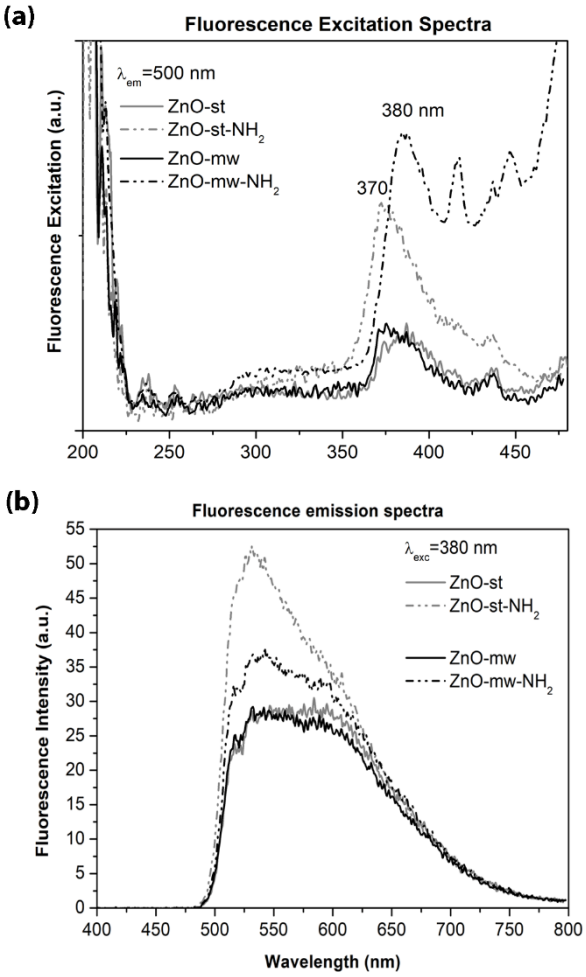

Figure 2.11: (a) Excitation spectra (recorded at λ_{Em}=550 nm) and **(b)** emission spectra (λ_{Ex}=380 nm) of pristine ZnO NCs obtained by conventional synthesis and microwave-assisted synthesis (solid lines) and their functionalized counterparts (dashed lines).

2.3.6 Biological effects of ZnO NCs on cancerous cells

The comparison between the two synthetic procedure was concluded analysing their interaction and cytotoxicity toward KB cancerous cells. As already pointed out in the introductive section, the biological behaviour of the nanoparticles is deeply influenced by their morphology, size and surface properties resulting from the synthetic procedure.

The biological tests were conducted only on amino-propyl functionalized ZnO-st-NH_2 and ZnO-mw-NH_2 NCs. This choice was mainly dictated by the necessity to label the NCs with fluorescent dye for their visualization during the internalization assays, as already described in the Material and Methods section. However, the presence of amino groups could be further exploited for the attachment of targeting ligands or other functionalizing moieties and was proven to cause an enhancement of photoluminescent properties of ZnO NCs (see **Figure 2.11**) and so it could be particularly valuable for biomedical applications.

The viability of KB cells was evaluated through WST-1 assay, comparing the effect of ZnO-st-NH_2 and ZnO-mw-NH_2 at different concentrations after a 24 hours treatment. The results, reported in **Figure 2.12**:, highlighted big differences in the cytotoxic behaviour of the NCs obtained by the two synthetic procedures. In particular, conventionally synthesized ZnO-st-NH_2 NCs (**Figure 2.12a**) exhibited a low reproducible cytotoxic response, with fluctuating toxicity and high standard error means, which hindered the identification of any significant dose-dependent toxicity. In contrast, ZnO-mw-NH_2 NCs obtained by microwave-assisted method caused a decrease in KB cell viability in a concentration-dependent manner, as clearly shown in **Figure 2.12b**. The lower standard error means with respect to those obtained with NCs synthesized by traditional solvothermal method evidenced the major reproducibility of the treatment, which produced a significant ($p \leq 0.001$) decrease in cell viability at 20 μg/ml and 25 μg/ml compared to 10 μg/ml. Besides, the intermediate concentration of 15 μg/ml showed the highest variability, suggesting that this concentration was a sort of threshold between biocompatibility and toxicity of ZnO-mw-NH_2 NCs, as also confirmed by the calculated IC_{50} value equal to 14 μg/ml.

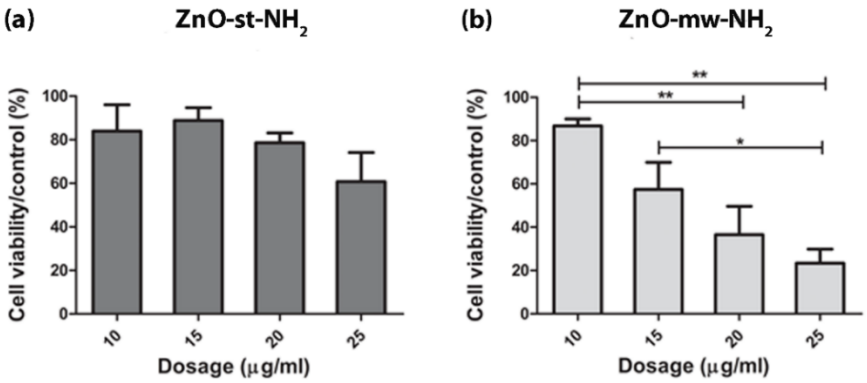

Figure 2.12: Cell viability of KB cells after a 24 hours treatment with escalating concentration of **(a)** ZnO-st-NH_2 NCs and **(b)** ZnO-mw-NH_2 NCs. Results are expressed as percentages with respect to the control. ** $p \leq 0.001$ and * $p = 0.05$.

To have a better comprehension of the interaction between nanocrystal and cells, the cellular uptake of both ZnO-st-NH_2 and ZnO-mw-NH_2 was evaluated by flow-cytometry.

For these tests, the non-toxic concentration of 10 μg/ml was used. The functionalized nanocrystals were labelled with a red emitting fluorescent dye (Atto633-NHS Ester, AttoTech) and its fluorescence was used to calculate the extent of internalization of NCs in KB cells after a 24 hours treatment. Briefly, flow cytometry allowed single cell analysis and the identification of the percentage of cells that internalized the NCs (positive cells) in the overall population was possible by the detection of fluorescent signal related to labelled ZnO-st-NH_2 or ZnO-mw-NH_2 NCs.

Representative results are reported in **Figure 2.13**, where the black curves represent the untreated cell baseline signal while the blue curves represent cells incubated with ZnO-st-NH_2 (**Figure 2.13a**) and ZnO-mw-NH_2 (**Figure 2.13b**). The percentages of positive cells were quantified setting a threshold upon untreated cells control histogram and were equal to 74 ± 9% for ZnO-st-NH_2 and 98.0 ± 0.4% for ZnO-mw-NH_2 NCs, with no significant differences between the two treatments. However, NCs produced by microwave-assisted method presented a considerably lower standard error, indicating a higher experimental reproducibility as already pointed out for cytotoxicity tests. In addition, the histogram related to ZnO-mw-NH_2 NCs showed a higher shift on the x-axis compared to that of conventionally synthesized NCs, indicating that a major number of ZnO-mw-NH_2 NCs were internalized within single cells.

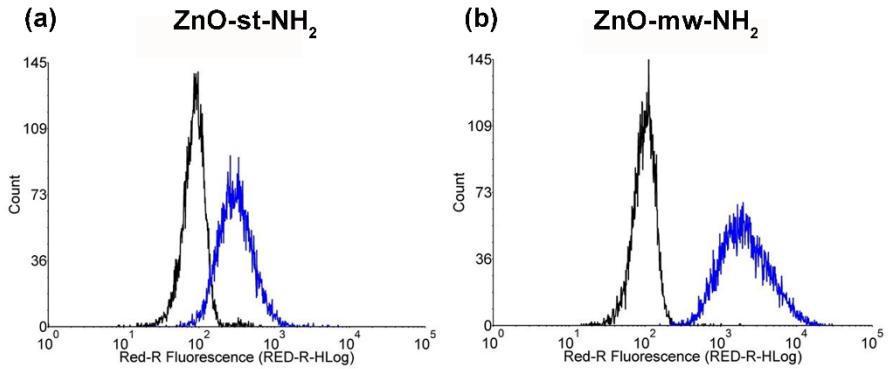

Figure 2.13: Representative histograms of cellular uptake of **(a)** ZnO-st-NH_2 NCs and **(b)** ZnO-mw-NH_2 NCs. Black curves represent the untreated KB cell baseline signal and blue curves represent cells after 24 hours incubation with 10 μg/ml of NCs.

2.4 Conclusions

Physico-chemical and biological characterization of synthesized ZnO NCs confirmed the higher reproducibility and reliability of microwave-assisted synthetic approach compared to conventional solvothermal method. As reported in literature, in fact, the microwave-assisted heating could guarantee a homogenous heating of the precursors and a simultaneous nucleation of the NCs, producing crystalline particles with greater quality.

In particular, the detailed physico-chemical characterization performed on both ZnO-st NCs and ZnO-mw NCs, highlighted that the two synthetic procedures allowed to obtain nanocrystals with analogous surface chemistry and crystal structure, as displayed by XPS and XRD analyses respectively. However, electron microscopy measurement displayed that ZnO-mw NCs obtained by microwave-assisted synthesis possessed more homogeneous size and morphologies compared to conventional ZnO-st NCs.

These dimensional and morphological differences were reflected by the colloidal and biological behavior of the nanocrystals. Indeed, ZnO NCs produced by microwave-assisted solvothermal synthesis presented a better colloidal stability, with narrower size distribution, lower polydispersity and higher inter-batches reproducibility with respect to the conventionally synthesized counterpart. In addition, ZnO-mw NCs possessed a more reproducible cytotoxic response toward KB cancerous cells, accompanied by a more efficient internalization.

The presented results well evidenced the strong influence of synthetic procedure on the nanomaterials properties and applicative potential, showing that NCs produced by similar synthesis methods could present little physico-chemical differences which deeply affect their biological response. In particular, more homogenous and reproducible ZnO NCs produced by microwave-assisted method were characterized by a more efficient cellular interaction and cytotoxicity, highlighting the importance of synthesis control and optimization and the reliability of microwave-assisted procedure.

Furthermore, the success of functionalization with amino-propyl groups was assessed. This surface functionalization had the practical role of enabling the attachment of dye molecules and the fluorescent detection of ZnO-NH_2 NCs. However, the presence of amino-propyl groups conferred other interesting features to the NCs, like great colloidal stability and enhanced luminescent properties, useful in the perspective of application of ZnO NCs as bio-imaging tools.

Chapter 3

Enhanced biostability of zinc oxide nanocrystals through surface functionalization

3.1 Introduction

3.1.1 Nanoparticles 'biological identity'

In the previous chapter was described the influence of the size, morphology and surface properties on the behaviour of nanoparticles in biological applications. These properties together define the so-called synthetic identity of the particles. However, once inserted in biological environment, nanoparticles physically and chemically interact with the surrounding media, affecting the material properties. In this way a new biological identity is defined and this will determine the physiological response. In particular, after the interaction with media components nanoparticles could be subjected to aggregation phenomena, protein adsorption and material degradation or speciation, as schematically represented in **Figure 3.1** and explained in details in the next subsections.

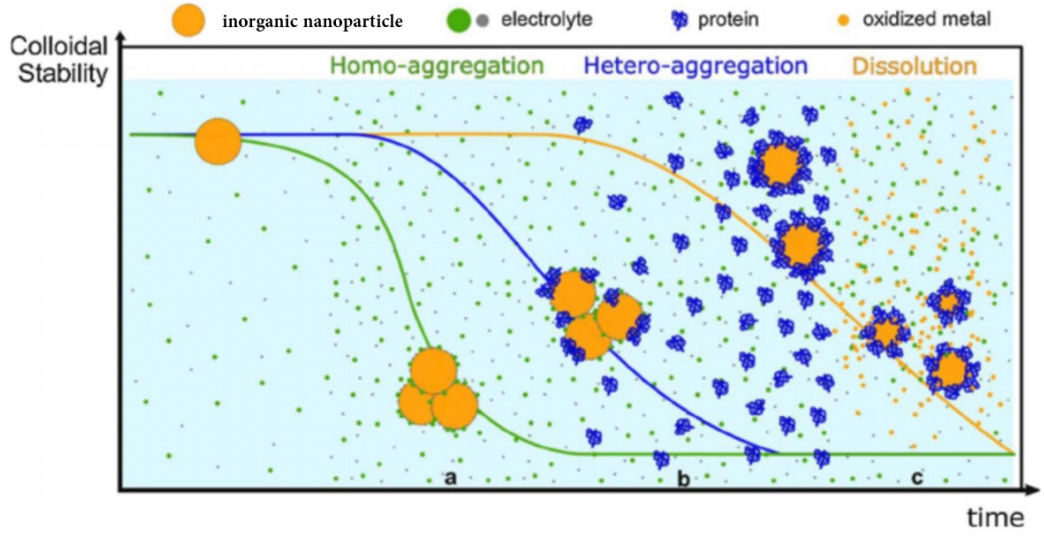

Figure 3.1: Schematic representation of interactions between inorganic NPs and media components. **(a)** Aggregation of NPs as consequence of the high ionic strength of the fluid in which NPs are immersed; **(b)** protein adsorption causing the partial stabilization of NPs aggregates and the formation of protein corona; **(c)** NPs transformation and dissolution due to the chemical interaction with media components. Figure from (Barbero et al., 2017).

3.1.1.1 Colloidal stability of NPs in biological media

A careful assessment of nanoparticles colloidal stability and aggregation extent in physiological media is of paramount importance for an effective evaluation of their biological effects both *in vivo* and *in vitro*. In fact, stable NPs possess a greater biodistribution in living organism, with prolonged circulation half-life and lower clearance by the immune system (Albanese et al., 2012). Aggregation phenomena deeply affect also the cellular response *in vitro*, regulating NPs uptake and subsequent cytotoxicity both directly, due to their dimensional increase, and indirectly, due to NPs altered diffusion and sedimentation rates (Moore et al., 2015).

The behaviour of nanoparticles in solution is the result of the equilibrium between attractive intermolecular forces (i.e. Van der Waals forces) and repulsive

forces, directly connected to net surface charge of nanoparticles. The colloidal stability in simple systems can be efficiently modelled by Derjaguin-Landau-Verwey-Overbeek (DLVO) theory considering the physico-chemical properties of the nanomaterials (Moore et al., 2015). However, in case of more complex solutions, like physiological fluids and cell culture media, also the composition of the solution must be taken into account considering the effect of the high ionic content and the presence of reactive macromolecules. For instance, a high ionic strength contributes to NPs agglomeration directly acting on the electric repulsive forces and compressing the electrical double layer (Bian et al., 2011).

In particular, concerning ZnO NPs studied in this PhD thesis, several literature reports show their aggregation in different biological environments, like physiological media or body fluids. The formation of large aggregates was described for ZnO NPs resuspended in phosphate buffer (Z. J. Deng et al., 2009), cell culture media (Mu et al., 2014), simulated saliva (Pokrowiecki et al., 2019) and lung interstitial fluid (Adamcakova-Dodd et al., 2014). Agglomerated ZnO NPs were also detected inside the cells through direct observation with TEM, obtaining an interesting insight on the influence of aggregation on cellular uptake. In fact, according to their intracellular location, it was proposed that single NPs and small aggregates were internalized through passive diffusion while larger aggregates were subjected to endocytic uptake mechanism (Condello et al., 2016). Another study reported the effect of ZnO NPs aggregation on their cytotoxic effect, indicating small aggregates as more cytotoxic (Tripathy et al., 2014). Moreover, aggregation could deeply influence the NPs dissolution rate and could both be affected or affect the protein absorption on the material surface, highlighting the great complexity and interconnection of these phenomena.

3.1.1.2 Protein adsorption and formation of protein corona

Once injected in biological fluids, the nanoparticles promptly interact with media components forming a layer of adsorbed biomolecules, mainly proteins, called protein corona. As schematically represented in **Figure 3.2**, the protein corona could be divided into two layer: a first monolayer composed by high affinity proteins closely bound to NPs surface which constitute the ‘hard corona’ and a second layer of mildly bounded proteins, called ‘soft corona’. This outer layer is highly dynamic and its composition is mainly determined by the media formulation, comprising generally albumin and other abundant serum proteins (Westmeier et al., 2017).

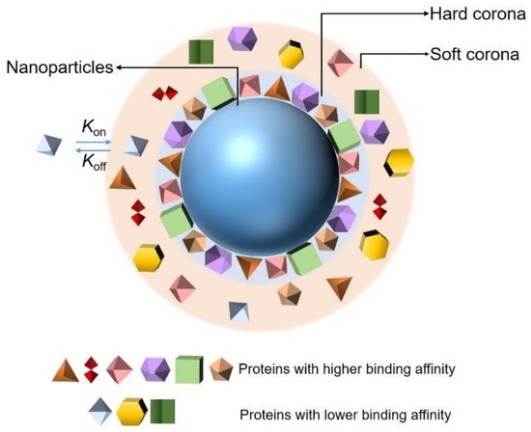

Figure 3.2: Schematic representation of the protein corona formation on NPs surface; figure from (Y. Li & Lee, 2020).

As already mentioned in the introductive chapter, the formation of NPs-protein complexes deeply influences the distribution inside the body determining the nanoparticles interaction with immune systems along with their cellular uptake and intracellular distribution (Salvioni et al., 2019). Thus, the careful evaluation of protein corona formation and composition could be a valuable instrument to understand the nanoparticle biological behavior both *in vivo* and *in vitro*. Actually, some authors pointed out that the different fluids composition and especially the different proteins concentration could be responsible for the changes in materials behavior from *in vitro* to *in vivo* tests (Nierenberg et al., 2018).

The formation of protein corona is governed by NPs-protein and protein-protein interaction and, thus, it is strictly dependent from both NPs physicochemical properties and media formulation. Concerning the intrinsic characteristics of nanoparticles, the size, radius of curvature, hydrophobicity, charge and eventual surface functionalization are all factors that could influence the formation of protein corona. Among the media properties, the protein corona is of course influenced by protein composition and concentration as already described, but also by pH, temperature and time of exposure (Nguyen & Lee, 2017).

A study on the proteins absorption on metal oxide nanoparticles reported that ZnO NPs effectively bind to several plasma proteins with important biological functions including immunoglobulins, lipoproteins, acute-phase proteins and proteins involved in complement pathways and coagulation (Z. J. Deng et al., 2009). Moreover, the same authors indicated that, besides the particle composition, also their aggregation state could influence the type and amount of proteins forming the protein corona. Interestingly, the proteins adsorption could be also exploited to limit the ZnO NPs aggregation and sedimentation in biological media. Literature studies, in fact, indicated the addition of serum to cell culture media as an advantage which could improve the stability of ZnO NPs, producing more reliable cytotoxicity and uptake values (Anders et al., 2015).

3.1.1.3 NPs dissolution and chemical interaction with biological media

The last aspect which contribute to define the biological identity of nanoparticles is their chemical stability in biological media. The chemical resistance, in fact, should be optimized to ensure a correct biodistribution and to control the therapeutic activity of the nanomaterial.

Actually, the evaluation of ZnO NPs dissolution is particularly important since the release of Zn^{2+} ions is considered one of the main mechanisms of ZnO cytotoxicity, as widely explained in the previous chapter. As already mentioned, the dissolution rate is influenced by NPs physico-chemical features, like size and surface properties. However, also the media composition, pH and temperature play a crucial role. *In vitro* studies performed on ZnO nanowires exposed to different simulated body fluids highlighted that they dissolved very rapidly at acidic pH value of artificial fluid mimicking the lysosomal conditions (H. Müller et al., 2010). Similarly, the intracellular dissolution was tested by *in vitro* experiments. In this case a fluorescent probe sensible to Zn^{2+} ions was used together with dye specific for cellular organelles confirming the uptake of ZnO NPs and their dissolution inside the acidic environment of lysosomes (Condello et al., 2016).

Concerning the chemical interactions between ZnO NPs and the components of media employed in biological tests, it is recognized that ZnO is highly reactive towards phosphate ions contained in different amount in all common cell culture media. In particular, the reaction between zinc and phosphate groups would lead to the formation of amorphous zinc phosphate species, involving not only the surface but the whole nanoparticle potentially causing the complete degradation of NPs in dependence of components concentration (Herrmann et al., 2014). The effect of this extracellular dissolution and reprecipitation on the cytotoxicity of ZnO NPs is complex and not fully elucidated. Indeed, some studies indicated that extracellularly released zinc tend to precipitate in form of poorly soluble zinc-phosphate species reducing the Zn^{2+} ions to sub-toxic concentrations (Lv et al., 2012). However, these newly formed zinc species could contribute to the cytotoxicity eliciting a toxic response (Turney et al., 2012). A similar interaction with carbonates species was also reported together with the Zn^{2+} complexation capacity of amino acid and other ligands contained in cell culture medium, which could regulate zinc extracellular levels (Mu et al., 2014). From these results it emerges the importance of the evaluation of ZnO NPs dissolution and speciation in biological media in order to ensure reliable estimates of their toxicity.

3.1.2 Surface modifications for NPs stabilization

For the effective application of nanoparticles in biomedical field, not only the comprehension but also the control of their interaction with media components is of paramount importance. As just described, the understanding of complex and interconnected mechanisms that define the NPs biological identity is fundamental for the correct evaluation of the physiological responses generated in cells, organs, tissues or living organisms. Nevertheless, the high reactivity with biologically

active molecules and the poor colloidal and chemical stability, reported for ZnO NPs but extendable to many other nanomaterials, is detrimental for their effective therapeutic application. In fact, an ideal therapeutic nanoconstruct would possess great blood stability and low immunogenicity among its main characteristic. In this perspective, NPs surface functionalization constitutes a valuable option to implement and optimize nanoparticles stability and compatibility in the biological environment. As widely reported in the literature, the main categories of functionalizing agents for nanoparticles stabilization in biomedical applications include synthetic and natural polymers and biological molecules like lipids or proteins (Limongi et al., 2019).

3.1.2.1 Polymers functionalization

The surface modification of different types of nanoparticles with hydrophilic and zwitterionic polymers is well established. Firstly, the functionalization of NPs surface with appropriate polymeric chains provide the creation of a physical barrier that hinder the particles contact and subsequent aggregation through steric stabilization. Moreover, polymer functionalization could also affect the protein adsorption on NPs surface, acting on the NPs biological identity and, thus, on the pathophysiological response. In particular, several polymer parameters, like grafting densities, chain length and flexibility, presence of charged groups and branches, could be opportunely modelled to guarantee a precise control on the formation of protein corona (Angioletti-Uberti, 2017).

In the category of polymers, polyethylene glycol (PEG) is one of the most commonly used and it is considered the gold standard to prolong blood circulation of NPs in biomedical applications. PEG compounds with different chain length and molecular weights can be synthesized by polymerization processes starting from ethylene oxide. In addition, PEG terminal groups can be easily modified imparting a great versatility to the polymer and allowing its selective attachment to NPs with different surface chemistry or its further conjugation with additional functionalizing agents (Guerrini et al., 2018). PEG polymer is particularly suitable for biological applications thank to its hydrophilic nature which guarantees the formation of a strong hydration layer around the particles, providing short-range repulsive forces even in solution with extreme pH value and high ionic strength (Sakura et al., 2005). Moreover, PEG coating reduces the non-specific interaction of NPs with plasma proteins, limiting also the binding with opsonin and the subsequent recognition by mononuclear phagocytic system (Guerrini et al., 2018). This anti-fouling effect of PEG is normally called ‘stealth effect’, since it makes the NPs almost invisible to the organism, guaranteeing a lower immunogenicity and a prolonged half-life in bloodstream. However, the surface modification with PEG presents also some limitations, like a reduced NPs-cell interaction ascribable to the presence of PEG coating (Pelaz et al., 2015). In addition, the development of anti-PEG antibodies responsible for unexpected immune response is also accounted and attributed to the increasing use in pharmaceutical and clinical applications.

To overcome these issues, several researches are devoted to the development of alternative polymers with similar physico-chemical characteristics. Besides other hydrophilic polymers (like poly-glycerol, poly-vinylpyrrolidone, poly-hydroxyl propyl methacrylate, …) also zwitterionic polymers have attracted great attention (Thi et al., 2020). This class of materials, comprising for instance poly(carboxybetaine) or poly(sulfobetaine), possesses stealth feature. Moreover, thanks to their zwitterionic nature they possess interesting charge properties, presenting a neutral charge at physiological pH and a positive charge in tumor acidic microenvironment. The prevalence of cationic behavior near the negative membrane of cancerous cells could result in an enhanced cellular uptake of functionalized nanoparticles (P. Zhang et al., 2018).

Nevertheless, also these newly-investigated materials presented multiple issues related to their biodegradability and difficult synthesis and reliability (Guerrini et al., 2018). In this context, the possibility to apply biological molecules like proteins or lipids for the NPs stabilization was also considered.

3.1.2.2 Protein coating

One of the advantages of using proteins for the colloidal and chemical stabilization of NPs in the biological environment is that they are naturally occurring biomolecules and are therefore stable under physiological conditions. The controlled adsorption of specific protein on NPs surface could provide steric and electrostatic stabilization to the hybrid system (Guerrini et al., 2018). In addition, the pre-coating with selected proteins would limit the further adsorption of biologically active proteins contained in the physiological media. For instance, nanoparticles pre-coated with an artificial corona of albumin presented a decreased adsorption of biological source proteins determining a lower immunogenicity (Barui et al., 2020).

The major drawbacks of NPs functionalization with proteins are connected to the large increase of hydrodynamic diameters of the functionalized NPs and to the conformational stability of proteins which requests the use of buffers with high ionic strength, detrimental for the initial resuspension of NPs (Limongi et al., 2019).

3.1.2.3 Lipid coating

Another class of biologically relevant molecules used for nanoparticles stabilization are lipids.

Lipids are different types of organic molecules with amphiphilic nature constituted by a hydrophilic polar head and a hydrophobic tail. The combination of different heads groups with different number of acyl chains possessing peculiar length and saturation level originates multiple classes of lipid molecules, like phospholipids, glycolipids, sphingolipids, sterols, etc, (Fahy et al., 2011). However, the generic chemical structure unites the different lipid classes and is responsible for the formation of their characteristic bilayer arrangement in aqueous biological environment. In this arrangement, in fact, the lipids self-organize themselves in order to protect the hydrophobic tails from the surrounding media.

Lipids are the main components of cellular membranes in which they have a structural role and act as a barrier protecting the intracellular milieu from the external environment. Considering their biological functions, lipids are therefore considered good candidates for the stabilization of NPs, providing a defensive and biocompatible barrier (Luchini & Vitiello, 2019). As already mentioned in the introductive chapter, several liposomes, i.e. spherical vesicles constituted by one or more lipid bilayer, are currently used as drug nanocarriers in clinical applications (Petre & Dittmer, 2007). More recently, lipids are proposed as stabilizing agents to improve the colloidal and chemical stability of inorganic nanoparticles in the biological environment. The lipid coating introduced on NPs surface goes under the name of supported lipid bilayer (SLB).

In general, different types of phospholipids, applied either singularly or in mixtures, are the most widely used lipid molecules in biomedical applications. Indeed, they are the main constituent of plasma membranes and, moreover, they possess an amphiphilic behavior which ensures their good interaction with several kinds of NPs (Weingart et al., 2013). However, they are also reportedly used in combination with other types of lipids like cholesterol or sphingomyelin (Ip et al., 2011).

Concerning the preparation methods of SLB, they can be divided essentially in two main categories: vesicles fusion and solvent exchange method. A schematic representation of the two different procedures is shown in **Figure 3.3**.

In case of vesicles fusion, liposome structures are created and reduced to appropriate size with sonication or extrusion and then put in contact with NPs in aqueous solution. The formation of SLB would involve the adsorption and the subsequent spontaneous rupture of vesicles on the nanoparticles surface (**Figure 3.3a**). This process is strictly dependent from electrostatic interactions between liposomes and substrate and is deeply influenced by both vesicles properties (like lipid composition, size and osmotic pressure) and nanoparticles properties (like elemental composition, morphology, surface groups) (Jackman & Cho, 2020). This method is well documented for the formation of SLB on silica NPs (Mornet et al., 2005) but it results ineffective with other types of nanomaterial with less favorable substrate-vesicles interactions.

The other strategy is more versatile and is based on the self-assembly behavior of lipids. In the solvent exchange method, the liposomes are not preformed but the lipids are dispersed as monomers in organic solvents and put in contact with the NPs. The solvent is then changed, increasing the water fraction and causing the rearrangement of lipids molecules that would form a SLB onto the solid surface (**Figure 3.3b**). Indeed, the presence of NPs in solution offers a support for the lipid bilayer formation, acting as energetically favorable nucleation sites with respect to the formation of vesicles in the bulk phase (Hohner et al., 2010). The solvent exchange method is successfully applied to envelop different types of nanoparticles like mesoporous silica (Cauda, Engelke, et al., 2010), metal-organic framework (Wuttke et al., 2015) or gold substrate (Jackman & Cho, 2020) employing different lipids mixtures.

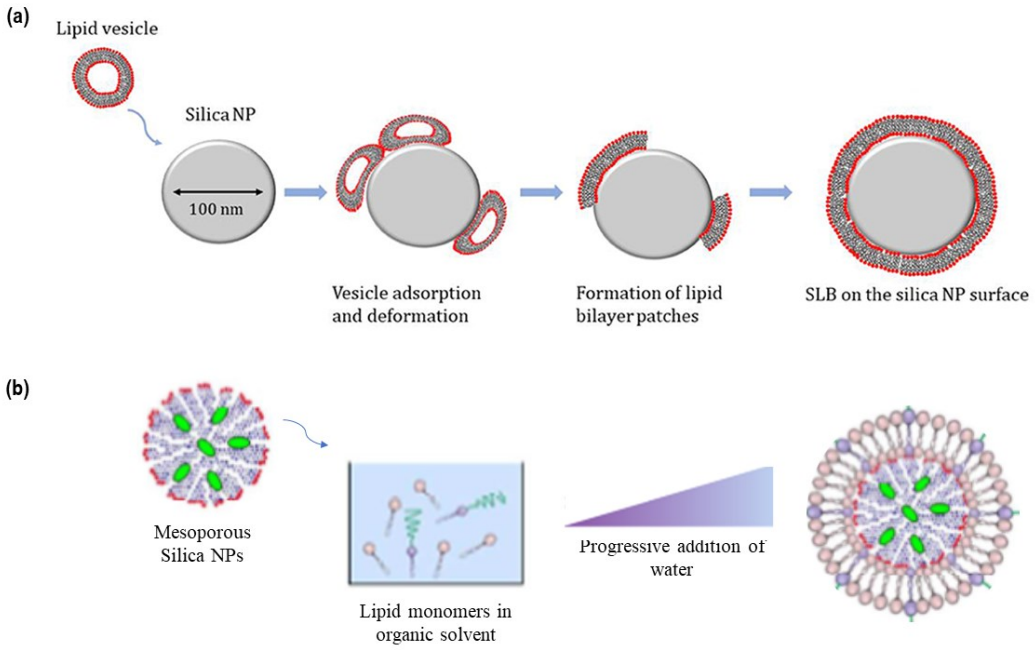

Figure 3.3: Schematic representation of the two main methods for the formation of supported lipid bilayer on NPs surface. **(a)**Vesicle fusion (figure from (Luchini & Vitiello, 2019)); **(b)** Solvent exchange method (figure modified from (Tan et al., 2013)).

As clearly visible from the schematic representation, the supported lipid bilayer guarantees a very uniform coverage of NPs ensuring an effective barrier from surrounding media, in particular against protein adsorption. Several *in vitro* studies confirmed the enhanced colloidal stability of lipid-coated NPs (Durfee et al., 2016) as well as their improved biocompatibility, certified by the absence of hemolysis and blood aggregation (Zeng et al., 2015). In addition, the presence of lipid coating ensures a greater NPs internalization inside the cells and offers the possibility to further functionalize it for targeting purposes (Durfee et al., 2016).

Considering these literature results, the high reactivity of ZnO nanomaterials in the biological environment result clear. Therefore, a careful evaluation of colloidal and chemical stability of synthesized ZnO NCs was performed. In particular, the aggregation extent, dissolution and reactivity with biological media components were analyzed through long-term biostability tests performed in cell culture medium, phosphate-buffered saline (PBS) and simulated body fluid (SBF), an artificial buffer solution which mimics the inorganic composition of human blood plasma. In order to improve the colloidal and chemical stability, different surface functionalization were also tested. Pristine ZnO NCs, characterized by a surface rich of hydroxyl groups typical of metal oxides NPs, were chemically conjugated with amino-propyl groups, imparting a more positive surface charge and a slight steric hindrance. The second functionalization procedure envisaged the combination of ZnO NCs with lipid molecules through a solvent exchange method, generating more stable and biocompatible lipid-coated nanoparticles.

3.2 Materials and Methods

3.2.1 Preparation of ZnO, ZnO-NH_2 and ZnO-DOPC NCs

Pristine (ZnO) and amino-propyl functionalized (ZnO-NH_2) nanocrystals were produced as already described in chapter 2 (Garino et al., 2019).

Lipid-coated nanocrystals (ZnO-DOPC NCs) were prepared combining ZnO NCs with 1,2-dioleoyl-sn-glycero-3-phosphocholine (DOPC, Avanti Polar Lipids, Inc.) using the solvent exchange method. To prepare the lipid stock solution, 2.5 mg of DOPC dispersed in chloroform were dried overnight under vacuum and redispersed with 400 µl of ethanol and 600 µl of bd water. 1 mg of ZnO NCs were then centrifuged to discard ethanol and the obtained pellet was resuspended with 100 µl of lipid solution by pipetting. Finally, 700 µl of bd water were added, inducing the formation of a supported lipid bilayer at the NCs surface. For the biostability assays, the process was scaled up to obtain 100 mg of ZnO-DOPC NCs.

3.2.2 ZnO, ZnO-NH_2 and ZnO-DOPC NCs Characterization

3.2.2.1 X-ray Diffraction

The crystalline structure of the three types of NCs was analyzed by X-ray diffraction (XRD). The samples were deposited drop by drop on a silicon wafer, obtaining an appropriately thick layer of dried ZnO NCs, and then analyzed with a Panalytical X'Pert diffractometer with the same settings described in Chapter 2.

3.2.2.2 Electron Microscopy

The morphology of the three types of NCs was analyzed with Filed Emission Scanning Electron Microscopy (FESEM Auriga and Merlin, Carl Zeiss) and Transmission Electron Microscopy (TEM, Tecnai F20ST, FEI). For both analyses the samples were diluted at a final concentration of 25 µg/ml and deposited on a silicon wafer or on a holey carbon-coated copper grid respectively.

3.2.2.3 Energy Dispersive X-ray Spectroscopy (EDS) and Fourier Transformed Infrared (FT-IR) Spectroscopy

Energy Dispersive X-ray Spectroscopy were performed on the same samples prepared for FESEM analyses by a microanalysis system (AZTec, Oxford Instruments, coupled to the FESEM Merlin, Carl Zeiss).

To complete the compositional analysis, Fourier Transformed Infrared (FT-IR) spectra were recorded in transmission mode with a Bruker Equinox 55, registering the absorbance in the range of 4000-400 cm^{-1}.

3.2.2.4 Zeta-Potential and Dynamic Light Scattering (DLS) measurements

Zeta-Potential measurements were performed using a Zetasizer Nano ZS90 (Malvern Instruments). The three types of NCs were resuspended in bd water at

concentration 500 μg/ml and the pH was adjusted from 2 to 11 with HCl and NaOH 1 M. The same instrument was used to determine the hydrodynamic size distribution of nanocrystals in ethanol and bd water, through Dynamic Light Scattering (DLS) technique.

3.2.2.5 Fluorescence Microscopy

To confirm the formation of the supported lipid bilayer on the NCs surface ZnO-DOPC NCs were characterized with fluorescence microscopy.

For these experiments, the ZnO-NH_2 NCs in ethanol were labelled with Atto 550-NHS Ester (Atto-Tec) as described in Chapter 2. The labelling of lipid bilayer was obtained by adding 0.5 μg of Bodipy-FL-DHPE (Thermo Fisher Scientific), a lipid conjugated with a fluorescent probe, to the 2.5 mg DOPC stock solution before the evaporation of chloroform.

The labeled sample were imaged with a wide-field fluorescence inverted microscope (Nikon Eclipse Ti-E) equipped with a super bright wide-spectrum source (Shutter Lambda XL) and a high-resolution camera (Zyla 4.2 Plus, 4098×3264 pixels, Andor Technology) using a 60× immersion oil objective (Apo 1.40, Nikon). Fluorescence images of red and green channels, corresponding to fluorescence of Atto 550-NHS Ester and Bodipy-FL-DHPE respectively, were acquired and then superimposed to evaluate colocalization.

3.2.3 Biostability tests

3.2.3.1 Media Composition

The biostability assay was performed in cell culture medium (Eagle's minimal essential medium, EMEM), supplemented with 10% fetal bovine serum (FBS) and in two buffer solutions: phosphate-buffered saline (PBS), commonly used in biological research, and simulated body fluid (SBF), a buffer solution that mimic the inorganic composition of human plasma.

The detailed composition of PBS and EMEM, both purchased from Sigma-Aldrich, are reported in Table 3.1 and 3.2.

The SBF was prepared following protocol by Kokubo et al. (Kokubo et al., 1990). Briefly the following reagents were dissolved in 500 ml of bd water, under continuous stirring: 7.996 g NaCl, 0.350 g $NaHCO_3$, 0.224 g KCl, 0.228 g $K_2HPO_4 \cdot 3H_2O$, 0.305 g $MgCl_2 \cdot 6H_2O$, 0.278 g $CaCl_2$, 0.071 g Na_2SO_4, 40 mL HCl 1 M e 6.057 g $NH_2C(CH_2OH)_3$ (TRIS). The solution was heated up to 37°C and the pH was adjusted at 7.4 by titration with HCl 1 M. The solution was then made up to 1 L by adding bd water and stored at 4°C until use. The composition of the SBF, compared to that of human plasma, is shown in Table 3.3.

Table 3.1: Composition of Phosphate-buffered saline (Sigma-Aldrich)

Component	*Concentration [g/l]*
KCl	0.2
KH_2PO_4	0.24
NaCl	8.0
NaH_2PO_4 (anhydrous)	1.44

Table 3.2: Composition of Eagle's minimal essential medium (EMEM M4655, Sigma-Aldrich). The presence of additional salts, electrolytes, plasma proteins and hormones derived from the addition of 10% FBS must be considered.

Component	*Concentration [g/l]*
$CaCl_2$	0.265
$MgSO_4$ (anhydrous)	0.09767
KCl	0.4
$NaHCO_3$	2.2
NaCl	6.8
NaH_2PO_4 (anhydrous)	0,122
Amino Acids	0.8707
Vitamins	0.0081
D-Glucose	1.0

Table 3.3: Ionic composition (mM) of Simulated Body Fluid (SBF) and human blood plasma (Kokubo et al., 1990).

Ion	*SBF*	*Blood Plasma*
Na^+	142.0	142.0
K^+	5.0	5.0
Mg^{2+}	1.5	1.5
Ca^{2+}	2.5	2.5
Cl^-	148.8	103.0
HCO^{3-}	4.2	27.0
HPO_4^{2-}	1.0	1.0
SO_4^{2-}	0.5	0.5

3.2.3.2 Biostability assay

ZnO, ZnO-NH_2 and ZnO-DOPC NCs were separated from ethanol or water by centrifugation, washed three times with bd water and resuspended in the aforementioned biological media at the concentration of 2 mg/ml (25 mg of NCs in 12.5 ml of pre-heated solutions). The obtained suspensions were then kept at 37°C

under continuous stirring and at selected time points (1, 24, 72 hours and 25 days) 5 mg of NCs, corresponding at 2.5 ml of solution, were collected and centrifuged.

The supernatants were opportunely diluted in bd water for ICP/MS analyses. The pellets were washed twice with bd water and retained for further characterizations. XRD, electron microscopy, EDS and FT-IR analyses were performed on the samples collected after each time points to investigate changes in crystalline structure, morphology and composition respectively.

DLS measurements on ZnO, ZnO-NH_2 and ZnO-DOPC NCs redispersed in the three different biological media at the concentration of 500 μg/ml were also performed, monitoring the size distribution at t_0 and over-time.

3.3 Results and discussion

3.3.1 Preparation and characterization of pristine, amino-propyl functionalized and lipid-coated ZnO NCs

3.3.1.1 Preparation of ZnO, ZnO-NH_2 and ZnO-DOPC NCs

In order to evaluate the influence of surface properties on the colloidal and chemical stability of ZnO nanomaterials in biological environment, three different types of ZnO nanocrystals with defined surface charge and chemistry were prepared.

Pristine ZnO NCs were synthesized following the conventional solvothermal method described in detail in Chapter 2, that allowed to produce round nanometric crystals exposing neutral hydroxyl groups (–OH) at the surface.

The obtained ZnO NCs were functionalized with amino-propyl groups, by chemical reaction with APTMS molecules. Briefly, according to the reactions between amino-silanes and metal oxides nanoparticles reported in literature (Mallakpour & Madani, 2015), the hydrolysis of methoxy groups of APTMS molecules occurred producing silanol groups that could react with –OH groups of ZnO to form covalent bonds. Functionalizing agent molecules were thus grafted on ZnO NCs surface, exposing new amino groups that imparted at ZnO-NH_2 NCs a predominant positive surface charge.

Finally, pristine ZnO NCs coated by a lipid bilayer (ZnO-DOPC NCs) were obtained through solvent exchange method as described in detail in the Materials and Methods section. Briefly, thanks to the favorable interactions between lipids and alcoholic solutions, DOPC molecules were stable as monomers in the ethanol/water stock solution. By increasing the water content, the lipids began to self-assemble into liposomes, characterized by a bilayer arrangement in which the polar heads were exposed on the outside and the hydrophobic tails of lipid molecules were in the inner region, protected from water. The presence of nanoparticles in solution offered an energetically favorable support to lipid self-assembly and the bilayer was formed at their surfaces (Hohner et al., 2010).

The success of DOPC lipid coating was firstly confirmed by fluorescence microscopy (**Figure 3.4**). The DOPC lipid shell was labeled by adding 1% Bodipy-FL-DHPE (λ_{Exc}=488 nm) to the lipid formulation while ZnO-NH_2 NCs, exceptionally used as core nanomaterial to allow the attachment of fluorescent dye, were labeled with Atto550-NHS ester (λ_{Exc}=550 nm). The two components were imaged in green channel (**Figure 3.4a**) and red channel (**Figure 3.4b**) respectively and then the images were superimposed (Merge, **Figure 3.4c**) highlighting an almost complete co-localization of the spots which confirmed the success of lipid shielding. Different experiments were performed and a conjugation yield of ~96% was estimated.

A complete morphological and physico-chemical characterization of the three different types of nanocrystals was also performed as reported in the following sections.

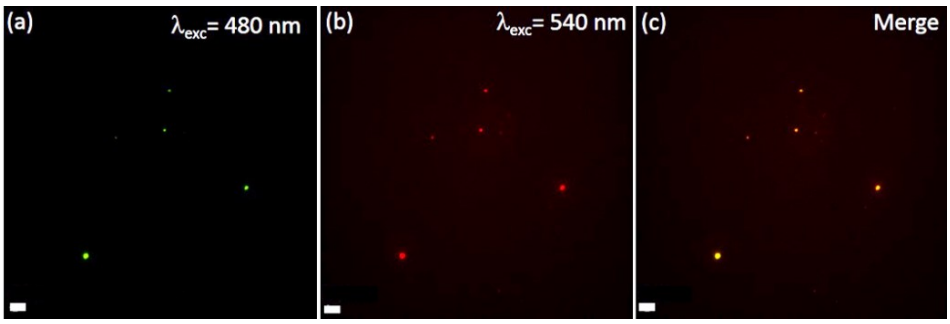

Figure 3.4: Wide-field fluorescence images of **(a)** DOPC shell labeled with Bodipy-FL-DHPE (green chanel), **(b)** ZnO-NH_2 NCs labeled with Atto550-NHS Ester (red channel) and **(c)** merge of the two channels, showing complete colocalization. Scale bar: 10 μm.

3.3.1.2 Morphological and structural characterization

Information on the size and morphology and on the crystalline structure of the three different types of ZnO NCs were obtained by electron microscopy **(Figure 3.5**) and XRD measurements (**Figure 3.6**) respectively.

FESEM, TEM and STEM images of pristine ZnO NCs (**Figure 3.5a**) showed well-dispersed nanocrystals with an almost spherical shape and a diameter of about 14 nm. Microscopy images of both amino-propyl functionalized ZnO-NH_2 NCs (**Figure 3.5b**) and lipid coated ZnO-DOPC NCs (**Figure 3.5c**) confirmed that the morphology of the particles was not modified by functionalization processes. However, ZnO-DOPC sample presented a slightly higher dimension (≥ 20 nm from FESEM image) and the presence of a sort of covering around the nanocrystals, ascribable at the formation of the lipid bilayer obtained by the solvent exchange method.

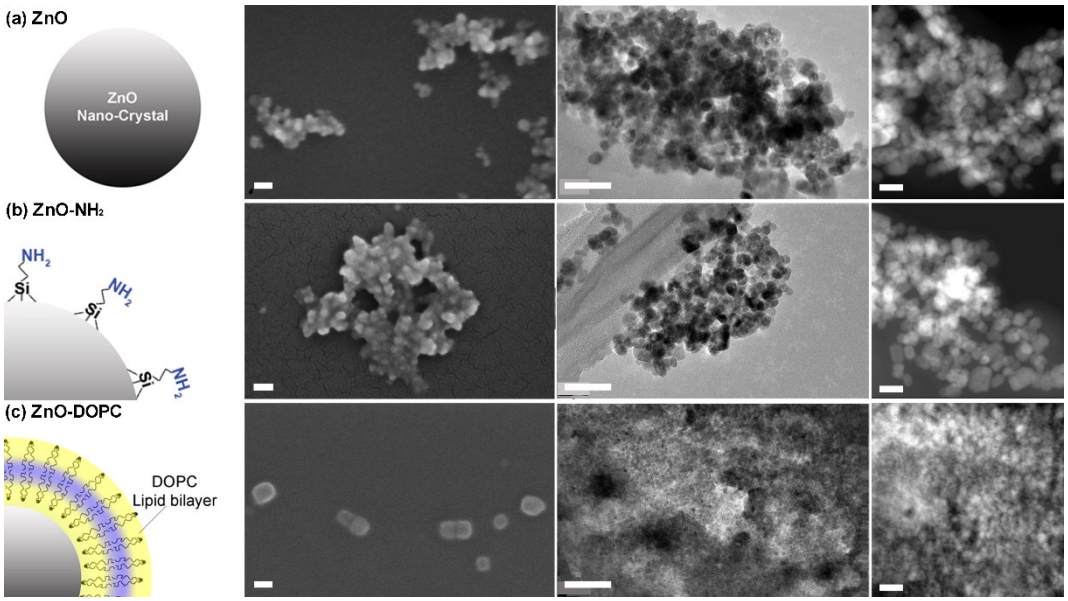

Figure 3.5: Morphological characterization of **(a)** pristine ZnO NCs, **(b)** amino-propyl functionalized ZnO-NH_2 NCs and **(c)** lipid-coated ZnO-DOPC NCs. From left to right: scheme of the particles, FESEM (scale bars 50 nm), TEM (scale bars 50 nm) and STEM (scale bar 20 nm) images. For FESEM images all the nanocrystals were coated by a thin layer of Pt.

X-ray diffraction pattern of pristine ZnO NCs (blue curve in **Figure 3.6**) confirmed the crystalline nature of the particles, corresponding to single-phase hexagonal wurtzite structure of ZnO (JCPDS card n° 36-1451). As expected, the same structure was maintained after both functionalization processes (red and green curves).

In order to estimate the dimension of single crystallites, the Debye-Sherrer equation was applied to the broad (100), (101) and (002) diffraction peaks, obtaining an average particles size equal to 15 nm. This was in good accordance with size from FESEM and TEM images, evidencing that ZnO NCs were monocrystalline structures.

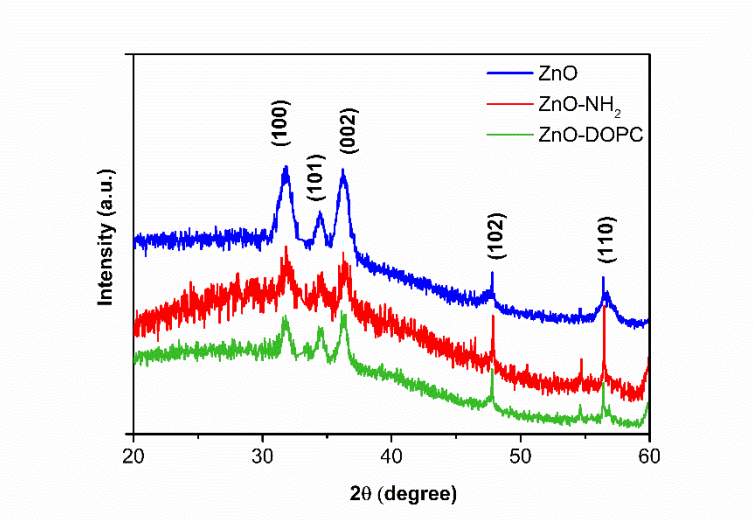

Figure 3.6: XRD spectra of ZnO NCs (blue curve), ZnO-NH_2 NCs (red curve) and ZnO-DOPC (green curve).

3.3.1.3 Surface properties

The surface composition of pristine and functionalized nanocrystals was investigated through FT-IR spectroscopy.

As clearly shown in **Figure 3.7a**, ZnO and ZnO-NH_2 spectra (blue and red curve respectively) presented several common features, due to similarities in their surface composition. In particular, both samples presented an intense mode at 440 cm^{-1}, typical Zn–O vibration and a peak at 3800 cm^{-1} along with a broad band between 3600 and 3200 cm^{-1}, both ascribable to the stretching vibration of hydroxyl groups. However, it is worth to observe that the relative intensity of the last two peaks was lower for ZnO-NH_2 NCs with respect to the pristine ZnO sample. This could be explained considering the reaction mechanism of amino-propyl functionalization, in which APTMS molecules form covalent bonds with hydroxyl groups of ZnO surface, decreasing thus the number of free –OH groups. Moreover, the ZnO-NH_2 spectrum presented a peak near 3200 cm^{-1}, characteristic of primary amines, and new bands at 1020 and 1100 cm^{-1}, corresponding to symmetric and asymmetric of O–Si–O bond, which directly confirmed the presence of APTMS moieties on NCs surfaces. Finally, both ZnO and ZnO-NH_2 spectra presented the typical vibration modes of C=O (1570 cm^{-1}) and C–O (1420 cm^{-1}) and the

symmetric and asymmetric stretching of $–CH_2$ and $–CH_3$ at 2860 and 2925 cm^{-1}, respectively. These peaks were attributed to residual acetate groups deriving from synthesis precursor or to methoxy groups derived from the reflux conditions applied in the synthetic procedure. In case of ZnO-NH_2 sample the $–CH_x$ stretching modes appeared more intense, due to the presence of propyl chain of functionalizing agent APTMS.

ZnO-DOPC spectrum (**Figure 3.7a**, green curve) presented multiple intense peaks at 2860, 2925 and 1750 cm^{-1} ascribable to stretching vibrations of $–CH_x$ and C=O groups respectively, widely present in the phospholipidic hydrophobic tails. Contributions due to the phosphates groups present in the phospholipid heads were also detected at 1100 cm^{-1} (P=O stretching) and 1230 cm^{-1} (P–O stretching). The disappearance of the –OH broad band between 3600 and 3200 cm^{-1} and the attenuation of Zn–O vibration peak at 440 cm^{-1} further confirmed the success of DOPC shell formation at the ZnO surface.

The effects of the functionalization processes on the NCs surface charge were evaluated through Zeta-Potential measurements (**Figure 3.7b**), performed in bd water varying the pH values between 2 and 11.

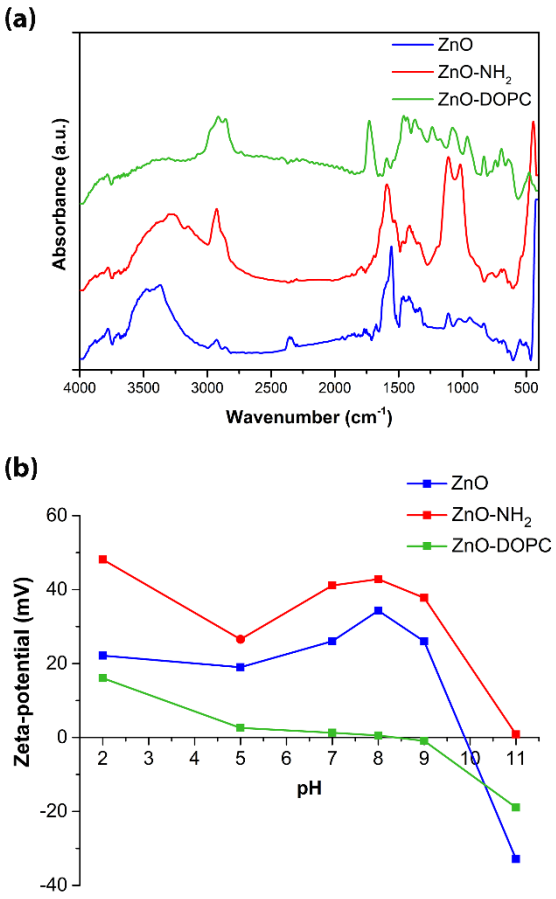

Figure 3.7: (a) Fourier Transform-Infrared (FT-IR) spectra and **(b)** Zeta-potential measurements of pristine ZnO (blue curves), amino-propyl functionalized (red curves) and lipid-coated (green curves) NCs.

According to the literature, the surface charge of ZnO particles is basically governed by the hydroxyl surface groups (Degen & Kosec, 2000). The –OH groups tend to release chemisorbed protons at high pH values, inducing a negatively charged surface formed by ZnO^- species. In contrast, at low pH values the protons of the medium are transferred at the nanocrystals surface, leading to the formation of positively charged $ZnOH_2^+$ groups. The Zeta-Potential values obtained for pristine ZnO NCs (**Figure 3.7b**, blue line) were in good accordance with the described behavior and leaded to an isoelectric point (IEP) at pH 9.85, consistent with the values reported in literature (Degen & Kosec, 2000).

Amino-propyl functionalized ZnO-NH_2 sample showed a similar trend of Zeta-Potential values (**Figure 3.7b**, red line), but they were shifted to higher positive values with an IEP around pH 11. At acidic pH values, this behavior could be ascribed to the protonation of amino groups, forming $–NH^{3+}$ species and thus confirmed the success of functionalization procedure.

In contrast, an important shift toward lower Zeta-Potential values were observed for ZnO-DOPC sample (**Figure 3.7b**, green line), that presented slightly positive or negative Zeta-Potential values at acidic or basic conditions respectively and IEP at pH 7.8. This flatter trend of Zeta-Potential can be explained considering the DOPC molecular structure, that comprehend both negative phosphate and positive amine head groups, responsible for the neutralization of the ZnO NCs surface charge.

Taken together, the FT-IR and Zeta-Potential measurements allowed to analyze the different surface composition of the prepared NCs, confirming both the chemical functionalization with amino-propyl groups and the formation of DOPC phospholipid bilayer.

3.3.2 Colloidal behavior in biological media

The influence of the surface modifications on the colloidal stability was evaluated through Dynamic Light Scattering (DLS) technique, measuring the hydrodynamic size distribution of the three different types of NCs in various media.

In particular, the colloidal behavior was investigated in bd water, PBS (i.e. Phosphate-buffered saline, a water-based buffer solution widely used as dispersant medium in biological applications), artificial physiological medium (Simulated Body fluid, SBF) and in cell culture medium completed with the 10% of fetal bovine serum (EMEM). As already described in details in the Material and Methods section, SBF is an inorganic buffered solution that simulate the inorganic composition of the human plasma (**Table 3.3**) while EMEM is a cell culture medium commonly used for cells and tissue culturing, composed by inorganic salts and biological components, derived also from serum addition (**Table 3.2**). Therefore, in the perspective of a biological application, DLS measurements in these two solutions were particularly interesting because allowed a preliminary evaluation of ZnO NCs colloidal and chemical stability in biological environment. In addition, DLS analyses of the different types of ZnO NCs were compared in order to understand how surface properties affect the NCs behavior in solution and

which surface modification produced the best colloidal behavior, with stable and well-dispersed nanocrystals.

The obtained results are presented in **Figure 3.8**. As clearly shown in the top panel, all the three NCs resulted stable in bd water with monodisperse distributions centered at 44 nm for pristine ZnO NCs and at 88 nm and 120 nm for functionalized ZnO-NH_2 NCs and ZnO-DOPC NCs respectively. As already mentioned, the increase of mean size could be caused by the presence of functional layer, formed in this case by lipids bilayer or APTMS molecules.

In PBS, pristine ZnO NCs formed micrometric aggregates showing a drastic diminution of their colloidal stability, whereas lipid-coated ZnO-DOPC NCs remained highly stable confirming the hydrodynamic size obtained in bd water.

The improvement of colloidal behaviour provided by the phospholipid shell was observed also in SBF and EMEM, in which ZnO-DOPC sample showed narrow size distribution centred at 66 nm and 108 nm respectively. In contrast, ZnO NCs and ZnO-NH_2 NCs formed large aggregates in both media, although to a lesser extent for amino-propyl functionalized sample with respect to the pristine one.

Overall, these data suggested that the DOPC lipid shell could efficiently prevent the aggregation phenomena, stabilizing the ZnO NCs. It could be assumed that lipid shielding limited the interaction between the nanocrystals and reactive media components preserving the chemical and colloidal integrity of ZnO NCs.

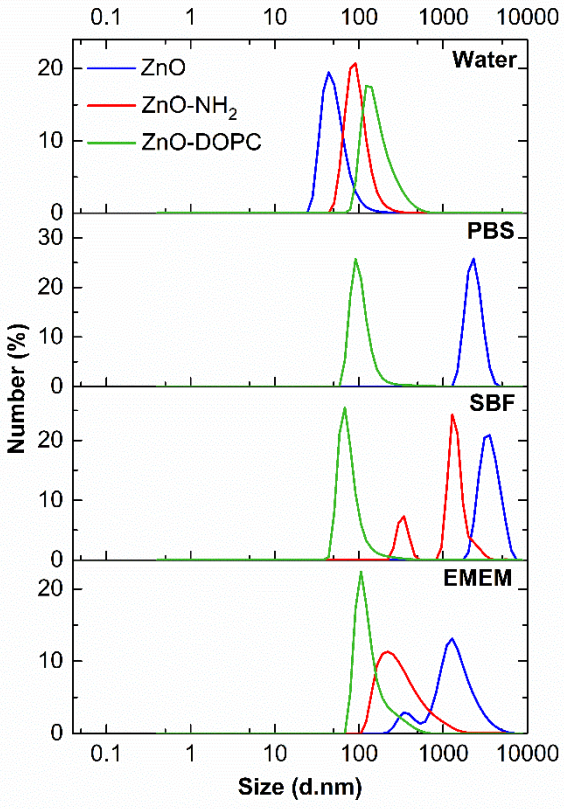

Figure 3.8: Hydrodynamic size distributions of pristine ZnO NCs (blue curves), amino-propyl functionalized ZnO-NH_2 NCs (red curves) and lipid coated ZnO-DOPC NCs (green curves) in: bd water, Phosphate-Buffered Saline (PBS), Simulated Body fluid (SBF) and complete cell culture media (EMEM + 10% FBS). ZnO-NH_2 sample was not evaluated in PBS solution.

3.3.3 Biostability tests

The colloidal and chemical stability of ZnO NCs in the biological environment as well as the influence of surface modification were assessed through long-term biostability tests.

For this assay, the three types of NCs were immersed in SBF, a simulated solution that mimics the inorganic composition of the human blood plasma, and in EMEM, cell culture medium widely used for biological research. In particular, this test was intended with the purpose of preliminarily evaluate the behavior of pristine and functionalized ZnO NCs during *in vitro* biological experiments or during their contact with plasma fluids, in a hypothetical injection for *in vivo* therapy. The temperature was kept at 37°C, to simulate physiological conditions, and the NCs were analyzed after different time points, varying between 1 hour and 25 days, in order to evaluate both the short term and the prolonged interaction between nanoparticles and media components. At the selected time points the ZnO, ZnO-NH_2 and ZnO-DOPC NCs were collected and fully characterized, assessing their colloidal, structural and chemical stability.

3.3.3.1 Long-term colloidal stability

To evaluate the persistence of the greater colloidal stability showed by the lipid coated sample, DLS measurements over time were performed. In particular, the recorded hydrodynamic dimensions were expressed as z-average size, i.e. the intensity-weighted harmonic mean hydrodynamic diameter of the ensemble collection of particles. This parameter was chosen since it is mathematically stable and very sensitive to the presence of aggregates. The z-average values of lipid-coated ZnO-DOPC NCs and of the uncoated samples ZnO and ZnO-NH_2 were monitored in real-time in both simulated and biological media. **Figure 3.9a** and **b** show the evolution of z-average of the three samples during the first hour of contact with SBF and EMEM respectively.

As clearly visible, both pristine and amino-propyl functionalized NCs showed immediate aggregation when immersed in SBF medium (**Figure 3.9a**, blue and red lines), which persisted for the entire hour of monitoring. In details, the mean hydrodynamic diameters of pristine ZnO samples ranged between 3529 nm and 4870 nm, while ZnO-NH_2 NCs exceeded 3000 nm after few minutes. The formation of huge aggregates was also visually assessed, observing the presence of white fluffy precipitates on the bottom of the measurements cuvette and this high instability hindered the prosecution of the analyses for $t > 60$ minutes, since the further measurements did not meet the quality criteria requested from DLS technique.

A similar behavior was observed in EMEM in which both ZnO and ZnO-NH_2 samples showed z-average values fluctuating around 1800 nm (**Figure 3.9b**, blue and red lines). However, the slightly less extent of aggregation allowed to extend DLS analyses and study the NCs colloidal behavior in complete cell culture media until 25 days (**Figure 3.9c**). In details, the pristine ZnO NCs (blue line) showed a

decrease in z-average values from 1800 nm down to 360 nm, accompanied by a decrease in the count rate signal which could be interpreted as aggregation and consequent precipitation of the nanocrystals. The amino-propyl functionalized ZnO-NH_2 NCs (red line) showed an almost constant z-average value (~1100 nm) with no changes in the count rate signal, indicating that the sample was formed by large but still suspended aggregated NCs.

In contrast, the lipid coated sample confirmed its better colloidal stability, remaining stable and well-dispersed also for prolonged period. In fact, ZnO-DOPC NCs showed small and constant z-average values, ranging between 194 and 314 nm, during the first hour of immersion in both SBF and EMEM solutions (green lines in **Figure 3.9a** and **b** respectively). The analyses until 25 days (**Figure 3.9c**), performed only in EMEM for consistency with their uncoated counterparts, displayed that ZnO-DOPC NCs maintained constant value of z-average (~200-300 nm) for the first 72 hours with a little increase up to 500 nm after 25 days.

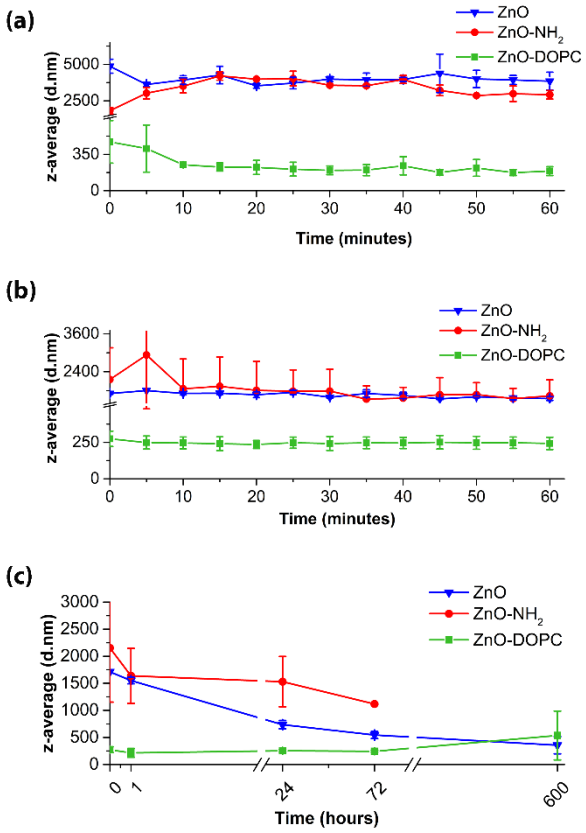

Figure 3.9: DLS analyses of ZnO (blue lines), ZnO-NH_2 (red lines) and ZnO-DOPC (green lines) NCs for 1 hours in **(a)** SBF and **(b)** EMEM and **(c)** for longer time periods (25 days) in EMEM. Since no significant changes in the aggregation of ZnO-NH_2 sample were detected in the first 72 hours, the analysis was not extended until 25 days.

3.3.3.2 Effects on structure and morphology

In order to investigate eventual changes in morphology possibly caused by the strong aggregation of nanocrystals and their interaction with media components, FESEM analyses of the three types of NCs collected at selected time points (1 hour, 72 hours and 25 days) were performed.

As already highlighted by DLS measurements, both uncoated ZnO and ZnO-NH_2 samples showed a strong tendency to aggregation, forming spherical aggregates already after the first hour of immersion in SBF and EMEM solutions whose dimensions further increased over time. As an example, the evolution of pristine ZnO NCs in EMEM is reported in **Figure 3.10**. The images after 1 and 72 hours revealed the presence of spherical aggregates of micrometric size but evidenced that the morphology of singles NCs was still recognizable (insets of **Figure 3.10a** and **b**). In contrast, after 25 days the nanocrystals appeared strongly aggregated and incorporated by a smooth matrix (**Figure 3.10c** and **Figure 3.11d**), possibly constituted by solution components precipitated around the ZnO NCs As shown in **Figure 3.11**, which collects all the analyzed samples at the time point of 25 days, a similar behavior could be described for ZnO NCs in SBF (**Figure 3.11a**) and for ZnO-NH_2 NCs in SBF (**Figure 3.11b**) and EMEM (**Figure 3.11**Figure 3.10**e**). In SBF both ZnO and ZnO-NH_2 NCs showed well-defined spherical aggregates of micrometric size formed by almost indistinguishable single nanocrystals fused together. Similar to what has been described for pristine NCs, the ZnO-NH_2 sample in EMEM formed large and compact clusters closely encapsulated by a smooth matrix.

In contrast, ZnO-DOPC NCs maintained a well-distinguishable round shaped morphology at all the time points in both EMEM and SBF solutions. In particular, as clearly visible in **Figure 3.11c**, tiny and well-dispersed lipid-coated NCs could be observed after 25 days of immersion in SBF solution. Also in EMEM the ZnO-DOPC NCs preserved their spherical morphology until 25 days, but the formation of small aggregates embedded in a soft matrix was also accounted (**Figure 3.11f**). However, the greater colloidal stability of lipid-coated samples in EMEM was confirmed at previous time points, as reported in **Figure 3.10** in which ZnO-DOPC NCs appeared completely stable and well-dispersed until 72 hours (inset of **Figure 3.10e**) in contrast with their uncoated counterpart.

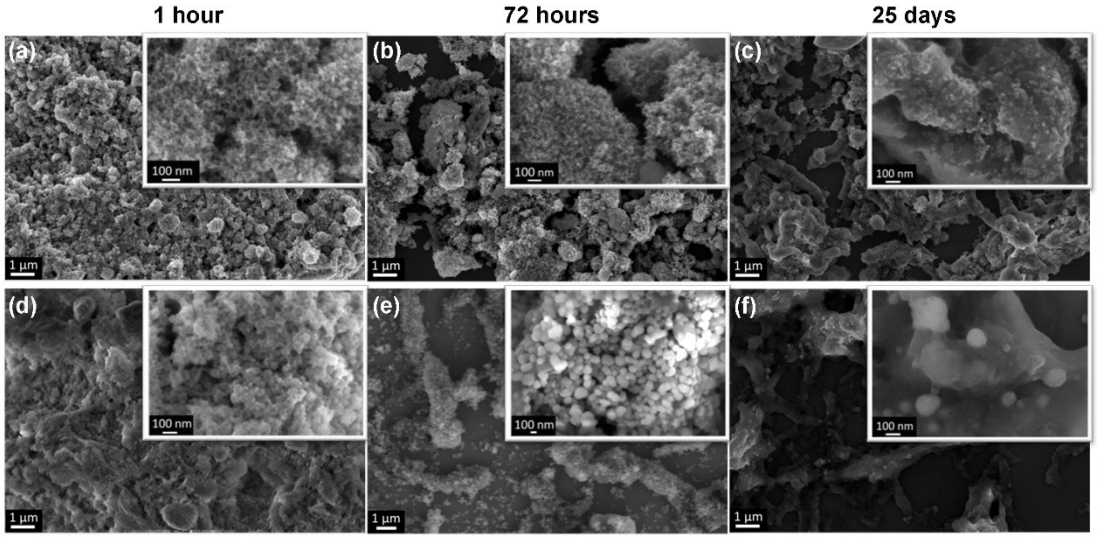

Figure 3.10: FESEM images after 1 hour, 72 hours and 25 days in EMEM; (**(a)-(c)**) pristine ZnO NCs; (**(d)-(f)**) lipid-coated ZnO-DOPC NCs. Scale bars: 1 µm for larger panels and 100 nm for insets.

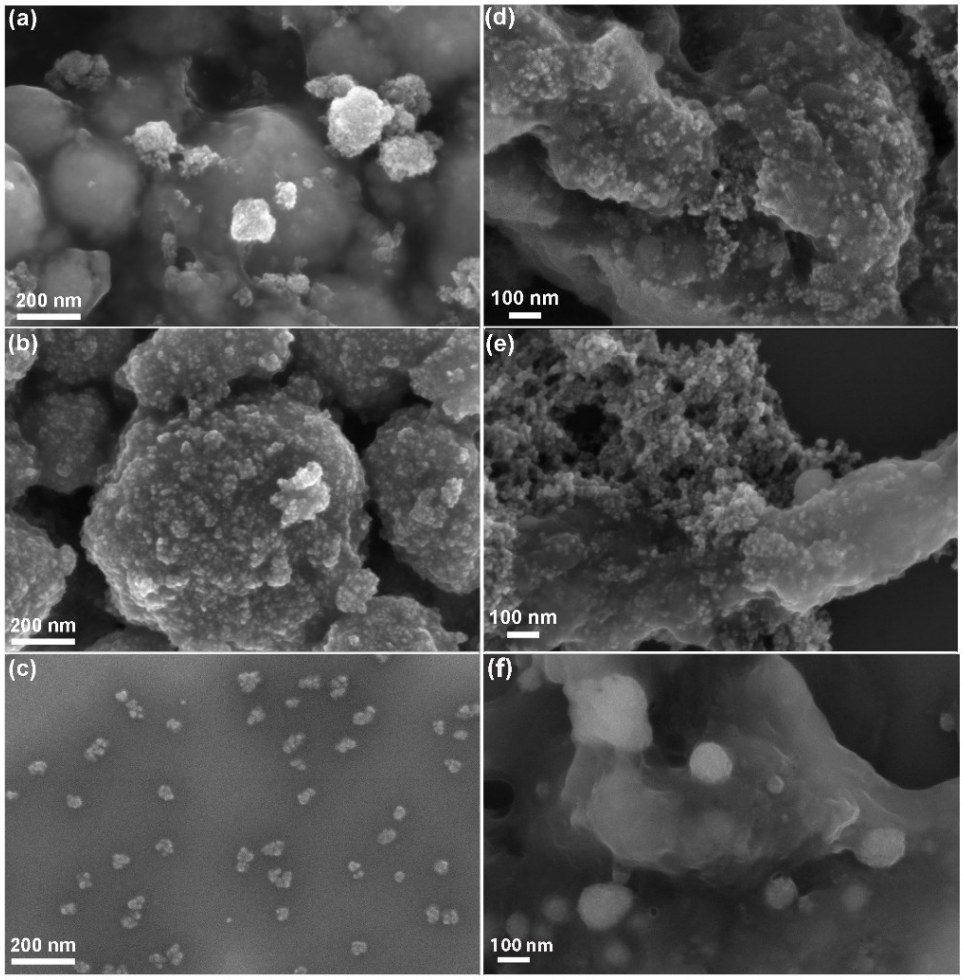

Figure 3.11: FESEM images of the three types of NCs after 25 days in SBF (left column) and EMEM (right column): **(a)** and **(d)** pristine ZnO NCs; **(b)** and **(e)** amino-propyl functionalized ZnO-NH_2 NCs; **(c)** and **(f)** lipid-coated ZnO-DOPC NCs.

Overall, the FESEM results confirmed the DLS data and highlighted the profound effects produced by the contact with biological media on ZnO and ZnO-NH_2 NCs, which were deeply aggregates and almost indistinguishable at prolonged time points. To investigate more in details the morphological and structural changes of nanocrystals, XRD analyses and Transmission Electron Microscopy were performed.

The X-Ray diffraction patterns of the three types of NCs recorded before the immersion and after each time points of biostability assay in both SBF and EMEM are collected in **Figure 3.12**. All the analyzed samples possessed the (100), (002) and (101) reflections, typical of wurtzite ZnO crystalline structure at all the time points. However, both pristine and amino-propyl functionalized samples (**Figure 3.12**, blue and red curves) showed a slight decrease of the relative intensity of the typical diffraction peaks. In addition, in some ZnO-NH_2 samples was detected the presence of a sharp peak at $2\theta \sim 32°$, ascribable to NaCl crystals. Combining these results with compositional analyses (presented in details in the next section), XRD measurements suggested the interaction with media components and a possible partial dissolution of ZnO and ZnO-NH_2 NCs.

In contrast, the diffraction peaks of ZnO-DOPC sample at the different time points of biostability assay (**Figure 3.12**, green curves) displayed no differences, confirming the preservation of the original crystalline structure thanks to the presence of the DOPC lipid shell.

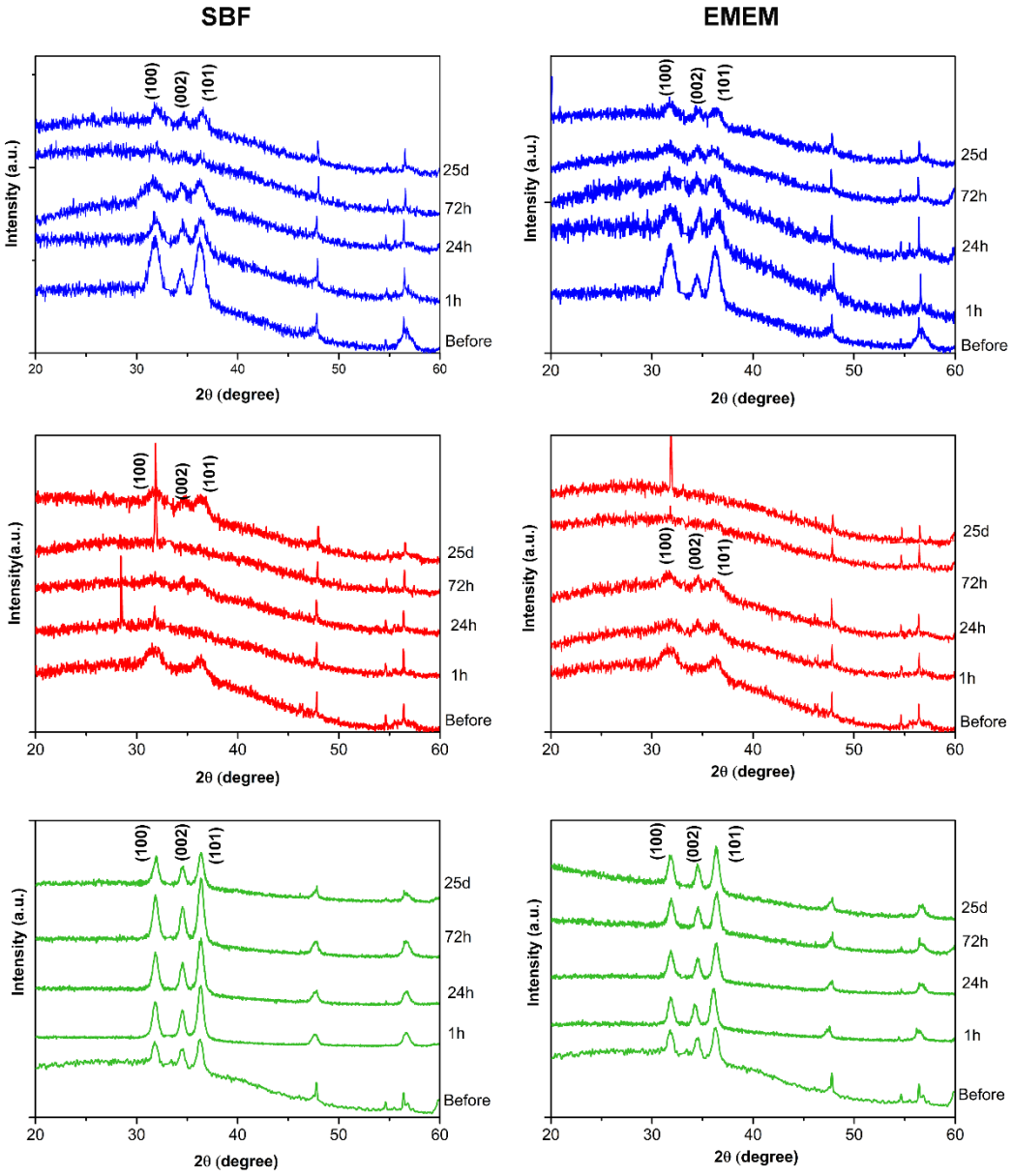

Figure 3.12: XRD spectra of ZnO NCs (blue curves), ZnO-NH_2 NCs (red curves) and ZnO-DOPC (green curves) before and after each time points (i.e. 1, 24. 72 hours and 25 days) of biostability assay in SBF (left column) and EMEM (right column).

To fully analyze the crystalline structure, High Resolution Transmission Electron Microscopy (HR-TEM) was performed, comparing the three NCs samples before and after 25 days of immersion in SBF or EMEM solution.

All HR-TEM images (**Figure 3.13**, first column) evidenced the presence of crystalline particles formed by singles crystalline mono-domains either before and after the biostability assay as further confirmed by Fast Fourier Transform (FFT) (**Figure 3.13**, first column insets referring to the areas marked with the white squares). These results showed that the crystalline structure was still preserved after

prolonged immersion in both SBF and EMEM solutions by all the three samples, suggesting that the dissolution hypothesized on the basis of XRD analyses was only partial as will be further discussed.

In addition, HR-TEM images of ZnO-DOPC sample (first column of **Figure 3.13c**) confirmed the formation of DOPC phospholipidic shell and its conservation for the whole duration of the test. In fact, the nanocrystals appeared immersed in an amorphous structure attributable to the lipidic shielding. To better appreciate this detail, Scanning Transmission Electron Microscopy (STEM) was performed (second column of **Figure 3.13c**), showing well-distinguishable single NCs completely surrounded by a smooth matrix identified as the lipid shell. In contrast, STEM images of ZnO and ZnO-NH_2 samples (second column of **Figure 3.13a** and **b**) confirmed the occurrence of important aggregation phenomena during the biostability assay, that made single NCs less clearly identifiable.

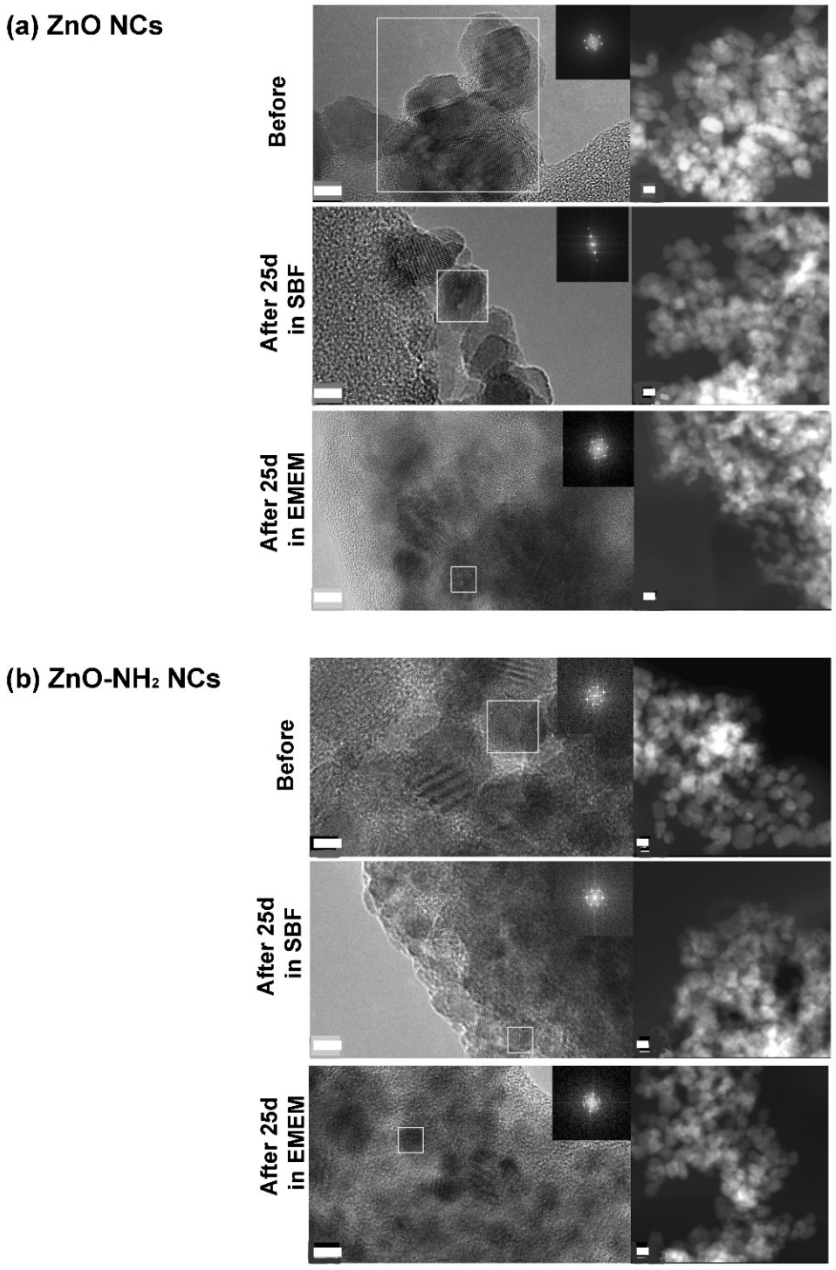

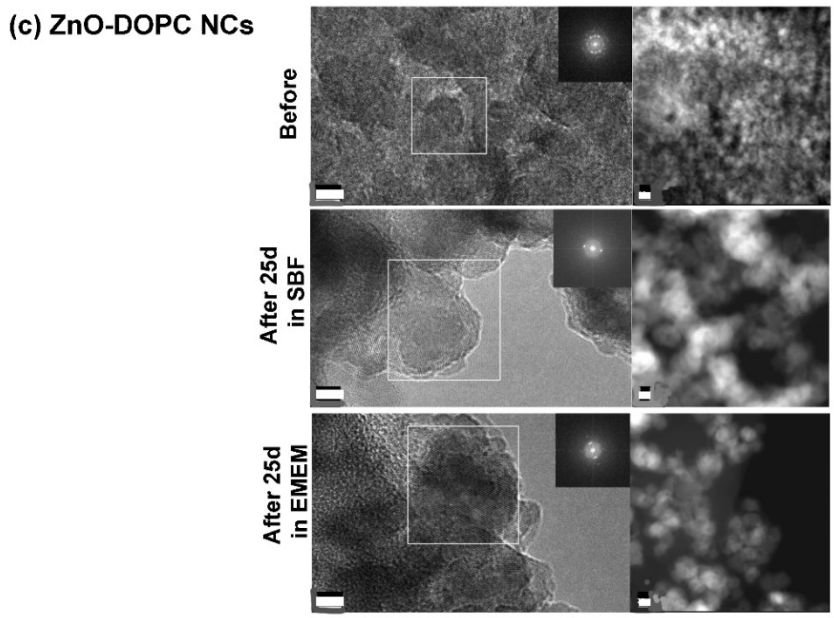

Figure 3.13: HR-TEM images (first column), FFT analyses (inset) and STEM images (second column) of **(a)** pristine ZnO NCs, **(b)** amino-propyl functionalized ZnO-NH_2 NCs and **(c)** lipid-coated ZnO-DOPC NCs before and after 25 days of immersion in SBF and EMEM. Scale bars are 5 nm.

3.3.3.3 Chemical stability: interaction with biological media components and dissolution behavior

To complete the characterization, differences in the chemical stability of the three types of nanocrystals were assessed. First of all, the interaction with the components of both simulated and biological media was investigated through Energy Dispersive Spectroscopy (EDS) and Fourier Transform-Infrared (FT-IR) Spectroscopy.

EDS analyses of ZnO, ZnO-NH_2 and ZnO-DOPC samples performed before the biostability tests (first columns of **Table 3.4** and **Table 3.5**) confirmed the expected composition of NCs, constituted by zinc and oxygen along with carbon and sodium, ascribed to synthesis residues. In addition, the ZnO-DOPC sample showed an increase in the carbon content and the appearing of phosphorous, both ascribable to the DOPC lipid shell. After the contact with both SBF and EMEM solutions (sections headed 1h, 72h and 25days in **Table 3.4** and **Table 3.5**), the presence of carbon, phosphorous, sodium, calcium and chlorine at the surface of all the three types of nanocrystals was evidenced. Confronting these results with the composition of EMEM and SBF reported in the Materials and Methods section (**Table 3.2** and **Table 3.3** respectively), the interaction between the nanocrystals and the media components resulted clear. In addition, for the samples in contact with EMEM the presence of sulphur, potassium and magnesium together with a higher content of carbon were detected. The presence of these elements, characteristic of various biomolecules and in particular of proteins and amino-acids, highly present in supplemented cell culture medium, supported the idea that the matrix observed around the nanocrystals (in particular ZnO and ZnO-NH_2 samples) was made of such biomolecules.

Table 3.4: Results of EDS analyses (reported in atom %) performed on ZnO, ZnO-NH_2 and ZnO-DOPC NCs before and after 1 hour, 72 hours and 25 days of immersion in SBF.

	Before			1h			72h			25days		
	ZnO	ZnO-NH_2	ZnO-DOPC	ZnO	ZnO-NH_2	ZnO-DOPC	ZnO	ZnO-NH_2	ZnO-DOPC	ZnO	ZnO-NH_2	ZnO-DOPC
Zn	33.88	24.24	13.05	24.14	22.83	22.37	26.95	29.91	25.41	22.73	20.51	22.31
O	51.53	41.3	33.55	43.85	46.56	50.11	47.68	45.03	51.74	41.20	32.23	48.77
C	3.73	28.6	50.01	24.47	23.54	16.46	16.84	18.34	8.72	26.52	42.33	18.31
Na	10.86	6.17	2.31	6.04	7.09	7,68	6.47	5.25	5.59	7.13	3.97	5.97
P	-	-	1.09	1.42	-	2.99	1.93	1.48	5.98	2.27	0.97	4.03
Cl	-	-	-	0.10	-	-	-	-	0.29	-	-	-
Ca	-	-	-	-	-	0.40	0.13	-	2.05	0.16	-	0.60

Table 3.5: Results of EDS analyses (reported in atom %) performed on ZnO, ZnO-NH_2 and ZnO-DOPC NCs before and after 1 hour, 72 hours and 25 days of immersion in supplemented cell culture medium (EMEM + 10% FBS).

	Before			1h			72h			25days		
	ZnO	ZnO-NH_2	ZnO-DOPC	ZnO	ZnO-NH_2	ZnO-DOPC	ZnO	ZnO-NH_2	ZnO-DOPC	ZnO	ZnO-NH_2	ZnO-DOPC
Zn	33.88	24.24	13.05	18.47	16.02	27.71	22.80	33.12	3.86	7.33	8.48	3.99
O	51.53	41.3	33.55	41.69	39.51	42.22	41.41	44.07	37.25	23.15	21.40	19.12
C	3.73	28.6	50.01	39.42	41.52	23.77	31.43	21.15	49.55	66.63	67.97	74.06
Na	10.86	6.17	2.31	-	2.68	3.25	2.42	-	0,91	1.43	1.85	1.44
P	-	-	1.09	-	-	2.21	1.46	1.23	4.14	0.59	0.42	0.74
Cl	-	-	-	-	-	-	-	-	-	-	0.04	0.05
Ca	-	-	-	0.43	-	0.83	0.49	0.44	3.93	0.50	0.37	0.35
S	-	-	-	-	-	-	-	-	0.11	0.36	0.23	0.19
K	-	-	-	-	0.27	-	-	-	-	-	0.03	0.05
Mg	-	-	-	-	-	-	-	-	0.52	-	-	-

Further confirmation about the surface modifications due to the interaction between NCs and media components was given by FT-IR spectroscopy (**Figure 3.14**). Compared to the untreated samples, the spectra of all the three types of nanocrystals collected at the different time points of biostability assay showed an increase in either number or intensity of vibrational peaks.

In particular, all the three types of NCs displayed an increasing peak at 1045 cm^{-1}, corresponding to the stretching vibration of P–O bond, along with the appearance of peaks at 1220 cm^{-1} and 1150 cm^{-1}, both ascribable to the stretching of P=O bond, for prolonged time points (i.e. 72 hours and 25 days). These peaks suggested the formation of phosphate based precipitates on the NCs surface, derived from their interaction with phosphate compounds highly present in both SBF and EMEM solution. In addition, vibrations typical of the stretching of C–O bond appeared in the region between 1700 and 1500 cm^{-1}, indicating the formation of carbonate precipitates. Actually, these peaks were more evident for the samples in contact with EMEM solution (right column of **Figure 3.14**), suggesting that these peaks were mainly related to the presence of carbon based structures derived from the biological medium.

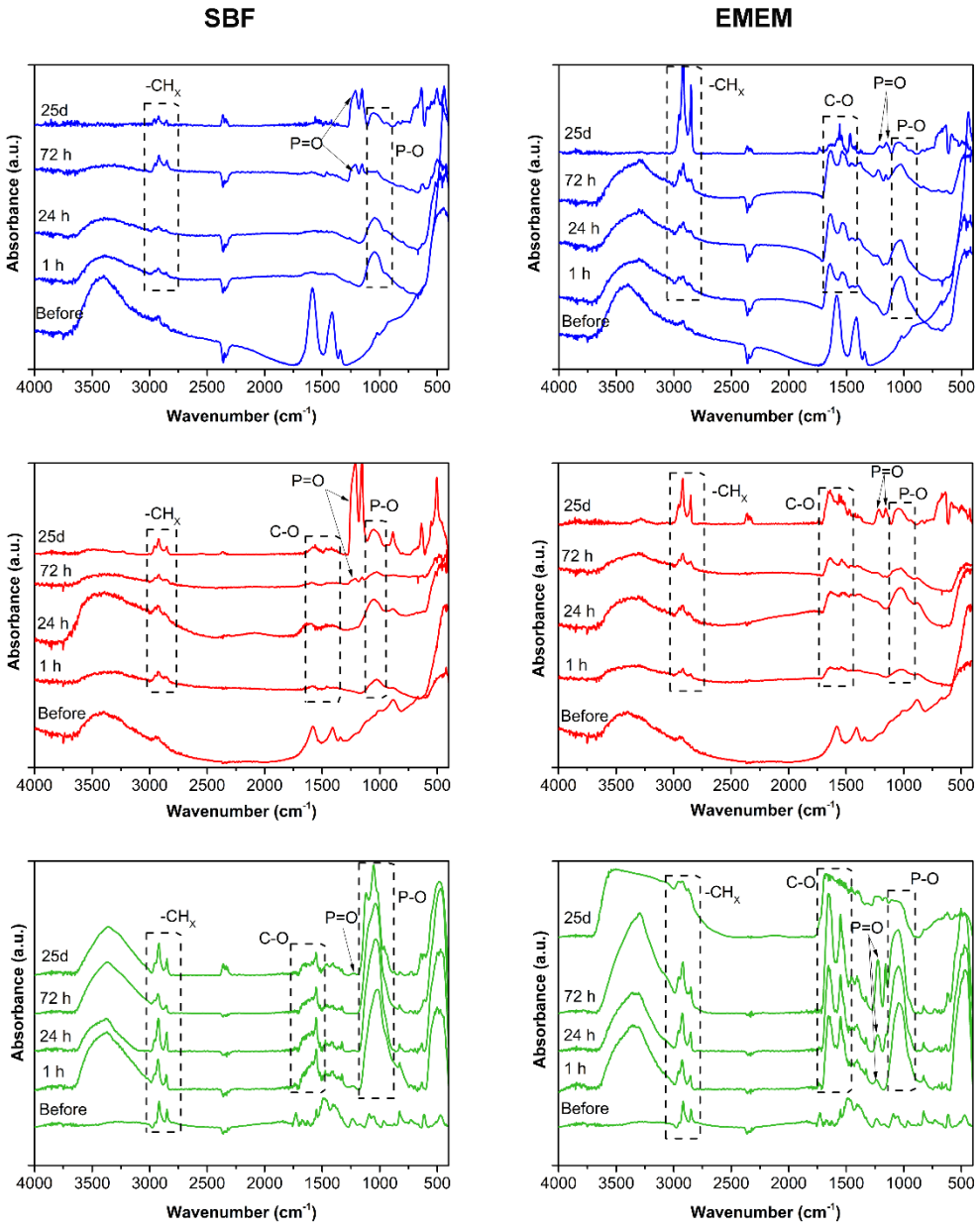

Figure 3.14: FT-IR spectra of ZnO NCs (blue curves), ZnO-NH_2 NCs (red curves) and ZnO-DOPC (green curves) before and after each time points (i.e. 1, 24. 72 hours and 25 days) of biostability assay in SBF (left column) and EMEM (right column).

Concerning the $–CH_x$ groups, their stretching vibrations displayed constant intensities at all time points in both EMEM and SBF for the ZnO-DOPC sample (**Figure 3.14**, green curves). These, together with C=O peak at 1750 cm^{-1}, confirmed the presence of the phospholipid layer at the NCs surface, which was no modified during the contact with simulated and biological media.

Stretching vibrations of $–CH_2$ and $–CH_3$ groups at 2955, 2915 and 2855 cm^{-1} were also present in the spectra of untreated ZnO and ZnO-NH_2 NCs as already described. Although, at prolonged time points, the spectra of both uncoated NCs (**Figure 3.14**, blue and red curves) displayed an increase of the intensity of these peaks, accompanied by a specular decrease of the hydroxyl stretching vibrations between 3600 and 3000 cm^{-1}. This behavior had two possible explanations,

depending on the medium composition. In case of SBF, the increase of $–CH_x$ stretching vibration was attributed to the interaction with the solution components and, in particular, with TRIS (i.e. Tris(hydromethyl)aminomethane chlorohydrate). The NCs partial hydrolysis and reaction with methyl groups of this buffer component resulted in the described changes of the $–CH_x$ and –OH peaks and could be a possible explanation of to the partial dissolution of both pristine and amino-propyl functionalized samples, as further detailed below.

The increasing trend was even more visible for ZnO and ZnO-NH_2 samples immersed in EMEM solution. In this case, the $–CH_x$ peaks growth was attributed to interaction between the NCs and all the biomolecules, proteins and amino-acids present in the serum that formed a soft matrix enveloping the crystals as already observed in FESEM and TEM images. Also the gradual reduction of –OH band could be ascribed to the interaction with new bounded molecules.

In contrast, a consistent increase of the hydroxyl broad band was observed for lipid-coated sample in both SBF and EMEM at all the time points. These variations could be the result of the physical absorption and coordination of water molecules on the surfaces of ZnO-DOPC NCs, promoted by the phospholipidic bilayer. A positive influence was attributed to this interaction, which could be responsible for the great colloidal stability displayed by ZnO-DOPC sample during the DLS measurements in water-based media.

Finally, to assess the chemical resistance of the three types of ZnO NCs dissolution measurements were performed, analyzing the elemental concentration of the supernatants collected at different time points of biostability assay. In particular, the concentration of zinc, phosphorus and calcium in both SBF and EMEM was monitored through Inductively Coupled Plasma Mass Spectrometry (ICP-MS) measurements. The monitoring of Zn level was a direct measurement of the NCs dissolution, which would release Zn^{2+} cations, while Ca and P were checked due to their reactivity toward ZnO nanomaterials.

The results are reported in **Figure 3.15** and showed similar extent of dissolution for the uncoated ZnO and ZnO-NH_2 NCs (blue and red lines respectively) in both SBF and EMEM solutions. In particular, the major release of Zn^{2+} ions occurred in the first hour of assay and then the level underwent to slight fluctuations for the subsequent time points. The maximum recorded level of zinc cations was equal to 180 ppm in SBF and 165 ppm in EMEM for ZnO NCs and to 121 ppm and 188 ppm for ZnO-NH_2 NCs in SBF and EMEM respectively. These amounts allowed to estimate the extent of dissolution that was included between the 7.5 and 11 mol% with respect to the initial amount of Zn in the NCs, confirming the occurrence of a slight dissolution of the uncoated nanocrystals already hypothesized from XRD and FT-IR data.

In addition, a rapid decrease of phosphorus level of both SBF and EMEM in contact with ZnO and ZnO-NH_2 NCs was observed. Specifically, the P concentration decreased from 30 ppm to ~1 ppm in SBF and from 40 ppm to <10 ppm in EMEM, confirming the precipitation of phosphate species already evidenced by EDS and FT-IR analyses.

Concerning Ca^{2+} ions, their concentration was constant for the whole duration of biostability test in SBF, in good accordance with the EDS analyses that showed almost negligible percentages of calcium on both ZnO and ZnO-NH_2 surfaces (**Table 3.4**). This behavior differed from what reported in literature for other nanomaterials, like silica or bioglass-based compounds that, when immersed in SBF, caused the co-precipitation of calcium and phosphate ions leading to the formation of hydroxyapatite compound on the material surface (Cauda, Schlossbauer, et al., 2010). However, numerous literature studies (Herrmann et al., 2014, Lv et al., 2012) described the strong interaction between phosphate anions and ZnO nanoparticles, suggesting that this high reactivity could be detrimental for the combination of PO_4^{3-} with calcium cations. In case of ZnO nanomaterials the sole formation of carbonate and phosphate-based precipitates occurred, as already observed. The absence of precipitated hydroxyapatite was also confirmed by XRD patterns, which presented only the peaks related to the wurtzite phase of ZnO (**Figure 3.12**). In EMEM the level of Ca^{2+} presented a slow decrease after 72 hours of contact with ZnO and ZnO-NH_2 samples, in good accordance with the EDS analyses that evidenced the presence of calcium at the surface of NCs immersed in cell culture medium (**Table 3.5**).

As expected, the lipid coated ZnO-DOPC NCs showed quite opposite behavior, with almost no release of Zn^{2+} ions in both SBF and EMEM solutions for the whole duration of biostability tests (green lines in **Figure 3.15**). These results confirmed the previous data, evidencing that the phospholipidic shell fully preserve the NCs structure preventing hydrolysis and dissolution. Also Ca^{2+} concentration was almost constant in both SBF and EMEM, together the P level in SBF. Instead, an oscillating trend accompanied by a reduction for longer time points was observed for the P level in EMEM, confirming the formation of phosphate-based precipitates already observed from FT-IR and EDS analyses.

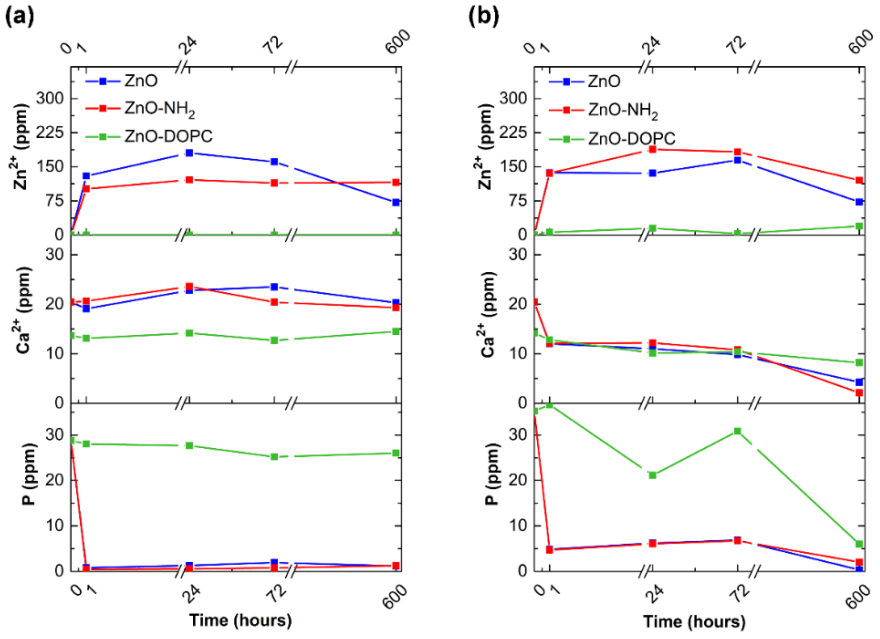

Figure 3.15: ICP-MS analyses reporting the concentration of zinc, calcium and phosphorus elements in **(a)** SBF and **(b)** EMEM at different time points of the biostability assay for the three types of NCs.

3.3.4 Colloidal and chemical stability in Phosphate-buffered saline

As already detailed in the Introduction section, the interaction of ZnO with phosphate groups is widely reported in the literature and has a prominent role in the ZnO NPs colloidal and chemical stability in biological environment. However, in complex media, like SBF or EMEM, the effect of phosphates is combined with other interactions and it is difficult to discriminate the different contributions.

In this perspective, additional biostability tests were performed using PBS solution, a buffer with a very simple composition constituted mainly by phosphates ions together with other elements that do not interact with ZnO NCs (see **Table 3.1**). In particular, the aggregation and dissolution behavior was monitored for only one week, comparing pristine ZnO and lipid-coated ZnO-DOPC NCs.

The DLS results, reported in **Figure 3.16**, confirmed again the positive effect of the lipid shell on the ZnO NCs colloidal stability. The z-average values of ZnO samples (**Figure 3.16a**, blue line) ranged between 1700 and 3700 nm, indicating a strong and rapid aggregation of the NCs in PBS solution, with the formation of micrometric aggregates. As already reported for SBF solution, the analysis was interrupted after 1 hour, since the following measurements did not meet the quality criteria requested from DLS technique. The moderate decrease of z-average over time suggested the partial precipitation of the largest aggregates. This hypothesis was strongly supported by the trend of the derived count rate (**Figure 3.16b**), that represents the scattering intensity in absence of the laser light attenuation filter. The decrease of this parameter indicates a diminution of particles in solution and, in presence of aggregates, is ascribable to sample precipitation.

In contrast, the coated ZnO-DOPC NCs, showed constant z-average values and constant derived count rate (**Figure 3.16a** and **b**, green lines). In particular, the hydrodynamic diameters were comprised between 100 and 250 nm and were similar to the value of just prepared ZnO-DOPC NCs in bd water confirming the high colloidal stability of lipid coated NCs.

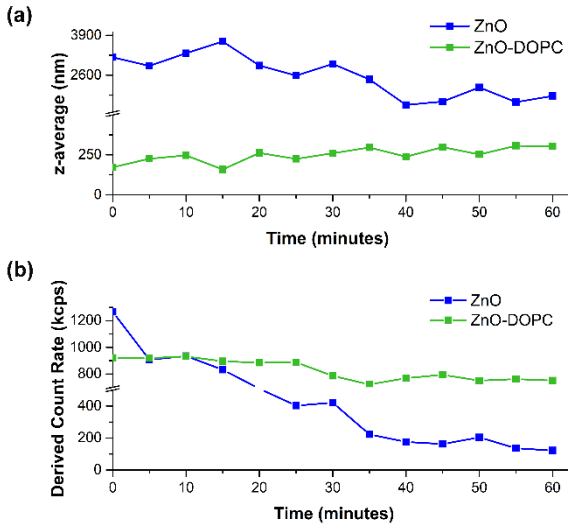

Figure 3.16: Over-time monitoring of **(a)** z-average and **(b)** derived count rate of pristine ZnO NCs (blue lines) and coated ZnO-DOPC NCs (green lines) in PBS solution.

As already explained for the biostability assay in SBF and EMEM solutions, the chemical stability of the NCs was assessed through ICP-MS analyses monitoring the concentration of Zn and P elements in the supernatants collected at different time points. Obviously, the calcium concentration was not evaluated in this case, since it is not part of PBS formulation.

The results are reported in **Figure 3.17**. The maximum level of zinc cations released from uncoated ZnO NCs was equal to 70 ppm. Compared to the previous results in both SBF and EMEM solutions (see **Figure 3.15**), the dissolution rate was slower, with a small increase in the first hour followed by a more consistent increase after 24 hours. Then, the Zn^{2+} concentration was almost constant up to one week, resembling to the behavior already observed for the other tested solutions.

The decrease of phosphorous, which is almost constant over time, confirmed the previous results indicating a great interaction between the PO_4^{3+} groups and the surface of ZnO NCs. The protective action of DOPC lipid shell was also confirmed, registering a very low concentration of Zn^{2+} in the supernatants of ZnO-DOPC sample at all time points.

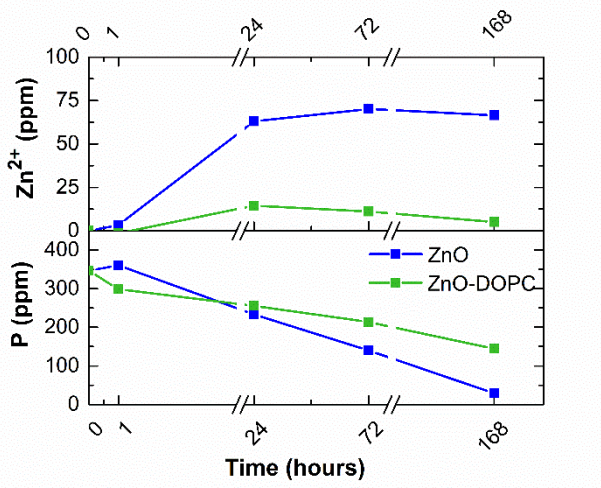

Figure 3.17: ICP-MS analyses reporting the concentration of zinc and phosphorus elements in PBS at different time points for pristine ZnO and coated ZnO-DOPC NCs.

Overall, the results of the analyses in PBS evidenced the great influence of phosphate groups on ZnO NCs colloidal and chemical stability. The DLS data displayed a high aggregation, also due to the high ionic strength of the buffer solution. ICP-MS measurements also confirmed the detrimental interaction of ZnO NCs with PO_4^{3+} groups that led to the release in solution of Zn^{2+} ions. However, the kinetics and the extent of the dissolution were relatively lower if compared to the those measured in SBF and EMEM, suggesting that the chemical instability could be also ascribed to the presence of other species in solution like carbonates or proteins. Furthermore, these results confirmed again the efficacy of phospholipidic shell in the prevention of ZnO NCs aggregation and dissolution.

3.4 Conclusions

Biostability tests performed in different biological media confirmed the high colloidal and chemical instability of ZnO material in the biological environment and the efficacy of phospholipidic shell in the prevention of ZnO NCs aggregation and dissolution.

In particular, both uncoated ZnO and ZnO-NH_2 NCs presented high aggregation extents in the tested buffer solutions and cell culture medium accompanied by a high reactivity towards media components (particularly phosphate and carbonates species and proteins) with a subsequent partial dissolution. In contrast, lipid coated ZnO-DOPC NCs, obtained through simple solvent exchange method, showed significantly improved biostability. The presence of phospholipid bilayer around the NCs surfaces efficiently prevents their aggregation in biological media and their dissolution into potentially cytotoxic Zn^{2+} ions. Actually, the colloidal and chemical stabilization provided by the lipid shielding was confirmed also at prolonged time points, highlighting the high reliability of lipids surface functionalization.

Overall, these results confirmed the opportunity to develop a hybrid nanoconstruct formed by ZnO NCs shielded by lipid bilayer as a more reliable therapeutic tool. The lipid coating, in fact, ensured the preservation of morphological, chemical and structural features of synthesized ZnO NCs even after a prolonged immersion in reactive biological media. Functionalization with lipid shell also imparted a great colloidal and chemical stabilization in both cell culture medium and simulated biological fluids suggesting a more predictable and controllable therapeutic effect both *in vitro* and *in vivo*.

Chapter 4

Development of TNHs hybrid nanoconstructs constituted by zinc oxide nanocrystals shielded by extracellular vesicles

4.1 Introduction

4.1.1 Extracellular Vesicles (EVs): definition and biological role

4.1.1.1 EVs classification

Extracellular vesicles (EVs) comprehend different types of cell-derived membranous structures composed by a lipid bilayer containing cytosolic material and nuclear components. EVs are secreted into surrounding environment by prokaryotes and different types of eukaryotic cells, including normal and diseased cells, and they are present in various biological fluids and involved in different physiological and pathological processes (Villata et al., 2020). According to a common and widespread classification method, the EVs are divided in two main subcategories, i.e. exosomes and microvesicles, based on their dimension and different biogenesis. Exosomes present dimensions ranging from 50 to 150 nm and an endocytic derivation. In particular, they are formed as intraluminal vesicles which are then released in the extracellular milieu after the fusion of multivesicular bodies with the plasma membrane. Microvesicles, instead, have size between 50 and 500 nm, sometime extended up to 1 μm or even 10 μm in case of cancer-derived microvesicles oncosomes, and derive directly from the budding and subsequent fission of plasma membrane (Van Niel et al., 2018). In addition, other classifications report also a third category of EVs, named apoptotic bodies, which comprehend larger vesicles of about 1-2 μm released by cells during the apoptotic process and containing a portion of dying cells cytoplasm (Kanada et al., 2016).

A schematic representation of the three described categories is shown in **Figure 4.1**, whereby the differences in content and surface proteins, which reflect their different derivation, are also highlighted. For instance, microvesicles present cellular receptors and transmembrane proteins specific of the cell of origin (Lawson et al., 2016), whereas exosome are rich of proteins associated with the endosomal compartment (Théry et al., 2002). Conversely, apoptotic bodies normally contain cellular organelles and fragmented genomic DNA (Saraste & Pulkki, 2000). However, the current EVs isolation methods, that will be described in the next subsection, do not permit a complete separation and purification of the different vesicles subtypes. In particular, exosomes and microvesicles present very similar size ranges and densities and, therefore, their separation is almost unachievable. Thus, many studies especially in the fields of nanomedicine and drug delivery employ both exosomes and microvesicles generically identifying them as extracellular vesicles (EVs) (Marcus & Leonard, 2013).

In addition, the identification of specific and univocal markers to discriminate the biogenesis of different EVs subtypes is really difficult and it is still missing. For this reason, recently, the International Society for Extracellular Vesicles (ISEV) has proposed new classification methods based on physico-chemical characteristics of EVs. For instance, EVs could be categorized as small (sEVs <100 or 200 nm) or medium/large (m/lEVs>200 nm) considering their dimension or as low/middle/high dense EVs considering their density (Théry et al., 2018).

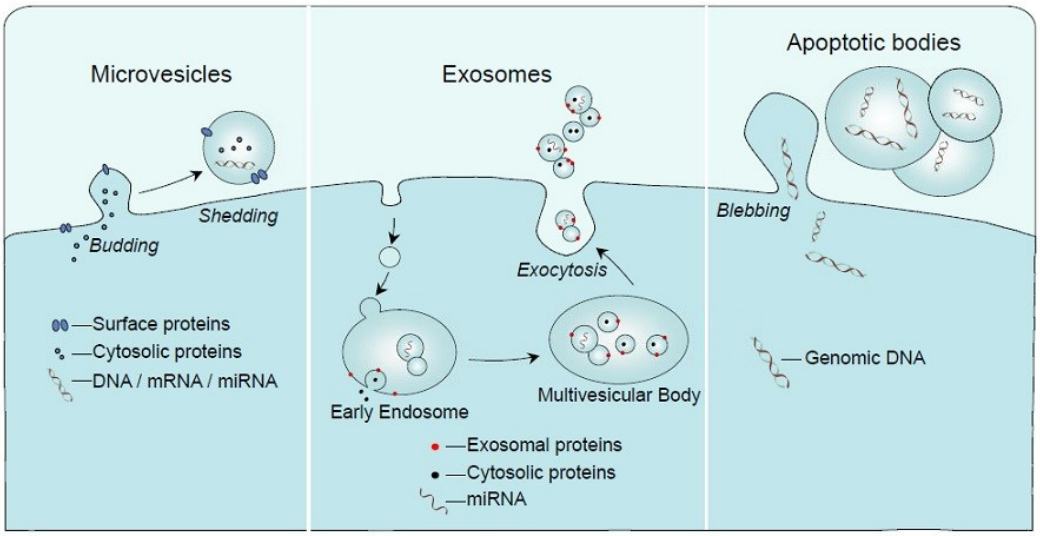

Figure 4.1: Schematic representation of EVs subcategories, i.e. microvesicles, exosomes and apoptotic bodies, and their different formation mechanisms; figure from (Lawson et al., 2016).

4.1.1.2 EVs biological function: intercellular communication

The first observation of small spheroidal membrane structures released by cells dates back to 1983 when two different research groups observed the production of these vesicles from maturing reticulocytes (Harding & Stahl, 1983; Pan & Johnstone, 1983). In the same years the terms exosomes (Johnstone et al., 1987) and microvescicles (Dalton, 1975) were coined, but the interest in these biological entities remained restrained. In fact, at first it was thought that exosomes and microvesicles were responsible for the disposal of unwanted cellular material and only after more detailed studies EVs were indicated as vehicles for cell-cell communication. In particular, an *in vitro* study conducted in middle 1990s demonstrated that exosomes secreted by B lymphocytes contained particular transmembrane proteins responsible for antigen presentation and that they were capable to induce immune response (Raposo et al., 1996). Starting from 2006, several groups reported that EVs could contain and transfer bioactive molecules present in the cytosol of originating cells (Ratajczak et al., 2006), including functional mRNA and miRNA which could be translated after the entrance in recipient cells, conferring new functionalities (Valadi et al., 2007). Detailed studies report about the different EVs contents which varies according to the physiological or pathological conditions of the cell of origin at the time of secretion (Giusti et al., 2015). Thus, EVs could affect many processes of the recipient cells like differentiation, infections, immune response, and the initiation of a wide range of diseases (Roballo et al., 2019; Rodrigues et al., 2018).

As already mentioned, EVs contain many functional molecules like different types of proteins, structural lipids, metabolites or nucleic acids derived from secreting cells. The bioactive material is located on the membranes of the vesicles or in their core, protected from extracellular environment by the lipid bilayer, and it is shuttled to neighboring or considerably distant recipient cells as schematically reported in **Figure 4.2**.

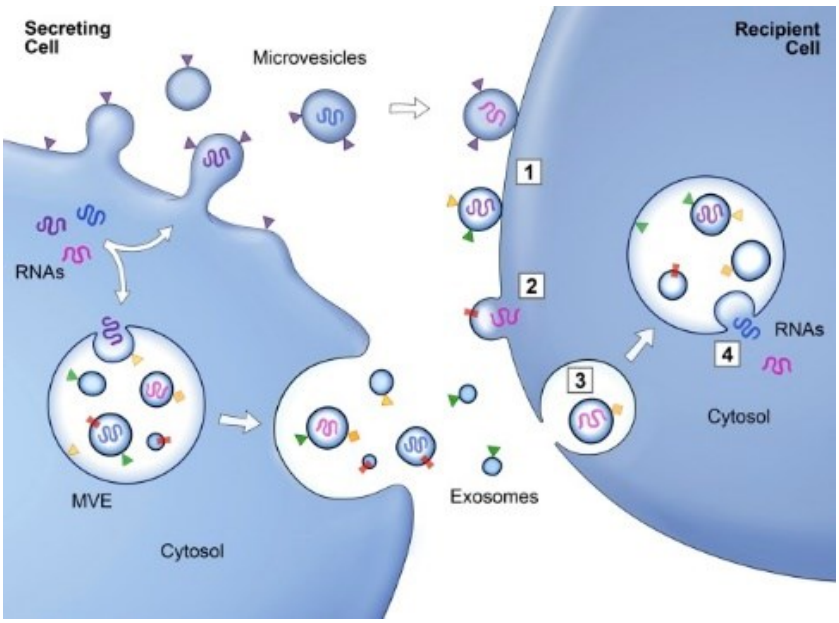

Figure 4.2: Schematic representation of EVs (i.e. exosomes and microvesicles) production by secreting cell and uptake by recipient cell. In particular, EVs can interact with target cell through **(1)** receptor-ligand interaction, **(2)** direct membrane fusion, **(3)** endocytosis and **(4)** subsequent release from endocytic compartment; figure from (Raposo & Stoorvogel, 2013).

The interaction between EVs and recipient cells and the ultimate delivery of bioactive information involves different mechanisms. EVs can recognize particular target cells thanks to specific surface ligands and then they can remain stably associated with the plasma membrane of recipient cell or be internalized either by fusion or endocytic mechanisms (Raposo & Stoorvogel, 2013). During the internalization processes, EVs directly release their membrane components and cargos into recipient cells, while the combination of EVs with cell surface receptors may be responsible for the activation of different signaling pathways. In both cases, the interaction with EVs would cause functional changes in the recipient cells (Valadi et al., 2007).

Since, the EVs-based intercellular communication could be associated with physiological but also pathological conditions like cancer, infectious and neurodegenerative diseases, EVs result interesting diagnostic biomarkers (Lane et al., 2018; Raeven et al., 2018). Moreover, the possibility to modify the EVs cargo encapsulating different therapeutic payloads allows their use as naturally derived drug delivery carriers, as will be discussed in the following sections.

4.1.2 EVs isolation methods

EVs can be isolated from *in vitro* cell culture supernatants and numerous biological fluids, including blood, saliva, urine, semen, bile, breast milk, cerebrospinal and ascitic fluid. However, several issues associated with EVs isolation, such as time-consuming processes, low yields, poor purity and reproducibility and lack of standardization, are among the major limitations for their applications.

The isolation methods currently applied rely on different properties of the secreted vesicles like size, density and antigen expression or on the change of their solubility in case of precipitation methods (Konoshenko et al., 2018).

The most widely applied method is differential ultracentrifugation which allows the separation of the vesicles according to their different size and density with respect to other fluid components. Briefly, the ultracentrifugation protocol envisages the execution of several centrifugation steps at progressively increasing speed. The first steps allow the elimination of larger or denser components like cells, cells debris, apoptotic bodies and biopolymers aggregates while the final steps at the highest centrifugal speed (i.e. 100.000g) consent the recovery and wash of EVs. This procedure produces reasonably clean samples but large proteins aggregates might co-sediment with EVs (Théry et al., 2006).

Purer preparation could be obtained through the application of density gradient. According to this method the samples are resuspended in sucrose- or iodixanol-based solutions and ultracentrifuged. The EVs move according to their equilibrium density with respect to the medium and are thus separated from other components that possess different characteristic buoyancy (Rosado et al., 2019). At present, the density gradient ultracentrifugation is considered the gold standard method to obtain highly pure EVs samples. However, it is characterized by low recovery yields, complexity and long operating times. Moreover, also density gradient ultracentrifugation does not guarantee the separation of vesicles subtypes which all present similar sedimentation rates.

Conversely, high purity and selectivity can be obtained through immunoaffinity methods, which exploit the bond between specific antibodies and EVs surface proteins to immobilize and capture the vesicles. The antibodies can be attached to different solid supports like magnetic beads, plates, columns or other carriers and they can be opportunely selected to interact with specific protein markers, therefore harvesting a single EVs subcategory (Carnino et al., 2019). The main disadvantages of immunoaffinity methods are the high costs and the limited efficiency, especially when handling blood or other body fluids which contain substances with high affinity for both antibodies and solid substrates.

Other isolation techniques rely on the size of EVs, which are separated from other medium components after the passage through porous membranes or columns of porous beads in ultrafiltration and size exclusion chromatography respectively.

Finally, EVs can be isolated using commercial kits containing mainly PEG or other superhydrophilic polymers. Appropriate buffers or polymer solutions cause change in solubility and aggregation of the vesicles, allowing their precipitation at low centrifugation speed. Obviously, this method would cause also the precipitation of protein contaminants that present similar solubility features but possess several advantages in term of costs, time and required equipment (Weng et al., 2016).

Since every separation technique possesses its advantages and limitations, the choice of the most suitable EVs isolation method is mainly associated with their application. Indeed, in case of diagnostic purposes the recovery yield is the parameter to be optimized, while for drug delivery applications it is more important

to preserve the vesicles structure and to select an appropriate cellular source, able to ensure proper specificity and targeting ability.

4.1.3 EVs in drug delivery applications

4.1.3.1 EVs as naturally biomimetic nanocarriers

Thanks to their cellular origin and biological role of intercellular messengers, EVs represent good candidates for the formulation of specific, non-immunogenic and stable delivery vehicles for different therapeutic payloads.

For instance, EVs possess natural stability in blood and other biological fluids and an intrinsic ability to cross different biological barriers, ascribable to their small size and particular structure which ensure optimal extravasation capability and tissues penetration (Sander A.A. Kooijmans, Schiffelers, et al., 2016). Moreover, their lipid bilayer allows the loading of either hydrophilic and hydrophobic compounds, stable in the EVs core or membrane respectively (Luan et al., 2017). In this perspective, EVs can be assimilated to liposomes, i.e. synthetic lipid vesicles widely applied as nanocarriers for drugs and inorganic nanoparticles. As described in the previous chapter the lipid bilayer could provide a suitable defensive barrier to preserve the colloidal and chemical stability of different materials in the biological environment. However, in addition to this protective feature, EVs possess further characteristics with respect to synthetic liposomes, like low immunogenicity, absence of toxicity and better biocompatibility (Meng et al., 2020). Actually, in a perspective of personalized drug delivery systems, it was reported that EVs collected directly from patient blood or tissues (i.e. autologous EVs) could provide a well-tolerated and safe therapeutic option (Batrakova & Kim, 2015). More in general, EVs are characterized by a prolonged blood circulation and immune-privileged status. Several studies, in fact, reported the presence of particular receptors on EVs surface which inhibit their interaction with mononuclear phagocyte system (MPS), ensuring a lower clearance and a better biodistribution (Antimisiaris et al., 2018). Finally, some *in vitro* studies indicate that EVs could possess also intrinsic tropism and could be selectively distributed to particular organs and tissues, thanks to their peculiar molecular composition precisely controlled by the cellular source (Rana et al., 2012).

Thanks to these promising features, EVs have been recently evaluated as carriers for the delivery of different therapeutic cargos like low molecular drugs, nucleic acids, genes and nanoparticles. For instance, cell-derived membrane vesicles are proven to efficiently mediate the intercellular distribution of hydrophobic compounds, providing new options for the delivery and penetration of chemotherapeutics across biological barriers (Haney et al., 2020). *In vitro* and *in vivo* studies on nanoconstructs composed by EVs and doxorubicin, a common chemotherapeutic agent for the treatment of different cancer types, confirmed the targeted delivery of the drug to breast cancer cells reducing the side effects and, thus, enhancing the therapeutic efficacy (Hadla et al., 2016). Similar results were obtained using EVs loaded with Paclitaxel, a chemotherapeutic drug used for the

treatment of multi-drug resistant cancers. The encapsulation in EVs ensured an increased release of the cargo and a higher targeting ability with respect to the free drug (Kim et al., 2016). A comparative study demonstrated the superior delivery of RNA by cell-derived EVs with respect to synthetic liposomes due to the lower clearance of EVs and their potentially favorable internalization mechanism, which protect the payload from lysosomes degradation (Kamerkar et al., 2017). Recent studies in the field of cancer nanomedicine reported also the combination of EVs with inorganic nanoparticles. For instance, iron oxide NPs were encapsulated in EVs and efficiently delivered to cancer cells for both imaging and therapeutic purposes based on the magnetic properties of NPs (Silva et al., 2013). EVs were also reportedly combined with gold NPs (Srivastava et al., 2016; Betzer et al., 2017) or metal-organic frameworks (Illes et al., 2017), in order to exploit the stabilization effect and the biomimetic features of the vesicles together with the imaging properties and the high drug loading capacity of inorganic nanocarriers.

4.1.3.2 EVs loading methods

EVs can be loaded with different therapeutic cargos and exploited as biomimetic drug delivery vehicles. However, due to their role as intercellular messengers, the cell-derived vesicles naturally enclose proteins and other bioactive molecules that may reduce the EVs intrinsic loading potential. Indeed, the efficient encapsulation of external cargos is one of the major challenges in the application of EVs as drug delivery systems, together with the maintenance of their integrity and functionalities after the loading processes (Kibria et al., 2018). Thus, the development of efficient and conservative loading strategies is of paramount importance.

As schematically represented in **Figure 4.3**, the current loading strategies comprehend several options essentially divided in (1) endogenous methods, which envisage the modification of progenitor cells with the desired cargo and the subsequent isolation of loaded EVs, and (2) exogenous methods in which the EVs are modified after their isolation. Furthermore, post-isolation exogenous methods can follow two main approaches, i.e. passive or active encapsulation. In case of passive encapsulation, EVs and therapeutic cargos are simply co-incubated to achieve the loading while active methods involve the application of different external stimuli to permeabilize EVs membrane and favor the cargos entrance (Sutaria et al., 2017).

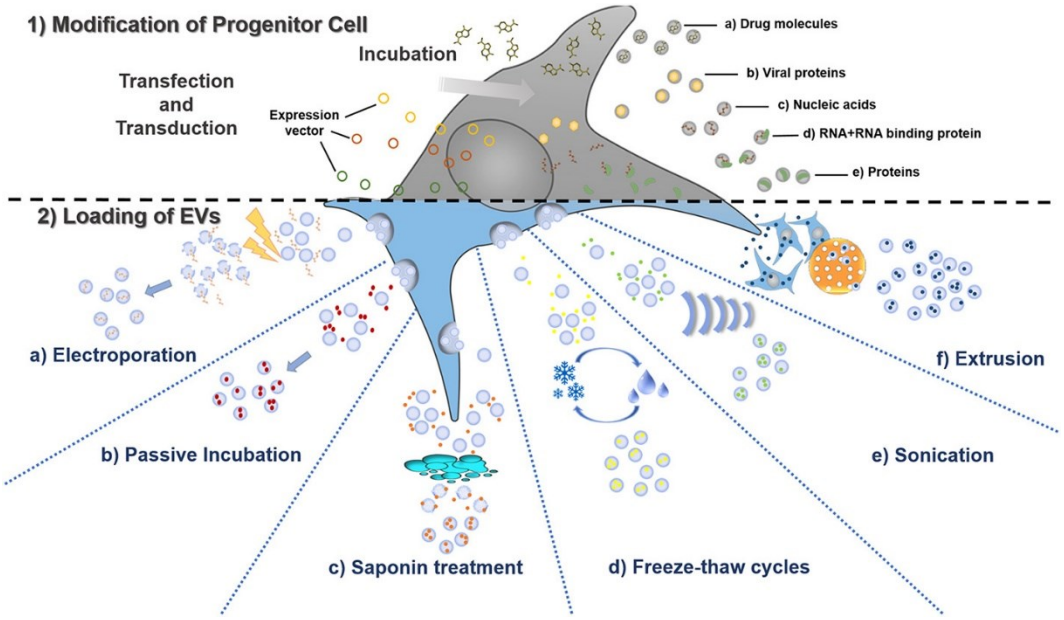

Figure 4.3: Schematic representation of EVs loading strategies, categorized as (1) modification of progenitor cells (i.e. endogenous methods) and (2) post-isolation loading methods (i.e. exogenous methods); figure from (Rufino-Ramos et al., 2017).

A brief description of the principal loading strategies reported in literature are presented in the following subsections with particular attention to post-isolation methods, more interesting for the purposes of this PhD thesis.

Modification of progenitor cells

Endogenous loading methods involve the modification of progenitor cells which will then secrete EVs loaded with the desired therapeutic payload. This mechanism envisages the engineering of parent cells through incubation or transfection with therapeutic agents, which are internalized by cells and inserted into the different types of vesicles during their biogenesis. The modified cells would then produce pre-loaded EVs (Elsharkasy et al., 2020).

As represented in **Figure 4.3**, this method is primarily reported for the encapsulation of nucleic acids, proteins or drug molecules. For instance, EVs containing therapeutically active miRNA (Kosaka et al., 2010) and siRNA (Shtam et al., 2013) were efficiently produced following the transfection of parent cells. In addition, the production of EVs pre-loaded with chemotherapeutic agents like the already mentioned paclitaxel was also achieved (Pascucci et al., 2014). The internalization of drug molecules in secreting cells could be obtained by incubating the compounds directly dispersed in cell culture medium or transported by nanocarriers. The use of nanocarriers would allow the delivery of drug in appropriate cellular compartments, reducing unwanted lysosomal degradation and enhancing EVs loading (Lee et al., 2015). Finally, endogenous loading methods were recently reported also for solid nanoparticles. For instance, EVs pre-loaded with hollow gold (Sancho-Albero et al., 2019), iron oxide (Mulens-Arias et al., 2018) or porous silica NPs (Yong et al., 2019) were isolated from opportunely treated cells, allowing imaging and therapeutic applications.

The major drawback of endogenous loading methods relies on the low efficiency, since only a small fraction of therapeutic agents present in the parent cells would be transferred to the secreted EVs (Armstrong et al., 2017).

Post-isolation loading methods

As already mentioned exogenous or post-isolation loading methods can be divided in two subcategories, i.e. passive and active loading methods.

Passive method basically consists in the co-incubation of EVs and cargos without the addition of any external reagent. The two components would interact on the basis of their physicochemical properties, exploiting, for instance, the presence of concentration gradients or the hydrophobicity of payloads to efficiently cross the EVs lipid membrane (Luan et al., 2017). Passive co-incubation is normally performed at room temperature or at 37°C with different duration times ranging from few minutes to several hours. Thanks to its intrinsic simplicity, this method is widely applied in the literature for the encapsulation of different entities, like drugs, macromolecules and inorganic nanoparticles. For instance, the hydrophobic chemotherapeutic agents doxorubicin and paclitaxel were loaded into isolated EVs thanks to their lipophilic nature, obtaining a targeted and sustained release in cancer cells (Smyth et al., 2015; Kim et al., 2016). Similarly, rapid passive incubation allowed the encapsulation of hydrophobic curcumin inside EVs, increasing its biostability, solubility and cellular delivery (Zhuang et al., 2011). The co-incubation strategy was applied also for the loading of EVs with inorganic nanoparticles like the already mentioned drug-conjugated gold NPs (Srivastava et al., 2016) or metal-organic frameworks (Illes et al., 2017). In these cases, the encapsulation within the EVs was achieved through a fusion method similar to the one cited for pre-formed liposomes, comprising a first step of close interaction between vesicles and nanoparticle and the subsequent engulfment of NPs through the rearrangement of lipid bilayer. In addition, glucose-coated gold NPs were reportedly loaded into EVs through an energy-dependent mechanism mediated by a glucose transporter located on vesicles membrane helping the particle encapsulation (Betzer et al., 2017).

The main advantages of the passive co-incubation method are its simplicity and the preservation of EVs membrane integrity, while it is adversely characterized by low loading efficiencies. Conversely, active loading methods try to overcome this limitation applying an external stimulus to facilitate the cargo entrance. As schematically depicted in **Figure 4.3**, several options are currently analyzed, including electroporation, saponin treatment, application of freeze-thaw cycles, sonication and extrusion. These methods are primarily applied in presence of large or hydrophilic cargos, which cannot easily diffuse through EVs lipid bilayer as envisaged by passive incubation method (Vader et al., 2016).

Briefly, electroporation consists in the creation of temporary pores in the EVs membranes, following their resuspension in a conductive solution and the application of an electric field which causes the destabilization of phospholipid bilayer. This technique was primarily reported for the encapsulation of exogenous

RNA (Wahlgren et al., 2012; Alvarez-Erviti et al., 2011), but it was also applied for the encapsulation of doxorubicin (Y. Tian et al., 2014) or small hydrophilic molecules used for photodynamic therapy (Fuhrmann et al., 2015). Moreover, superparamagnetic iron oxide NPs of about 5 nm were efficiently loaded in EVs through electroporation methods, opening the promising possibility to monitor loaded-EVs with magnetic resonance imaging (Hood et al., 2014). The main disadvantage of electroporation method is the complexity of operating parameters that need to be carefully optimized also as a function of EVs type (Pomatto et al., 2019). Furthermore, both EVs and cargos aggregation are frequently reported (Sander A.A. Kooijmans et al., 2013).

The membrane destabilization can be also achieved by the application of a mechanical stimulus, like mechanical shear forces exerted on EVs-cargos solution by means of sonicator probes or extruders equipped with porous membranes. Actually, the extrusion method could be applied directly to the isolated EVs (Haney et al., 2015; Fuhrmann et al., 2015) or starting from the whole cells, as depicted in **Figure 4.3**. According to the second strategy, several extrusion steps through progressively smaller pores were carried out on the cells previously incubated with cargos producing loaded vesicles composed by fragment of cellular membranes mimicking the EVs (Jang et al., 2013). Concerning the sonication method, the reduction of membrane microviscosity caused by the application of ultrasounds ensured high loading efficiencies of nucleic acids (Lamichhane et al., 2016), paclitaxel (Kim et al., 2016) and catalase enzyme (Haney et al., 2015). However, since both sonication and extrusion methods are based on the disruption and reconstitution of the lipid membranes, major EVs aggregation is reportedly associated to these type of procedures. In addition, the preservation of membrane biomimicry and the drug retention have to be carefully assessed after these treatments (Luan et al., 2017).

Another active loading strategy envisages the chemical permeabilization of EVs membrane through saponin treatment. Indeed, saponin surfactant is able to dissolve cholesterol molecules forming pores which would allow the cargo penetration. A comparative study evidenced the high loading efficacy of saponin-assisted encapsulation with respect to passive incubation or other active methods (Fuhrmann et al., 2015). Anyway, due to saponin potential toxicity, the amount of detergent must be precisely controlled and the loaded-EVs carefully purified before their application (Sutaria et al., 2017).

Finally, the application of sequences of freeze-thaw cycles is also evaluated. EVs-containing solutions are often frozen for preservation and storage, but repeated freezing and thawing could lead to membrane damage caused by ice crystals formation. In addition, the lipid bilayer would be stressed by the expansion of the liquid contained in the lumen during freezing and this would cause membranes strain and, eventually, rupture, facilitating the encapsulation of external cargos (Seneviratne et al., 2020). Literature studies reported the effective encapsulation of chemotherapeutic agents (Goh et al., 2017) and catalase enzyme (Haney et al., 2015) as well as the fusion between EVs and synthetic liposomes (Sato et al., 2016) through the application of repeated freeze-thaw cycles. As for other active methods,

the main drawbacks of freeze-thaw strategy are the aggregation and potential loss of membrane integrity, which could be mitigated by reducing the number of cycles.

The high stability, the extended blood circulation and low immunogenicity together with the possibility of their efficient loading with different therapeutic cargos, made EVs one of the most promising drug delivery systems. In this context, relies the development of the hybrid nanoconstruct, called TNH (i.e. TrojaNanoHorse), described in this chapter. Briefly, TNHs nanoconstructs were obtained combining therapeutically active ZnO NCs and EVs derived from KB cancerous cells through an optimized passive co-incubation method. The experimental results reported in Chapter 3 already demonstrated that the shielding with synthetic supported lipid bilayer could efficiently prevent ZnO NCs aggregation and degradation in biological environment. However, with respect to synthetic lipids, the use of cell-derived vesicles would guarantee not only the biostability but also the improvement of the biocompatibility of TNH hybrid nanoconstruct. Thus, the effect of the EVs lipid-shielding on the colloidal stability, cellular toxicity and internalization was evaluated, comparing the behaviour of the obtained TNHs with uncoated ZnO NCs.

4.2 Materials and method

4.2.1 ZnO NCs synthesis and characterization

4.2.1.1 Synthesis of amino-propyl functionalized ZnO NCs

The ZnO NCs were synthesized through microwave-assisted method and functionalized with amino-propyl groups as described in Chapter 2 (Garino et al., 2019). The nanocrystals were labeled by conjugation with Atto647-NHS Ester (AttoTec) or Atto550-NHS Ester (Attotec) as already described.

4.2.1.2 ZnO NCs Characterization

Electron Microscopy

The morphology of the amino-propyl functionalized ZnO NCs was evaluated by conventional and High-Resolution Transmission Electron Microscopy (TEM and HR-TEM). The sample was prepared by diluting ZnO NCs in ethanol (99%, Sigma-Aldrich) and depositing one drop of the obtained solution on a holey carbon-coated copper grid. The deposited sample was then dried overnight and analyzed using a FEI Tecnai F20 ST transmission electron microscope operating at 200 kV.

Selected Area Electron Diffraction (SAED) pattern was also acquired in order to confirm ZnO NCs crystalline structure.

X-ray diffraction

The crystalline structure of the amino-propyl functionalized ZnO NCs was also analyzed by X-ray diffraction (XRD) The samples were deposited drop by drop on a silicon wafer, obtaining an appropriately thick layer of dried ZnO NCs, and then analyzed with a Panalytical X'Pert diffractometer with the same settings described in Chapter 2.

Dynamic Light Scattering (DLS) and Nanoparticle Tracking Analysis (NTA)

The hydrodynamic size distributions of ZnO NCs dispersed in different media, i.e. ethanol, bd water, PBS and physiologic solution, were determined by Dynamic Light Scattering (DLS) technique using a Zatasizer Nano ZS90 (Malvern Instruments). The samples were analyzed at concentration 100 μg/ml and sonicated 10 minutes before the acquisition. Zeta-Potential measurements in bd water, PBS and physiologic solution were acquired with the same instrument.

Size distribution of ZnO NCs in bd water was also measured by Nanoparticle Tracking Analysis (NTA) technique, using Nanosight NS300 (Malvern Panalytical), equipped with a λ=505 nm laser beam and a NanoSight syringe pump. The samples were appropriately diluted to meet the ideal particles per frame value (20-100 particles/frame) and measured by capturing three videos of 60 seconds with an infusion rate of 30 and a camera level value between 11 and 15. The collected

videos were then analyzed by the NTA 3.3 software (Malvern Panalytical), setting the detection threshold at 5.

4.2.2 EVs extraction and characterization

4.2.2.1 EVs production and extraction

The EVs used in this study were extracted from conditioned media of KB cells (ATCC® CCL17). KB cells were cultured in Eagle's minimal essential medium (EMEM, Sigma), supplemented with 10% heat inactivated fetal bovine serum (FBS, Sigma), penicillin (100 units/ml) and streptomycin (100 µg/ml). After 48 hours, the media was removed and the cells were washed with PBS and resuspended in fresh media supplemented with EVs-depleted FBS.

Depleted FBS was produced by overnight centrifugation at 100,000g, 4°C; the supernatants were collected and used to complement cell culture media up to the final concentration of 10%.

The cells were cultured in EVs-free medium for 48 hours and then the conditioned supernatants were collected for EVs isolation, performed according to a sterile ultracentrifugation protocol, optimized from Thery et al. (Théry et al., 2006). Before each isolation, the cell viability was assessed and only samples with viability >95% were processed in order to reduce the possibility of apoptotic bodies recovery.

In details, the collected cell culture medium was centrifuged at 130g at 4°C for 10 minutes to remove dead cells. The supernatant was then centrifuged at 2,000g at 4°C for 20 minutes to remove cell debris and subsequently recollected, aliquoted in ultracentrifuge tubes (32 ml Optiseal tubes, Beckman Coulter) and ultracentrifuged at 10,000g at 4°C for 30 minutes using a OptiMax Ultracentrifuge (Beckman Coulter) equipped with a MLA-50 rotor. The supernatant was recollected and ultracentrifuged at 100,000g at 4°C for 70 minutes to pellet EVs. Finally, a washing step was performed resuspending the EVs-containing pellet in cold, 0.1 µm-filtered PBS and ultracentrifuging again at 100,000g at 4°C for 60 minutes. The final pellet was then resuspended in 600 µl of PBS or physiologic solution, divided in aliquot of 50 µl and stored at -80°C for further use.

To perform analysis involving fluorescence, the EVs were labeled with DiOC18(3) 3,3'-dioctadecyloxacarbocyanine perchlorate (DiO, Invitrogen) and DiDC18(5) 1,1'-dioctadecyl-3,3,3',3'-tetramethylindodicarbocyanine perchlorate (DiD, Invitrogen) with a λ_{Ex} of 488 nm and 648 nm, respectively.

Briefly, stored EVs were thawed out at 37°C in a water bath and then labelled by adding 0.5 µl of dye (10 µM in DMSO) for each EVs aliquot, containing averagely $7 \cdot 10^9$ particles. The solution was kept at 37°C, in dark and under agitation (180 rpm) for 30 minutes and then washed once with PBS by ultracentrifuging at 100,000g at 4°C for 60 minutes. The obtained pellet was finally resuspended in cold 0.1 µm-filtered PBS or physiologic solution.

4.2.2.2 EVs characterization

Electron Microscopy

The morphology of the EVs extracted from KB cells was evaluated by Field Emission Scanning Electron Microscopy (FESEM) and Trasmission Electron Microscopy (TEM).

For FESEM analyses, performed with a Merlin field emission scanning electron microscope (Carl Zeiss), the samples were diluted in 0.1 µm-filtered PBS and deposited on silicon wafer.

For TEM, the vesicles were diluted in a solution 1:1 v/v of bd water and physiologic solution. One drop of the obtained dispersion was deposited on a holey carbon-coated copper grid, dried overnight at room temperature and then analyzed using a FEI Tecnai F20 ST transmission electron microscope operating at 80 kV. Energy Dispersive X-ray Spectroscopy was also performed on the same sample.

Nanoparticle Tracking Analysis (NTA) and Zeta-Potential measurements

Concentration and size distribution of EVs dispersed in PBS and physiologic solution were analyzed by Nanoparticle Tracking Analysis (NTA) technique. The samples were diluted 1:100 and analyzed with the same instrument used for nanocrystals characterization (i.e. Nanosight NS300, Malvern Panalytical). The camera level was set at 15 or 16 and the detection threshold at 5.

Zeta-Potential measurements were performed with Zetasizer Nano ZS90 (Malvern Instruments), by diluting the EVs aliquot (50 µl) in 950 µl of PBS or physiologic solution.

4.2.3 TNHs construction and characterization

4.2.3.1 TNHs optimization

The optimization of the coupling process between amino-propyl functionalized ZnO NCs and EVs was carried out by varying several parameters, i.e. the mixing method, the duration and the temperature of the reaction, the dispersing medium and the ratio between the components.

In general, 50 µl of fluorescently labelled EVs dispersed in PBS or physiologic solution were added to 50 µl of bd water containing different amount of labeled ZnO NCs, as further detailed in the discussion section. At the end of the coupling procedure, the samples were centrifuged at 5,000g for 5 minutes to recover the EVs coupled with ZnO NCs, contained in the pellet. The pellet (TNH Run 1) was resuspended in 100 µl of 1:1 v/v of bd water and PBS or physiologic solution. The supernatant, containing uncoupled EVs, was mixed with a new aliquot of ZnO NCs repeating the incubation and centrifugation steps; the obtained second pellet constitute the TNH Run 2.

4.2.3.2 TNHs characterization

Fluorescence Microscopy

The coupling efficacy was evaluated through fluorescence microscopy using a wide-field fluorescence-inverted microscope (Eclipse Ti-E, Nikon) equipped with a super bright wide-spectrum source (Shutter Lambda XL), a high resolution camera (Zyla 4.2 Plus, 4098x3264 pixels, Andor Technology) and a 60× immersion oil objective (Apo 1.40, NIkon). The images were analyzed with colocalization tool of NIS-Element software (NIS-Element AR 4.5, Nikon). In brief, the spots in red and green channels (corresponding to ZnO NCs and EVs respectively) were counted and then a merge of the two images were performed, counting only the spots in which the two fluorescence were superimposed. The percentage of colocalization with respect to the ZnO NCs (%co-ZnO) was then calculated doing the ratio between the number of colocalized spots and the total number of red spots.

Electron Microscopy

The morphology of TNHs obtained with the optimized protocol was studied with TEM analyses, operating at the same condition described for EVs.

Energy Dispersive X-ray Spectroscopy was also performed on the same sample, to confirm the presence of Zn.

Nanoparticle Tracking Analysis (NTA) and Zeta-Potential measurements

Size distribution of TNHs obtained with the optimized protocol were measured by NTA technique with Nanosight NS300 (Malvern Panalytical) and compared to pristine EVs and ZnO NCs, prepared following the same protocol. The samples, diluted in 1:1 v/v of bd water and physiologic solution to reach ZnO NC concentration of 15 μg/ml or the corresponding EV concentration, were analyzed setting the camera level at 15 and the detection threshold at 5.

Zeta-Potential measurements of TNH obtained with the optimized protocol were performed with Zetasizer Nano ZS90 (Malvern Instruments), diluting the sample in 1:1 v/v of bd water and physiologic solution to reach the volume of 1 ml.

4.2.3.3 TNHs for biological tests

The optimized protocol derived from the initial parameter screening was amended for the biological assays to respect the experimental conditions needed for tests on KB cancer cells.

Cells were treated with 1 ml of solution containing ZnO NCs at concentrations 5, 15, 25 and 50 μg/ml. In the first run, EVs were coupled with half of ZnO NCs and, after the centrifugation, the pellet was directly resuspended in 635 μl of cell culture medium. The supernatant, made by 365 μl of mixed bd water and physiologic solution containing empty EVs, was coupled with the second half of ZnO NCs. At the end of the second run, no centrifugation was performed and TNH Run 1 and Run 2 were reunited, reaching the final volume of 1 ml.

Details on solution composition and on ZnO NCs and EVs quantity for each treatment are reported in Table 4.1.

EVs and amino-propyl functionalized ZnO NCs which have followed all the steps of TNH formation protocol without the addition of nanocrystals and vesicles respectively were also prepared as control samples.

Table 4.1: Amounts of ZnO NCs and EVs and volumes of solutions used for the preparation of TNHs at different concentrations for the biological tests on KB cells.

Treatment	**Run 1 (90' @ 37°C, 180 rpm)**		**Centrifugation (5'000 g, 5min)**	**Run 2 (90' @ 37°C, 180 rpm)**
5 µg/ml	2.5 µg ZnO NCs in 25 µl H_2O + 31.5 µl EVs in physiologic solution (conc: $1.9 \cdot 10^{11}$ part/ml)	+283.5 µl physiologic solution	-Pellet + 635 µl EMEM -Supernatant: at Run 2	Supernatant + 2.5 µg ZnO NCs in 25 µl H_2O
15 µg/ml	7.5 µg ZnO NCs in 25 µl H_2O + 94 µl EVs in physiologic solution (conc: $1.9 \cdot 10^{11}$ part/ml)	+221 µl physiologic solution	-Pellet + 635 µl EMEM -Supernatant: at Run 2	Supernatant + 7.5 µg ZnO NCs in 25 µl H_2O
25 µg/ml	12.5 µg ZnO NCs in 25 µl H_2O + 157.5 µl EVs in physiologic solution (conc: $1.9 \cdot 10^{11}$ part/ml)	+157.5 µl physiologic solution	-Pellet + 635 µl EMEM -Supernatant: at Run 2	Supernatant + 12.5 µg ZnO NCs in 25 µl H_2O
50 µg/ml	25 µg ZnO NCs in 25 µl H_2O + 315 µl EVs in physiologic solution (conc: $1.9 \cdot 10^{11}$ part/ml)	-	-Pellet + 635 µl EMEM -Supernatant: at Run 2	Supernatant + 25 µg ZnO NCs in 25 µl H_2O

4.2.4 Biological Tests

4.2.4.1 Cytotoxicity assay

For cell viability tests, 1.5×10^3 cells/well were seeded in 96-well culture plate (Corning® 96 Well TC-Treated Microplates) and grown for 24 hours at 37°C under 5% CO_2 atmosphere. Then the cell culture medium was replaced with the treatments solution containing ZnO NCs, TNHs or EVs at concentration 5, 15, 25 or 50 µg/ml.

After 24 hours of incubation, WST-1 cell proliferation assay was performed. Briefly, 10 µl of WST-1 reagent (Roche) were added to each well and, after 2 hours in dark at 37°C and 5% CO_2, the formazan absorbance was measured at 450 nm with the Multiskan GO microplate spectrophotometer (Thermo Fisher Scientific) using 620 nm as reference wavelength.

4.2.4.2 Cell internalization assay

The internalization of ZnO NCs, TNHs at EVs in KB cells was investigated by flow cytometry, using a Guava Easycyte 6-2L (Merck Millipore).

For these experiments ZnO NCs labelled with Atto647-NHS Ester and EVs labelled with DiO were used.

3×10^4 cells/well were seeded in a 24-well culture plate (Corning® TC-Treated) and grown for 24 hours at 37°C under 5% CO_2 atmosphere. The cell culture medium was then replaced with treatments solution containing ZnO NCs, TNHs (concentration 5, 15 and 25 µg/ml) or EVs (concentration corresponding to 15 µg/ml of TNHs).

After 24 hours of incubation the cells were washed twice with PBS, trypsinized, pelleted (130g for 5 minutes) and resuspended in 500 µl of PBS for the analysis. For each sample were recorded 10^4 events positioned in a gate designed to exclude cells debris. The red laser (λ_{Ex}=642 nm) was used for the excitation of the labelled NCs and the blue laser (λ_{Ex}=488 nm) for EVs. The detected fluorescence was analyzed with Guava Incyte software (Merck Millipore); the results were expressed in percentages of positive events calculated with respect to a threshold set upon untreated cells (control) histogram.

Both cytotoxicity and cell internalization assays were performed at least in triplicate and values were expressed as mean ± SEM (standard error of mean). For statistical analyses, he experimental data were analyzed using Sigmaplot 14 (demo version, Systat Software Inc.) performing one-way or two-ways ANOVA. ***p value < 0.001 and *p value < 0.05 were considered significant.

4.2.4.3 Live cell fluorescence microscopy

To further characterize the interaction of ZnO NCs, TNHs and EVs with KB cancer cells, live cell fluorescence microscopy was performed using a wide-field fluorescence-inverted microscope (Eclipse Ti-E, Nikon) combined with an incubator gas chamber (Okolab) equipped with a CO_2 sensor, a temperature unit and an active humidity controller.

For these experiments ZnO NCs were labelled with Atto647-NHS Ester and EVs were labelled with DiO, when used for the TNHs construction, or DiD, when used alone.

3×10^4 cells/well were seeded in a 4 well chamber slide (Nunc Lab-Tek II CC2 Chamber Slide System) and grown for 24 hours in standard conditions. The medium was then replaced with 500 µl of treatment solutions containing 15 µg/ml of ZnO NCs or TNHs or the corresponding number of EVs. After 24 hours of incubation the cells were washed twice with PBS. For the labelling of cell membrane, 2.5 µl of Wheat Germ Agglutiinin (WGA) conjugated with Alexa Fluor 488 dye (λ_{Ex}=495 nm), were added to the cells. After 10 minutes incubation cells were washed twice with Live Cell Imaging solution (LCI, 1×, Molecular Probes) and then imaged.

4.3 Results and discussion

4.3.1 TNH therapeutically active core: ZnO NCs

The ZnO NCs were synthesized through the microwave-assisted solvothermal synthesis method described in Chapter 2, that allowed to produce homogenous and reproducible particles with controlled physico-chemical and biological properties. The obtained NCs were further functionalized with APTMS molecules as described in details in Chapter 2. The amino-propyl groups were primarily required for the anchoring of fluorescent dyes (i.e. Atto550-NHS Ester or Atto647-NHS Ester), necessary for subsequent characterizations. In addition, as already shown in previous chapters, the presence of amino-propyl groups allowed to improve the NCs colloidal stability and imparted a higher positive surface charge, advantageous for the interactions with negatively charged EVs as described in details below. Therefore, the nanocrystals used for the TNHs construction, characterizations and biological tests described in this chapter must be intended always as amino-propyl functionalized NCs, even if called ZnO NCs for brevity.

The morphology and structure of the obtained ZnO NCs were studied through Transmission Electron Microscopy that showed tiny and round-shaped particles, presenting some hexagonal edges and an average diameter of around 17 nm **(Figure 4.4a**). The crystalline nature of the obtained particles was confirmed by HR-TEM analyses (**Figure 4.4b**), showing that NCs were formed by single crystals without evident defects and with lattice d-spacing typical of the ZnO hexagonal wurtzite structure. The crystalline phase of ZnO NCs was also confirmed by Selected Area Electron Diffraction (SAED, **Figure 4.4c**) and X-Ray Diffraction (**Figure 4.4d**), both showing the typical features of ZnO hexagonal wurtzite phase.

The hydrodynamic size distribution of ZnO NCs in different solutions was also assessed with DLS and NTA techniques. In particular, NTA measurement (**Figure 4.4e**) was performed in bd water, showing well-dispersed nanocrystals with a narrow monomodal distribution centered at 99 nm. The same behavior was observed from DLS measurements (**Figure 4.4f**) which displayed well-dispersed ZnO NCs in both ethanol and bd water with hydrodynamic diameters of 91 nm and 103 nm respectively. Instead, the colloidal stability was largely decreased for nanocrystals dispersed in mixture of bd water and salt-rich solutions, i.e. Phosphate Buffered Saline (PBS) or physiologic solution (0.9%w NaCl). As known, these solutions are necessary to preserve the osmolarity and thus the integrity of EVs membranes but they were disadvantageous for the ZnO NCs stability in solution, causing NCs aggregation. In particular, shifts toward hydrodynamic diameters equal to 550 nm in physiologic solution and 720 nm in PBS were detected (**Figure 4.4f**, dotted lines).

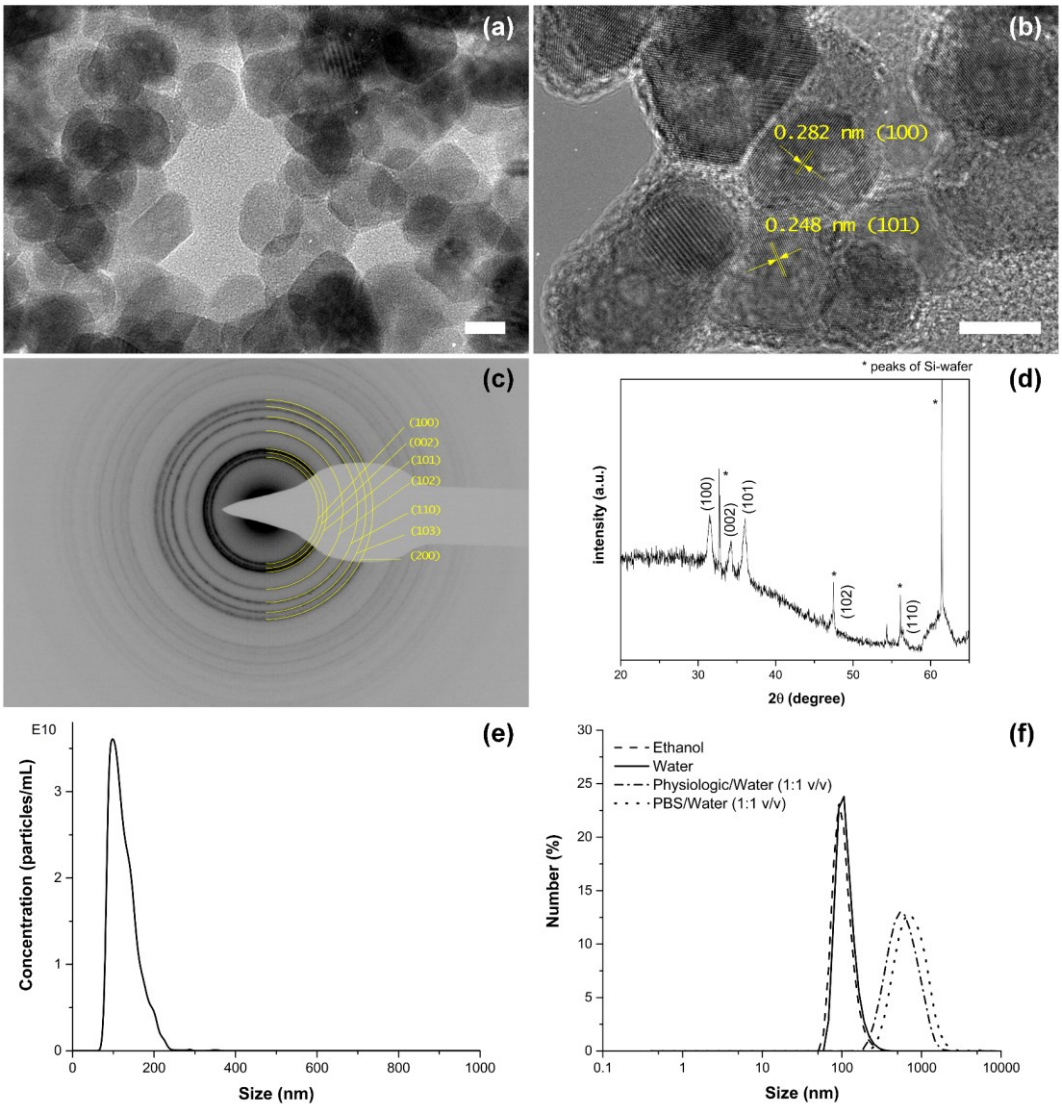

Figure 4.4: Characterization of ZnO NCs. Transmission Electron Microscopy images (**(a)** TEM and **(b)** HR-TEM; scale bars are 10 nm); **(c)** Selected area electron diffraction pattern; **(d)** X-ray diffractogram; **(e)** NTA measurement of nanocrystals dispersed in bd water and **(f)** DLS measurements of nanocrystals dispersed in different media.

4.3.2 TNH biomimetic shell: EVs extracted from KB cells

The EVs were extracted from conditioned supernatants of KB cells, according to the protocol created by Thery et al. (Théry et al., 2006) with some modifications, as fully detailed in the Materials and Methods section. The obtained final pellet, properly stored at -80°C, were characterized through Electron Microscopy, evidencing the presence of round-shaped vesicles with quite constant diameters of about 100 nm (TEM and FESEM images in **Figure 4.5a** and **b** respectively).

EVs elemental composition was analysed with Energy Dispersive Spectroscopy (EDS, **Figure 4.5c**) and the presence of carbon and oxygen was obviously detected, due to the lipidic nature of the vesicles, together with high amounts of sodium, calcium and chlorine, ascribable to buffer solution used as dispersant medium.

Finally, NTA measurements were performed in order to analyse the EVs size distribution in solution and to measure their concentration, expressed in particles/ml. Several measurements (27 experiments) were performed, analysing EVs derived from different extractions to ensure the good reproducibility of the protocol. Representative results are reported in **Figure 4.5d**, showing narrow and monomodal size distributions centred at 110 nm for EVs dispersed in both PBS and physiologic solution. The measured EVs concentrations were ranging between 1.1 $\times$ 10^{10} part/ml and 2 $\times$ 10^{11} part/ml.

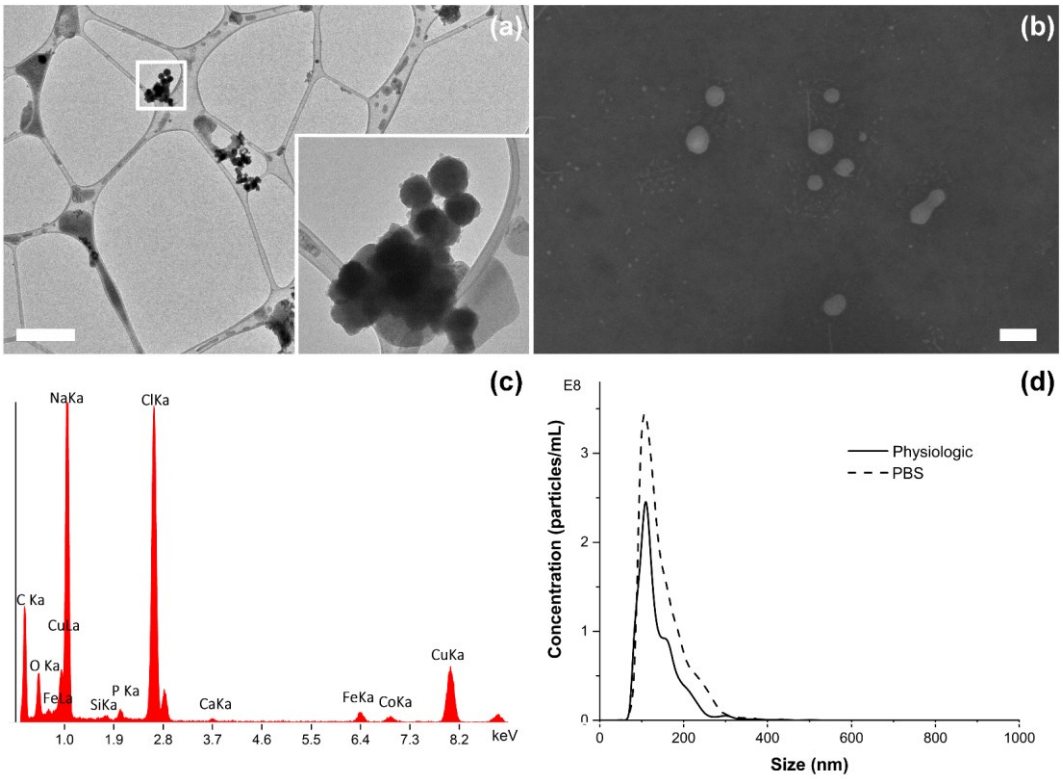

Figure 4.5: Characterization of EVs extracted from KB cells. **(a)** TEM image at 80 kV and magnification of a detail in the inset (scale bar: 1 μm); **(b)** FESEM image (scale bar: 100 nm); **(c)** Energy Dispersive Spectroscopy analysis performed in the region reported in (a); **(d)** NTA measurements of EVs dispersed in PBS (dashed line) or physiologic solution (solid line).

4.3.3 TNHs construction and characterization

The encapsulation of ZnO NCs into the EVs derived from KB cells was performed using a co-incubation method, i.e. by simply mixing the two components in solution without the application of external stimuli. As already detailed in the Introduction, this method could guarantee a good preservation of EVs integrity but is often accompanied by low loading efficiencies. Therefore, the influence of several operating parameters was analysed in order to find the better combination and maximize the coupling efficiency.

The results of the coupling optimization are reported in the next section. In particular, during the screening of operating parameters the obtained TNHs were characterized through fluorescence microscopy, which allowed to detect the fluorescent signals of labelled ZnO NCs and EVs and evaluate their colocalization.

The coupling efficiencies were then expressed as percentages of colocalized spots with respect to the red signal of labelled ZnO NCs (%co-ZnO), as reported in details in the Materials and Methods section. The percentages with respect to the EVs (%co-EVs) and the overall percentages (%TNHs) were also monitored (data not shown), but the %co-ZnO was used as reference variable for the optimization of the coupling process. In fact, the main goal of the TNHs construction was to increase the biocompatibility and the colloidal and chemical stability of ZnO NCs thanks to the shielding of biological EVs. In this perspective, the limiting variable was the amount of uncoupled ZnO NCs, evaluable as complement of the %co-ZnO.

The morphology, composition and colloidal stability of the TNHs obtained with the optimized protocol were then fully characterized through Electron Microscopy, NTA and Zeta-Potential measurements.

4.3.3.1 Optimization of ZnO NCs and EVs coupling process

The coupling protocol between ZnO NCs and EVs was optimized exploiting a combination of thermodynamic, kinetic and electrostatic mechanisms directly related to the EVs and NCs properties. The ZnO colocalization percentages obtained during the screening of the operating parameters are summarized in **Table 4.2** and are an average of the %co-ZnO of the two runs performed as described in details in the Materials and Methods section.

The first tested parameter was the mixing method, confronting an orbital shaker set at 180 rpm with a tube-rotator working at the fixed speed of 20 min^{-1}. The %co-ZnO obtained with the tube rotator was very low, probably due to the continuous turning upside-down of the test-tube containing the coupling solution. This motion could cause the spread of EVs and ZnO NCs on the tube walls, reducing the probability of contact between the TNHs components. Almost double percentages were obtained using the orbital shaker (highlighted in green in the second row of **Table 4.2**), identified as the best mixing method and thus used in all the subsequent experiments.

The second operating parameter investigated in this screening process was the temperature, which was varied between 4°C, room temperature and 37°C. The best coupling efficiency was reached at 37°C, showing a significant increment with respect to lower temperatures (second set of data in **Table 4.2**). These results could be explained considering the coupling as a thermodynamic process, favored by the increase of temperature that directly act on the fluidity of phospholipid membrane of EVs and determine the effective encapsulation of solid ZnO NCs. Therefore, the inferior colocalization percentages at lower temperatures were ascribed to the superior rigidity of EVs, while the physiologic temperature of 37°C ensured an optimal membrane fluidity and permeability.

Considering the duration of co-incubation procedure, variable between 5 minutes and several hours according to previous literature studies (Luan et al., 2017), two runs of co-incubation of 90 minutes each were initially performed and then compared with longer incubation times, i.e. 8 hours and 24 hours. For both extended incubations, a single run was performed due to the already prolonged time

of processing. As reported in **Table 4.2**, the best %co-ZnO was achieved for the two runs of 90 minutes and these values were not improved by extending the process length. This behavior suggested that the kinetic of the process was relatively fast, allowing the incorporation of ZnO NCs into the EVs membrane already at the shorter times. In addition, the effect of the progressive aggregation of ZnO NCs in the suspension medium was also considered. Indeed, aggregation would negatively affect the availability of NCs in solution over time.

The fourth parameter evaluated was the ratio between the EVs and ZnO NCs. The two components were mixed considering their concentration in number (i.e. particles/ml), supposing that a single EVs could encapsulate several ZnO NCs. In particular, in a first set of experiments the ZnO NCs were added at the beginning of the process (t_0) with number ratio equal of 50:1 or 500:1 with respect to the EVs. The increment of NCs concentration was performed in order to enhance the probability of collision between the two components and, thus, the coupling. However, very low colocalization percentages were obtained with the higher NCs amount (see **Table 4.2**). This result could be explained considering the tendency of ZnO NCs to aggregate in the used solution, which would be promoted by the increase of their concentration. Therefore, another approach to increment the ZnO NCs:EVs number ratio avoiding the simultaneous addition of high amount of nanocrystals and their subsequent aggregation was tempted. In this case, the ZnO NCs were added in 50:1 ratio consecutively at time t_0, 1 hour and 2 hours, for a final ratio equal to 150:1. Though, also this strategy did not improve the coupling efficiency (**Table 4.2**) and the initial protocol consisting in the addition of the ZnO NCs in a ratio 50:1 at the beginning of the two runs was identified as the best option. Furthermore, if considering the percentages of colocalized EVs (data not shown) a limit in the EVs loading was clearly observed. In fact, the %co-EVs was always below the 40%, with no appreciable improvement connected to the variation of ZnO concentration.

Finally, the influence of the dispersing medium was evaluated. As detailed in the Materials and Methods section, the ZnO NCs were always resuspended in bd water, while the EVs were dispersed in PBS or physiologic solution. A modest improvement of the colocalization percentage was obtained with the coupling performed with EVs dispersed in physiologic solution (last line of **Table 4.2**). In fact, even if the coupling occurred in a diluted solution of 1:1 in volume of bd water and PBS or physiologic solution, the buffer composition affected both the colloidal stability and the surface properties of ZnO NCs. As already illustrated in **Figure 4.4f**, the hydrodynamic size distributions measured by DLS showed a strong aggregation of the nanocrystals in contact with salt-rich solutions, that was slightly lower for physiologic solution with respect to PBS. More interesting were the effects of buffer composition on the Zeta-Potential values. In fact, EVs displayed a negative Zeta-potential value (-9.53 mV) in both media in good accordance with literature results (Fuhrmann et al., 2015), while the ZnO NCs showed a shift from negative value (-15.5 mV) in PBS/water to positive Zeta-Potential (+12.3 mV) in physiologic solution/water mixture. This results suggested that also the electrostatic interactions played an important role in the coupling process. In particular, the

opposite surfaces charges detected in physiologic solution favored the interaction between the two components, giving the final improvement to the coupling efficiency.

The screening of the operating parameter allowed to define the optimal coupling protocol that enclosed the best options highlighted in green in **Table 4.2** as schematically represented in **Figure 4.6**.

Table 4.2: Percentages of ZnO NCs colocalized with EVs (%co-ZnO) by varying the operating parameters; the best choice for each parameters and the corresponding percentage are highlighted in green.

Mixing Method	Temperature	Time	ZnO NCs:EVs number ratio	Medium	%co-ZnO
Tube rotator	RT	90’	50:1	PBS	11
Orbital shaker					21
Orbital shaker	4°C	90’	50:1	PBS	20
	RT				21
	37°C				47
Orbital shaker	37°C	90’	50:1	PBS	47
		8h			31
		24h			38
Orbital shaker	37°C	90’	50:1	PBS	47
			500:1 at t_0		11
			50:1 x 3		22
Orbital shaker	37°C	90’	50:1	PBS	47
				NaCl 0,9%	50

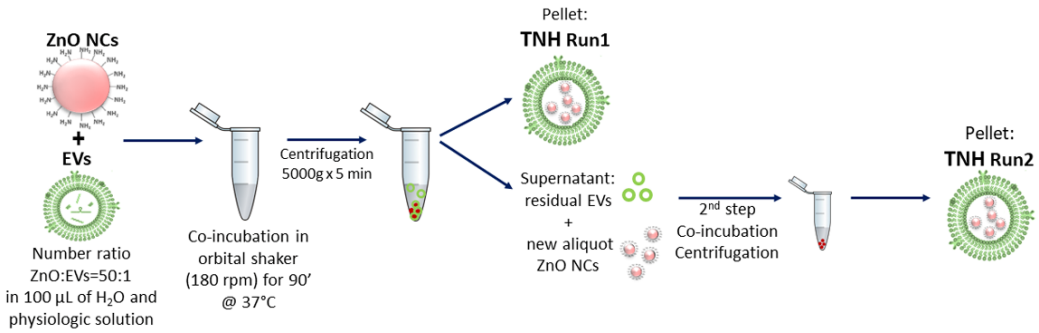

Figure 4.6: Scheme of the optimized coupling process between ZnO NCs and EVs extracted from KB cells for the TNHs construction.

As already stated, the obtained TNHs were firstly characterized through fluorescence microscopy, in order to evaluate the coupling efficiency quantified as colocalization between the fluorescence signals of labelled ZnO NCs and EVs. **Figure 4.7** shows an example of fluorescence images of TNHs obtained by the optimized protocol using ZnO NCs and EVs labelled with a red emitting dye (Atto550-NHS Ester, **Figure 4.7a**) and a green emitting lipophilic probe (DiO, **Figure 4.7b**), respectively. The merge of the two images (**Figure 4.7c**) showed a good colocalization between the red and green spots, confirming the success of TNHs construction. In particular, applying the defined optimal protocol, an average ZnO colocalization percentage (%co-ZnO) of 59% was obtained after the Run1. This was lowered after the Run 2 (%co-ZnO=22%), possibly due to the reduction of residual EVs in the supernatants. However, combining Run 1 and Run 2, a final

colocalization percentage of about 40% was calculated, overcoming the coupling efficiencies obtained by similar studies (Haney et al., 2015, Kim et al., 2016).

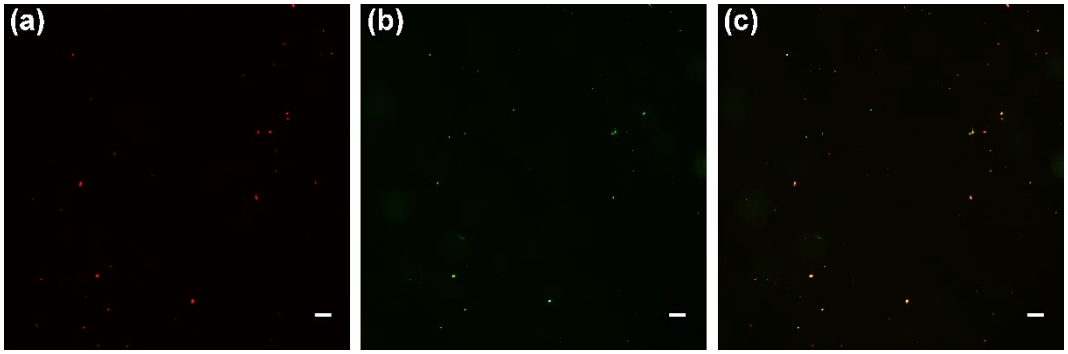

Figure 4.7: Wide-field fluorescence images of **(a)** ZnO NCs labeled with Atto550-NHS Ester (red channel) **(b)** EVs labeled with DiO (green channel) and **(c)** merge of the two channels, showing TNHs as colocalized yellow spots. Scale bar: 10 μm.

4.3.3.2 TNHs characterization

More details on the TNHs morphology were obtained through Electron Microscopy. The freshly-prepared samples were imaged at 80 kV, without any further fixation or staining with contrasting agents. TEM images, reported in **Figure 4.8** from **(a)** to **(d)**, displayed single or partially overlapped round-shaped EVs together with more dense crystalline structures of about 15 nm, corresponding to ZnO NCs. To better visualize the two different components and their spatial arrangement, TEM images were provided both in bright field and dark field modes, clearly showing that ZnO NCs were quite homogenously distributed all over the EVs volumes or near their surfaces. The crystalline nature and phase of the more dense structures was confirmed by SAED measurements (**Figure 4.8e**), showing the typical d-spacing of ZnO nanomaterials already described during the characterization of pristine ZnO NCs (see **Figure 4.4c**). In addition, the compositional analyses performed through Energy Dispersive Spectroscopy (**Figure 4.8f**), confirmed both the presence of EVs, detecting all the elements typical of biological samples, and of Zn element. The appearance of Zn peak, not detected in the EDS spectrum of uncoupled vesicles (see **Figure 4.5c** as reference), further confirmed the successful TNHs construction.

Additional analyses were performed with TEM operating at 200 kV. The higher accelerating voltage, applied to freshly-prepared samples without fixation or staining, caused the progressive melting of the EVs biological structures deposited on the TEM grid (**Figure 4.9a** and **b**). The degradation of the organic phase allowed the appearance of denser structures corresponding to ZnO NCs, that appeared clearly visible and arranged in a circular fashion, recalling the morphology of the EV in which they were encapsulated (inset in **Figure 4.9b**).

Overall these results clearly demonstrated the effective interaction between the EVs and ZnO NCs during the optimized coupling procedure, leading to the construction of TNHs composed by EVs encapsulating or retaining at their surfaces the ZnO NCs.

The success of the coupling procedure was also studied analyzing the modification of surfaces properties in response to EVs shielding through Zeta-Potential measurements. As already mentioned, the EVs presented a negative Zeta-Potential equal to -9.5 mV, while ZnO NCs had a positive Zeta-Potential value equal to +12.3 mV in the coupling mixture of bd water/physiologic solution. Interestingly, the TNHs showed a negative surface charge, with a Zeta-Potential of -13.2 mV, very close to the one obtained for uncoupled EVs and far from the positive value of ZnO NCs. The slight variation measured between TNHs and uncoupled EVs could be ascribed to the rearrangement of phospholipids in the vesicles membranes, and specifically of their polar heads bearing negative phosphate groups. This effect was already reported in literature regarding EVs loaded with photosensitive components (Fuhrmann et al., 2015) and was attributed to the insertion of ZnO NCs in the EVs membrane. Therefore, this result confirmed the occurrence of a very close interaction between ZnO NCs and EVs, probably leading to an actual internalization.

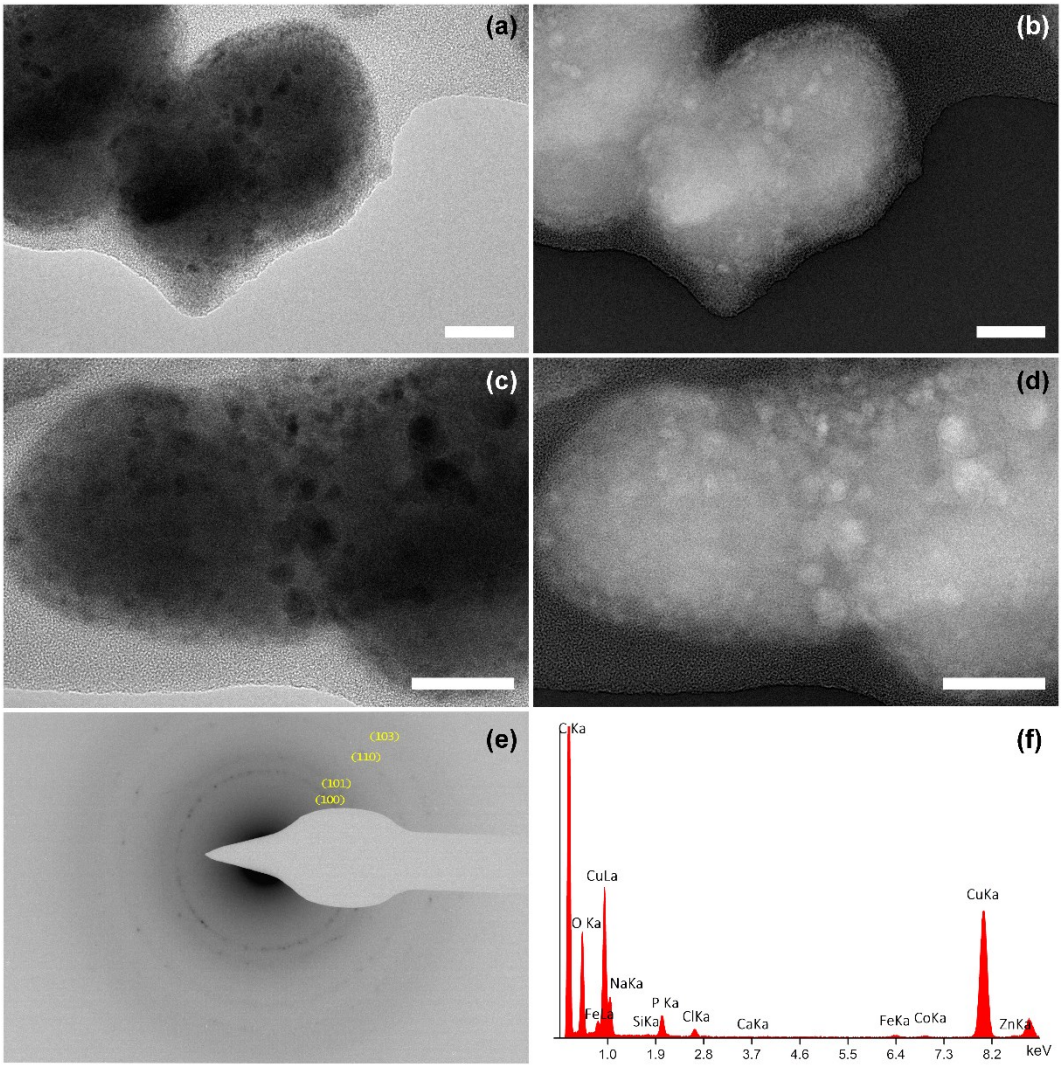

Figure 4.8: Characterization of TNHs through Electron Microscopy. TEM images at 80 kV of TNHs (from **(a)** to **(d)**; scale bars are 30 nm). Pictures in **(b)** and **(d)** are the same of **(a)** and **(c)**, respectively, with inverted colors. **(e)** Selected area electron diffraction pattern and **(f)** Energy Dispersive Spectroscopy,

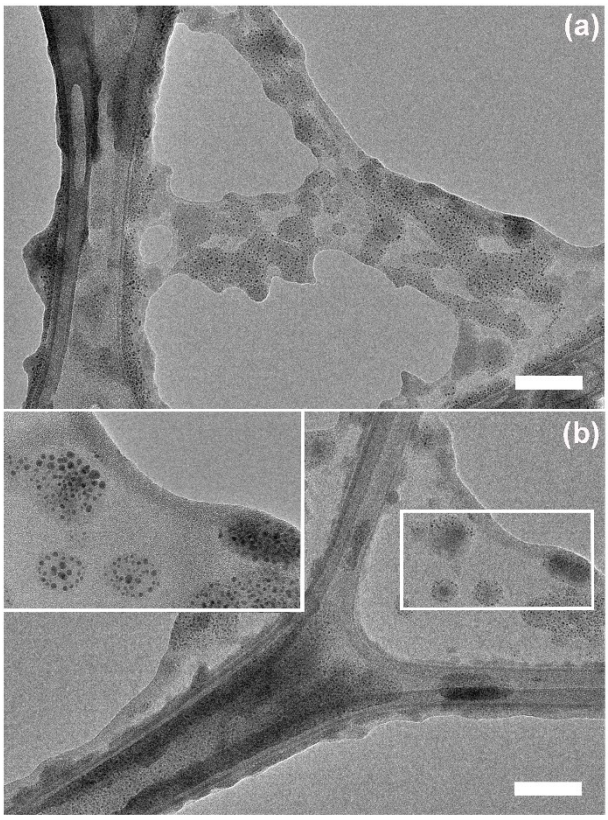

Figure 4.9: TEM images at 200 kV of TNHs. Scale bars: 100 nm in both **(a)** and **(b)**. The inset in **(b)** report a higher magnification of the area indicated with the white square, showing the details of ZnO NCs and their circular arrangement.

Finally, the colloidal stability of TNHs prepared by the defined optimal protocol was analyzed through NTA technique, confronting their colloidal behavior with that of their pristine components. In fact, as already observed in Chapter 3 for the synthetic lipid-coated samples, the encapsulation of ZnO NCs in the EVs shielding could guarantee an improvement of nanocrystals biostability, preventing their aggregation in salt-rich biological solutions.

The hydrodynamic size distributions of ZnO NCs, EVs and TNHs dispersed in bd water and physiologic solution (1:1 in volume) are reported in **Figure 4.10a**, **b** and **c** respectively and confirmed what expected. In particular, by comparing the size distribution of the ZnO NCs in presence of physiologic solution (**Figure 4.10a**) with the one obtained redispersing the NCs in only bd water (see **Figure 4.4e**), the aggregation caused by the salt-rich solution resulted clear. In fact, here the ZnO NCs presented a multimodal hydrodynamic distribution and the aggregation was testified by the appearance of peaks at high size values, i.e. 273 nm and 561 nm.

In contrast, TNHs samples resulted quite well-dispersed in the bd water and physiologic solution coupling mixture, showing a size distribution centered at 115 nm with minor peaks at 157 nm and 398 nm (**Figure 4.10c**). This clearly resembled the almost monomodal distribution of uncoupled EVs (**Figure 4.10b**), further confirming the success of coupling procedure and the effective stabilization of NCs provided by the EVs shielding.

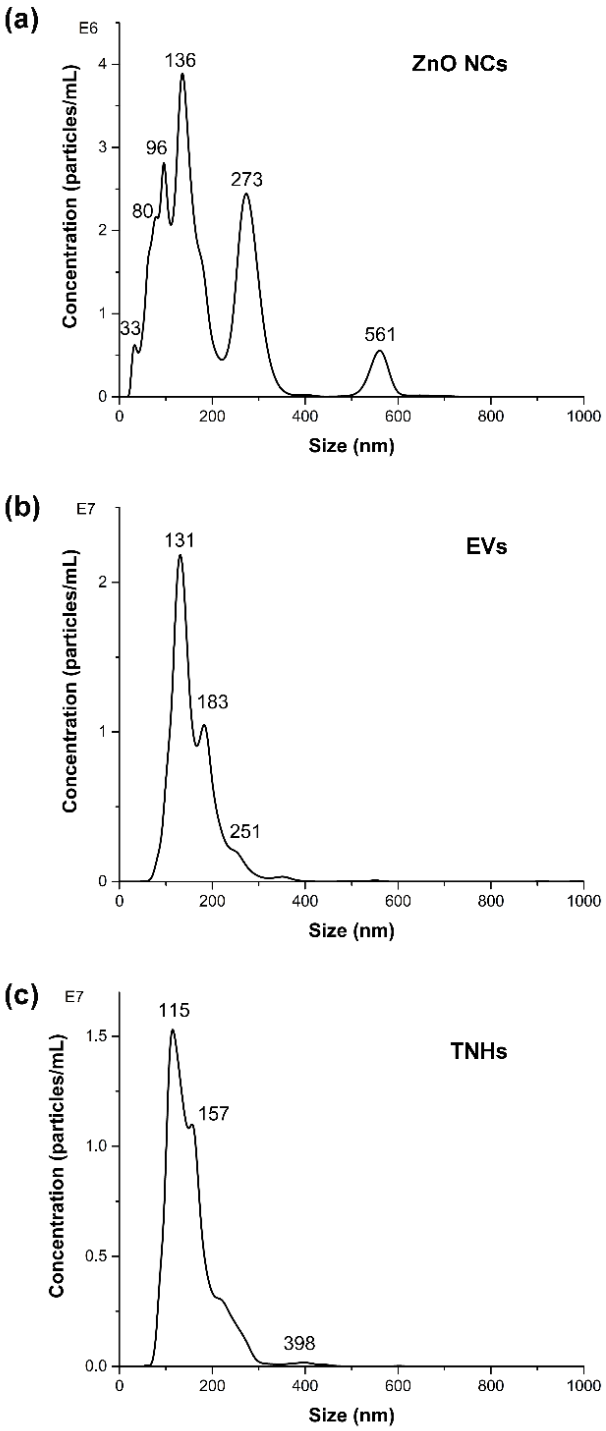

Figure 4.10: NTA measurements of **(a)** ZnO NCs **(b)** EVs and **(c)** TNHs dispersed in 1:1 v/v of bd water and physiologic solution.

4.3.4 TNHs biological effect

After the optimization of the preparing procedure and the physico-chemical characterization, the biological effects of the obtained TNHs with respect to their pristine components were evaluated.

The cytotoxic effect of TNHs and ZnO NCs on KB cancerous cells was compared through WST-1 assay, testing the cells proliferation after a 24 hours treatment with different concentrations. Details on the treatments preparation are reported in the Material and Methods section (**Table 4.1**) and the obtained results are showed in **Figure 4.11a**, expressed as proliferation percentages referred to the untreated control. In particular, ZnO concentration of 5, 15, 25 and 50 μg/ml were tested and both TNHs and ZnO NCs showed a similar dose-dependent cytotoxicity with a significant inhibition of cell viability at 50 μg/ml ($p \leq 0.001$). An initial reduction of cell viability, with a high variability, was measured already at 25 μg/ml ($p \leq 0.001$ with respect to 5 μg/ml). Although, no significant differences between the TNHs and uncoated ZnO NCs were detected, suggesting that the EVs shielding provided during the TNHs construction did not affect the intrinsic toxicity of ZnO.

To exclude an eventual contribution of EVs to the detected cytotoxicity and assess their full biocompatibility, the same assay was performed treating the KB cells with the amount of uncoupled EVs corresponding to 5, 15, and 25 μg/ml treatments. This test was mainly performed in a perspective of theranostic application of TNHs, hence the higher and most toxic concentration, i.e. EVs corresponding to 50 μg/ml of NCs, was excluded. The results are shown in **Figure 4.11b**, confirming that EVs alone did not affect the cells viability at all the tested concentrations.

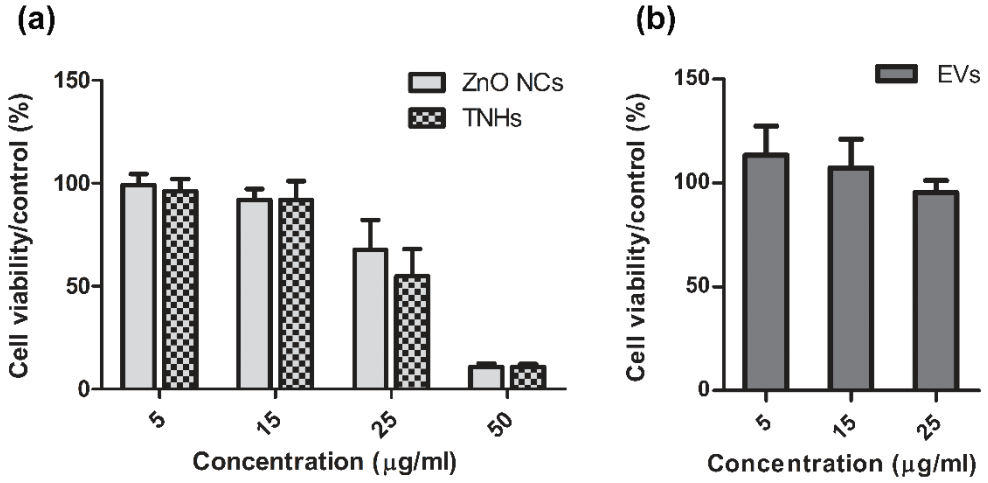

Figure 4.11: Cell viability of KB cells after a 24 hours treatment with escalating concentration of **(a)** ZnO NCs and TNH and **(b)** corresponding quantities of EVs. Results are expressed as percentages with respect to the control.

To further elucidate the interactions between the TNHs and the cancerous cells, the cellular uptake of the developed hybrid nanoconstruct with respect to the pristine components was analyzed.

With this purpose, flow-cytometry analyses were performed, evaluating the TNHs, ZnO NCs and EVs internalization after a 24 hours treatment. Considering the cytotoxicity results, the concentration of 5, 15 and 25 μg/ml, which guaranteed a good cell viability, were tested. The ZnO NCs and EVs were labelled with red or green emitting fluorescent dye, as described in detail in the Materials and Methods section, and the level of internalization was expressed as percentages of positive events detected in the corresponding channel with respect to the untreated control. For the TNHs both red and green signals were collected, as shown in **Figure 4.12**.

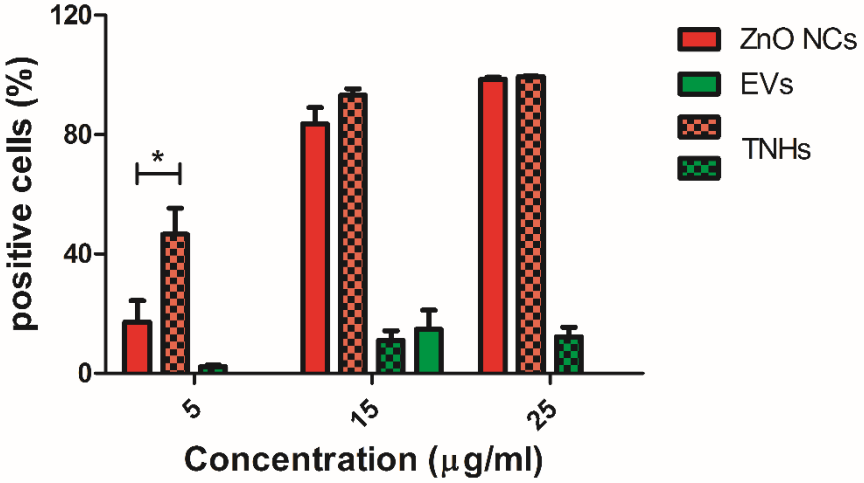

Figure 4.12: Cellular internalization of pristine ZnO NCs (red bars), EVs (green bars) and TNHs (red and green dashed bars, related to ZnO and EVs components respectively). The uptake was evaluated through flow-cytometry assay after a 24 hours treatment with different concentration of ZnO NCs or TNHs (i.e. 5, 15, 25 μg/ml) and with the amount of pristine EVs corresponding to 15 μg/ml. Results represent the percentages of positive events (fluorescent cells) with respect to untreated control and are expressed as mean ± SEM. *$p<0.05$.

Concerning the red signal related to the ZnO component, the results showed a higher extent of internalization for the TNHs sample with respect to the pristine ZnO NCs without the EVs shielding (red bars in **Figure 4.12**). In particular, a significant difference between the two treatments was detected at the lower dosage of 5 μg/ml ($p < 0.05$). At higher dosages the difference was no more appreciable due to the really effective internalization displayed also by the single ZnO NCs, which was already near to 100%.

In contrast, the green signal corresponding to the lipidic part of TNHs or to the uncoupled EVs (tested only at the intermediate concentration of 15 μg/ml), showed lower internalization levels and no differences between the samples or dosages (**Figure 4.12**, green bars). These results could possibly be explained considering the green autofluorescence of KB cells, which possessed a high background signal in the green channel responsible of the partial overcasting of samples green fluorescence.

This assumption was confirmed by fluorescence microscopy analyses, performed with a wide-field fluorescence microscope equipped with appropriate filters able to cut the typical cytoplasmic autofluorescence and fully detect the DiO green fluorescence. These tests were performed on cells treated with 15 μg/ml of ZnO NCs and TNHs or the corresponding amount of EVs for 24 hours. Exemplificative images derived by selected z-stack are shown in **Figure 4.13.** The cellular membrane was opportunely labelled to better assess its interaction with the nanoconstructs and represented in green while, to guarantee an optimal visualization, ZnO NCs and EVs were depicted in false colours, i.e in purple and orange respectively.

As clearly displayed, both uncoupled ZnO NCs (**Figure 4.13a**) and EVs (**Figure 4.13b**) were efficiently internalized by KB cells and preferentially accumulated in the cytoplasmic perinuclear area, where they are distinguishable as single spots or small aggregates. Considering different regions of interest (ROIs), it was noted that EVs exhibited a higher uptake level with respect to ZnO NCs.

A similar internalization behaviour was shown by TNHs sample (**Figure 4.13c**), with both purple and orange spots present in the cellular cytosolic space. The magnification reported in **Figure 4.13d** clearly shows the presence of yellow spots, corresponding to THNs, colocalized with cellular membrane demonstrating the entering of the nanoconstructs inside the cells. Although, a poor colocalization between the two signals were detected inside the cells in which were present several purple spots together with few colocalized structures (yellow spots). This could be explained assuming a partial loss or destabilization of the TNHs lipidic shielding during the crossing of the membrane for cell internalization. According to this hypothesis, the ZnO would be released as pristine nanomaterial inside the cytoplasmic space, greatly explain also the similarities observed between the cytotoxic response of TNHs and uncoupled ZnO NCs. In addition, literature results (T. Tian et al., 2010) reported that EVs are commonly degraded and recycled for cell physiological function after their internalization, supporting the idea that the EVs shielding could be disrupted after TNHs internalization.

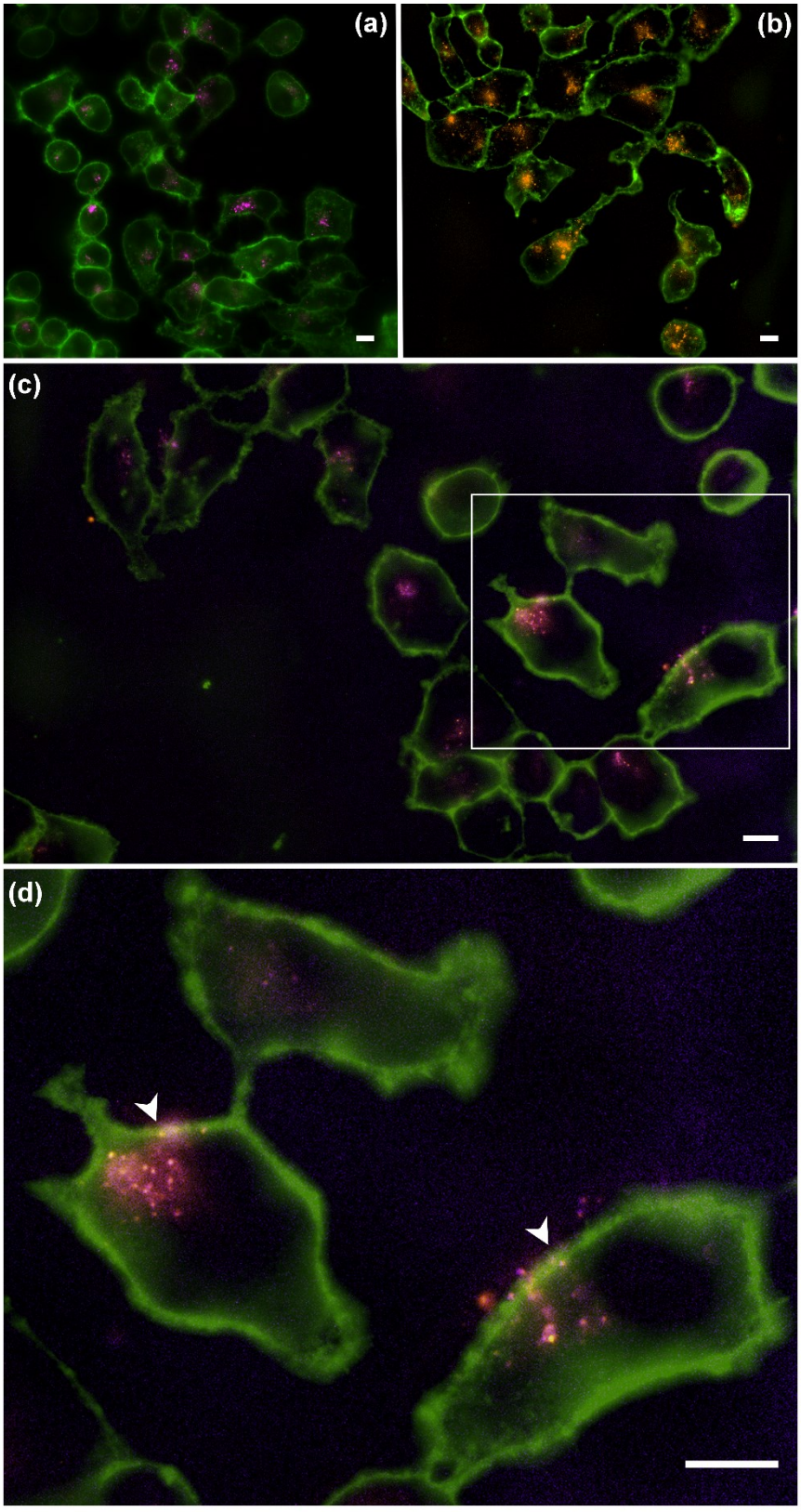

Figure 4.13: Fluorescence Microscopy z-stack images of **(a)** ZnO NCs, **(b)** EVs and **(c)** TNHs internalized in KB cells after a 24 hours treatment; **(d)** Magnification of the area indicated with the white square in (c), showing the colocalization between ZnO NCs and EVs. Cells membranes were labelled with WGA-Alexa488 (in green); ZnO NCs and EVs were labelled as described in detail in the Material and Methods section and represented in purple and orange, respectively. Scale bars: 10 μm.

4.4 Conclusions

The results reported in this chapter refer to the development and characterization of Trojan nano-horses (TNHs) hybrid nanoconstructs composed by a therapeutically active core of ZnO NCs shielded by cell-derived lipid vesicles (EVs). The synthesized ZnO NCs were efficiently encapsulated in EVs extracted from KB cancerous cells through an optimized co-incubation protocol, which harnesses the combination of thermodynamic, kinetic and electrostatic mechanisms to guarantee the best interaction between the two components. In particular, the influence of several operating parameters (including temperature, duration, concentration of the components and dispersing medium) was evaluated allowing the definition of a final coupling procedure. The optimized coupling efficiency, evaluated with respect to ZnO component, was equal to 40% overcoming the loading efficiencies obtained by similar literature studies.

Further characterizations allowed to visualize the morphology of obtained TNHs nanoconstructs, composed by several ZnO NCs encapsulated within a single EV. The improvement of the colloidal stability in biological media of the EVs-shielded sample was also assessed, confirming the results preliminarily obtained with synthetic lipid-shell. Indeed, the biological origin of EVs would allow also the improvement of biomimetic and biocompatible features of TNHs hybrid nanoconsructs in the perspective of therapeutic applications.

In vitro tests performed on KB cancerous cells showed the dose-dependent cytotoxic effect of TNHs nanoconstructs, confirming their potential use as therapeutic nanotools for cancer treatment. Actually, TNHs samples displayed a similar toxicity with respect to uncoated ZnO NCs, highlighting that EVs shielding did not affect the intrinsic toxicity of pristine ZnO. In addition, the interaction between hybrid TNHs nanoconstructs and cancerous cells was studied evaluating their internalization with flow-cytometry and fluorescence microscopy. These tests confirmed that TNHs were efficiently internalized and in higher extent with respect to uncoated ZnO NCs. This enhancement was ascribed to the presence of the lipid shell constituted by EVs that stabilize the NCs in biologic environment and favour their delivery in target cells.

Chapter 5

Optimization of TNH nano-construct: active loading method and functionalization with targeting ligands

5.1 Introduction

5.1.1 Toward EVs clinical application: challenges and perspectives

Thanks to their primary role on cell-cell communication, EVs are currently widely investigated in the field of cancer therapy and diagnosis. When generated in pathological conditions EVs carry diseased-related genetic material as well as specific surface proteins which reflect the cell of origin and make EVs promising biomarkers for cancer diagnosis and prognosis (Lane et al., 2018). Concerning the therapeutic applications, and in particular their use as drug delivery vehicles, EVs possess several interesting features. As discussed in the previous chapter, EVs are highly stable in biological environment, biocompatible, low immunogenic, with a prolonged circulation time and an intrinsic ability to cross biological barriers (Sander A.A. Kooijmans, Schiffelers, et al., 2016). Furthermore, they can be loaded with different exogenous cargos both during their formation, i.e. through parent cells engineering, or after the isolation (Sutaria et al., 2017).

These promising properties have made exosomes, and more generally EVs, subject of an increasing number of research studies with an exponential growth from their discovery to the present and a deep connection with cancer nanomedicine (Munson & Shukla, 2018). According to the US-NIH clinical trials database (www.clinicaltrials.gov) 249 clinical trials on EVs or exosomes are currently registered, 107 of which are connected to cancer disease employing cell-derived vesicles for both diagnostic and therapeutic purposes.

However, the effective application of EVs in the clinical field is still hindered by several issues. As already mentioned in Chapter 4, the low yields of EVs isolation methods and the small efficiencies in cargo-loading are some of the main limitations. Furthermore, concerning their encapsulation, another major issue is to achieve an efficient loading while preserving the overall structure and integrity of EVs which guarantee, for instance, the low immunogenicity and targeting ability of the vesicles (Batrakova & Kim, 2015).

In the perspective of a clinical application, several studies point out the necessity to institute standardized procedures and regulatory points for the production of EVs-based formulations. A position paper of the International Society of extracellular vesicles (ISEV) reiterates this need, suggesting that EVs-based therapeutics could be classified as biological medicinal products and follow the related existing regulatory framework with the addition of specific guidelines. Briefly, in the perspective of a progression toward EVs clinical application, it was recommended to carefully consider the EVs source and standardize the isolation, characterization and storage procedures. In addition, the importance of the reproducibility and consistency of cargos loading, the need of quality control of produced lots and the evaluation of *in vivo* toxicology and distribution of EVs were emphasized (Lener et al., 2015).

Concerning the cellular source, no consensus has been reached on the most appropriate type of cells to produce EVs for drug delivery applications. For instance, EVs produced directly by cancerous cells are considered, even though

with some concerns (Sun et al., 2018). Indeed, tumor-derived EVs possess an intrinsic targeting ability and organotropism which are mainly determined by their integrin profile and could be exploited for the specific delivery of different therapeutic agents. Actually, the targeted co-delivery of therapeutic miRNAs and imaging agents using tumor-derived EVs was proved (Jc Bose et al., 2018) while another recent study showed that drug-loaded cancerous EVs were able to selectively home their parent tumors thanks to the presence of particular proteins and lipids in the EVs membrane (Qiao et al., 2020). However, tumor-derived EVs possess also a role in cancer progression and, thus, their application as delivery platforms presents several concerns. Recent studies demonstrated that tumor-derived EVs are responsible to mediate the interactions between cells of tumor microenvironment, modulating the development and progression of cancer (Sun et al., 2018). EVs derived from cancerous cells could stimulate the formation of new tumor vessel and the migration of endothelial cells even without their actual uptake, thanks to the presence of specific growth factors on the vesicle membrane (Ko et al., 2019). Similarly, tumor-derived EVs could directly suppress the anti-tumor immune response through the interaction of specific surface molecules (Taylor & Gercel-Taylor, 2011), while the delivery of oncogenic contents could induce the acquisition of inflammatory phenotype by recipient cells (C. Chen et al., 2017). Furthermore, the pro-tumor activity of EVs is not limited to the tumor microenvironment, but involves also distant organs that could be reached by circulating tumor-derived vesicles. Indeed, EVs have a main role in the metastases promotion since they are responsible for the formation of pre-metastatic niches, i.e. the induction of favorable environmental conditions for the subsequent arrival and outgrowth of tumor cells (Peinado et al., 2017). Interestingly, the integrin expression profiles of tumor-derived EVs directly determine their distribution in specific organs or tissues and, thus, the organotropic metastasis (Bebelman et al., 2018). Finally, tumor-derived EVs possess also a role in mediating drug resistance in different types of cancers and through multiple mechanisms. Cancerous EVs could directly bind or encapsulate the therapeutic agent limiting its bioavailability or act as carriers of RNA, enzymes and regulatory proteins able to transform recipient cells in drug-resistant cells (Namee & O'Driscoll, 2018).

Considering the outlined duality, the application of tumor-derived EVs as drug delivery systems require a more careful evaluation of their specificity, functionality and safety profile while less hazardous alternatives are intensively investigated, including EVs derived from food, like fruits (Rome, 2019) and bovine milk (Munagala et al., 2016), or from healthy cells. For instance, EVs derived from dendritic cells, macrophages or mesenchymal stem cells are widely investigated for either immunotherapy and drug delivery applications (Meng et al., 2020)

Another issue experimented in the progression toward a clinical application of EVs concerns the *in vivo* biodistribution of exogenously administered vesicles. In fact, even though EVs are generally considered biocompatible and stable in blood circulation thanks to their biological nature, recent researches indicated that their pharmacokinetics profile is not completely favourable (Takakura et al., 2020). The development of progressively sophisticated imaging and detection tools allowed the

extensive study of biodistribution of exogenously administrated EVs. Several studies demonstrated that the biodistribution of systematically administrated EVs is a very dynamic process, with a rapid phase of clearance and preferential accumulation in liver, spleen, and lungs, organs rich in macrophages, within approximately 30 minutes upon administration. This is followed by an elimination phase *via* hepatic and renal filtration that leads to a total removal of EVs from circulation in 1 to 6 hours upon administration (Lu et al., 2018). The *in vivo* distribution patterns of EVs is also influenced by their administration route. For instance, a study compared intravenous, intraperitoneal and subcutaneous injection showing that the administration route significantly affects the tissue distribution of infused EVs and determines also the total detected amount of vesicles (Wiklander et al., 2015). Similarly, intravenously-injected EVs showed a rapid clearance and a minimal tumor accumulation, while intratumorally administered vesicles remained associated with tumor tissues in a greater extent with respect to synthetic liposomes (Smyth et al., 2015). Considering the limited specificity and the short *in vivo* half-life of EVs, many research efforts are devoted to the engineering of vesicles membrane with appropriate additional functionalities which would provide a valuable improvement of their circulation time and targeting ability (Susa et al., 2019).

5.1.2 EVs surface functionalization

The therapeutic application of EVs could deeply benefit from different modification strategies which enable the functionalization of their surface with specific moieties. The engineering of EVs membrane is mainly devoted to improve their circulation kinetics and target specificity, allowing a more effective delivery of encapsulated therapeutic payloads. As schematically represented in **Figure 5.1**, the functionalization of EVs membrane is obtained by the insertion of several types of natural ligands or synthetic molecules employing different modification techniques.

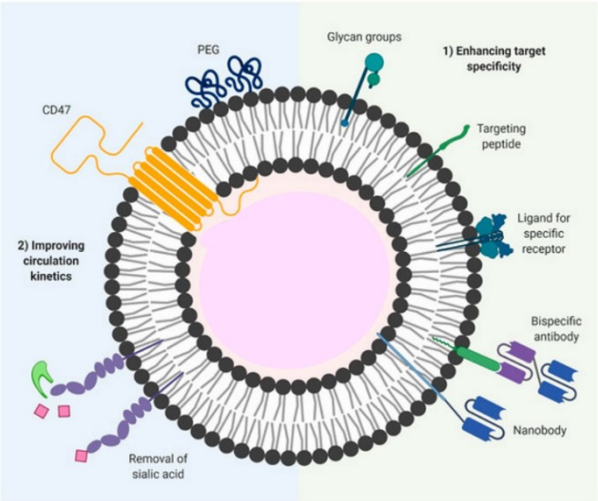

Figure 5.1: Schematic representation of the different types of functionalizing moieties used to modify the EVs surface for therapeutic applications. In general, the modifications are mainly devoted to **(1)** enhance the EVs targeting specificity and **(2)** improve EVs circulation kinetics; figure modified from (Dang et al., 2020).

5.1.2.1 Surface functionalization techniques

As already mentioned for cargo-loading methods, the functionalization strategies are mainly classified as indirect methods, in which the parent cells are engineered to produce functionalized EVs, or as post-isolation methods, that envisage the direct modification of EVs after their extraction (Susa et al., 2019).

The indirect approach, also called biological approach, normally involves the genetic engineering of parent cells with chimeric gene or protein that are composed by the actual functionalizing protein fused with a gene or protein typical of EVs. The chimeric entity will be encoded and expressed by engineered cells and, thanks to the presence of the EVs-related portion, it will be included in the EVs during their biogenesis (Dang et al., 2020).

Conversely, the post-isolation techniques include the direct modification of EVs membrane exploiting either chemical and physical interactions. Indeed, the EVs surface is characterized by the presence of reactive groups, mainly amine groups, which are able to react with the functionalizing molecules or opportune chemical linkers and form stable covalent bonds. The chemical functionalization of EVs follows essentially the click chemistry approach and comprises efficient one or two-steps reactions, like azide-alkyne cycloaddition, thiol-maleimide reaction, EDC-NHS reaction or amidation (Rayamajhi & Aryal, 2020). As reported in literature, one of the major advantages of this approach resides in the precise control of the amount of linked moieties, avoiding the overmodification of vesicles membranes which would lead to the loss of EVs properties and functionalities (Smyth et al., 2014). Although, reaction conditions and reagents must be thoughtfully regulated in order to avoid inappropriate osmolarity, temperature or pressure which would lead to EVs disruption or aggregation (Antimisiaris et al., 2018). The post-isolation physical modifications of EVs, instead, involve the formation of non-covalent bonds under milder reaction conditions. These strategies are based on electrostatic interactions, receptor-ligand binding and on the post-insertion of lipophilic or lipid-conjugated compounds into the EVs membrane through hydrophobic interactions (Armstrong et al., 2017), For instance, a recent study compared the EVs functionalization with PEG moieties obtained through either chemical approach or physical insertion of lipids conjugated with PEG molecules. The characterization of the two preparations highlighted that the physical incorporation *via* lipid post-insertion allowed a facile and effective surface modification, while the direct covalent conjugation of PEG with primary amine of EVs proteins resulted in vesicles aggregation (Choi et al., 2019).

Finally, the engineering of native EVs functional groups was also considered as valuable tool to improve their distribution and targeting capability. For instance, carbohydrate structures linked to lipids and proteins as glycans or as repeating glycosaminoglycan chains in proteoglycans possess roles in EVs cellular recognition and uptake and, thus, their modification was recently explored (Williams et al., 2018).

5.1.2.2 Functionalization for extended circulation half-life

Concerning the improvement of *in vivo* half-life and biodistribution of exogenously administered EVs, several functionalizing moieties are adopted (**Figure 5.1**). With respect to synthetic vesicles, EVs derived from certain cellular source are naturally equipped with CD47, an endogenous transmembrane protein which could interact with particular regulatory protein on macrophages membrane (i.e. signal regulatory protein α, SIRPα) guaranteeing phagocytosis evasion and protecting EVs from clearance (Yoosoo Yang et al., 2018). However, the EVs pharmacokinetic profile is still not completely favorable and could benefit from the modification with apposite functionalizing moieties. As already mentioned, PEG polymer is commonly employed to prevent opsonization and increases the systemic circulation of synthetic liposomes and nanoparticles. The PEG functionalization was efficiently applied also to natural EVs, reducing their recognition by mononuclear phagocytic systems and extending their circulation kinetics from 10 minutes to 60 or even 240 minutes after intravenous injection (S. A.A. Kooijmans et al., 2016). To date, PEG functionalization of EVs was obtained through different modification methods like direct covalent bonding or physical post-insertion of PEG-conjugated lipids (Choi et al., 2019).

Furthermore, EVs stabilization *in vivo* could be obtained through the direct manipulation of components of vesicles membrane. The modification of specific glycans and, in particular, the enzymatic removal of sialic acid from EVs surfaces resulted in a great improvement of their circulation time after intravenous administration (Royo et al., 2019).

5.1.2.3 Functionalization with targeting ligands

Even though EVs harbor intrinsic homing properties and a preferential accumulation within specific organ and tissues, this natural targeting ability is often not sufficient to achieve an adequate targeted delivery for therapeutic purposes. In this perspective, the modification of EVs surface with specific targeting ligands is widely explored. In particular, concerning the application of EVs in the treatment of cancer disease, three main modification approaches were applied conferring targeting capabilities by the introduction of appropriate targeting entities directed against *(i)* antigens or *(ii)* receptors present on the surface of target cells or against *(iii)* specific molecules present in the tumor microenvironment (Meng et al., 2020). As represented in **Figure 5.1**, the utilized moieties comprehend several types of ligands including single domain antibodies, monoclonal antibodies, peptides and various types of proteins and glycans which can mediate the binding and subsequent receptor mediated endocytosis (Dang et al., 2020).

The surface modification of EVs for targeting purposes could be obtained by the indirect engineering of parent cells or by the direct modification of isolated EVs through either chemical or physical methods. For instance, click chemistry reactions were exploited to conjugate different targeting peptides to alkine- (Smyth et al., 2014) or azide-functionalized (Lee et al., 2016) EVs membranes. Moreover,

a physical approach involving the adsorption of cationic lipids and the development of electrostatic interactions was used to attach a negatively charged fusogenic peptide to EVs (Nakase et al., 2011). Furthermore, a very common approach envisaged the use of PEG chains as cross-linkers. In this approach, EVs membranes are primarily functionalized with PEG and then the second distal end of polymer chain is conjugated to appropriate targeting ligands, originating promising functionalized EVs with stealth properties and targeting abilities (S. A.A. Kooijmans et al., 2016).

Particularly interesting for this PhD thesis purposes is the EVs functionalization with antibodies. Several literature studies reported the EVs functionalization with targeting antibodies through parent cell engineering. The obtained targeted EVs guarantee an efficient delivery to specific cancer cells (J. H. Wang et al., 2018) and an improved cell association even under flow conditions (Sander A.A. Kooijmans, Aleza, et al., 2016). Moreover, multivalent targeted EVs caused antitumor immunity, inducing the crosslinking between T cells and cancer cells (Q. Cheng et al., 2018). An efficiently prolonged circulation time and targeting specificity was obtained also through the physical post-insertion of a lipid conjugated with PEG and a targeting nanobody (S. A.A. Kooijmans et al., 2016).

To address some of the discussed issues, the TrojaNanoHorses (TNHs) construction procedure was revised in order to impart more suitable features for an eventual future therapeutic application. Primarily, to overcome the safety concerns related to the application of EVs derived from cancer cells, the EVs cell source was changed. In particular, the target of the experiments described in this chapter were lymphomas cells (Daudi cell line) and the EVs were extracted from B lymphocytes, their normal counterpart. Moreover, to optimize the EVs loading efficiency, two new coupling procedures were tested. These relied on the application of a different number of freeze-thaw cycles as active stimulus to destabilize EVs membranes. The obtained TNHs were characterized in terms of encapsulation efficiency, colloidal stability and morphology. Finally, to improve the TNHs selectivity, a functionalization method to decorate the EVs surface with anti-CD20 antibodies was designed and preliminarily validated.

5.2 Materials and methods

5.2.1 ZnO NCs synthesis and characterization

The ZnO NCs were synthesized through microwave-assisted method and functionalized with amino-propyl groups (Garino et al., 2019) and fully characterized as already described in previous chapters. For experiments involving fluorescence optical signals, the nanocrystals were labeled by conjugation with Atto647-NHS Ester (AttoTec) or Atto550-NHS Ester (Attotec) dye as already described.

5.2.2 EVs extraction and characterization

5.2.2.1 EVs production and extraction

The EVs used in this study were extracted from conditioned media of B lymphocyte cells (IST-EBV-TW6B, purchased from cell bank IRCCS AOU San Martino IST).

For the EVs extraction, cells were cultured in advanced Roswell Park Memorial Institute (RPMI 1640, Gibco), supplemented with 20% depleted fetal bovine serum (FBS, Gibco), 1% of L-Glutammine 200 mM (Lonza), penicillin (100 units/ml) and streptomycin (100 µg/ml) for 72 hours.

Cells culture medium was collected for EVs isolation, performed according to a sterile ultracentrifugation protocol, optimized from Thery et al. (Théry et al., 2006) as already described in Chapter 4. Before each isolation, the cell viability was assessed and only samples with viability >90% were processed in order to reduce the possibility of apoptotic bodies recovery.

For the characterizations involving fluorescence, the EVs were labelled using Wheat Germ Agglutinin (WGA) conjugated with Alexa Fluor 488 dye (λ_{Ex}= 495 nm, Thermo Fisher) or Alexa Fluor 647 (λ_{Ex}= 650 nm, Thermo Fisher). Briefly, stored EVs were thawed out and diluted 1:2 with physiologic solution and then labeled by adding 1 µl of WGA (100 µg/ml in PBS) for each EVs aliquot. The solution was kept under agitation (180 rpm) in dark at 37 °C for 30 minutes and then purified from unbound dye molecules by ultrafiltration with centrifugal filter (Amicon Ultra 0.5 with molecular weight cut off of 50 kDa, Merck).

5.2.2.2 EVs characterization

Transmission Electron Microscopy

EVs morphology were analyzed trough Transmission Electron Microscopy (TEM) using a Jeol JEM 1011 electron microscope operating with an acceleration voltage of 100 kV and equipped with a 2 Mp charge-coupled device (CCD) camera (Gatan Orius SC100). The sample of EVs diluted in physiological solution were sonicated for few minutes and then a drop was deposited on a copper grid 150 mesh, previously coated with an amorphous carbon film and plasma treated to remove

hydrocarbon residues. The EVs sample was then stained, treating the sample grid with a 1% uranyl acetate solution in water for 30 seconds before the specimen dried.

Nanoparticle Tracking Analysis (NTA)

The concentration and the size distribution of the EVs was measured by nanoparticle tracking analysis (NTA) technique with a NanoSight NS300 (Malvern Panalytical) equipped with λ=505 nm laser beam and a NanoSight syringe pump. All the samples were diluted in a final volume of 500 µl of 0.1 µm-filtered physiologic solution to meet the ideal particles per frame value (20-100 particles/frame) and measured by capturing three videos of 60 seconds with an infusion rate of 50 and a camera level value between 14 and 16. The collected videos were then analyzed by the NTA 3.4 software (Malvern Panalytical), setting the detection threshold at 5.

Bradford Assay

The protein content of EVs extracted from B-lymphocytes was measured by Bradford assay. The Bradford assay is a colorimetric assay, based on the use of Comassie Brilliant Blue, a dye which after the binding with proteins changes its color from red (maximum absorbance, A_{max}=470 nm) to blue (A_{max}=590 nm).

Briefly, Bradford reagent (Bio-Rad) was diluted 1:5 in bd water and added to EVs samples (diluted 1:2 in 0.1 µm-filtered PBS) and to serially diluted bovine serum albumin (BSA) standards, with known concentration. The absorbance at 590 nm was detected with the Multiskan GO microplate spectrophotometer (Thermo Fisher Scientific) and the protein concentration of EVs samples was extrapolated comparing their absorbance values with the calibration curve made on BSA standards. All samples were analyzed in triplicate.

Analysis of EVs surface markers

The analysis of membrane protein expression was performed through flow cytometry. In details, 5 µg of pristine EVs measured by Bradford assay, were adsorbed on 10 µl of aldehyde/sulphate latex beads (4% w/v, 3 µm, Thermo Fisher). EVs and beads were incubated for 15 minutes at RT, then PBS was added to reach the final volume of 1 ml and the incubation was continued on a test tube rotator for 2 hours at room temperature. To saturate the remaining binding sites on latex beads, 110 µl of glycine (1 M in PBS) were added to each samples and let stand at RT for 30 minutes. The samples were then washed three times by centrifugation (4,000rpm for 3 minutes) and redispersed in 500 µl of PBS with 0.5% (w/v) BSA. EVs immobilized on latex beads were therefore incubated with CD63-PE or CD81-APC antibodies and with the respective non-specific isotype antibody (Biolegends) for 30 minutes at 4°C. After two washing steps, the samples were analyzed with Guava Easycyte 6-2L (Merck Millipore). For each sample were recorded 5,000 events positioned in a gate designed on unstained beads+EVs to discard debris and buffer impurities. PE signal was excited with blue laser (488 nm) and the emission was detected through band pass filter Yellow-B (583/26 nm). APC signal was excited

with red laser (633 nm) and detected with band pass filter Red-R (661/15 nm). Results were analyzed with Guava Incyte software (Merck Millipore) and expressed in percentages of positive events calculated with respect to a threshold set upon isotype control.

5.2.3 TNHs construction and characterization

5.2.3.1 TNHs construction by freeze-thaw method

For the TNHs construction, 10 μg of labelled amino-functionalized ZnO NCs were combined with an amount of EVs corresponding to 5 μg of protein measured by Bradford assay. The encapsulation process was performed in a solution 1:1 (v/v) of 0.1 μm-filtered bd water and physiologic solution, with a final concentration of 75 μg/ml for ZnO NCs and 37.5 μg/ml for EVs.

Two different procedures, both based on repeated freeze-thaw cycles, were used. In Method 1 (samples named TNH-$1_{1:2}$), the EVs, opportunely labeled and dispersed in the proper amount of physiologic solution were added to the same amount of water containing half aliquot of ZnO NCs. The mixture was then rapidly frozen in liquid nitrogen for 3 minutes and thawed at RT for 15 minutes. The freeze-thaw cycle was repeated 5 times, then the second half of ZnO NCs were added and a second set of 5 cycles were performed. Finally, the TNH samples were incubated under agitation (180 rpm) at 37 °C for 1 hours.

In Methods 2 (samples named TNH-$2_{1:2}$), EVs alone dispersed in physiologic solution were subjected at 2 freeze-thaw cycles and then mixed with bd water containing the corresponding whole amount of ZnO NCs. The obtained mixture was then incubated under agitation (250 rpm) at 45 °C for 10 minutes and then at 37 °C for 2 hours. A further overnight incubation at RT was also performed.

Another set of experiments were performed combining only 5 μg of amino-functionalized ZnO NCs with an amount of EVs corresponding to 5 μg of protein. The TNHs construction was performed at ZnO and EVs concentration equal to 37.5 μg/ml following the Method 2 procedure (samples named TNH-$2_{1:1}$).

In order to redisperse the obtained TNHs in cell culture media for biological tests, a final step of centrifugation was added. The samples of TNH-2 were centrifuged at 5,000 g for 5 minutes, suspended in the desired media and redispersed by vortexing for 3 minutes.

5.2.3.2 TNHs characterization

Fluorescence Microscopy

The coupling efficiency was evaluated through fluorescence microscopy using a wide-field fluorescence-inverted microscope (Eclipse Ti-E, Nikon) with a 100× immersion oil objective (Nikon). The samples were imaged and analyzed with colocalization tool of NIS-Element software (NIS-Element AR 4.5, Nikon) as described in Chapter 4.

Electron Microscopy

The morphology of TNHs was studied by TEM analyses, operating at the same condition described for pristine EVs. In this case the samples were observed both with and without staining to appreciate the presence of ZnO NCs, more clearly visible in absence of the contrasting agent.

Energy Dispersive X-ray Spectroscopy was also performed on the same samples to analyze the elemental composition of obtained nanoconctructs. A JEM-1400 Plus with thermionic source (LaB6) was used operating at 120 kV.

Nanoparticle Tracking Analysis (NTA)

The size distribution of TNHs was measured by NTA measurements. The samples were diluted 1:5 in bd water and physiologic solution 1:1 (v/v) and the camera level and detection threshold during acquisition and analysis were set at 16 and 5 respectively.

CD20 surface expression

In order to prosecute the engineering of the TNHs with the insertion of targeting ligand, the surface expression of CD20 was analyzed through flow cytometry. The test was performed on both EVs and TNHs samples following the protocol already described for the surface EVs markers with some variation. The incubation on the tube rotator was performed overnight at 4°C. In this case CD20-PE antibody and the respective not specific isotype control were used (Miltenyi), exciting the fluorophore with blue laser (488 nm) and detecting the emission signal through band pass filter Yellow-B (583/26 nm).

5.2.4 Functionalization of EVs surface with targeting ligands

5.2.4.1 Functionalization of EVs surface with Rituximab

The surface of pristine EVs was functionalized with a recombinant monoclonal chimeric antibody directed against CD20 antigen (Rituximab). To optimize the functionalization protocol, pristine EVs were used. In details, 5 µg of EVs, measured by Bradford assay, were labelled with Wheat Germ Agglutinin (WGA) conjugated with Alexa Fluor 488 (λ_{Ex}= 650 nm, Thermo Fisher) as previously described. After ultrafiltration with centrifugal filter (Amicon Ultra 0.5 ml 50 kDa, Merck), the samples were resuspended in approximately 100 µl of 0.1 µm-filtered PBS and incubated with 40 µl of Rituximab (1 mg/ml in PBS, Creative Biolabs, Cat. n° TAB-016) for 1 hour at RT on a test tubes rotator. Then, 20 µl of secondary antibody (1.5 mg/ml in bd water, $F(ab')_2$ fragment Goat Anti-Human IgG, Immuno Jackson. Cod N°109-156-008) conjugated with Coumarin (λ_{Ex}=350 nm), were added and second incubation step (1 hour at RT) was performed. Finally, a second aliquot of Rituximab (40 µl) was added and a third 1 hour incubation at RT was performed.

A sample which has followed all the described steps without the addition of Rituximab was also prepared as control in order to exclude the aspecific adsorption of secondary antibody.

5.2.4.2 Characterization

Fluorescence Microscopy

The success of antibodies conjugation was evaluated through fluorescence microscopy using a wide-field fluorescence-inverted microscope (Eclipse Ti-E, Nikon) with a 100× immersion oil objective (NIkon). Fluorescence images of green and blue channels, corresponding to fluorescence of WGA-Alexa Fluor 488 (λ_{Ex}=495 nm) and Coumarin conjugated secondary antibodies (λ_{Ex}=350 nm) respectively, were acquired and then superimposed to evaluate colocalization.

Nanoparticle Tracking Analysis (NTA)

The size distribution of functionalized EVs was measured by NTA technique, analyzing the EVs^{CD20} and the relative control after each incubation step with Rituximab or secondary antibody. The samples were diluted 1:13 in PBS and the camera level and detection threshold during acquisition and analysis were set at 15 and 5 respectively.

5.3 Results and discussion

5.3.1 TNHs components: ZnO NCs and EVs extracted from B lymphocytes

The ZnO NCs used for the TNH construction were synthesized through microwave-assisted method and functionalized with amino-propyl groups as reported in previous chapters, obtaining round-shaped particles of about 20 nm with wurtzite crystalline structure and a positive surface charge as already described in details.

The nanoconstruct studied in this phase was intended for the treatment of Daudi cancerous cells and EVs isolated from B lymphocytes were used, in order to address safety issues related to the cell of origin. Actually, recent literature studies evidenced that tumour-derived EVs carry signalling messenger and biological substances secreted from parent cells that could be involved in the development, progression and metastasis of cancer (Sun et al., 2018). Tumour-derived EVs, in fact, possess specific glycoproteins that are probably responsible for the modulation of the microenvironment facilitating the growth of metastatic cancer cells (Hoshino et al., 2015). Thus, EVs derived from healthy cells are considered a better option for the construction of safe and effective drug delivery systems.

The EVs were extracted from B lymphocytes supernatants applying the already described differential ultracentrifugation protocol and fully characterized. The size distribution and the concentration expressed in particles/ml were measured through NTA technique, analysing the samples obtained from different extractions. An example of the derived size distribution is shown in **Figure 5.3a**, displaying a single and narrow peak, centred at ~120 nm. The average particles concentration, obtained considering 20 different extractions, was equal to $1 \cdot 10^{11} \pm 1 \cdot 10^{10}$ particles/ml.

The average EVs protein concentration was also evaluated through Bradford assay. The test was performed on the extracted vesicles without any lysis pre-treatment considering the same samples analysed with NTA technique and obtaining an average concentration equal to 160 ± 11 μg/ml.

The morphology of EVs was analysed by Transmission Electron Microscopy (TEM), contrasting the sample with uranyl acetate. Representative image are reported in **Figure 5.3b** and **c**, showing a mixed population of round-shaped structures with size distribution in good accordance with NTA measurements. The smallest entities were identified as proteins and lipoproteins derived from the FBS added to the cell culture media during the EVs production, which could co-precipitate during the extraction procedure (Bachurski et al., 2019). The presence of larger vesicles with dimensions of ~100 nm or slightly larger and the typical cup-shaped morphology of stained EVs (Jung & Mun, 2018) was also clearly accounted.

The composition of the sample was analysed through EDS analysis, performed on the area reported in **Figure 5.2c**. The elemental maps (**Figure 5.2d**) showed the presence of carbon, oxygen, nitrogen and phosphorous, typical elements of lipidic

vesicles membrane, together with a consistent amount of sodium ascribable to the physiologic solution used as dispersant medium.

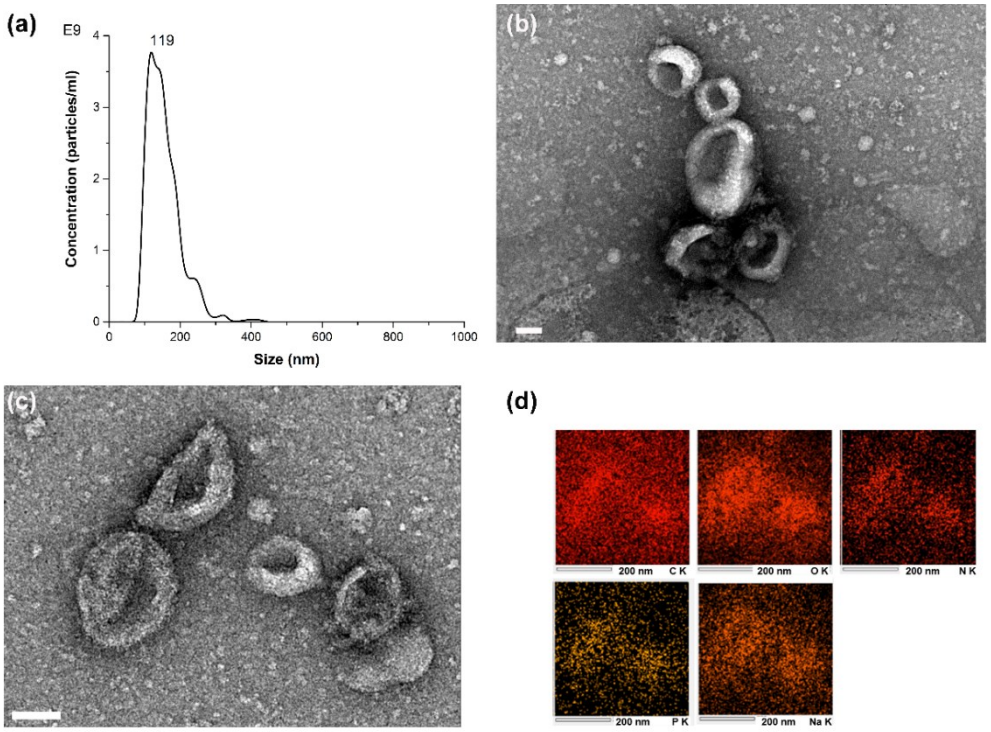

Figure 5.2: Characterization of EVs extracted from B lymphocytes through differential ultracentrifugation. **(a)** NTA measurements of EVs dispersed in physiologic solution; **(b)** and **(c)** TEM image of EVs negatively stained with uranyl acetate (scale bar 50 nm); **(d)** EDS elemental maps of the area and the reported in **(b)**.

Finally, the immunephenotypic characterization of the extracted EVs were studied through flow-cytometry, analysing the expression of typical membrane proteins, i.e. CD63 and CD81. These two tetraspanins belong to the first category of markers that must be tested in any preparation to demonstrate the presence of EVs according to MISEV2018 guidelines (Théry et al., 2018).

Representative graphs of the obtained results are reported in **Figure 5.3a** and **b**, showing the expression of CD63 and CD81 respectively. Both red curves, corresponding to the signals related to the EVs conjugated with anti-CD63 or anti-CD81 labelled antibodies, showed a shift toward higher fluorescence with respect to the isotype control (blue curves) and untreated control (black curves), indicating the expression of both antigens. In particular, a more marked shift was observed for CD81, indicating its major expression. Actually, this behaviour was in good accordance with literature results which indicate that CD63 tetraspanin marker is less abundant on B-cells derived exosomes (Andreu & Yáñez-Mó, 2014).

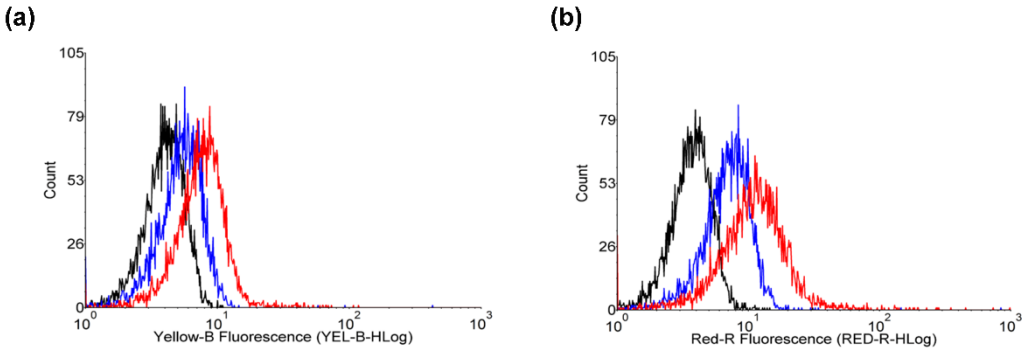

Figure 5.3: Characterization of EVs extracted from B lymphocytes through differential ultracentrifugation. Expression of **(a)** CD63 and **(b)** CD81 evaluated by flow-cytometry (black curves: untreated control; blue curves: isotype control; red curves: EVs with anti-CD63-PE or anti-CD81-APC).

5.3.2 TNHs construction and characterization

5.3.2.1 Definition of EVs:ZnO NCs ratio

The ratio between the ZnO NCs and EVs used for the TNHs construction was defined on the basis of theoretical calculations. In particular, the number of nanocrystals which could be geometrically encapsulated within a single vesicle was calculated considering the EVs and ZnO NCs as hard spheres with diameter of 100 nm and 20 nm, respectively. A packing density of ~74% was considered, assuming the maximum possible density corresponding to cubic close packing arrangement (Conway & Sloane, 1999). With these hypotheses, it was calculated an amount of about 93 ZnO NCs per EVs. Since the size of synthesized ZnO NCs ranged between 15 and 20 nm as experimentally observed from TEM and FESEM analyses, it was approximately assumed that each EVs could contain up to 100 nanocrystals.

This number ratio was then transformed in a mass ratio. Briefly, the number of vesicles corresponding to a fixed amount of EVs protein was calculated making the ratio between the mean concentration in particles/ml and µg/ml, obtained from NTA and Bradford techniques respectively. Moreover, the number of ZnO NCs was transformed in µg considering the particles volume (i.e. the volume of a sphere with diameter equal to 20 nm) and the ZnO density (ρ_{ZnO}=5.606 g/cm^3). Considering for example 5 µg of EVs protein, the resulting theoretical amount of ZnO NCs was equal to ~7.3 µg.

In order to favor the probability of collision and thus the interaction between the two components, an excess of ZnO with respect to the theoretical amount was envisaged. More in details, 10 µg of ZnO NCs each 5 µg of EVs were used, defining an experimental ratio EVs:ZnO NCs equal to 1:2.

5.3.2.2 Coupling efficiency and colloidal stability

Preliminary experiments were conducted applying the optimized co-incubation protocol defined in Chapter 4 to EVs derived from B lymphocytes. However, the resulting coupling efficiencies were considerably lower with respect of those previously obtained with EVs derived from KB cells. In particular, the percentages of colocalized ZnO NCs evaluated by fluorescence microscopy ranged between 8% and 27%, showing a low degree of encapsulation and a high variability and, thus, making the obtained nanoconstruct not ideal for biological applications. The different results could be ascribed to a different rigidity of the lipid membrane. Literature studies, in fact, reported that EVs extracted from non-cancerous cells lines contained more cholesterol than tumour-derived vesicles (Pfrieger & Vitale, 2018) and in particular EVs extracted from human B-cells presented a large enrichment of sphingolipids and cholesterol in their membrane (Wubbolts et al., 2003). Indeed, cholesterol deeply influence the membrane fluidity, interfering with the movement of phospholipid fatty acid chains and reducing the permeability of biological membranes.

The obtained results and these observations encouraged the transition from passive co-incubation method to the application of an active method. The new methodology was based on the application of freeze-thaw cycles as active stimulus to induce the destabilization of EVs membrane and consequently promote the encapsulation of ZnO NCs. Literature studies reported the encapsulation of drug molecules like catalase (Haney et al., 2015) or doxorubicin (Goh et al., 2017) through the application of three freeze-thaw cycles while fusion between EVs membrane and synthetic liposomes was achieved performing up to ten cycles to guarantee an effective engineering of the EVs (Sato et al., 2016).

Considering these literature results, two distinct methods to encapsulate the ZnO NCs within EVs derived from B lymphocytes were developed. The first procedure (Method 1) involved the use of the higher reported number of freeze-thaw cycles (i.e. ten cycles), while the second procedure (Method 2) reduced the number of cycles at two and added a short incubation at high temperature (45°C), to ensure a higher fluidity of the already weakened EVs membranes. A detailed description of the two methods and the characterization in terms of coupling efficiency and colloidal stability of the obtained TNHs are reported below.

Freeze-thaw Method 1

The first tested procedure, schematized in **Figure 5.4** envisaged the application of 10 freeze-thaw cycles, performed by rapidly freezing in liquid nitrogen the solution containing the nanocrystals and the EVs for 3 minutes and then thawing it for 15 minutes at room temperature. As already observed for the TNHs produced with EVs derived from KB cells, the addition of the ZnO NCs in two steps was a valuable option, allowing the containment of NCs aggregation which could be promoted by concentration increments. Thus, half aliquot of NCs was added at the beginning of the procedure and the second half after 5 cycles. The coupling procedure was terminated performing an incubation of 1 hour at 37 °C, in order to

restore the EVs membrane. According to literature results, in fact, the application of physiologic temperature could guarantee a great recovery of the microviscosity of the vesicles membrane after the application of an active stimulus (Kim et al., 2016).

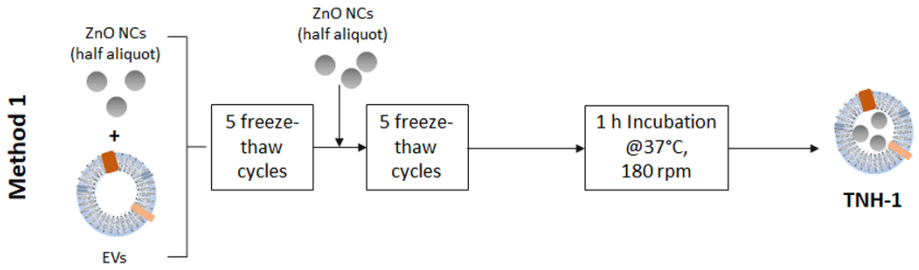

Figure 5.4: Scheme of the first coupling procedure (Method 1) combining ZnO NCs and EVs extracted from B lymphocytes for the TNHs construction

The efficiency of the coupling procedure was evaluated through fluorescence microscopy as widely explained in Chapter 4 and in the Materials and Methods section, analyzing several regions of interest (ROIs) of 5 different samples. The TNHs obtained with Method 1 (denominated TNH-$1_{1:2}$) presented an average coupling efficiency with respect to ZnO equal to 48% ± 14% (**Table 5.1**). This was an appreciable result considering the value initially obtained with passive co-incubation method and the encapsulation efficiencies reported in literature which normally do not exceed 20-30% (Kim et al., 2016, Haney et al., 2015).

As already performed in the previous chapter, the colloidal stability of the obtained TNHs was analyzed by NTA measurements (**Figure 5.5**). In particular, the hydrodynamic size distribution of TNHs dispersed in the coupling mixture of bd water and physiologic solution was measured and compared with those of the single components. For consistency, also pristine EVs and ZnO NCs were subjected to the whole coupling protocol.

Both the singular components and the TNHs showed a behavior similar to the one observed for TNHs obtained using EVs from KB cells (see **Figure 4.10**). The ZnO NCs (**Figure 5.5a**) presented a wide size distribution with multiple peaks centered also at high size values between 200 and 300 nm, confirming again the nanocrystals aggregation caused by the prolonged contact with physiologic solution. In addition, the formation of aggregates could be also justified considering the numerous freezing cycles which could negatively influence the materials stability in solution. For instance, the tendency of EVs to aggregate in consequence of freeze-thaw cycles is well documented in literature (Luan et al., 2017). However, the EVs subjected to the whole Method 1 procedure displayed a good size distribution (**Figure 5.5b**). This was quite similar to the one registered for unmodified EVs (see **Figure 5.2**) with a major peak at ~100 nm and other minor peaks at 142 nm and 212 nm, evidencing very low extents of aggregation. Also, TNHs sample resulted well-dispersed in the bd water and physiologic solution coupling mixture (**Figure 5.5c**), resembling the distribution of pristine EVs. This

result confirmed the success of coupling procedure and the effective nanocrystals stabilization provided by the EVs shielding.

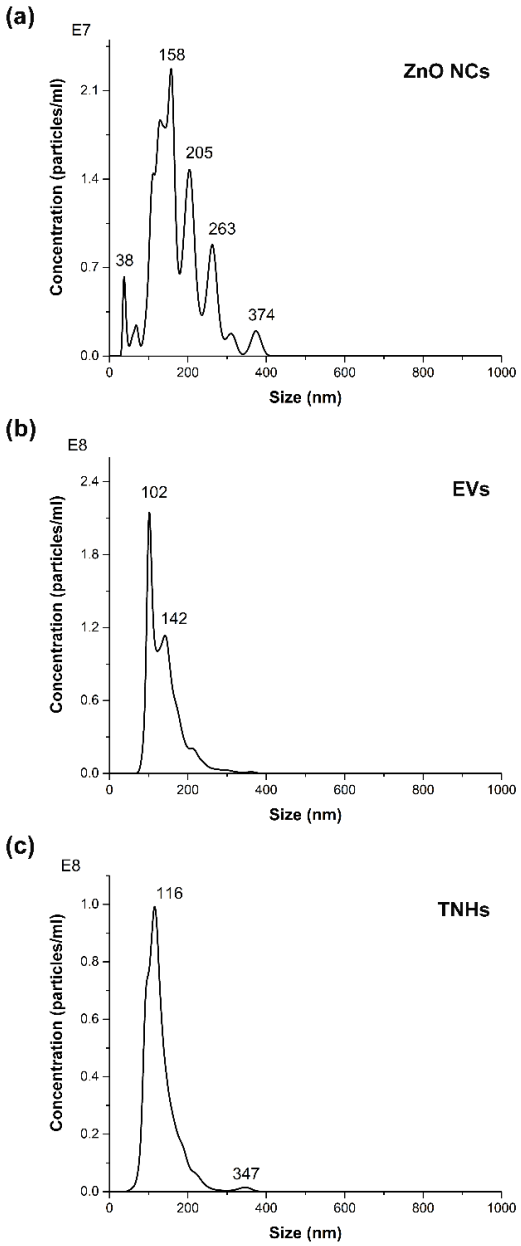

Figure 5.5: NTA measurements of **(a)** ZnO NCs **(b)** EVs and **(c)** TNH-$1_{1:2}$ dispersed in 1:1 v/v of bd water and physiologic solution.

Freeze-thaw Method 2

Literature data indicated that a high number of freeze-thaw cycles could affect EVs number and protein concentration as consequence of their degradation (Y. Cheng et al., 2019). In this perspective, in Method 2 the number of cycles were reduced at 2 prolonging instead the duration of co-incubation step, to ensure a high coupling efficiency combining active and passive loading methods.

In details, in the second coupling procedure, the number of freeze-thaw cycles was reduced to 2 and they were performed without the addition of ZnO NCs in

order to reduce also the mechanical stresses possibly induced by the presence of nanocrystals in the solution. The entire aliquot of NCs was added after the second cycle and the obtained mixture was subjected to a quick heating step (45°C for 10 minutes) to promote the higher fluidity of the already weakened EVs membranes. The process was completed with an incubation of 2 hours at 37°C and a further overnight (O/N) incubation at room temperature. The coupling efficiency was evaluated after both incubation steps and the samples were indicated as TNH-$2_{1:2}$ 2H and TNH-$2_{1:2}$ O/N respectively. Before the characterization a final centrifugation step was performed in view of biological tests that would require the redispersion of the samples in appropriate cell culture medium. The results, reported in **Table 5.1**, indicated the implementation of the O/N incubation as the best option with an average value of %co-ZnO = 49% ± 13%. A scheme of the defined Method 2 procedure is reported in **Figure 5.6**.

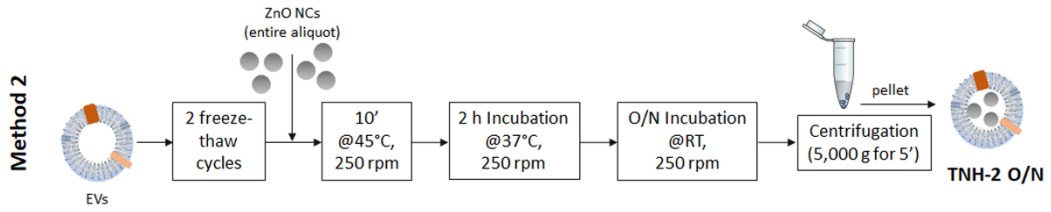

Figure 5.6: Scheme of the second coupling procedure (Method 2) combining ZnO NCs and EVs extracted from B lymphocytes for the TNHs construction.

A second set of experiments was performed reducing the amount of ZnO NCs to 5 µg every 5 µg of EVs, i.e. with an EVs:ZnO NCs ratio equal to 1:1 (TNH-$2_{1:1}$ O/N). The selected amount was lower than the calculated maximum theoretical value of 7.3 µg to evaluate the possibility of maximizing the coupling percentages working with a defect of NCs. Literature studies, in fact, evidenced an intrinsic limit in the EVs loading connected to the fact that the vesicles already contain proteins, nucleic acid and other biological materials which relatively restricts their loading capacities of exogenous cargos (Batrakova & Kim, 2015). In addition, the decrease of NCs concentration would allow to contain their aggregation in solution, contributing to an easier encapsulation by EVs. However, the obtained percentages (**Table 5.1**) indicated that the ZnO NCs diminution was not an effective solution to overcome the EVs loading limit. Conversely, the coupling efficiency were even lower with respect to the previous results, evidencing that the higher concentration of ZnO NCs was able to guarantee a major interaction and, thus, a better coupling.

Table 5.1: Percentages of ZnO NCs colocalized with EVs (%co-ZnO) obtained by Method 1 and the three described variants of Method 2. In particular, the number of incubation steps and the ratio between EVs and ZnO NCs were varied.

TNH-$1_{1:2}$	TNH-$2_{1:2}$-2H	TNH-$2_{1:2}$-O/N	TNH$2_{1:1}$-O/N
48% ± 14%	40% ± 11%	49% ± 13%	27% ± 14%

To complete the preliminary characterization, the colloidal stability of the best nanoconstruct among those obtained by Method 2 (i.e. TNH-$2_{1.2}$ O/N) was assessed through NTA measurements. Also in this case, uncoupled EVs and ZnO NCs subjected to the entire coupling protocol were tested and compared with TNHs, analyzed both before and after the centrifugation step.

Both single EVs and ZnO NCs showed results completely similar to those obtained for Method 1, confirming the aggregation of nanocrystals in contact with physiologic solution and the good distribution of EVs, centered at ~100 nm (data not shown). The TNH-$2_{1:2}$ O/N before the centrifugation step (**Figure 5.7a**) resulted well-dispersed, resembling the hydrodynamic distribution of pristine EVs with only minor peaks at larger diameters (i.e. 150 and 315 nm). The distribution of TNH-$2_{1:2}$ O/N after the centrifugation step (**Figure 5.7b**), instead, was slightly broader with a major peak centered at ~140 nm and a secondary peak at 250 nm, suggesting a partial aggregation due to the application of the centrifugal force. However, the size presented by centrifuged TNHs could still be suitable for biological applications and constitute a great improvement with respect to randomly-aggregated ZnO NCs confirming the stabilization effect provided by the EVs lipid shell.

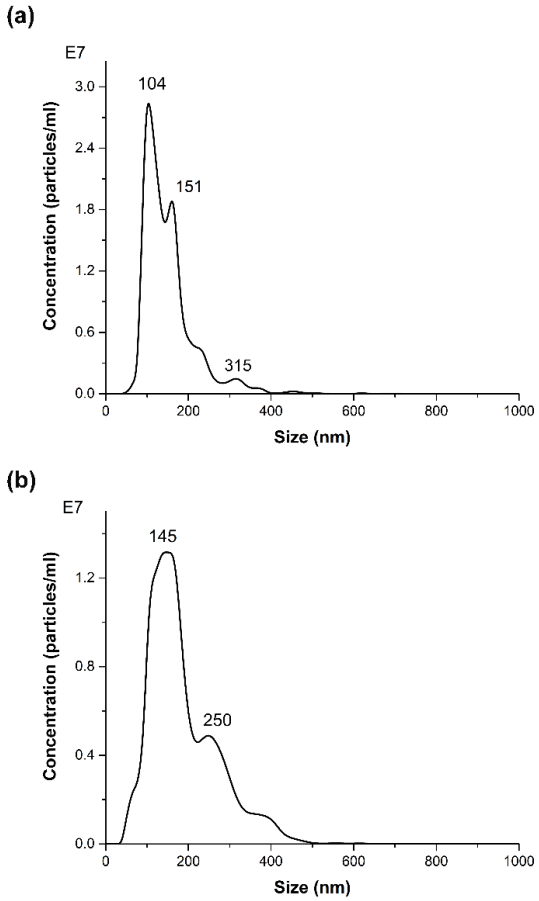

Figure 5.7: NTA measurement of TNH-$2_{1:2}$ O/N dispersed in 1:1 v/v of bd water and physiologic solution **(a)** before and **(b)** after the centrifugation step.

5.3.2.3 TNHs characterization: morphological and compositional analyses

To analyze in detail their morphology and elemental composition, the samples with the higher percentages (i.e. TNH-$1_{1:2}$ and TNH-$2_{1:2}$ O/N) were both characterized with Transmission Electron Microscopy (TEM) and Energy Dispersive Spectroscopy (EDS).

The results related to the TNHs obtained by Method 1 are reported in **Figure 5.8**. The sample was imaged both with and without negative staining to ensure a good visualization of both components of the nanoconstruct. As already mentioned, negative staining is considered the best method for EVs imaging, allowing to identify the typical cup-shaped structure ascribable to an artifact of the drying process (Jung & Mun, 2018). However, the presence of heavy metal could partially prejudice the visualization of ZnO NCs, that would not possess enough contrast whit respect to the uranyl acetate used as contrasting agent. For this reason, the sample was imaged also without staining, to show the presence of ZnO NCs and their position inside the vesicles.

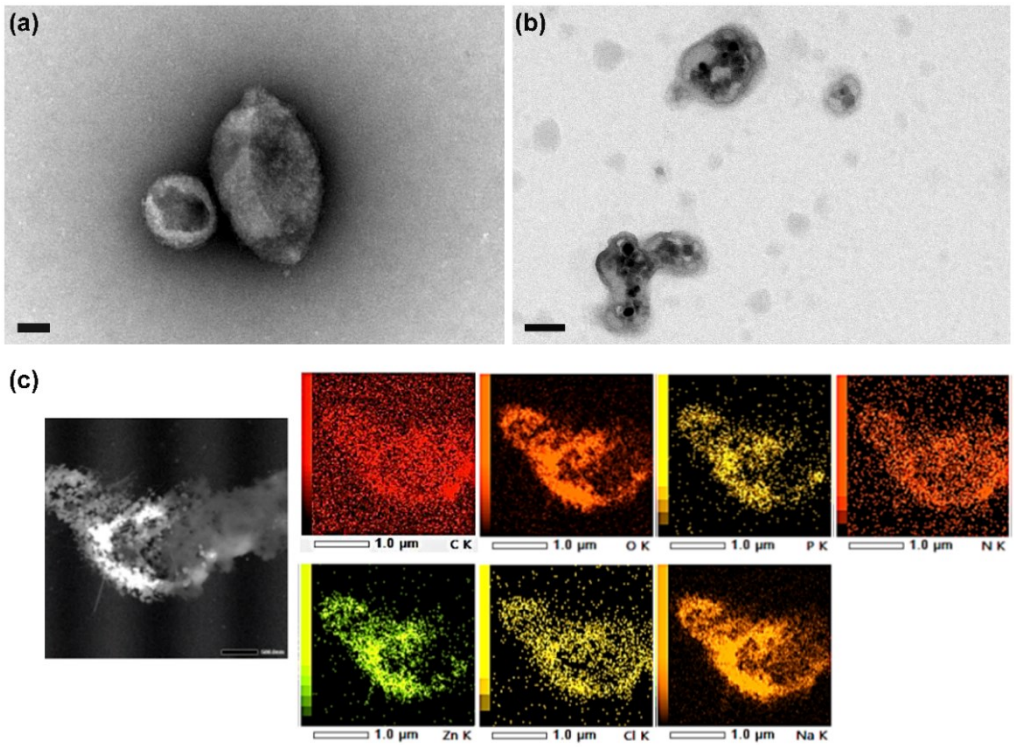

Figure 5.8: TEM images of TNH-$1_{1:2}$ **(a)** with and **(b)** without negative staining of uranyl acetate (scale bars 50 nm); **(c)** EDS analysis of unstained TNH-$1_{1:2}$, reporting the STEM image of the analyzed area and the related elemental maps.

The image with the negative staining (**Figure 5.8a**) showed that the vesicles adequately maintained their original morphology even after multiple freeze-thaw cycles. Conversely, the image without the staining (**Figure 5.8b**) clearly showed the presence of numerous ZnO NCs within a single round-shaped vesicle or small aggregates, confirming their effective encapsulation. The success of the coupling was also confirmed by EDS analyses, performed on the unstained sample, that displayed the presence of Zn element together with C, O, P and N elements typical

of EVs phospholipidic membrane. Furthermore, Na and Cl elements, ascribable to contamination of physiologic solution, were detected. The STEM image of the analyzed area together with the obtained EDS maps are reported in **Figure 5.8c**. As clearly shown in the picture, the analysis was performed on a small aggregate of vesicles, partially disrupted as a consequence of measurement conditions and absence of any fixation or contrast. However, this partial degradation allowed the leakage of EVs content and the clear detection of Zn signal. From elemental maps, Zn resulted near or included in the region delimited by C, O, P and N elements which are part of vesicle membranes, suggesting a successful encapsulation of ZnO NCs within the EVs.

Concerning the TNHs obtained by Method 2 (TNH-$2_{1:2}$ O/N), only images of the stained sample were reported (**Figure 5.9a** and **b**). Actually, an attempt of analysis without the negative staining was also performed, but without appreciable results. The sample, in fact, contained spherical salts aggregates with dimensions similar to those of the vesicles, probably formed during the prolonged incubation steps. Thus, the formation of typical cup-shaped structure provided by the negative staining with uranyl acetate allowed the certain recognition of the EVs, guaranteeing an accurate analysis of the sample. The reported images clearly show that EVs subjected to Method 2 procedure maintained their original morphology. The presence of ZnO NCs was confirmed through EDS analysis performed on the area reported on the related STEM image (**Figure 5.9c**). The object presented the characteristic concave shape and the signals of O, C and P elements, typical components of vesicles membranes. Zn signal was also detected, confirming the presence of the NCs and suggesting their effective encapsulation within the EVs.

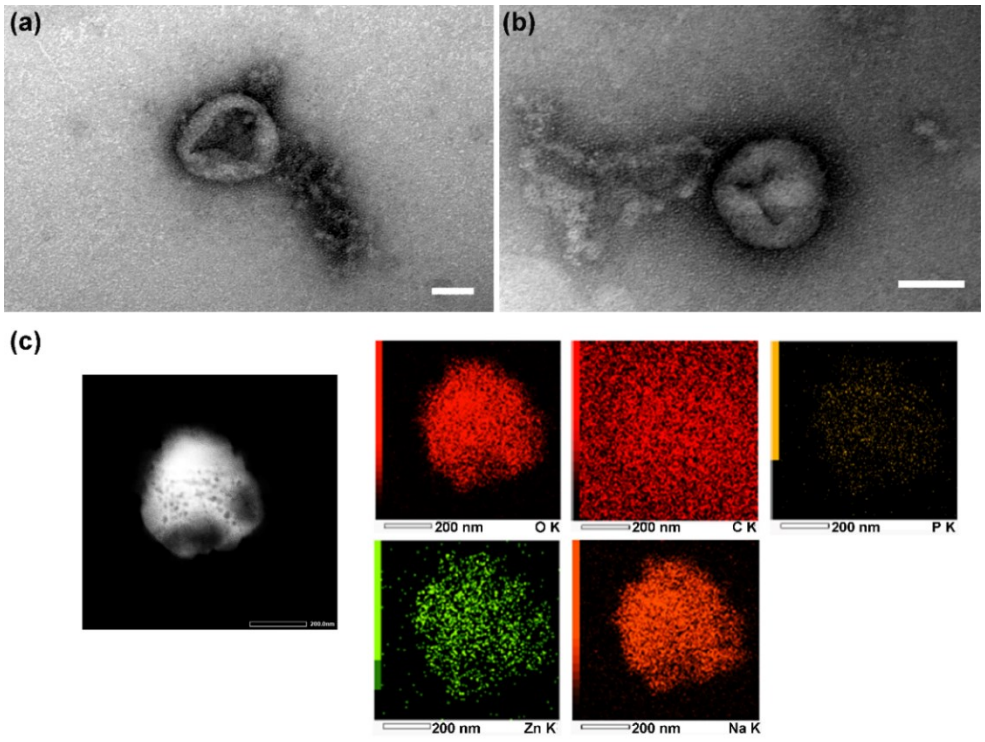

Figure 5.9: (a) and **(b)** TEM images of TNH-$2_{1:2}$ O/N with negative staining of uranyl acetate (scale bars 50 nm); **(c)** EDS analysis of TNH-$1_{1:2}$, reporting the STEM image of the analyzed area and the related elemental maps.

Overall, TEM analyses further confirmed the efficiency of the two implemented loading methods. Indeed, the presence of Zn element, absent in pristine EVs (see **Figure 5.2**), was accounted in the EDS maps of both samples suggesting that both Method 1 and 2 guaranteed an efficient encapsulation of the ZnO NCs. In addition, the EV original morphology was adequately preserved by both methods, even though the presence of small aggregates was detected in TNH-$1_{1:2}$ sample. Conversely, TNH-$2_{1:2}$ O/N sample contained single vesicles with a better preserved spherical morphology, as expected considering the minor invasiveness of the procedure which apply only two freeze-thaw cycles. Moreover, in a perspective of further functionalization or applications, the TNH-$2_{1:2}$ O/N could be selected as the best option since its good coupling efficiency and colloidal stability are accompanied by a convenience in terms of operating times, which would allow a greater flexibility for subsequent manipulations.

5.3.3 Functionalization with targeting ligands

The surface of EVs was functionalized with Rituximab, a recombinant monoclonal chimeric antibody directed against CD20 antigen. Rituximab is a genetically engineered IgG1-κ immunoglobulin composed by murine variable binding regions and human constant regions and it was the first monoclonal antibody approved by FDA for therapeutic use in 1997. Originally, it was approved for the treatment of B-cell non-Hodgkin's lymphoma, but its use is now extended for the treatment of various pathological conditions. The therapeutic action of Rituximab involves different mechanisms, inducing the apoptosis of targeted cells either directly or through the recruitment of immune effector functions mediated by the human Fc portion of the antibody (Maloney, 2012). However, for the purposes of this PhD thesis, Rituximab was mainly selected for its specificity toward CD20 antigen and constitute the targeting moiety of the TNH hybrid nanoconstruct. Indeed, CD20 antigen is a general marker for B cells on various developmental stages and it is expressed also by the majority of B-cell lymphomas with a variable intensity of expression, depending on the types and differentiation of neoplastic cells (Prevodnik et al., 2011). In particular, several studies reported the CD20 expression by Daudi cells (Dorvignit et al., 2012; Singh et al., 2014), which are the therapeutic object of the nanoconstruct developed in this PhD thesis.

The proposed functionalization technique is fully based on antigen-antibody interactions, as schematically represented in **Figure 5.10**, and relies on the expression of CD20 antigen also on the lymphocytes-derived EVs. As already mentioned, in fact, the produced vesicles reflect the protein expression of their parent cells and, thus, EVs extracted from B lymphocytes should contain CD20 transmembrane protein. Briefly, a Rituximab primary antibody was anchored to CD20 antigens present on EVs surface. Then, a secondary antibody directed against the Fc human constant region was added and employed as cross-linker to connect a second Rituximab antibody, this time directed against the CD20 antigens present on Daudi cells surface. To limit the steric hindrance and the overall dimensions of the created functionalizing assembly, a secondary antibody constituted only by

F(ab')$_2$ fragment (i.e. the two antigen binding portions linked by disulphide bonds) was chosen. Furthermore, the use of a F(ab')$_2$ fragment with respect to a whole secondary antibody would also reduce the potential immunogenicity avoiding the Fc mediated immune activation (Bates & Power, 2019).

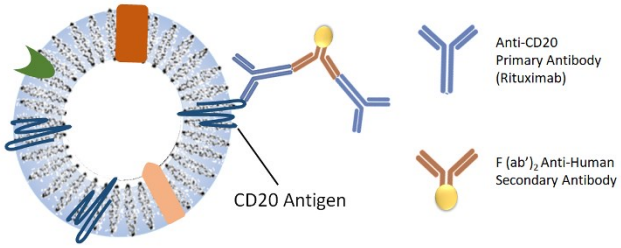

Figure 5.10: Schematic representation of the strategy of functionalization of EVs derived from B lymphocytes, using Rituximab primary antibody as targeting agent and a F(ab')$_2$ fragment of a secondary antibody direct against the Fc human region as cross-linker.

5.3.3.1 EVs^{CD20} and TNHs^{CD20} characterization

Firstly, to investigate the feasibility of the proposed functionalization strategy, the surface expression of CD20 antigen was verified through flow-cytometry. In particular, pristine EVs derived by B lymphocytes and TNHs nanocontructs obtained by either Method 1 and 2 were analysed. Representative results are reported in **Figure 5.11a**, **b** and **c** respectively. All three red curves, corresponding to the signals of samples treated with anti-CD20 labelled antibody, showed a shift toward higher fluorescence with respect to the isotype control (blue curves) and untreated control (black curves), confirming the presence of CD20 antigen in all the tested samples. Furthermore, the percentages of positive events calculated setting a threshold upon the isotype control were compared, in order to evaluate eventual differences in the intensity of surface expression. In particular, the experiments were performed in triplicate and the obtained mean ± SEM (reported in the caption of **Figure 5.11**) were confronted, evidencing no significant differences.

Overall these results, confirmed the presence of CD20 transmembrane protein on EVs derived from B lymphocytes and highlighted that both the implemented loading method efficiently preserved the surface expression of CD20 protein.

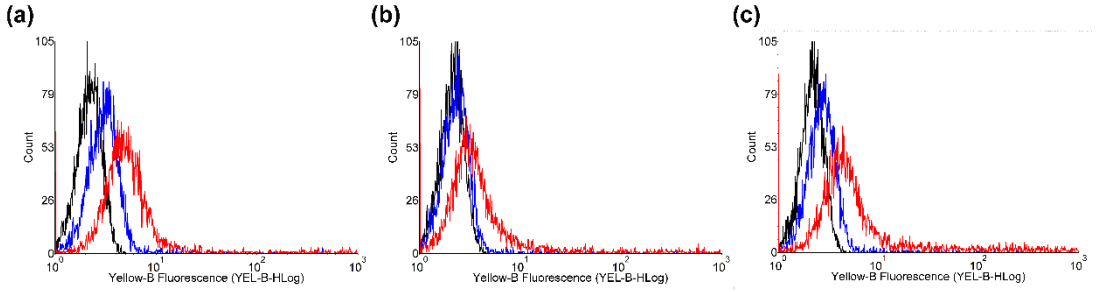

Figure 5.11: Representative flow-cytometry evaluation of the expression of CD20 protein on the surface of **(a)** pristine EVs, **(b)** TNH-1$_{1:2}$ and **(c)** TNH-2$_{1:2}$O/N (black curves: untreated control; blue curves: isotype control; red curves: sample with anti-CD20-PE antibodies). Percentages of positive events with respect to isotype control were calculated in triplicate and expressed as mean ± SEM: EVs = 16 ± 8 %: TNH-1$_{1:2}$ = 18 ± 5 %; TNH-2$_{1:2}$O/N = 24 ± 3 %.

Given the similarity of CD20 surface expression between EVs and TNHs nanoconstructs, the functionalization procedure with targeting antibodies was firstly optimized and verified only on pristine EVs (sample named EVs^{CD20}). In particular, the optimization of functionalizing procedure concerned the definition of the most suitable amount of antibodies, added in three consecutive incubation steps performed at room temperature for 1 hour. A rough estimate of the CD20 amount present on the surface of extracted EVs was made considering half of the protein content measured by Bradford assay equal to CD20 transmembrane proteins. Then, it was found that the addition of a large excess of Rituximab (i.e. 4:1 molar ratio with respect to the assumed antigen concentration) was the most suitable option, guaranteeing an adequate antigen-antibody interaction. The cross-linker secondary antibody $F(ab')_2$ fragment was subsequently added in a molar ratio 1:1 with respect to the Rituximab and finally a second aliquot of Rituximab was added in the same amount as the first.

The success of the functionalization was preliminary evaluated through fluorescence microscopy and NTA measurements.

For fluorescence microscopy experiments (**Figure 5.12**), the EVs membranes were labeled with WGA conjugated with Alexa Fluor 488 dye (λ_{Ex}= 495 nm), while a secondary antibody $F(ab')_2$ fragment labeled with Coumarin dye (λ_{Ex}=350 nm) was used to image the cross-linked assembly of antibodies. The two components were imaged in the green channel (**Figure 5.12a**) and blue channel (**Figure 5.12b**) respectively and then the two images were superimposed (**Figure 5.12c**). The resulting merge evidenced the presence of several colocalized spots, confirming a good extent of EVs membranes functionalization with targeting antibodies.

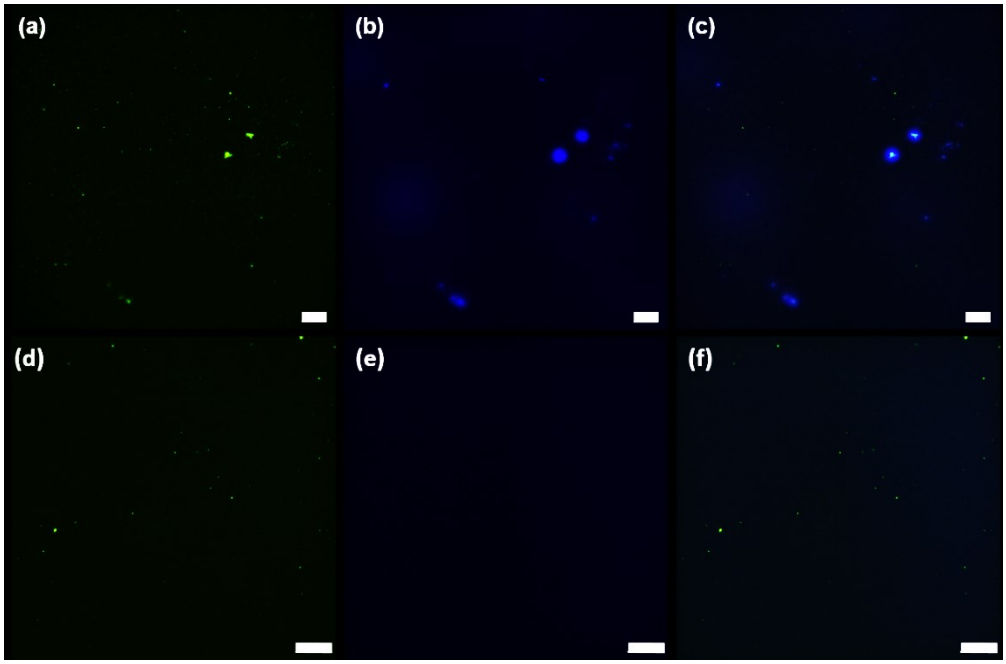

Figure 5.12: Wide-field fluorescence images of EVs^{CD20} (from **(a)** to **(c)**) and control (from **(d)** to **(f)**) samples. **(a)** and **(d)** green channel corresponding to EVs labeled with WGA-Alexa Fluor 488; **(b)** and **(e)** blue channel corresponding to Coumarin dye conjugated to secondary antibody $F(ab')_2$ fragment; **(c)** and **(f)** merge. Scale bar: 10 μm.

A control sample which had followed the whole functionalizing procedure, but without the addition of Rituximab primary antibody, was also analyzed (**Figure 5.12** from **d** to **f**). In this case, EVs were properly detected in the green channel (**Figure 5.12e**) but no blue fluorescence connected to Coumarin labeled secondary antibody was detected (**Figure 5.12e**). This allowed to exclude any aspecific adsorption of the F(ab')$_2$ fragment, confirming that the blue signal in the EVs^{CD20} sample was due to the effective conjugation of antibodies to vesicles surface.

The presence of functionalizing antibodies on the EVs surface was also preliminary investigated through NTA measurements. Also in this case, both EVs^{CD20} and the relative control sample obtained without the addition of the primary antibody were analyzed. Specifically, the two samples were measured at the end of each incubation step, i.e. after the addition of: (i) first Rituximab (**Figure 5.13**, top panel), (ii) secondary antibody F(ab')$_2$ fragment (**Figure 5.13**, middle panel) and (iii) second Rituximab (**Figure 5.13**, bottom panel).

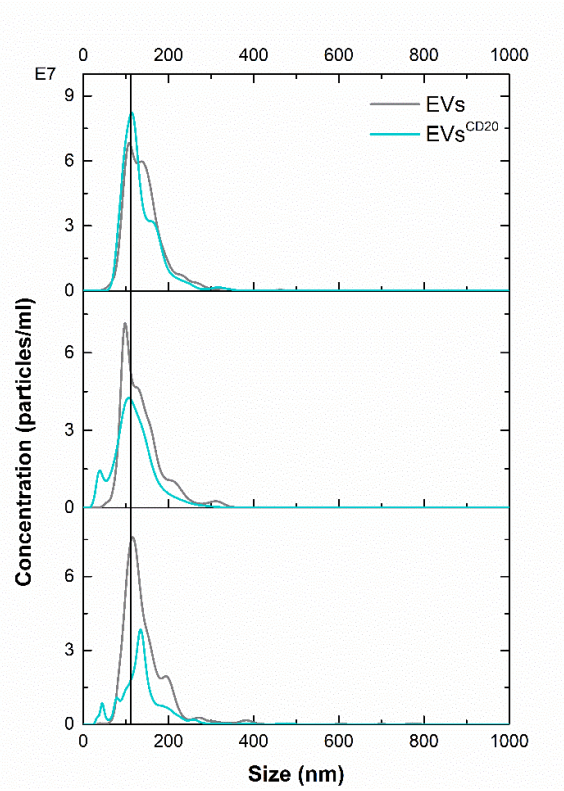

Figure 5.13: NTA measurements of antibody-functionalized sample (EVs^{CD20}, blue lines) and control sample (EVs, grey lines) after each incubation step performed during the functionalization procedure. From top to bottom: samples after the addition of first aliquot of Rituximab (top panel), secondary antibody F(ab')$_2$ fragment (middle panel) and second aliquot of Rituximab (bottom panel).

The three measurements allowed to monitor the evolution of the hydrodynamic size of the samples during the functionalization process. The EVs control sample (grey lines in **Figure 5.13**) maintained a constant dimension equal to ~110 nm after all three incubation steps, showing no evident surface modification or aggregation phenomena. Conversely, the size distribution of EVs^{CD20} sample (**Figure 5.13**, blue lines) showed a shift toward higher hydrodynamic size. In particular, the mode value moved from 114 nm after the first incubation step to 135 nm after the third step. This increment could be ascribed to the presence of cross-linked antibodies on

EVs surface causing an increment of the steric hindrance and, consequently, of the mean hydrodynamic size. As clearly observable, a minor peak at low hydrodynamic size (~40 nm) was also detected after the addition of the secondary antibody and the second aliquot of Rituximab. These peaks were tentatively attributed to residual unbound antibodies present in solution which have to be carefully removed before the application of targeted EVs^{CD20}.

Overall, fluorescence microscopy and NTA measurements preliminarily certify the feasibility of the engineering step of EVs with a specific antibody, confirming from a semi-quantitative point of view, the successful interaction between the antibody and its binding site on the vesicles membrane. The complete preservation of the expression of CD20 protein on the surfaces of the vesicular component of TNH nanoconstruct was also assessed through flow-cytometry, enabling the opportunity to transfer the functionalizing procedure to the optimized hybrid nanoconstructs.

Indeed, the final evaluation of the success of the proposed functionalizing procedure and of the suitability of the selected targeting moiety would come from *in vitro* tests, which, however, are beyond the purpose of the present PhD thesis. The study of the cytotoxicity and interactions with either normal and cancerous cell models *in vitro* would provide a preliminary insight of the specificity and therapeutic efficacy of the developed TNHs. Specifically considering the modification with targeting moieties, internalization assay of nanoconstructs with and without anti-CD20 antibody (i.e. TNHs and $TNHs^{CD20}$) would allow to analyse their selectivity, comparing the intrinsic targeting properties of unmodified EVs with the preferential accumulation conferred by the insertion of specific molecules for the active targeting.

5.4 Conclusions

The results presented in this chapter report on the further optimization of TNH hybrid nanoconstruct in terms of safety, loading efficiency and selectivity. The TNHs developed in this phase were intended for the treatment of lymphomas cancer cells (Daudi cell line) and the employed EVs were extracted from healthy B lymphocytes, in order to address the safety concerns related to the application of tumor-derived vesicles.

The encapsulation of synthesized ZnO nanocrystals was obtained through an active loading procedure, based on the application of freeze-thaw cycles as external stimulus to destabilize the lipid membrane of the biovesicles and favour the entrance of the nanocrystals. In particular, two procedures (i.e. Method 1 and Method 2) characterized by a different number of freeze-thaw cycles were tested and the obtained TNHs were characterized. Both methods ensured the production of TNHs with promising loading efficiencies, high colloidal stability and preserved morphology. However, the Method 2 procedure, which envisaged the application of only two freeze-thaw cycles and prolonged co-incubation steps, was identified as the best option. Indeed, the loading efficiency obtained through the application of Method 2 comprehensive of the overnight incubation step (TNH-$2_{2:1}$ O/N) was equal to 49% ± 13%, overcoming the loading efficiencies obtained in the previous chapter. Furthermore, the Method 2 ensured the minimization of potential morphological and compositional degradations connected to the repeated freezing and thawing, applying a reduced number of cycles. This is also accompanied by a convenience in terms of operating times, which would allow a greater flexibility for subsequent manipulations.

Finally, to improve the TNHs selectivity, a functionalization method for the decoration of EVs surface with specific targeting antibodies was tested. The selected targeting moiety was Rituximab, a recombinant monoclonal chimeric antibody directed against CD20 antigen, a common marker of lymphomas cells. The proposed functionalization technique, fully based on antigen-antibody interactions, was preliminarily verified on pristine EVs. The possibility to transfer the functionalization protocol to TNHs was also verified, assessing the expression of CD20 protein on EVs surface after the application of both loading methods.

Main conclusions and future perspectives

The results presented in this PhD thesis follow the development of an innovative hybrid nanoconstruct (TrojaNanoHorse – TNH) for cancer treatment based on therapeutically active ZnO NCs. The main goal of this study was the biostabilization of synthesized nanocrystals obtained through their encapsulation in lipid bilayer constituted by biologically derived EVs.

The first part of the experimental work concerned the production of ZnO NCs with the evaluation of two synthetic approaches. More in details, the developed microwave-assisted synthesis allowed the obtainment of single-crystalline ZnO nanoparticles with homogenous physico-chemical properties. Compared to the conventional solvothermal synthetic approach, the microwave-assisted synthesis ensured a more efficient and reproducible biological response. The stability of the synthesized ZnO NCs in the biological environment was then evaluated, evidencing their tendency to aggregation and their high reactivity toward biological media components. Indeed, the control of the NCs colloidal and chemical stability in biological environment is of paramount importance for the development of effective and reliable therapeutic tools. Thus, the possibility to efficiently stabilize the ZnO NCs through surface functionalization was evaluated. In particular, ZnO NCs coated with a shell made by DOPC synthetic phospholipids were tested, evidencing that the presence of lipid bilayer efficiently prevented the nanocrystals aggregation and preserved their morphological, chemical and structural features even after prolonged contact with simulated and biological fluids.

These results built the rationale for the development of TNH hybrid nanoconstruct, made by ZnO NCs encapsulated within EVs. The EVs, in fact, are cell-derived lipid vesicles and, thus, their shielding would guarantee the ZnO NCs stabilization while their biological origin would impart additional biomimetic and biocompatible features. Indeed, the application of EVs as innovative drug delivery systems is widely investigated but the development of efficient and conservative encapsulation strategies is still a major challenge. The combination of synthesized ZnO NCs and EVs derived from KB cancerous cells was obtained through a passive co-incubation method, optimized to maximize the interaction between the two

components. The obtained TNHs presented satisfying coupling efficiencies, overcoming those obtained by similar literature studies, and the TEM analyses confirmed the efficient encapsulation of several ZnO NCs within a single EV. The improvement of the colloidal biostability of the EVs-shielded NCs was also assessed, in good accordance with the preliminary results obtained with synthetic lipid bilayer-shells. Moreover, *in vitro* tests on KB cancerous cells confirmed the efficacy of the produced nanoconsruct. The presence of the EVs-shielding, in fact, promoted the cellular internalization of ZnO NCs while preserving their intrinsic cytotoxicity.

Considering some of the common issues reported in the literature, the TNH construction was further optimized in terms of loading efficiency, selectivity and safety concerns related to the EVs cellular source. The therapeutic target of this second TNH were Daudi cells, a cancerous cell line derived from Burkitt lymphoma, but tumour-derived vesicles were substituted with EVs derived from normal B lymphocytes. In fact, even though tumour-derived EVs could possess a convenient intrinsic specificity toward their parent cells, recent literature studies evidenced that they could also carry biological substances involved in the development, progression and metastases of cancer. Thus, EVs derived from healthy cells are considered a better option for the construction of safe and effective drug delivery systems. To increment the loading efficiency, the transition from a passive co-incubation to an active method was envisaged. In particular, the developed procedure was based on the application of freeze-thaw cycles as active stimulus to induce the destabilization of EVs membrane. Indeed, the freeze-thaw active method effectively promoted the encapsulation of ZnO NCs and the obtained coupling efficiency was near to 50%. Finally, to further improve the selectivity of the proposed TNH nanoconstruct, the functionalization of EVs surface with targeting moieties was studied. In fact, even though EVs harbor an innate specificity and preferential accumulation, their intrinsic targeting ability is often not sufficient and surface modifications are widely explored to achieve an adequate targeted delivery. As already specified, the therapeutic target of TNH nanoconstruct is the Daudi cell line. Thus, monoclonal antibodies directed against CD20 protein, a common marker of lymphomas cells, were selected as targeting moieties. More in details, Rituximab, a therapeutic monoclonal antibody already approved by FDA, was used. The proposed functionalization technique, fully based on antigen-antibody interactions, relied on the expression of CD20 antigen also on the surface of lymphocytes-derived EVs. The success of targeting functionalization was preliminarily verified on pristine EVs, but the possibility to transfer it to TNHs was also investigated, assessing the preservation of CD20 protein expression on the surface of final TNHs nanoconstructs. The final evaluation of the selectivity and therapeutic efficacy of the optimized TNH would come from *in vitro* tests, which are beyond the purpose of the present PhD thesis. The described optimized procedure allowed the production of TNHs characterized by high coupling efficiency, very good colloidal stability, preserved morphology and surface protein expression, as well as the possibility of specific surface modification. All these features should indeed favour an effective interaction with cells.

Overall, the results presented in this PhD thesis constitute a proof of concept for the creation of a hybrid nanoconstruct which would allow the stabilization of ZnO NCs in the biological environment. The produced TNH nanoconstruct harnesses the ZnO cytotoxic potential and the natural biostability and delivery features of EVs, proposing a strategy for the development of more reliable and effective therapeutic tools for the *in vitro* treatment of cancer cells. A further improvement would derive from the purification of the TNHs nanoconstruct from uncoupled ZnO NCs, achievable, for instance, through methods developed for the EVs isolation, like immunoaffinity capture or density gradient. In fact, even though the optimized coupling efficiencies were satisfactory and higher with respect to similar literature studies, a fraction of uncoated ZnO NCs was still present. The non-homogeneity of the product could complicate the interpretation of the obtained results and slow the transfer toward actual therapeutic applications.

Moreover, a more careful investigation of the TNH stability in different biological media together with the evaluation of its chemical stability and interaction with media components would deeply help to understand its behaviour in biological systems. For instance, the study of protein corona composition would allow to unravel the biological identity of the developed nanoconstruct, predicting its biodistribution, interaction with immune system, cellular uptake and intracellular distribution, also with respect to uncoated ZnO NCs. A more detailed investigation of the toxicity mechanisms and of the interactions of TNHs nanoconstructs with cells are also required before their translation toward subsequent applications. Indeed, insight into the internalization mechanism and intracellular trafficking as well as the distinction between the different possible pathways of ZnO-induced cell death would provide a better comprehension, control and optimization of TNHs therapeutic action.

Even if not directly analyzed in this thesis, TNH hybrid nanoconstruct could possess other valuable features like interesting optical properties, suitable for diagnostic purposes, and a high biocompatibility, guaranteed by the biological nature of EVs. Considering *in vivo* applications, in fact, EVs could constitute promising drug delivery systems characterized by lower immunogenitcity and prolonged blood circulation with respect to synthetic particles. However, several literature studies evidenced that also the EVs biodistribution profile is not completely favourable and that their therapeutic application could deeply benefit from the engineering of EVs membrane. As explained, a procedure for the EVs surface engineering with targeting ligands was here preliminary investigated, but the validation of the selectivity and therapeutic efficacy of the final TNH nanoconstruct by *in vitro* tests is still required. However, it is worth to mention that, by choosing different targeting ligands, the implemented TNH nanoconstruct could be in principle adapted for the treatment different types of cancer, indicating an interesting versatility.

Finally, the transfer of the developed procedures to EVs directly derived from patient blood or tissues (i.e. autologous EVs) could constitute a promising step toward the creation of a fully biocompatible system for the delivery of therapeutically active ZnO NCs in personalized nanomedicine applications.

References

Abbas, Z., & Rehman, S. (2018). An Overview of Cancer Treatment Modalities. In *Neoplasm*. https://doi.org/10.5772/intechopen.76558

Abercrombie, M., & Ambrose, E. J. (1962). The Surface Properties of Cancer Cells: A Review. *Cancer Research*.

Adamcakova-Dodd, A., Stebounova, L. V., Kim, J. S., Vorrink, S. U., Ault, A. P., O'Shaughnessy, P. T., Grassian, V. H., & Thorne, P. S. (2014). Toxicity assessment of zinc oxide nanoparticles using sub-acute and sub-chronic murine inhalation models. *Particle and Fibre Toxicology*. https://doi.org/10.1186/1743-8977-11-15

Akhtar, M. J., Alhadlaq, H. A., Alshamsan, A., Majeed Khan, M. A., & Ahamed, M. (2015). Aluminum doping tunes band gap energy level as well as oxidative stress-mediated cytotoxicity of ZnO nanoparticles in MCF-7 cells. *Scientific Reports*. https://doi.org/10.1038/srep13876

Al-Gaashani, R., Radiman, S., Daud, A. R., Tabet, N., & Al-Douri, Y. (2013). XPS and optical studies of different morphologies of ZnO nanostructures prepared by microwave methods. *Ceramics International*. https://doi.org/10.1016/j.ceramint.2012.08.075

Albanese, A., Tang, P. S., & Chan, W. C. W. (2012). The effect of nanoparticle size, shape, and surface chemistry on biological systems. In *Annual Review of Biomedical Engineering*. https://doi.org/10.1146/annurev-bioeng-071811-150124

Ali, A., Ambreen, S., Javed, R., Tabassum, S., ul Haq, I., & Zia, M. (2017). ZnO nanostructure fabrication in different solvents transforms physio-chemical, biological and photodegradable properties. *Materials Science and Engineering C*. https://doi.org/10.1016/j.msec.2017.01.004

Almeida, J. P. M., Chen, A. L., Foster, A., & Drezek, R. (2011). In vivo biodistribution of nanoparticles. In *Nanomedicine*. https://doi.org/10.2217/nnm.11.79

Alvarez-Erviti, L., Seow, Y., Yin, H., Betts, C., Lakhal, S., & Wood, M. J. A. (2011). Delivery of siRNA to the mouse brain by systemic injection of targeted exosomes. *Nature Biotechnology*. https://doi.org/10.1038/nbt.1807

Anders, C. B., Chess, J. J., Wingett, D. G., & Punnoose, A. (2015). Serum Proteins Enhance Dispersion Stability and Influence the Cytotoxicity and Dosimetry of ZnO Nanoparticles in Suspension and Adherent Cancer Cell Models. *Nanoscale Research Letters*. https://doi.org/10.1186/s11671-015-1158-y

Anders, C. B., Eixenberger, J. E., Franco, N. A., Hermann, R. J., Rainey, K. D., Chess, J. J., Punnoose, A., & Wingett, D. G. (2018). ZnO nanoparticle preparation route influences surface reactivity, dissolution and cytotoxicity. *Environmental Science: Nano*. https://doi.org/10.1039/c7en00888k

Andreu, Z., & Yáñez-Mó, M. (2014). Tetraspanins in extracellular vesicle formation and function. *Frontiers in Immunology*. https://doi.org/10.3389/fimmu.2014.00442

Angioletti-Uberti, S. (2017). Theory, simulations and the design of functionalized nanoparticles for biomedical applications: A Soft Matter Perspective. In *npj Computational Materials*. https://doi.org/10.1038/s41524-017-0050-y

Antimisiaris, S. G., Mourtas, S., & Marazioti, A. (2018). Exosomes and exosome-inspired vesicles for targeted drug delivery. In *Pharmaceutics*. https://doi.org/10.3390/pharmaceutics10040218

Armstrong, J. P. K., Holme, M. N., & Stevens, M. M. (2017). Re-Engineering Extracellular Vesicles as Smart Nanoscale Therapeutics. In *ACS Nano*. https://doi.org/10.1021/acsnano.6b07607

Arruebo, M., Vilaboa, N., Sáez-Gutierrez, B., Lambea, J., Tres, A., Valladares, M., & González-Fernández, Á. (2011). Assessment of the evolution of cancer treatment therapies. In *Cancers*. https://doi.org/10.3390/cancers3033279

Bachurski, D., Schuldner, M., Nguyen, P. H., Malz, A., Reiners, K. S., Grenzi, P. C., Babatz, F., Schauss, A. C., Hansen, H. P., Hallek, M., & Pogge von Strandmann, E. (2019). Extracellular vesicle measurements with nanoparticle tracking analysis–An accuracy and repeatability comparison between NanoSight NS300 and ZetaView. *Journal of Extracellular Vesicles*. https://doi.org/10.1080/20013078.2019.1596016

Bai Aswathanarayan, J., Rai Vittal, R., & Muddegowda, U. (2018). Anticancer activity of metal nanoparticles and their peptide conjugates against human colon adenorectal carcinoma cells. *Artificial Cells, Nanomedicine and Biotechnology*. https://doi.org/10.1080/21691401.2017.1373655

Barbero, F., Russo, L., Vitali, M., Piella, J., Salvo, I., Borrajo, M. L., Busquets-Fité, M., Grandori, R., Bastús, N. G., Casals, E., & Puntes, V. (2017). Formation of the Protein Corona: The Interface between Nanoparticles and the Immune System. In *Seminars in Immunology*. https://doi.org/10.1016/j.smim.2017.10.001

Barui, A. K., Oh, J. Y., Jana, B., Kim, C., & Ryu, J. (2020). Cancer-Targeted Nanomedicine: Overcoming the Barrier of the Protein Corona. *Advanced Therapeutics*. https://doi.org/10.1002/adtp.201900124

Bates, A., & Power, C. A. (2019). David vs. Goliath: The Structure, Function, and Clinical Prospects of Antibody Fragments. *Antibodies*. https://doi.org/10.3390/antib8020028

Batrakova, E. V., & Kim, M. S. (2015). Using exosomes, naturally-equipped nanocarriers, for drug delivery. *Journal of Controlled Release*. https://doi.org/10.1016/j.jconrel.2015.07.030

Bebelman, M. P., Smit, M. J., Pegtel, D. M., & Baglio, S. R. (2018). Biogenesis and function of extracellular vesicles in cancer. In *Pharmacology and Therapeutics*. https://doi.org/10.1016/j.pharmthera.2018.02.013

Betzer, O., Perets, N., Angel, A., Motiei, M., Sadan, T., Yadid, G., Offen, D., & Popovtzer, R. (2017). In Vivo Neuroimaging of Exosomes Using Gold Nanoparticles. *ACS Nano*. https://doi.org/10.1021/acsnano.7b04495

Bian, S. W., Mudunkotuwa, I. A., Rupasinghe, T., & Grassian, V. H. (2011). Aggregation and dissolution of 4 nm ZnO nanoparticles in aqueous environments: Influence of pH, ionic strength, size, and adsorption of humic acid. *Langmuir*. https://doi.org/10.1021/la200570n

Bisht, G., & Rayamajhi, S. (2016). ZnO Nanoparticles: A Promising Anticancer Agent. In *Nanobiomedicine*. https://doi.org/10.5772/63437

Bogdan, J., Pławińska-Czarnak, J., & Zarzyńska, J. (2017). Nanoparticles of Titanium and Zinc Oxides as Novel Agents in Tumor Treatment: a Review. *Nanoscale Research Letters*. https://doi.org/10.1186/s11671-017-2007-y

Canavese, G., Ancona, A., Racca, L., Canta, M., Dumontel, B., Barbaresco, F., Limongi, T., & Cauda, V. (2018). Nanoparticle-assisted ultrasound: A special focus on sonodynamic therapy against cancer. *Chemical Engineering Journal*. https://doi.org/10.1016/j.cej.2018.01.060

Carnino, J. M., Lee, H., & Jin, Y. (2019). Isolation and characterization of extracellular vesicles from Broncho-Alveolar lavage fluid: A review and comparison of different methods. In *Respiratory Research*. https://doi.org/10.1186/s12931-019-1210-z

Carofiglio, M., Barui, S., Cauda, V., & Laurenti, M. (2020). Doped zinc oxide nanoparticles: Synthesis, characterization and potential use in nanomedicine. In *Applied Sciences (Switzerland)*. https://doi.org/10.3390/app10155194

Cauda, V., Engelke, H., Sauer, A., Arcizet, D., Bräuchle, C., Rädler, J., & Bein, T. (2010). Colchicine-loaded lipid bilayer-coated 50 nm mesoporous nanoparticles efficiently induce microtubule depolymerization upon cell uptake. *Nano Letters*. https://doi.org/10.1021/nl100991w

Cauda, V., Gazia, R., Porro, S., Stassi, S., Canavese, G., Roppolo, I., & Chiolerio, A. (2014). Nanostructured ZnO Materials: Synthesis, Properties and Applications. In *Handbook of Nanomaterials Properties*. https://doi.org/10.1007/978-3-642-31107-9_32

Cauda, V., Schlossbauer, A., & Bein, T. (2010). Bio-degradation study of colloidal mesoporous silica nanoparticles: Effect of surface functionalization with organo-silanes and poly(ethylene glycol). *Microporous and Mesoporous Materials*. https://doi.org/10.1016/j.micromeso.2009.11.015

Champion, J. A., Katare, Y. K., & Mitragotri, S. (2007). Particle shape: A new design parameter for micro- and nanoscale drug delivery carriers. In *Journal of Controlled Release*. https://doi.org/10.1016/j.jconrel.2007.03.022

Chen, C., Luo, F., Liu, X., Lu, L., Xu, H., Yang, Q., Xue, J., Shi, L., Li, J., Zhang, A., & Liu, Q. (2017). NF-kB-regulated exosomal miR-155 promotes the inflammation associated with arsenite carcinogenesis. *Cancer Letters*. https://doi.org/10.1016/j.canlet.2016.11.027

Chen, P., Wang, H., He, M., Chen, B., Yang, B., & Hu, B. (2019). Size-dependent cytotoxicity study of ZnO nanoparticles in HepG2 cells. *Ecotoxicology and Environmental Safety*. https://doi.org/10.1016/j.ecoenv.2018.12.096

Cheng, Q., Shi, X., Han, M., Smbatyan, G., Lenz, H. J., & Zhang, Y. (2018). Reprogramming Exosomes as Nanoscale Controllers of Cellular Immunity. *Journal of the American Chemical Society*. https://doi.org/10.1021/jacs.8b10047

Cheng, Y., Zeng, Q., Han, Q., & Xia, W. (2019). Effect of pH, temperature and freezing-thawing on quantity changes and cellular uptake of exosomes. In *Protein and Cell*. https://doi.org/10.1007/s13238-018-0529-4

Chernenko, K. A., Gorokhova, E. I., Eronko, S. B., Sandulenko, A. V., Venevtsev, I. D., Wieczorek, H., & Rodnyi, P. A. (2018). Structural, Optical, and Luminescent Properties of ZnO:Ga and ZnO:In Ceramics. *IEEE Transactions on Nuclear Science*. https://doi.org/10.1109/TNS.2018.2810331

Cherukuri, P., Glazer, E. S., & Curley, S. A. (2010). Targeted hyperthermia using metal nanoparticles. In *Advanced Drug Delivery Reviews*. https://doi.org/10.1016/j.addr.2009.11.006

Choi, E. S., Song, J., Kang, Y. Y., & Mok, H. (2019). Mannose-Modified Serum Exosomes for the Elevated Uptake to Murine Dendritic Cells and Lymphatic Accumulation. *Macromolecular Bioscience*. https://doi.org/10.1002/mabi.201900042

Condello, M., De Berardis, B., Ammendolia, M. G., Barone, F., Condello, G., Degan, P., & Meschini, S. (2016). ZnO nanoparticle tracking from uptake to genotoxic damage in human colon carcinoma cells. *Toxicology in Vitro*. https://doi.org/10.1016/j.tiv.2016.06.005

Conway, J. H., & Sloane, N. J. A. (1999). Sphere Packings, Lattices and Groups -- 3rd ed. In *Media*. https://doi.org/10.1007/978-3-642-25847-3

Dalton, A. J. (1975). Microvesicles and vesicles of multivesicular bodies versus "virus like" particles. *Journal of the National Cancer Institute*. https://doi.org/10.1093/jnci/54.5.1137

Dang, X. T. T., Kavishka, J. M., Zhang, D. X., Pirisinu, M., & Le, M. T. N. (2020). Extracellular Vesicles as an Efficient and Versatile System for Drug Delivery. In *Cells* (Vol. 9, Issue 10). https://doi.org/10.3390/cells9102191

Degen, A., & Kosec, M. (2000). Effect of pH and impurities on the surface charge of zinc oxide in aqueous solution. *Journal of the European Ceramic Society*. https://doi.org/10.1016/S0955-2219(99)00203-4

DeLong, R. K., Mitchell, J. A., Tyler Morris, R., Comer, J., Hurst, M. N., Ghosh, K., Wanekaya, A., Mudge, M., Schaeffer, A., Washington, L. L., Risor-Marhanka, A., Thomas, S., Marroquin, S., Lekey, A., Smith, J. J., Garrad, R., Aryal, S., Abdelhakiem, M., & Glaspell, G. P. (2017). Enzyme and Cancer Cell Selectivity of Nanoparticles: Inhibition of 3-D Metastatic Phenotype and Experimental Melanoma by Zinc Oxide. *Journal of Biomedical Nanotechnology*. https://doi.org/10.1166/jbn.2017.2336

Deng, Y., & Zhang, H. (2013). The synergistic effect and mechanism of doxorubicin-ZnO nanocomplexes as a multimodal agent integrating diverse anticancer therapeutics. *International Journal of Nanomedicine*. https://doi.org/10.2147/IJN.S43657

Deng, Z. J., Mortimer, G., Schiller, T., Musumeci, A., Martin, D., & Minchin, R. F. (2009). Differential plasma protein binding to metal oxide nanoparticles. *Nanotechnology*. https://doi.org/10.1088/0957-4484/20/45/455101

Dorvignit, D., Palacios, J. L., Merino, M., Hernández, T., Sosa, K., Casacó, A., López-Requena, A., & De Acosta, C. M. (2012). Expression and biological characterization of an anti-CD20 biosimilar candidate antibody: A case study. *MAbs*. https://doi.org/10.4161/mabs.20761

Durfee, P. N., Lin, Y. S., Dunphy, D. R., Muñiz, A. J., Butler, K. S., Humphrey, K. R., Lokke, A. J., Agola, J. O., Chou, S. S., Chen, I. M., Wharton, W., Townson, J. L., Willman, C. L., & Brinker, C. J. (2016). Mesoporous Silica Nanoparticle-Supported Lipid Bilayers (Protocells) for Active Targeting and Delivery to Individual Leukemia Cells. *ACS Nano*. https://doi.org/10.1021/acsnano.6b02819

Elsharkasy, O. M., Nordin, J. Z., Hagey, D. W., de Jong, O. G., Schiffelers, R. M., Andaloussi, S. EL, & Vader, P. (2020). Extracellular vesicles as drug delivery systems: Why and how? *Advanced Drug Delivery Reviews*. https://doi.org/10.1016/j.addr.2020.04.004

Estanqueiro, M., Amaral, M. H., Conceição, J., & Sousa Lobo, J. M. (2015). Nanotechnological carriers for cancer chemotherapy: The state of the art. In *Colloids and Surfaces B: Biointerfaces*. https://doi.org/10.1016/j.colsurfb.2014.12.041

Fahy, E., Cotter, D., Sud, M., & Subramaniam, S. (2011). Lipid classification, structures and tools. *Biochimica et Biophysica Acta - Molecular and Cell Biology of Lipids*. https://doi.org/10.1016/j.bbalip.2011.06.009

Fang, X., Jiang, L., Gong, Y., Li, J., Liu, L., & Cao, Y. (2017). The presence of oleate stabilized ZnO nanoparticles (NPs) and reduced the toxicity of aged NPs to Caco-2 and HepG2 cells. *Chemico-Biological Interactions*. https://doi.org/10.1016/j.cbi.2017.10.002

Forrester, S. J., Kikuchi, D. S., Hernandes, M. S., Xu, Q., & Griendling, K. K. (2018). Reactive oxygen species in metabolic and inflammatory signaling. In *Circulation Research*. https://doi.org/10.1161/CIRCRESAHA.117.311401

Fuhrmann, G., Serio, A., Mazo, M., Nair, R., & Stevens, M. M. (2015). Active loading into extracellular vesicles significantly improves the cellular uptake and photodynamic effect of porphyrins. *Journal of Controlled Release*. https://doi.org/10.1016/j.jconrel.2014.11.029

Garino, N., Limongi, T., Dumontel, B., Canta, M., Racca, L., Laurenti, M., Castellino, M., Casu, A., Falqui, A., & Cauda, V. (2019). A microwave-assisted synthesis of zinc oxide nanocrystals finely tuned for biological applications. *Nanomaterials*. https://doi.org/10.3390/nano9020212

Giusti, I., Di Francesco, M., Cantone, L., D'Ascenzo, S., Bollati, V., Carta, G., & Dolo, V. (2015). Time-dependent release of extracellular vesicle subpopulations in tumor CABA i cells. *Oncology Reports*. https://doi.org/10.3892/or.2015.4199

Goh, W. J., Lee, C. K., Zou, S., Woon, E. C. Y., Czarny, B., & Pastorin, G. (2017). Doxorubicin-loaded cell-derived nanovesicles: An alternative targeted approach for anti-tumor therapy. *International Journal of Nanomedicine*. https://doi.org/10.2147/IJN.S131786

Guerrini, L., Alvarez-Puebla, R. A., & Pazos-Perez, N. (2018). Surface modifications of nanoparticles for stability in biological fluids. In *Materials*. https://doi.org/10.3390/ma11071154

H. Müller, K., Kulkarni, J., Motskin, M., Goode, A., Winship, P., Skepper, J. N., Ryan, M. P., & Porter, A. E. (2010). PH-dependent toxicity of high aspect ratio ZnO nanowires in macrophages due to intracellular dissolution. *ACS Nano*. https://doi.org/10.1021/nn101192z

Hadla, M., Palazzolo, S., Corona, G., Caligiuri, I., Canzonieri, V., Toffoli, G., & Rizzolio, F. (2016). Exosomes increase the therapeutic index of doxorubicin in breast and ovarian cancer mouse models. *Nanomedicine*. https://doi.org/10.2217/nnm-2016-0154

Hanahan, D., & Weinberg, R. A. (2000). The hallmarks of cancer. In *Cell*. https://doi.org/10.1016/S0092-8674(00)81683-9

Hanahan, D., & Weinberg, R. A. (2011). Hallmarks of cancer: The next generation. In *Cell*. https://doi.org/10.1016/j.cell.2011.02.013

Haney, M. J., Klyachko, N. L., Zhao, Y., Gupta, R., Plotnikova, E. G., He, Z., Patel, T., Piroyan, A., Sokolsky, M., Kabanov, A. V., & Batrakova, E. V. (2015). Exosomes as drug delivery vehicles for Parkinson's disease therapy. *Journal of Controlled Release*. https://doi.org/10.1016/j.jconrel.2015.03.033

Haney, M. J., Zhao, Y., Jin, Y. S., Li, S. M., Bago, J. R., Klyachko, N. L., Kabanov, A. V., & Batrakova, E. V. (2020). Macrophage-Derived Extracellular Vesicles as Drug Delivery Systems for Triple Negative Breast Cancer (TNBC) Therapy. *Journal of Neuroimmune Pharmacology*. https://doi.org/10.1007/s11481-019-09884-9

Hanley, C., Layne, J., Punnoose, A., Reddy, K. M., Coombs, I., Coombs, A., Feris, K., & Wingett, D. (2008). Preferential killing of cancer cells and activated human T cells using ZnO nanoparticles. *Nanotechnology*. https://doi.org/10.1088/0957-4484/19/29/295103

Harding, C., & Stahl, P. (1983). Transferrin recycling in reticulocytes: pH and iron are important determinants of ligand binding and processing. *Biochemical and Biophysical Research Communications*. https://doi.org/10.1016/0006-291X(83)91776-X

He, L., Liu, Y., Mustapha, A., & Lin, M. (2011). Antifungal activity of zinc oxide nanoparticles against Botrytis cinerea and Penicillium expansum. *Microbiological Research*. https://doi.org/10.1016/j.micres.2010.03.003

Hernández, S., Cauda, V., Chiodoni, A., Dallorto, S., Sacco, A., Hidalgo, D., Celasco, E., & Pirri, C. F. (2014). Optimization of 1D ZnO@TiO2 core-shell nanostructures for enhanced photoelectrochemical water splitting under solar light illumination. *ACS Applied Materials and Interfaces*. https://doi.org/10.1021/am501379m

Herrmann, R., García-García, F. J., & Reller, A. (2014). Rapid degradation of zinc oxide nanoparticles by phosphate ions. *Beilstein Journal of Nanotechnology*. https://doi.org/10.3762/bjnano.5.209

Hohner, A. O., David, M. P. C., & Rädler, J. O. (2010). Controlled solvent-exchange deposition of phospholipid membranes onto solid surfaces. *Biointerphases*. https://doi.org/10.1116/1.3319326

Hood, J. L., Scott, M. J., & Wickline, S. A. (2014). Maximizing exosome colloidal stability following electroporation. *Analytical Biochemistry*. https://doi.org/10.1016/j.ab.2013.12.001

Hoshino, A., Costa-Silva, B., Shen, T. L., Rodrigues, G., Hashimoto, A., Tesic Mark, M., Molina, H., Kohsaka, S., Di Giannatale, A., Ceder, S., Singh, S., Williams, C., Soplop, N., Uryu, K., Pharmer, L., King, T., Bojmar, L., Davies, A. E., Ararso, Y., … Lyden, D. (2015). Tumour exosome integrins determine organotropic metastasis. *Nature*. https://doi.org/10.1038/nature15756

Illes, B., Hirschle, P., Barnert, S., Cauda, V., Wuttke, S., & Engelke, H. (2017). Exosome-Coated Metal–Organic Framework Nanoparticles: An Efficient Drug Delivery Platform. *Chemistry of Materials*, *29*(19), 8042–8046. https://doi.org/10.1021/acs.chemmater.7b02358

Ip, S., MacLaughlin, C. M., Gunari, N., & Walker, G. C. (2011). Phospholipid membrane encapsulation of nanoparticles for surface-enhanced raman scattering. *Langmuir*. https://doi.org/10.1021/la200212c

Jackman, J. A., & Cho, N. J. (2020). Supported Lipid Bilayer Formation: Beyond Vesicle Fusion. *Langmuir*. https://doi.org/10.1021/acs.langmuir.9b03706

Jang, S. C., Kim, O. Y., Yoon, C. M., Choi, D. S., Roh, T. Y., Park, J., Nilsson, J., Lötvall, J., Kim, Y. K., & Gho, Y. S. (2013). Bioinspired exosome-mimetic nanovesicles for targeted delivery of chemotherapeutics to malignant tumors. *ACS Nano*. https://doi.org/10.1021/nn402232g

Jc Bose, R., Uday Kumar, S., Zeng, Y., Afjei, R., Robinson, E., Lau, K., Bermudez, A., Habte, F., Pitteri, S. J., Sinclair, R., Willmann, J. K., Massoud, T. F., Gambhir, S. S., & Paulmurugan, R. (2018). Tumor Cell-Derived Extracellular Vesicle-Coated Nanocarriers: An Efficient Theranostic Platform for the Cancer-Specific Delivery of Anti-miR-21 and Imaging Agents. *ACS Nano*. https://doi.org/10.1021/acsnano.8b02587

Jiang, J., Pi, J., & Cai, J. (2018). The Advancing of Zinc Oxide Nanoparticles for Biomedical Applications. In *Bioinorganic Chemistry and Applications*. https://doi.org/10.1155/2018/1062562

Johnstone, R. M., Adam, M., Hammond, J. R., Orr, L., & Turbide, C. (1987). Vesicle formation during reticulocyte maturation. Association of plasma membrane activities with released vesicles (exosomes). *Journal of Biological Chemistry*.

Jung, M. K., & Mun, J. Y. (2018). Sample preparation and imaging of exosomes by transmission electron microscopy. *Journal of Visualized Experiments*. https://doi.org/10.3791/56482

Kamarulzaman, N., Kasim, M. F., & Rusdi, R. (2015). Band Gap Narrowing and Widening of ZnO Nanostructures and Doped Materials. *Nanoscale Research Letters*. https://doi.org/10.1186/s11671-015-1034-9

Kamerkar, S., Lebleu, V. S., Sugimoto, H., Yang, S., Ruivo, C. F., Melo, S. A., Lee, J. J., & Kalluri, R. (2017). Exosomes facilitate therapeutic targeting of oncogenic KRAS in pancreatic cancer. *Nature*. https://doi.org/10.1038/nature22341

Kanada, M., Bachmann, M. H., & Contag, C. H. (2016). Signaling by Extracellular Vesicles Advances Cancer Hallmarks. In *Trends in Cancer*. https://doi.org/10.1016/j.trecan.2015.12.005

Kang, T., Guan, R., Chen, X., Song, Y., Jiang, H., & Zhao, J. (2013). In vitro toxicity of different-sized ZnO nanoparticles in Caco-2 cells. *Nanoscale Research Letters*. https://doi.org/10.1186/1556-276X-8-496

Kibria, G., Ramos, E. K., Wan, Y., Gius, D. R., & Liu, H. (2018). Exosomes as a Drug Delivery System in Cancer Therapy: Potential and Challenges. In *Molecular Pharmaceutics*. https://doi.org/10.1021/acs.molpharmaceut.8b00277

Kim, M. S., Haney, M. J., Zhao, Y., Mahajan, V., Deygen, I., Klyachko, N. L., Inskoe, E., Piroyan, A., Sokolsky, M., Okolie, O., Hingtgen, S. D., Kabanov, A. V., & Batrakova, E. V. (2016). Development of exosome-encapsulated paclitaxel to overcome MDR in cancer cells. *Nanomedicine: Nanotechnology, Biology, and Medicine*. https://doi.org/10.1016/j.nano.2015.10.012

Ko, S. Y., Lee, W. J., Kenny, H. A., Dang, L. H., Ellis, L. M., Jonasch, E., Lengyel, E., & Naora, H. (2019). Cancer-derived small extracellular vesicles promote angiogenesis by heparin-bound, bevacizumab-insensitive VEGF, independent of vesicle uptake. *Communications Biology*. https://doi.org/10.1038/s42003-019-0609-x

Kokubo, T., Kushitani, H., Sakka, S., Kitsugi, T., & Yamamuro, T. (1990). Solutions able to reproduce in vivo surface-structure changes in bioactive glass-ceramic A-W3. *Journal of Biomedical Materials Research*. https://doi.org/10.1002/jbm.820240607

Konoshenko, M. Y., Lekchnov, E. A., Vlassov, A. V., & Laktionov, P. P. (2018). Isolation of Extracellular Vesicles: General Methodologies and Latest Trends. In *BioMed Research International*. https://doi.org/10.1155/2018/8545347

Kooijmans, S. A.A., Fliervoet, L. A. L., Van Der Meel, R., Fens, M. H. A. M., Heijnen, H. F. G., Van Bergen En Henegouwen, P. M. P., Vader, P., & Schiffelers, R. M. (2016). PEGylated and targeted extracellular vesicles display enhanced cell specificity and circulation time. *Journal of Controlled Release*. https://doi.org/10.1016/j.jconrel.2016.01.009

Kooijmans, Sander A.A., Aleza, C. G., Roffler, S. R., van Solinge, W. W., Vader, P., & Schiffelers, R. M. (2016). Display of GPI-anchored anti-EGFR nanobodies on extracellular vesicles promotes tumour cell targeting. *Journal of Extracellular Vesicles*. https://doi.org/10.3402/jev.v5.31053

Kooijmans, Sander A.A., Schiffelers, R. M., Zarovni, N., & Vago, R. (2016). Modulation of tissue tropism and biological activity of exosomes and other extracellular vesicles: New nanotools for cancer treatment. *Pharmacological Research*. https://doi.org/10.1016/j.phrs.2016.07.006

Kooijmans, Sander A.A., Stremersch, S., Braeckmans, K., De Smedt, S. C., Hendrix, A., Wood, M. J. A., Schiffelers, R. M., Raemdonck, K., & Vader, P. (2013). Electroporation-induced siRNA precipitation obscures the efficiency of siRNA loading into extracellular vesicles. *Journal of Controlled Release*. https://doi.org/10.1016/j.jconrel.2013.08.014

Kosaka, N., Iguchi, H., Yoshioka, Y., Takeshita, F., Matsuki, Y., & Ochiya, T. (2010). Secretory mechanisms and intercellular transfer of microRNAs in living cells. *Journal of Biological Chemistry*. https://doi.org/10.1074/jbc.M110.107821

Kumar, S., Bhushan, P., & Bhattacharya, S. (2018). *Fabrication of Nanostructures with Bottom-up Approach and Their Utility in Diagnostics, Therapeutics, and Others*. https://doi.org/10.1007/978-981-10-7751-7_8

Lamichhane, T. N., Jeyaram, A., Patel, D. B., Parajuli, B., Livingston, N. K., Arumugasaamy, N., Schardt, J. S., & Jay, S. M. (2016). Oncogene Knockdown via Active Loading of Small RNAs into Extracellular Vesicles by Sonication. *Cellular and Molecular Bioengineering*. https://doi.org/10.1007/s12195-016-0457-4

Lane, R. E., Korbie, D., Hill, M. M., & Trau, M. (2018). Extracellular vesicles as circulating cancer biomarkers: opportunities and challenges. *Clinical and Translational Medicine*. https://doi.org/10.1186/s40169-018-0192-7

Latorre, M., & Rinaldi, C. (2009). Applications of magnetic nanoparticles in medicine: Magnetic fluid hyperthermia. *Puerto Rico Health Sciences Journal*.

Lawson, C., Vicencio, J. M., Yellon, D. M., & Davidson, S. M. (2016). Microvesicles and exosomes: New players in metabolic and cardiovascular disease. In *Journal of Endocrinology*. https://doi.org/10.1530/JOE-15-0201

Lee, J., Kim, J., Jeong, M., Lee, H., Goh, U., Kim, H., Kim, B., & Park, J. H. (2015). Liposome-based engineering of cells to package hydrophobic compounds in membrane vesicles for tumor penetration. *Nano Letters*. https://doi.org/10.1021/nl5047494

Lee, J., Lee, H., Goh, U., Kim, J., Jeong, M., Lee, J., & Park, J. H. (2016). Cellular Engineering with Membrane Fusogenic Liposomes to Produce Functionalized Extracellular Vesicles. *ACS Applied Materials and Interfaces*. https://doi.org/10.1021/acsami.6b01315

Lener, T., Gimona, M., Aigner, L., Börger, V., Buzas, E., Camussi, G., Chaput, N., Chatterjee, D., Court, F. A., del Portillo, H. A., O'Driscoll, L., Fais, S., Falcon-Perez, J. M., Felderhoff-Mueser, U., Fraile, L., Gho, Y. S., Görgens, A., Gupta, R. C., Hendrix, A., … Giebel, B. (2015). Applying extracellular vesicles based therapeutics in clinical trials - An ISEV position paper. *Journal of Extracellular Vesicles*. https://doi.org/10.3402/jev.v4.30087

Li, J. H., Liu, X. R., Zhang, Y., Tian, F. F., Zhao, G. Y., Yu, Q. L. Y., Jiang, F. L., & Liu, Y. (2012). Toxicity of nano zinc oxide to mitochondria. *Toxicology Research*. https://doi.org/10.1039/c2tx20016c

Li, S., Sun, Z., Li, R., Dong, M., Zhang, L., Qi, W., Zhang, X., & Wang, H. (2014). ZnO nanocomposites modified by hydrophobic and hydrophilic silanes with dramatically enhanced tunable fluorescence and aqueous ultrastability toward biological imaging applications. *Scientific Reports*. https://doi.org/10.1038/srep08475

Li, Y., & Lee, J. S. (2020). Insights into characterization methods and biomedical applications of nanoparticle-protein corona. In *Materials*. https://doi.org/10.3390/ma13143093

Lim, E. K., Kim, T., Paik, S., Haam, S., Huh, Y. M., & Lee, K. (2015). Nanomaterials for theranostics: Recent advances and future challenges. In *Chemical Reviews*. https://doi.org/10.1021/cr300213b

Limongi, T., Canta, M., Racca, L., Ancona, A., Tritta, S., Vighetto, V., & Cauda, V. (2019). Improving dispersal of therapeutic nanoparticles in the human body. *Nanomedicine*. https://doi.org/10.2217/nnm-2019-0070

Liu, D., Yang, F., Xiong, F., & Gu, N. (2016). The smart drug delivery system and its clinical potential. In *Theranostics*. https://doi.org/10.7150/thno.14858

Lodish, H., Berk, A., Zipursky, S. L., Matsudaira, P., Baltimore, D., & Darnell, J. (2000). Section 24.2, Proto-Oncogenes and Tumor-Suppressor Genes. In *Molecular Cell Biology*.

Lu, M., Xing, H., Xun, Z., Yang, T., Zhao, X., Cai, C., Wang, D., & Ding, P. (2018). Functionalized extracellular vesicles as advanced therapeutic nanodelivery systems. In *European Journal of Pharmaceutical Sciences*. https://doi.org/10.1016/j.ejps.2018.05.001

Luan, X., Sansanaphongpricha, K., Myers, I., Chen, H., Yuan, H., & Sun, D. (2017). Engineering exosomes as refined biological nanoplatforms for drug delivery. In *Acta Pharmacologica Sinica*. https://doi.org/10.1038/aps.2017.12

Luchini, A., & Vitiello, G. (2019). Understanding the nano-bio interfaces: Lipid-coatings for inorganic nanoparticles as promising strategy for biomedical applications. In *Frontiers in Chemistry*. https://doi.org/10.3389/fchem.2019.00343

Luo, M., Shen, C., Feltis, B. N., Martin, L. L., Hughes, A. E., Wright, P. F. A., & Turney, T. W. (2014). Reducing ZnO nanoparticle cytotoxicity by surface modification. *Nanoscale*. https://doi.org/10.1039/c4nr00458b

Lv, J., Zhang, S., Luo, L., Han, W., Zhang, J., Yang, K., & Christie, P. (2012). Dissolution and microstructural transformation of ZnO nanoparticles under the influence of phosphate. *Environmental Science and Technology*. https://doi.org/10.1021/es301027a

Mallakpour, S., & Madani, M. (2015). A review of current coupling agents for modification of metal oxide nanoparticles. In *Progress in Organic Coatings*. https://doi.org/10.1016/j.porgcoat.2015.05.023

Maloney, D. G. (2012). Anti-CD20 Antibody Therapy for B-Cell Lymphomas. *New England Journal of Medicine*. https://doi.org/10.1056/nejmct1114348

Marcus, M. E., & Leonard, J. N. (2013). FedExosomes: Engineering therapeutic biological nanoparticles that truly deliver. In *Pharmaceuticals*. https://doi.org/10.3390/ph6050659

Maret, W. (2017). Zinc in cellular regulation: The nature and significance of "zinc signals." In *International Journal of Molecular Sciences*. https://doi.org/10.3390/ijms18112285

Matsumura, Y., & Maeda, H. (1986). A New Concept for Macromolecular Therapeutics in Cancer Chemotherapy: Mechanism of Tumoritropic Accumulation of Proteins and the Antitumor Agent Smancs. *Cancer Research*.

Meng, W., He, C., Hao, Y., Wang, L., Li, L., & Zhu, G. (2020). Prospects and challenges of extracellular vesicle-based drug delivery system: considering cell source. *Drug Delivery*. https://doi.org/10.1080/10717544.2020.1748758

Moghimi, S. M., Hunter, A. C., & Andresen, T. L. (2012). Factors controlling nanoparticle pharmacokinetics: An integrated analysis and perspective. *Annual Review of Pharmacology and Toxicology*. https://doi.org/10.1146/annurev-pharmtox-010611-134623

Mohd Yusof, H., Mohamad, R., Zaidan, U. H., & Abdul Rahman, N. A. (2019). Microbial synthesis of zinc oxide nanoparticles and their potential application as an antimicrobial agent and a feed supplement in animal industry: A review. In *Journal of Animal Science and Biotechnology*. https://doi.org/10.1186/s40104-019-0368-z

Molnár, Á., Papp, M., Zoltán Kovács, D., Bélteky, P., Oláh, D., Feigl, G., Szőllősi, R., Rázga, Z., Ördög, A., Erdei, L., Rónavári, A., Kónya, Z., & Kolbert, Z. (2020). Nitro-oxidative signalling induced by chemically synthetized zinc oxide nanoparticles (ZnO NPs) in Brassica species. *Chemosphere*. https://doi.org/10.1016/j.chemosphere.2020.126419

Moore, T. L., Rodriguez-Lorenzo, L., Hirsch, V., Balog, S., Urban, D., Jud, C., Rothen-Rutishauser, B., Lattuada, M., & Petri-Fink, A. (2015). Nanoparticle colloidal stability in cell culture media and impact on cellular interactions. *Chemical Society Reviews*. https://doi.org/10.1039/c4cs00487f

Morales-Flores, N., Galeazzi, R., Rosendo, E., Diaz, T., Velumani, S., & Pal, U. (2013). Morphology control and optical properties of ZnO nanostructures grown by ultrasonic synthesis. *Advances in Nano Research*. https://doi.org/10.12989/anr.2013.1.1.059

Morkoç, H., & Özgür, Ü. (2009). Zinc Oxide: Fundamentals, Materials and Device Technology: General Properties of ZnO. In *WILEY-VCH*.

Mornet, S., Lambert, O., Duguet, E., & Brisson, A. (2005). The formation of supported lipid bilayers on silica nanoparticles revealed by cryoelectron microscopy. *Nano Letters*. https://doi.org/10.1021/nl048153y

Mousavi, S. H., Haratizadeh, H., & Minaee, H. (2011). The effect of morphology and doping on photoluminescence of ZnO nanostructures. *Optics Communications*. https://doi.org/10.1016/j.optcom.2011.03.078

Mu, Q., David, C. A., Galceran, J., Rey-Castro, C., Krzemiński, Ł., Wallace, R., Bamiduro, F., Milne, S. J., Hondow, N. S., Brydson, R., Vizcay-Barrena, G., Routledge, M. N., Jeuken, L. J. C., & Brown, A. P. (2014). Systematic investigation of the physicochemical factors that contribute to the toxicity of ZnO nanoparticles. *Chemical Research in Toxicology*. https://doi.org/10.1021/tx4004243

Mulens-Arias, V., Nicolás-Boluda, A., Silva, A. K. A., & Gazeau, F. (2018). Theranostic Iron Oxide Nanoparticle Cargo Defines Extracellular Vesicle-Dependent Modulation of Macrophage Activation and Migratory Behavior. *Advanced Biosystems*. https://doi.org/10.1002/adbi.201800079

Munagala, R., Aqil, F., Jeyabalan, J., & Gupta, R. C. (2016). Bovine milk-derived exosomes for drug delivery. *Cancer Letters*. https://doi.org/10.1016/j.canlet.2015.10.020

Munson, P. B., & Shukla, A. (2018). Introduction to exosomes and cancer. In *Diagnostic and Therapeutic Applications of Exosomes in Cancer*. https://doi.org/10.1016/B978-0-12-812774-2.00001-8

Mura, S., Nicolas, J., & Couvreur, P. (2013). Stimuli-responsive nanocarriers for drug delivery. In *Nature Materials*. https://doi.org/10.1038/nmat3776

Nair, S., Sasidharan, A., Divya Rani, V. V., Menon, D., Nair, S., Manzoor, K., & Raina, S. (2009). Role of size scale of ZnO nanoparticles and microparticles on toxicity toward bacteria and osteoblast cancer cells. *Journal of Materials Science: Materials in Medicine*. https://doi.org/10.1007/s10856-008-3548-5

Nakase, I., Kogure, K., Harashima, H., & Futaki, S. (2011). Application of a fusiogenic peptide GALA for intracellular delivery. *Methods in Molecular Biology (Clifton, N.J.)*. https://doi.org/10.1007/978-1-60761-919-2_37

Namee, N. M., & O'Driscoll, L. (2018). Extracellular vesicles and anti-cancer drug resistance. In *Biochimica et Biophysica Acta - Reviews on Cancer*. https://doi.org/10.1016/j.bbcan.2018.07.003

Naveed Ul Haq, A., Nadhman, A., Ullah, I., Mustafa, G., Yasinzai, M., & Khan, I. (2017). Synthesis Approaches of Zinc Oxide Nanoparticles: The Dilemma of Ecotoxicity. In *Journal of Nanomaterials*. https://doi.org/10.1155/2017/8510342

Nguyen, V. H., & Lee, B. J. (2017). Protein corona: A new approach for nanomedicine design. In *International Journal of Nanomedicine*. https://doi.org/10.2147/IJN.S129300

Nicolas, J., Mura, S., Brambilla, D., Mackiewicz, N., & Couvreur, P. (2013). Design, functionalization strategies and biomedical applications of targeted biodegradable/biocompatible polymer-based nanocarriers for drug delivery. *Chemical Society Reviews*. https://doi.org/10.1039/c2cs35265f

Nierenberg, D., Khaled, A. R., & Flores, O. (2018). Formation of a protein corona influences the biological identity of nanomaterials. *Reports of Practical Oncology and Radiotherapy*. https://doi.org/10.1016/j.rpor.2018.05.005

NIH. (2007). Understanding Cancer. In National Institutes of Health (US) (Ed.), *Biological Sciences Curriculum Study. NIH Curriculum Supplement Series*. https://www.ncbi.nlm.nih.gov/books/NBK20362/

Norberg, N. S., & Gamelin, D. R. (2005). Influence of surface modification on the luminescence of colloidal ZnO nanocrystals. *Journal of Physical Chemistry B*. https://doi.org/10.1021/jp0535285

Ogata, K., Komuro, T., Hama, K., Koike, K., Sasa, S., Inoue, M., & Yano, M. (2004). Characterization of undoped ZnO layers grown by molecular beam epitaxy towards biosensing devices. *Physica Status Solidi (B) Basic Research*. https://doi.org/10.1002/pssb.200304196

Özgür, Ü., Alivov, Y. I., Liu, C., Teke, A., Reshchikov, M. A., Doğan, S., Avrutin, V., Cho, S. J., & Morko¸, H. (2005). A comprehensive review of ZnO materials and devices. In *Journal of Applied Physics*. https://doi.org/10.1063/1.1992666

Pacholski, C., Kornowski, A., & Weller, H. (2002). Self-assembly of ZnO: From nanodots to nanorods. *Angewandte Chemie - International Edition*. https://doi.org/10.1002/1521-3773(20020402)41:7<1188::AID-ANIE1188>3.0.CO;2-5

Pan, B. T., & Johnstone, R. M. (1983). Fate of the transferrin receptor during maturation of sheep reticulocytes in vitro: Selective externalization of the receptor. *Cell*. https://doi.org/10.1016/0092-8674(83)90040-5

Pandurangan, M., Enkhtaivan, G., & Kim, D. H. (2016). Anticancer studies of synthesized ZnO nanoparticles against human cervical carcinoma cells. *Journal of Photochemistry and Photobiology B: Biology*. https://doi.org/10.1016/j.jphotobiol.2016.03.002

Pascucci, L., Coccè, V., Bonomi, A., Ami, D., Ceccarelli, P., Ciusani, E., Viganò, L., Locatelli, A., Sisto, F., Doglia, S. M., Parati, E., Bernardo, M. E., Muraca, M., Alessandri, G., Bondiolotti, G., & Pessina, A. (2014). Paclitaxel is incorporated by mesenchymal stromal cells and released in exosomes that inhibit in vitro tumor growth: A new approach for drug delivery. *Journal of Controlled Release*. https://doi.org/10.1016/j.jconrel.2014.07.042

Peinado, H., Zhang, H., Matei, I. R., Costa-Silva, B., Hoshino, A., Rodrigues, G., Psaila, B., Kaplan, R. N., Bromberg, J. F., Kang, Y., Bissell, M. J., Cox, T. R., Giaccia, A. J., Erler, J. T., Hiratsuka, S., Ghajar, C. M., & Lyden, D. (2017). Pre-metastatic niches: Organ-specific homes for metastases. In *Nature Reviews Cancer*. https://doi.org/10.1038/nrc.2017.6

Pelaz, B., Del Pino, P., Maffre, P., Hartmann, R., Gallego, M., Rivera-Fernández, S., De La Fuente, J. M., Nienhaus, G. U., & Parak, W. J. (2015). Surface Functionalization of Nanoparticles with Polyethylene Glycol: Effects on Protein Adsorption and Cellular Uptake. *ACS Nano*. https://doi.org/10.1021/acsnano.5b01326

Perera, W. P. T. D., Dissanayake, R. K., Ranatunga, U. I., Hettiarachchi, N. M., Perera, K. D. C., Unagolla, J. M., De Silva, R. T., & Pahalagedara, L. R. (2020). Curcumin loaded zinc oxide nanoparticles for activity-enhanced antibacterial and anticancer applications. *RSC Advances*. https://doi.org/10.1039/d0ra05755j

Petre, C. E., & Dittmer, D. P. (2007). Liposomal daunorubicin as treatment for Kaposi's sarcoma. In *International Journal of Nanomedicine*.

Pfrieger, F. W., & Vitale, N. (2018). Cholesterol and the journey of extracellular vesicles. *Journal of Lipid Research*. https://doi.org/10.1194/jlr.r084210

Pokrowiecki, R., Wojnarowicz, J., Zareba, T., Koltsov, I., Lojkowski, W., Tyski, S., Mielczarek, A., & Zawadzki, P. (2019). Nanoparticles and human saliva: A step towards drug delivery systems for dental and craniofacial biomaterials. *International Journal of Nanomedicine*. https://doi.org/10.2147/IJN.S221608

Pomatto, M. A. C., Bussolati, B., D'Antico, S., Ghiotto, S., Tetta, C., Brizzi, M. F., & Camussi, G. (2019). Improved Loading of Plasma-Derived Extracellular Vesicles to Encapsulate Antitumor miRNAs. *Molecular Therapy - Methods and Clinical Development*. https://doi.org/10.1016/j.omtm.2019.01.001

Prevodnik, V. K., Lavrenčak, J., Horvat, M., & Novakovič, B. J. (2011). The predictive significance of CD20 expression in B-cell lymphomas. *Diagnostic Pathology*. https://doi.org/10.1186/1746-1596-6-33

Priyadharshini, R. I., Prasannaraj, G., Geetha, N., & Venkatachalam, P. (2014). Microwave-Mediated Extracellular Synthesis of Metallic Silver and Zinc Oxide Nanoparticles Using Macro-Algae (Gracilaria edulis) Extracts and Its Anticancer Activity Against Human PC3 Cell Lines. *Applied Biochemistry and Biotechnology*. https://doi.org/10.1007/s12010-014-1225-3

Punnoose, A., Dodge, K., Rasmussen, J. W., Chess, J., Wingett, D., & Anders, C. (2014). Cytotoxicity of ZnO nanoparticles can be tailored by modifying their surface structure: A green chemistry approach for safer nanomaterials. *ACS Sustainable Chemistry and Engineering*. https://doi.org/10.1021/sc500140x

Qiao, L., Hu, S., Huang, K., Su, T., Li, Z., Vandergriff, A., Cores, J., Dinh, P. U., Allen, T., Shen, D., Liang, H., Li, Y., & Cheng, K. (2020). Tumor cell-derived exosomes home to their cells of origin and can be used as Trojan horses to deliver cancer drugs. *Theranostics*. https://doi.org/10.7150/thno.39434

Qin, W., Huang, G., Chen, Z., & Zhang, Y. (2017). Nanomaterials in targeting cancer stem cells for cancer therapy. In *Frontiers in Pharmacology*. https://doi.org/10.3389/fphar.2017.00001

Raeven, P., Zipperle, J., & Drechsler, S. (2018). Extracellular vesicles as markers and mediators in sepsis. In *Theranostics*. https://doi.org/10.7150/thno.23453

Rana, S., Yue, S., Stadel, D., & Zöller, M. (2012). Toward tailored exosomes: The exosomal tetraspanin web contributes to target cell selection. *International Journal of Biochemistry and Cell Biology*. https://doi.org/10.1016/j.biocel.2012.06.018

Raposo, G., Nijman, H. W., Stoorvogel, W., Leijendekker, R., Harding, C. V., Melief, C. J. M., & Geuze, H. J. (1996). B lymphocytes secrete antigen-presenting vesicles. *Journal of Experimental Medicine*. https://doi.org/10.1084/jem.183.3.1161

Raposo, G., & Stoorvogel, W. (2013). Extracellular vesicles: Exosomes, microvesicles, and friends. In *Journal of Cell Biology*. https://doi.org/10.1083/jcb.201211138

Rasmussen, J. W., Martinez, E., Louka, P., & Wingett, D. G. (2010). Zinc oxide nanoparticles for selective destruction of tumor cells and potential for drug delivery applications. In *Expert Opinion on Drug Delivery*. https://doi.org/10.1517/17425247.2010.502560

Ratajczak, J., Wysoczynski, M., Hayek, F., Janowska-Wieczorek, A., & Ratajczak, M. Z. (2006). Membrane-derived microvesicles: Important and underappreciated mediators of cell-to-cell communication. In *Leukemia*. https://doi.org/10.1038/sj.leu.2404296

Rayamajhi, S., & Aryal, S. (2020). Surface functionalization strategies of extracellular vesicles. In *Journal of Materials Chemistry B*. https://doi.org/10.1039/d0tb00744g

Reed, R. B., Ladner, D. A., Higgins, C. P., Westerhoff, P., & Ranville, J. F. (2012). Solubility of nano-zinc oxide in environmentally and biologically important matrices. *Environmental Toxicology and Chemistry*. https://doi.org/10.1002/etc.708

Regan, P. O. (2007). The impact of cancer and its treatment on wound healing. In *Wounds UK*.

Roballo, K. C. S., da Silveira, J. C., Bressan, F. F., de Souza, A. F., Pereira, V. M., Porras, J. E. P., Rós, F. A., Pulz, L. H., Strefezzi, R. de F., Martins, D. D. S., Meirelles, F. V., & Ambrósio, C. E. (2019). Neurons-derived extracellular vesicles promote neural differentiation of ADSCs: a model to prevent peripheral nerve degeneration. *Scientific Reports*. https://doi.org/10.1038/s41598-019-47229-x

Rodrigues, M., Fan, J., Lyon, C., Wan, M., & Hu, Y. (2018). Role of extracellular vesicles in viral and bacterial infections: Pathogenesis, diagnostics, and therapeutics. In *Theranostics*. https://doi.org/10.7150/thno.20576

Rome, S. (2019). Biological properties of plant-derived extracellular vesicles. *Food and Function*. https://doi.org/10.1039/c8fo02295j

Rosado, M., Silva, R., G. Bexiga, M., G. Jones, J., Manadas, B., & Anjo, S. I. (2019). Advances in biomarker detection: Alternative approaches for blood-based biomarker detection. In *Advances in Clinical Chemistry*. https://doi.org/10.1016/bs.acc.2019.04.003

Royo, F., Cossío, U., Ruiz De Angulo, A., Llop, J., & Falcon-Perez, J. M. (2019). Modification of the glycosylation of extracellular vesicles alters their biodistribution in mice. *Nanoscale*. https://doi.org/10.1039/c8nr03900c

Rufino-Ramos, D., Albuquerque, P. R., Carmona, V., Perfeito, R., Nobre, R. J., & Pereira de Almeida, L. (2017). Extracellular vesicles: Novel promising delivery systems for therapy of brain diseases. In *Journal of Controlled Release*. https://doi.org/10.1016/j.jconrel.2017.07.001

Sakura, T., Takahashi, T., Kataoka, K., & Nagasaki, Y. (2005). One-pot preparation of mono-dispersed and physiologically stabilized gold colloid. *Colloid and Polymer Science*. https://doi.org/10.1007/s00396-005-1339-9

Salvioni, L., Rizzuto, M. A., Bertolini, J. A., Pandolfi, L., Colombo, M., & Prosperi, D. (2019). Thirty years of cancer nanomedicine: Success, frustration, and hope. In *Cancers*. https://doi.org/10.3390/cancers11121855

Sancho-Albero, M., Navascués, N., Mendoza, G., Sebastián, V., Arruebo, M., Martín-Duque, P., & Santamaría, J. (2019). Exosome origin determines cell targeting and the transfer of therapeutic nanoparticles towards target cells. *Journal of Nanobiotechnology*. https://doi.org/10.1186/s12951-018-0437-z

Saraste, A., & Pulkki, K. (2000). Morphologic and biochemical hallmarks of apoptosis. In *Cardiovascular Research*. https://doi.org/10.1016/S0008-6363(99)00384-3

Sasidharan, A., Chandran, P., Menon, D., Raman, S., Nair, S., & Koyakutty, M. (2011). Rapid dissolution of ZnO nanocrystals in acidic cancer microenvironment leading to preferential apoptosis. *Nanoscale*. https://doi.org/10.1039/c1nr10272a

Sato, Y. T., Umezaki, K., Sawada, S., Mukai, S. A., Sasaki, Y., Harada, N., Shiku, H., & Akiyoshi, K. (2016). Engineering hybrid exosomes by membrane fusion with liposomes. *Scientific Reports*. https://doi.org/10.1038/srep21933

Senapati, S., Mahanta, A. K., Kumar, S., & Maiti, P. (2018). Controlled drug delivery vehicles for cancer treatment and their performance. In *Signal Transduction and Targeted Therapy*. https://doi.org/10.1038/s41392-017-0004-3

Seneviratne, R., Jeuken, L. J. C., Rappolt, M., & Beales, P. A. (2020). Hybrid vesicle stability under sterilisation and preservation processes used in the manufacture of medicinal formulations. *Polymers*. https://doi.org/10.3390/POLYM12040914

Shen, C., James, S. A., De jonge, M. D., Turney, T. W., Wright, P. F. A., & Feltis, B. N. (2013). Relating cytotoxicity, zinc ions, and reactive oxygen in ZnO nanoparticle-exposed human immune cells. *Toxicological Sciences*. https://doi.org/10.1093/toxsci/kft187

Shen, S. I., Jasti, B. R., & Li, X. (2003). Chapter 22: DESIGN OF CONTROLLED-RELEASE DRUG DELIVERY SYSTEMS. In *Standard Handbook of Biomedical Engineering and Design*.

Shtam, T. A., Kovalev, R. A., Varfolomeeva, E. Y., Makarov, E. M., Kil, Y. V., & Filatov, M. V. (2013). Exosomes are natural carriers of exogenous siRNA to human cells in vitro. *Cell Communication and Signaling*. https://doi.org/10.1186/1478-811X-11-88

Silva, A. K. A., Kolosnjaj-Tabi, J., Bonneau, S., Marangon, I., Boggetto, N., Aubertin, K., Clément, O., Bureau, M. F., Luciani, N., Gazeau, F., & Wilhelm, C. (2013). Magnetic and photoresponsive theranosomes: Translating cell-released vesicles into smart nanovectors for cancer therapy. *ACS Nano*. https://doi.org/10.1021/nn400269x

Singh, V., Gupta, D., Arora, R., Tripathi, R. P., Almasan, A., & Macklis, R. M. (2014). Surface levels of CD20 determine anti-CD20 antibodies mediated cell death in vitro. *PLoS ONE*. https://doi.org/10.1371/journal.pone.0111113

Sirelkhatim, A., Mahmud, S., Seeni, A., Kaus, N. H. M., Ann, L. C., Bakhori, S. K. M., Hasan, H., & Mohamad, D. (2015). Review on zinc oxide nanoparticles: Antibacterial activity and toxicity mechanism. In *Nano-Micro Letters*. https://doi.org/10.1007/s40820-015-0040-x

Smyth, T., Kullberg, M., Malik, N., Smith-Jones, P., Graner, M. W., & Anchordoquy, T. J. (2015). Biodistribution and delivery efficiency of unmodified tumor-derived exosomes. *Journal of Controlled Release*. https://doi.org/10.1016/j.jconrel.2014.12.013

Smyth, T., Petrova, K., Payton, N. M., Persaud, I., Redzic, J. S., Graner, M. W., Smith-Jones, P., & Anchordoquy, T. J. (2014). Surface functionalization of exosomes using click chemistry. *Bioconjugate Chemistry*. https://doi.org/10.1021/bc500291r

Song, W., Zhang, J., Guo, J., Zhang, J., Ding, F., Li, L., & Sun, Z. (2010). Role of the dissolved zinc ion and reactive oxygen species in cytotoxicity of ZnO nanoparticles. *Toxicology Letters*. https://doi.org/10.1016/j.toxlet.2010.10.003

Srivastava, A., Amreddy, N., Babu, A., Panneerselvam, J., Mehta, M., Muralidharan, R., Chen, A., Zhao, Y. D., Razaq, M., Riedinger, N., Kim, H., Liu, S., Wu, S., Abdel-Mageed, A. B., Munshi, A., & Ramesh, R. (2016). Nanosomes carrying doxorubicin exhibit potent anticancer activity against human lung cancer cells. *Scientific Reports*. https://doi.org/10.1038/srep38541

Stefanidou, M., Maravelias, C., Dona, A., & Spiliopoulou, C. (2006). Zinc: A multipurpose trace element. In *Archives of Toxicology*. https://doi.org/10.1007/s00204-005-0009-5

Sun, W., Luo, J. D., Jiang, H., & Duan, D. D. (2018). Tumor exosomes: A double-edged sword in cancer therapy. In *Acta Pharmacologica Sinica*. https://doi.org/10.1038/aps.2018.17

Susa, F., Limongi, T., Dumontel, B., Vighetto, V., & Cauda, V. (2019). Engineered extracellular vesicles as a reliable tool in cancer nanomedicine. In *Cancers*. https://doi.org/10.3390/cancers11121979

Sutaria, D. S., Badawi, M., Phelps, M. A., & Schmittgen, T. D. (2017). Achieving the Promise of Therapeutic Extracellular Vesicles: The Devil is in Details of Therapeutic Loading. In *Pharmaceutical Research*. https://doi.org/10.1007/s11095-017-2123-5

Syama, S., Sreekanth, P. J., Varma, H. K., & Mohanan, P. V. (2014). Zinc oxide nanoparticles induced oxidative stress in mouse bone marrow mesenchymal stem cells. *Toxicology Mechanisms and Methods*. https://doi.org/10.3109/15376516.2014.956914

Takakura, Y., Matsumoto, A., & Takahashi, Y. (2020). Therapeutic application of small extracellular vesicles (SEVs): Pharmaceutical and pharmacokinetic challenges. In *Biological and Pharmaceutical Bulletin*. https://doi.org/10.1248/bpb.b19-00831

Tan, S., Li, X., Guo, Y., & Zhang, Z. (2013). Lipid-enveloped hybrid nanoparticles for drug delivery. In *Nanoscale*. https://doi.org/10.1039/c2nr32880a

Taylor, D. D., & Gercel-Taylor, C. (2011). Exosomes/microvesicles: mediators of cancer-associated immunosuppressive microenvironments. In *Seminars in immunopathology*. https://doi.org/10.1007/s00281-010-0234-8

Tee, J. K., Yip, L. X., Tan, E. S., Santitewagun, S., Prasath, A., Ke, P. C., Ho, H. K., & Leong, D. T. (2019). Nanoparticles' interactions with vasculature in diseases. In *Chemical Society Reviews*. https://doi.org/10.1039/c9cs00309f

Théry, C., Amigorena, S., Raposo, G., & Clayton, A. (2006). Isolation and Characterization of Exosomes from Cell Culture Supernatants and Biological Fluids. *Current Protocols in Cell Biology*. https://doi.org/10.1002/0471143030.cb0322s30

Théry, C., Witwer, K. W., Aikawa, E., Alcaraz, M. J., Anderson, J. D., Andriantsitohaina, R., Antoniou, A., Arab, T., Archer, F., Atkin-Smith, G. K., Ayre, D. C., Bach, J. M., Bachurski, D., Baharvand, H., Balaj, L., Baldacchino, S., Bauer, N. N., Baxter, A. A., Bebawy, M., … Zuba-Surma, E. K. (2018). Minimal information for studies of extracellular vesicles 2018 (MISEV2018): a position statement of the International Society for Extracellular Vesicles and update of the MISEV2014 guidelines. *Journal of Extracellular Vesicles*. https://doi.org/10.1080/20013078.2018.1535750

Théry, C., Zitvogel, L., & Amigorena, S. (2002). Exosomes: Composition, biogenesis and function. In *Nature Reviews Immunology*. https://doi.org/10.1038/nri855

Thi, T. T. H., Pilkington, E. H., Nguyen, D. H., Lee, J. S., Park, K. D., & Truong, N. P. (2020). The importance of Poly(ethylene glycol) alternatives for overcoming PEG immunogenicity in drug delivery and bioconjugation. In *Polymers*. https://doi.org/10.3390/polym12020298

Tian, T., Wang, Y., Wang, H., Zhu, Z., & Xiao, Z. (2010). Visualizing of the cellular uptake and intracellular trafficking of exosomes by live-cell microscopy. *Journal of Cellular Biochemistry*. https://doi.org/10.1002/jcb.22733

Tian, Y., Li, S., Song, J., Ji, T., Zhu, M., Anderson, G. J., Wei, J., & Nie, G. (2014). A doxorubicin delivery platform using engineered natural membrane vesicle exosomes for targeted tumor therapy. *Biomaterials*. https://doi.org/10.1016/j.biomaterials.2013.11.083

Tripathy, N., Hong, T. K., Ha, K. T., Jeong, H. S., & Hahn, Y. B. (2014). Effect of ZnO nanoparticles aggregation on the toxicity in RAW 264.7 murine macrophage. *Journal of Hazardous Materials*. https://doi.org/10.1016/j.jhazmat.2014.01.043

Tsumoto, K., Isozaki, Y., Yagami, H., & Tomita, M. (2019). Future perspectives of therapeutic monoclonal antibodies. *Immunotherapy*. https://doi.org/10.2217/imt-2018-0130

Turney, T. W., Duriska, M. B., Jayaratne, V., Elbaz, A., O'Keefe, S. J., Hastings, A. S., Piva, T. J., Wright, P. F. A., & Feltis, B. N. (2012). Formation of zinc-containing nanoparticles from Zn2+ ions in cell culture media: Implications for the nanotoxicology of ZnO. *Chemical Research in Toxicology*. https://doi.org/10.1021/tx300241q

Upponi, J. R., & Torchilin, V. P. (2014). *Passive vs. Active Targeting: An Update of the EPR Role in Drug Delivery to Tumors*. https://doi.org/10.1007/978-3-319-08084-0_1

Vader, P., Mol, E. A., Pasterkamp, G., & Schiffelers, R. M. (2016). Extracellular vesicles for drug delivery. In *Advanced Drug Delivery Reviews*. https://doi.org/10.1016/j.addr.2016.02.006

Valadi, H., Ekström, K., Bossios, A., Sjöstrand, M., Lee, J. J., & Lötvall, J. O. (2007). Exosome-mediated transfer of mRNAs and microRNAs is a novel mechanism of genetic exchange between cells. *Nature Cell Biology*. https://doi.org/10.1038/ncb1596

Van Niel, G., D'Angelo, G., & Raposo, G. (2018). Shedding light on the cell biology of extracellular vesicles. In *Nature Reviews Molecular Cell Biology*. https://doi.org/10.1038/nrm.2017.125

Vaseem, M., Umar, A., & Hahn, Y. (2010). ZnO Nanoparticles : Growth, Properties, and Applications. In *Metal Oxide Nanostructures and Their Applications*.

Viezbicke, B. D., Patel, S., Davis, B. E., & Birnie, D. P. (2015). Evaluation of the Tauc method for optical absorption edge determination: ZnO thin films as a model system. *Physica Status Solidi (B) Basic Research*. https://doi.org/10.1002/pssb.201552007

Villanueva-Flores, F., Castro-Lugo, A., Ramírez, O. T., & Palomares, L. A. (2020). Understanding cellular interactions with nanomaterials: Towards a rational design of medical nanodevices. In *Nanotechnology*. https://doi.org/10.1088/1361-6528/ab5bc8

Villata, S., Canta, M., & Cauda, V. (2020). Evs and bioengineering: From cellular products to engineered nanomachines. In *International Journal of Molecular Sciences*. https://doi.org/10.3390/ijms21176048

Vinhas, R., Mendes, R., Fernandes, A. R., & Baptista, P. V. (2017). Nanoparticles-Emerging potential for managing leukemia and lymphoma. In *Frontiers in Bioengineering and Biotechnology*. https://doi.org/10.3389/fbioe.2017.00079

Visvader, J. E. (2011). Cells of origin in cancer. In *Nature*. https://doi.org/10.1038/nature09781

Wahlgren, J., Karlson, T. D. L., Brisslert, M., Vaziri Sani, F., Telemo, E., Sunnerhagen, P., & Valadi, H. (2012). Plasma exosomes can deliver exogenous short interfering RNA to monocytes and lymphocytes. *Nucleic Acids Research*. https://doi.org/10.1093/nar/gks463

Wang, J. H., Forterre, A. V., Zhao, J., Frimannsson, D. O., Delcayre, A., Antes, T. J., Efron, B., Jeffrey, S. S., Pegram, M. D., & Matin, A. C. (2018). Anti-her2 scfv-directed extracellular vesicle-mediated mRNA-based gene delivery inhibits growth of her2-positive human breast tumor xenografts by prodrug activation. *Molecular Cancer Therapeutics*. https://doi.org/10.1158/1535-7163.MCT-17-0827

Wang, W., Wang, E. Q., & Balthasar, J. P. (2008). Monoclonal antibody pharmacokinetics and pharmacodynamics. In *Clinical Pharmacology and Therapeutics*. https://doi.org/10.1038/clpt.2008.170

Wang, X., Wang, Y., Chen, Z. G., & Shin, D. M. (2009). Advances of Cancer Therapy by Nanotechnology. *Cancer Research and Treatment*. https://doi.org/10.4143/crt.2009.41.1.1

Weingart, J., Vabbilisetty, P., & Sun, X. L. (2013). Membrane mimetic surface functionalization of nanoparticles: Methods and applications. In *Advances in Colloid and Interface Science*. https://doi.org/10.1016/j.cis.2013.04.003

Weng, Y., Sui, Z., Shan, Y., Hu, Y., Chen, Y., Zhang, L., & Zhang, Y. (2016). Effective isolation of exosomes with polyethylene glycol from cell culture supernatant for in-depth proteome profiling. *Analyst*. https://doi.org/10.1039/c6an00892e

Westmeier, D., Knauer, S. K., Stauber, R. H., & Docter, D. (2017). Bio-nano interactions. In *Adverse Effects of Engineered Nanomaterials: Exposure, Toxicology, and Impact on Human Health: Second Edition*. https://doi.org/10.1016/B978-0-12-809199-9.00001-X

Wiklander, O. P. B., Nordin, J. Z., O'Loughlin, A., Gustafsson, Y., Corso, G., Mäger, I., Vader, P., Lee, Y., Sork, H., Seow, Y., Heldring, N., Alvarez-Erviti, L., Edvard Smith, C. I., Le Blanc, K., Macchiarini, P., Jungebluth, P., Wood, M. J. A., & El Andaloussi, S. (2015). Extracellular vesicle in vivo biodistribution is determined by cell source, route of administration and targeting. *Journal of Extracellular Vesicles*. https://doi.org/10.3402/jev.v4.26316

Williams, C., Royo, F., Aizpurua-Olaizola, O., Pazos, R., Boons, G. J., Reichardt, N. C., & Falcon-Perez, J. M. (2018). Glycosylation of extracellular vesicles: current knowledge, tools and clinical perspectives. In *Journal of Extracellular Vesicles*. https://doi.org/10.1080/20013078.2018.1442985

Wojnarowicz, J., Chudoba, T., & Lojkowski, W. (2020). A review of microwave synthesis of zinc oxide nanomaterials: Reactants, process parameters and morphoslogies. In *Nanomaterials*. https://doi.org/10.3390/nano10061086

Wubbolts, R., Leckie, R. S., Veenhuizen, P. T. M., Schwarzmann, G., Möbius, W., Hoernschemeyer, J., Slot, J. W., Geuze, H. J., & Stoorvogel, W. (2003). Proteomic and biochemical analyses of human B cell-derived exosomes: Potential implications for their function and multivesicular body formation. *Journal of Biological Chemistry*. https://doi.org/10.1074/jbc.M207550200

Wuttke, S., Braig, S., Preiß, T., Zimpel, A., Sicklinger, J., Bellomo, C., Rädler, J. O., Vollmar, A. M., & Bein, T. (2015). MOF nanoparticles coated by lipid bilayers and their uptake by cancer cells. *Chemical Communications*. https://doi.org/10.1039/c5cc06767g

Xiong, H. M. (2013). ZnO nanoparticles applied to bioimaging and drug delivery. *Advanced Materials*. https://doi.org/10.1002/adma.201301732

Yamamoto, K. N., Nakamura, A., & Haeno, H. (2015). The evolution of tumor metastasis during clonal expansion with alterations in metastasis driver genes. *Scientific Reports*. https://doi.org/10.1038/srep15886

Yang, Yiping. (2015). Cancer immunotherapy: Harnessing the immune system to battle cancer. In *Journal of Clinical Investigation*. https://doi.org/10.1172/JCI83871

Yang, Yoosoo, Hong, Y., Cho, E., Kim, G. B., & Kim, I. S. (2018). Extracellular vesicles as a platform for membrane-associated therapeutic protein delivery. In *Journal of Extracellular Vesicles*. https://doi.org/10.1080/20013078.2018.1440131

Yong, T., Zhang, X., Bie, N., Zhang, H., Zhang, X., Li, F., Hakeem, A., Hu, J., Gan, L., Santos, H. A., & Yang, X. (2019). Tumor exosome-based nanoparticles are efficient drug carriers for chemotherapy. *Nature Communications*. https://doi.org/10.1038/s41467-019-11718-4

Zeng, K., Li, J., Zhang, Z., Yan, M., Liao, Y., Zhang, X., & Zhao, C. (2015). Lipid-coated ZnO nanoparticles as lymphatic-targeted drug carriers: study on cell-specific toxicity in vitro and lymphatic targeting in vivo. *Journal of Materials Chemistry B*. https://doi.org/10.1039/c5tb00486a

Zhang, L., Yin, L., Wang, C., Lun, N., Qi, Y., & Xiang, D. (2010). Origin of visible photoluminescence of ZnO quantum dots: Defect-dependent and size-dependent. *Journal of Physical Chemistry C*. https://doi.org/10.1021/jp101324a

Zhang, P., Jain, P., Tsao, C., Yuan, Z., Li, W., Li, B., Wu, K., Hung, H. C., Lin, X., & Jiang, S. (2018). Polypeptides with High Zwitterion Density for Safe and Effective Therapeutics. *Angewandte Chemie - International Edition*. https://doi.org/10.1002/anie.201802452

Zheng, Z., Mounsamy, M., Lauth-De Viguerie, N., Coppel, Y., Harrisson, S., Destarac, M., Mingotaud, C., Kahn, M. L., & Marty, J. D. (2019). Luminescent zinc oxide nanoparticles: From stabilization to slow digestion depending on the nature of polymer coating. *Polymer Chemistry*. https://doi.org/10.1039/c8py01387j

Zhou, J., Xu, N., & Wang, Z. L. (2006). Dissolving behavior and stability of ZnO wires in biofluids: A study on biodegradability and biocompatibility of ZnO nanostructures. *Advanced Materials*. https://doi.org/10.1002/adma.200600200

Zhu, J., Niu, Y., Li, Y., Gong, Y., Shi, H., Huo, Q., Liu, Y., & Xu, Q. (2017). Stimuli-responsive delivery vehicles based on mesoporous silica nanoparticles: recent advances and challenges. In *Journal of Materials Chemistry B*. https://doi.org/10.1039/C6TB03066A

Zhu, P., Weng, Z., Li, X., Liu, X., Wu, S., Yeung, K. W. K., Wang, X., Cui, Z., Yang, X., & Chu, P. K. (2016). Biomedical Applications of Functionalized ZnO Nanomaterials: From Biosensors to Bioimaging. In *Advanced Materials Interfaces*. https://doi.org/10.1002/admi.201500494

Zhuang, X., Xiang, X., Grizzle, W., Sun, D., Zhang, S., Axtell, R. C., Ju, S., Mu, J., Zhang, L., Steinman, L., Miller, D., & Zhang, H. G. (2011). Treatment of brain inflammatory diseases by delivering exosome encapsulated anti-inflammatory drugs from the nasal region to the brain. *Molecular Therapy*. https://doi.org/10.1038/mt.2011.164

Appendix

List of publications included in this thesis

Dumontel Bianca, Canta Marta, Engelke Hanna, Chiodoni Angelica, Racca Luisa, Ancona Andrea, Limongi Tania, Canavese Giancarlo, and Cauda Valentina, 2017, 'Enhanced biostability and cellular uptake of zinc oxide nanocrystals shielded with a phospholipid bilayer', *Journal of Materials Chemistry B*, 5: 8799-813.

Ancona Andrea, Dumontel Bianca, Garino Nadia, Demarco Banjamin, Chatzitheodoridou Dimitra, Fazzini Walter, Engelke Hanna, and Cauda Valentina. 2018, 'Lipid-coated zinc oxide nanoparticles as innovative ROS-generators for photodynamic therapy in cancer cells', *Nanomaterials*, 8(3): 143.

Racca Luisa, Canta Marta, Dumontel Bianca, Ancona Andrea, Limongi Tania, Garino Nadia, Laurenti Marco, Canavese Giancarlo, and Cauda Valentina, 2018, '12 - Zinc Oxide Nanostructures in Biomedicine.' in Gianni Ciofani (ed.), *Smart Nanoparticles for Biomedicine* (Elsevier).

Canavese Giancarlo, Ancona Andrea, Racca Luisa, Canta Marta, Dumontel Bianca, Barbaresco Federica, Limongi Tania, and Cauda Valentina, 2018, 'Nanoparticle-assisted ultrasound: A special focus on sonodynamic therapy against cancer', *Chemical Engineering Journal*, 340: 155-72.

Garino Nadia, Tania Limongi, Bianca Dumontel, Marta Canta, Luisa Racca, Marco Laurenti, Micaela Castellino, Alberto Casu, Andrea Falqui, and Valentina Cauda, 2019, 'A Microwave-Assisted Synthesis of Zinc Oxide Nanocrystals Finely Tuned for Biological Applications', *Nanomaterials*, 9: 212.

Dumontel Bianca, Susa Francesca, Limongi Tania, Canta Marta, Racca Luisa, Chiodoni Angelica, Garino Nadia, Chiabotto Giulia, Centomo Maria L, Pignochino Ymera, and Cauda Valentina, 2019, 'ZnO nanocrystals shuttled by extracellular vesicles as effective Trojan nano-horses against cancer cells', *Nanomedicine*, 14 (21): 2815-2833.

Susa Francesca, Limongi Tania, Dumontel Bianca, Vighetto Veronica, and Cauda Valentina, 2019, 'Engineered Extracellular Vesicles as a Reliable Tool in Cancer Nanomedicine', *Cancers*, 11(12): 1979.

Additional works published during PhD but not included in this thesis

Lops Carmine, Ancona Andrea, Di Cesare Katia, Dumontel Bianca, Garino Nadia, Canavese Giancarlo, Hernandez Simelys and Cauda Valentina, 2019, Sonophotocatalytic degradation mechanisms of Rhodamine B dye via radicals generation by micro- and nano-particles of ZnO, *Applied Catalysis B:Environmental*, 243: 629-640.

Garino Nadia, Sanvitale Pasquale, Dumontel Bianca, Laurenti Marco, Colilla Montserrat, Izquierdo-Barba Isabel, Cauda Valentina and Vallet-Regi Maria, 2019, 'Zinc oxide nanocrystals as a nanoantibiotic and osteoinductive agent', *RSC Advances*, 9: 11312-11321.

Racca Luisa, Limongi Tania, Vighetto Veronica, Dumontel Bianca, Ancona Andrea, Canta Marta, Canavese Giancarlo, Garino Nadia, Cauda Valentina, 2020, 'Zinc Oxide nanocrystals and high-energy shock waves: a new synergy for the treatment', *Frontiers in Bioengineering and Biotechnology- Nanobiotechnology*, 8: 577.

Ancona Andrea, Troia Adriano, Garino Nadia, Dumontel Bianca, Cauda Valentina and Canavese Giancarlo, 2020, 'Leveraging re-chargeable nanobubbles on amine-functionalized ZnO nanocrystals for sustained ultrasound cavitation towards echographic imaging', *Ultrasonic Sonochemistry*, 67: 105132.

Attended conferences and workshops

Euromat 2017 – European Congress and Exhibition on Advanced Materials and Processes, Thessaloniki, Greece, 17-22/09/2017.
Poster presentation: 'Controlling zinc oxide nanoparticles behavior in inorganic and biological fluids', Dumontel Bianca, Canta Marta, Racca Luisa, Canavese Giancarlo e Cauda Valentina.

Merck and Elsevier Young Chemists Symposium, Rimini, Italy, 19-21/11/2018.
Poster presentation: 'Enhanced biostability and biocompatibility of zin oxide nanocrystals shielded by a phosholipid bilayer', Dumontel Bianca, Canta Marta, Susa Francesca, Racca Luisa, Ancona Andrea, Garino Nadia, Limongi Tania, Chiodoni Angelica and Cauda Valentina.

School of Nanomedicine, Trieste, Italy, 11-13/12/2019.
Poster presentation: 'Zinc oxide nanocrystals shielded by extracellular vesicles as hybrid nanoconstructs against cancer cells', Dumontel Bianca, Canta Marta, Susa Francesca, Limongi Tania, Garino Nadia, Racca Luisa, Chiodoni Angelica and Cauda Valentina.

Prizes and awards

Award for ‘Best Poster Communication’ at Merck and Elsevier Young Chemists Symposium, Rimini, Italy, 19-21/11/2018.

Nanomaterials 2020 Best Paper Award for ‘Lipid-coated zinc oxide nanoparticles as innovative ROS-generators for photodynamic therapy in cancer cells’, Ancona Andrea, Dumontel Bianca, Garino Nadia, Demarco Banjamin, Chatzitheodoridou Dimitra, Fazzini Walter, Engelke Hanna, and Cauda Valentina, *Nanomaterials*, 2018, 8(3), 143.